

12-2014

# Phase transformation studies of metal oxides to dichalcogenides in 1-d structures.

Dustin Ray Cummins 1987-  
*University of Louisville*

Follow this and additional works at: <http://ir.library.louisville.edu/etd>

 Part of the [Chemical Engineering Commons](#)

---

## Recommended Citation

Cummins, Dustin Ray 1987-, "Phase transformation studies of metal oxides to dichalcogenides in 1-d structures." (2014). *Electronic Theses and Dissertations*. Paper 1718.  
<https://doi.org/10.18297/etd/1718>

This Doctoral Dissertation is brought to you for free and open access by ThinkIR: The University of Louisville's Institutional Repository. It has been accepted for inclusion in Electronic Theses and Dissertations by an authorized administrator of ThinkIR: The University of Louisville's Institutional Repository. This title appears here courtesy of the author, who has retained all other copyrights. For more information, please contact [thinkir@louisville.edu](mailto:thinkir@louisville.edu).

PHASE TRANSFORMATION STUDIES OF METAL OXIDES TO  
DICHALCOGENIDES IN 1-D STRUCTURES

By

Dustin Ray Cummins  
B.S., University of Louisville, 2008  
M.Eng., University of Louisville, 2009

A Dissertation  
Submitted to the Faculty of the  
J. B. Speed School of Engineering  
in Partial Fulfillment of the Requirements  
for the Degree of

Doctor of Philosophy

Department of Chemical Engineering  
University of Louisville  
Louisville, KY

December 2014



PHASE TRANSFORMATION STUDIES OF METAL OXIDES TO  
DICHALCOGENIDES IN 1-D STRUCTURES

By

Dustin Ray Cummins  
B.S., University of Louisville, 2008  
M.Eng., University of Louisville, 2009

A Dissertation Approved on

December 2, 2014

by the following Dissertation Committee:

---

Mahendra K. Sunkara (Dissertation Director)

---

Delaina A. Amos

---

Bruce W. Alphenaar

---

Thomas L. Starr

---

Gamini Sumanasekera

---

Francis P. Zamborini

## DEDICATION

To my mom, who never gave up and taught me to succeed

## ABSTRACT

### PHASE TRANSFORMATION STUDIES OF METAL OXIDES TO DICHALCOGENIDES IN 1-D STRUCTURES

Dustin R. Cummins

December 2, 2014

Recently, the use of materials with nanoscale morphologies has expanded, particularly with applications in energy conversion, catalysis, and energy storage. One drawback to single crystalline nanomaterials, especially 1D nanowires, is the difficulty in synthesizing these compounds, as the material chemistry becomes more complicated. Metal oxide nanowires can be synthesized easily and can be produced in relatively large quantities. However, more complex materials, such as metal chalcogenides, cannot typically be synthesized using facile methods, and currently very few techniques involve scalable methods. Phase transformation of metal oxides nanowires to form metal sulfides and selenides by gas-solid reactions is one viable route to scalable chalcogenide production. However, the transformation of 1D materials from oxides to other compositions using gas-solid reactions has not been well studied and the underlying mechanisms involved with phase transformation are minimally understood. A fundamental understanding of how gas phase reactants interact with nanomaterials is critical to not only making new materials on the nanoscale, but also allowing the engineering and optimization of nanomorphologies for functional applications.

Iron sulfide and molybdenum sulfide nanowires are chosen as the two model materials to investigate crystal phase transformations in 1D systems.

In reaction of  $\text{Fe}_2\text{O}_3$  single crystal nanowires with  $\text{H}_2\text{S}$  gas to form  $\text{FeS}$ , the formation of a hollow nanotube morphology is observed, caused by unequal diffusion of the cation and anion, resulting in the accumulation of voids. These findings suggest that the reactant (sulfur) does not diffuse into the nanostructure; rather, iron atoms diffuse outward and react on the surface. The resulting  $\text{FeS}$  compound also has interesting optical absorption properties that could be of use in solar applications.

The conversion of  $\text{MoO}_3$  nanowires in an attempt to form  $\text{MoS}_2$  nanowires resulted in a  $\text{MoS}_2/\text{MoO}_x$  shell/core nanowire morphology, with strong diffusion limits in formation of the sulfide shell. In this case, the sulfur diffusion through the  $\text{MoS}_2$  shell limits the reaction, leading to core-shell morphology.

The  $\text{MoS}_2/\text{MoO}_x$  shell/core architecture shows considerable activity for electrocatalysis of the hydrogen evolution reaction due to the high surface area architecture for edge plane sites. Chemical intercalation of the  $\text{MoS}_2$  shell shows a further change in the crystal morphology and an improvement in catalytic activity. Reducing agents (hydrazine) are also investigated in attempts to chemically modify the  $\text{MoS}_2$  surface, changing the surface charge carrier concentrations. This is the first report of the effect of hydrazine in any chalcogenide system and the hydrazine treated  $\text{MoS}_2$  nanowire architecture shows one of the best electrocatalytic performance to date. The chemical modifications of  $\text{MoS}_2$  1D structures suggest the electrocatalytic activity can be tuned and corresponding architectures could be synthesized through phase transformation by design.

To further understand oxide to sulfide phase transformations in a generic sense for 1D systems, compounds with differing cationic diffusion rates and kinetics, *i.e.* tin oxide and zinc oxide single crystal nanowires, are reacted with H<sub>2</sub>S and the transformation effects studied. Zinc oxide forms a hollow, polycrystalline ZnS structure similar to FeS, but the hollowing and crystallinity is much less defined, highlighting the importance of epitaxial relationships during transformation reaction. The reacted tin oxide forms single crystal tin sulfide branches, while the original oxide core remains unaffected. This morphology is due to the tendency of tin cations to surface diffuse, rather than typical bulk diffusion. These experiments help to demonstrate that crystal phase transformation is more complicated than simply the diffusion rates of cations and anions. In addition, these results suggest some insight to nanomaterial degradation during use in reactive environments.



## TABLE OF CONTENTS

DEDICATION.....	iii
ABSTRACT .....	iv
LIST OF FIGURES.....	ix
I. INTRODUCTION .....	1
II. BACKGROUND .....	9
2.1 Phase Transformation in 0D Chalcogenides.....	9
2.2 Phase Transformation in 1D Structures.....	13
2.3 Phase Transformation in 2D Layered Materials.....	18
2.4 Transition Metal Chalcogenide Material Systems.....	22
2.5 Summary.....	28
III. EXPERIMENTAL AND CHARACTERIZATION TECHNIQUES.....	30
3.1 Metal Oxide Nanowire Synthesis.....	30
3.1.1 Fe <sub>2</sub> O <sub>3</sub> Nanowire Synthesis by Atmospheric Plasma Oxidation.....	30
3.1.2 MoO <sub>3</sub> Nanowire Synthesis by Hot Filament CVD.....	32
3.1.3 SnO <sub>2</sub> Nanowire Synthesis by Hot Cup CVD.....	33
3.1.4 ZnO Nanowire Synthesis by Bulk Plasma Oxidation.....	34
3.2 Sulfurization and Selenization Reactor .....	36
3.2.1 H <sub>2</sub> S Reactor.....	36
3.2.2 Two Zone Furnace.....	38
3.3 Characterization Techniques.....	39

3.3.1 Crystallographic Techniques.....	39
3.3.2 Spectroscopic Techniques.....	44
3.3.3 Electrochemical and Electrocatalytic Characterization.....	51
IV. MOLYBDENUM OXIDE TO MOLYBDENUM SULFIDE.....	58
V. CHEMICAL MODIFICATION OF MoS <sub>2</sub> SHELL/CORE NANOWIRES.....	69
5.1 Lithium Intercalation of MoS <sub>2</sub> Nanowires.....	69
5.2 Exposure of MoS <sub>2</sub> Nanowires to Reducing Agents.....	82
VI. IRON OXIDE TO IRON SULFIDE.....	102
6.1 Conversion of Iron Oxide Nanowires to Iron Sulfide Nanotubes.....	102
6.2 Photo Excited Electron Injection of FeS Nanotubes.....	125
VII. SYNTHESIS OF OTHER TRANSITION METAL CHALCOGENIDES.....	131
7.1 Conversion of Tin Oxide Nanowires to Tin Sulfide Branched Wires.....	131
7.2 Conversion of Zinc Oxide Nanowires to Zinc Sulfide Nanowires.....	141
7.3 Summary of Phase Transformation in Various Systems.....	142
VIII. CONCLUSIONS.....	146
IX. RECOMMENDATIONS.....	153
REFERENCES .....	155
CURRICULUM VITAE.....	190

## LIST OF FIGURES

### FIGURE

1.1 Representation of the limitations in current techniques for phase transformation in 0D material systems and proposed benefits of 1D structures.....	6
2.1 HRTEM showing progressive reaction of cobalt nanoparticles to with selenium in solution to form hollow CoSe nanospheres.....	11
2.2 Molecular schematic demonstrating strain-induced phase transformation of MoS <sub>2</sub> from hexagonal to trigonal.....	21
2.3 Review of literature reports of absorption coefficients and optical band gaps for common TMCs.....	23
2.4 Ball and stick model showing layered structure of 2H-MoS <sub>2</sub> .....	26
3.1 A) Schematic showing upstream atmospheric plasma flame reactor. B) Photograph of metallic iron foil exposed to atmospheric oxygen plasma.....	31
3.2 A) Schematic of hot filament chemical vapor deposition reactor (HF-CVD) for metal oxide. B) Photograph highlighting metal filament coiled around boron nitride cylinder, in electronic contact with molybdenum rod.....	33
3.3 A) Schematic of “hot cup” vapor deposition reactor for tin oxide nanowire production. B) Photograph of alumina coated tungsten heating funnel.....	34
3.4 A) Schematic of microwave plasma jet reactor used in bulk production of nanowires. B) Photograph of high density plasma jet.....	35

3.5 A) Schematic of sulfurization reactor along with key dimensions. B) Photograph of sulfurization reactor .....	37
3.6 Plot showing correlation of voltage to sulfurization reactor stage temperature.....	37
3.7 Schematic of two-zone reactor for sulfur vaporization.....	39
3.8 Schematic showing common electron shell transitions for characteristic x-rays for Energy Dispersive Spectroscopy (EDS).....	41
3.9 Diagram showing elastic and inelastic scattering in Raman spectroscopy.....	47
3.10 Schematic showing typical experimental lay out and operating principle for XPS.....	50
3.11 Schematic of three electrode electrochemical testing set up.....	52
3.12 Cyclic voltammogram of electrochemical activity of blank carbon electrode.....	55
4.1 Summary schematic of MoS <sub>2</sub> /MoO <sub>x</sub> shell/core nanowires.....	59
4.2 Reaction scheme for MoO <sub>3</sub> nanowires and sulfurization.....	60
4.3 SEM imaging of MoS <sub>2</sub> /MoO <sub>x</sub> nanowires reacted with 10% H <sub>2</sub> S/90% H <sub>2</sub> A) As grown MoO <sub>3</sub> B) 200°C, C) 300°C, D) 400°C, E) 500°C and F) 700°C.....	61
4.4 HRTEM imaging of MoS <sub>2</sub> /MoO <sub>x</sub> nanowires reacted with 10% H <sub>2</sub> S/90% H <sub>2</sub> A) As grown MoO <sub>3</sub> B) 200°C, C) 300°C, D) 400°C, E) 500°C and F) 700°C.....	63
4.5 XRD spectra of MoO <sub>3</sub> and MoS <sub>2</sub> /MoO <sub>x</sub> nanowires.....	64
4.6 Electrochemical and electrocatalytic activity of MoS <sub>2</sub> /MoO <sub>x</sub> nanowires. A) Cyclic voltammogram of MoO <sub>3</sub> nanowire array, as grown and after exposure to H <sub>2</sub> S at 150°C. B) Voltammetry of sulfurized nanowires at 200°C and 300°C. The inset highlights electrochemical degradation of the MoO <sub>x</sub> core. C) Effects on linear voltammogram after iR correction. D) Tafel slope analysis of the MoS <sub>2</sub> /MoO <sub>x</sub> shell/core nanowires	

after iR correction. E) Comparison of the Tafel slop of this MoS <sub>2</sub> architecture to other electrocatalysts reported in literature.....	67
5.1 A) SEM of as grown MoS <sub>2</sub> /MoO <sub>x</sub> shell/core nanowire array. B) HRTEM of the as grown, “thick shelled” MoS <sub>2</sub> /MoO <sub>x</sub> shell/core nanowires. C) SEM of the MoS <sub>2</sub> /MoO <sub>x</sub> shell/core nanowires after lithium intercalation. D) HRTEM showing internal effects on MoS <sub>2</sub> shell after lithium intercalation. E) SEM image of bulk MoS <sub>2</sub> powder. F) SEM image of chemically exfoliated MoS <sub>2</sub> 2D sheets. G) STEM imaging of the 1T- MoS <sub>2</sub> chemically exfoliated 2D sheets.....	70
5.2 Raman spectroscopy for the MoS <sub>2</sub> architectures, showing the vibrational modes for the as grown MoS <sub>2</sub> nanowires, the MoS <sub>2</sub> after lithium intercalation, chemically exfoliated 1T- MoS <sub>2</sub> 2D sheets, and 2H-MoS <sub>2</sub> 2D sheets.....	72
5.3 XPS analysis of the various MoS <sub>2</sub> architectures (as grown MoS <sub>2</sub> nanowires, the MoS <sub>2</sub> after lithium intercalation, chemically exfoliated 1T- MoS <sub>2</sub> 2D sheets, and 2H-MoS <sub>2</sub> 2D sheets) focusing on the core level binding energies for Mo and S.....	73
5.4 A) Linear voltammagram showing HER electrocatalytic activity for the as grown MoS <sub>2</sub> nanowires, the MoS <sub>2</sub> after lithium intercalation, chemically exfoliated 1T- MoS <sub>2</sub> 2D sheets, and 2H-MoS <sub>2</sub> 2D sheets. B) Tafel slope analysis.....	74
5.5 A) Linear voltammagram of bulk 2H-MoS <sub>2</sub> powder. B) Tafel slope analysis of bulk 2H-MoS <sub>2</sub> powder.....	77
5.6 EELS spectrum of lithium intercalated MoS <sub>2</sub> /MoO <sub>x</sub> shell/core nanowires, showing strong signal for S, Mo, and O. The inset focuses on the lithium signal.....	77
5.7 A) Normalized current density of MoS <sub>2</sub> 2D sheets and nanowires during step-by-step annealing. B) Change in Tafel slope of MoS <sub>2</sub> 2D sheets and nanowires during step-by-	

step annealing. C) Linear voltammetry showing change in activity of lithiated nanowires during step-by-step annealing. D) Linear voltammetry showing change in activity of exfoliated 1T-MoS <sub>2</sub> 2D sheets during step-by-step annealing.....	79
5.8 A) SEM image of as grown “thin shelled” MoS <sub>2</sub> /MoO <sub>x</sub> shell/core nanowires. B) SEM image of MoS <sub>2</sub> /MoO <sub>x</sub> shell/core nanowires after hydrazine exposure.....	83
5.9 A) HRETM of the as grown “thin shelled” MoS <sub>2</sub> /MoO <sub>x</sub> shell/core nanowires with 1 – 3 nm MoS <sub>2</sub> shell. B) HRTEM of “thin shelled” MoS <sub>2</sub> /MoO <sub>x</sub> shell/core nanowires after exposure to dilute hydrazine.....	84
5.10 A) Linear voltammograms of the MoS <sub>2</sub> /MoO <sub>x</sub> shell/core nanowires, both as grown and after exposure to dilute hydrazine. B) Tafel slope analysis of the as grown and hydrazine treated MoS <sub>2</sub> /MoO <sub>x</sub> shell/core nanowires, as well as a platinum wire.....	85
5.11 Raman spectroscopy for the MoS <sub>2</sub> architectures, showing the vibrational modes for the as grown MoS <sub>2</sub> nanowires, the MoS <sub>2</sub> after hydrazine exposure, chemically exfoliated 1T- MoS <sub>2</sub> 2D sheets, and 2H-MoS <sub>2</sub> 2D sheets. The J <sub>2</sub> and J <sub>3</sub> vibrational modes for 1T-MoS <sub>2</sub> are highlighted in blue.....	86
5.12 XPS analysis of the Mo 3d, S 2s, and S 2p core level binding energies for “thin shelled” MoS <sub>2</sub> /MoO <sub>x</sub> shell/core nanowires, as grown and after hydrazine.....	88
5.13 Linear sweep voltammetry showing effects of dilute acid on hydrazine treatment...89	
5.14 Linear voltammetry showing effects of annealing on hydrazine treated MoS <sub>2</sub> /MoO <sub>x</sub> shell/core nanowires.....	91
5.15 Schematic showing experimental set up for gate dependent HER electrocatalysis measurements. B) Optical microscopy image of exposed MoS <sub>2</sub> flake.....	92

5.16 Linear sweep voltammogram showing gate dependence of HER electrocatalysis in single MoS <sub>2</sub> 2D sheet .....	93
5.17 Photograph of MoS <sub>2</sub> /MoO <sub>x</sub> shell/core nanowire array in four point probe.....	94
5.18 A) Change in four point probe resistance of “thin shelled” MoS <sub>2</sub> /MoO <sub>x</sub> shell/core nanowire array as the chamber is evacuated. B) Effect of temperature annealing on the four point probe resistance of MoS <sub>2</sub> /MoO <sub>x</sub> shell/core nanowire array.....	95
5.19 A) <i>In situ</i> change in four probe resistance of MoS <sub>2</sub> /MoO <sub>x</sub> shell/core nanowires after exposure to hydrazine vapor. B) Effect of ambient air on four probe resistance.....	96
5.20 Linear voltammetry of “thick shelled” MoS <sub>2</sub> /MoO <sub>x</sub> shell/core nanowires (8-10 nm shell) treated with hydrazine.....	97
5.21 Linear voltammetry of MoO <sub>3</sub> nanowires, as grown and hydrazine treated.....	99
6.1 SEM image of as grown hematite, iron oxide nanowire array. The inset shows HRTEM analysis demonstrating single crystal nature of wire.....	103
6.2 Gibb’s phase triangle of conversion of iron oxides and sulfides in a Fe–O–S system.....	104
6.3 A) SEM image of Fe <sub>7</sub> S <sub>8</sub> nanowires, grown at 450°C B) HRTEM analysis of Fe <sub>7</sub> S <sub>8</sub> nanowire, showing single crystallinity of each segment.....	105
6.4 A) SEM of FeS <sub>x</sub> small diameter nanowires. B) HRTEM analysis of single crystal small diameter FeS <sub>x</sub> nanowire after phase transformation.....	106
6.5 SEM of the Fe <sub>2</sub> O <sub>3</sub> nanowire array after exposure to H <sub>2</sub> S at 300°C.....	107
6.6 A) Bright field TEM image of hollow, crystalline iron sulfide nanotube formed by phase transformation. B) HRTEM of single crystal FeS grain.....	109
6.7 Experimental Raman spectrum of FeS nanowires grown on Fe/Fe <sub>2</sub> O <sub>3</sub> foil.....	110

6.8 Raman spectra showing theoretical vibrational mode for FeS with NiAs structure and the effects on peak position under isotropic strain.....	111
6.9 Nanoprobe electron diffraction from a single FeS crystal grain from multiple zone axes A) [1-21-3], B) [01-10], and C) [01-11].....	112
6.10 XRD pattern of vertically oriented iron sulfide nanowire and nanotube array on an iron substrate with iron oxide interfacial layer.....	113
6.11 A) HRTEM imaging of iron oxide core/ iron sulfide shell epitaxial interface. B) Selected area electron diffraction (SAED) showing epitaxial relationship between FeS (100) crystal planes and Fe <sub>2</sub> O <sub>3</sub> (210) planes.....	114
6.12 A) Optical Absorption coefficient of FeS nanowires as a function of wavelength. B) Zoomed spectrum highlighting feature at ~1350 nm.....	116
6.13 Tauc's plot analysis of FeS absorption feature.....	117
6.14 Results of first principles DFT calculations of FeS with NiAs structure, showing ball and stick model, as well as theoretical absorption and electron band positions.....	119
6.15 STEM and corresponding EDS line spectra showing progression of iron oxide nanowire sulfurization reaction over time.....	120
6.16 Experimental determination of activation energy for diffusion during iron oxide sulfurization reaction using an Arrhenius relationship.....	122
6.17 Schematic showing the progression of the reaction of Fe <sub>2</sub> O <sub>3</sub> nanowires with H <sub>2</sub> S detailing the diffusion processes.....	124
6.18 Schematic showing theoretical band edge positions for hot carrier injection from FeS into TiO <sub>2</sub> .....	125
6.19 TEM image of FeS nanowire coated with TiO <sub>2</sub> <i>via</i> ALD.....	126



6.20 Ultrafast transient absorption pump-probe spectrum (TAPPS) contour plot.....	127
6.21 Plot of $\Delta OD$ in FeS/TiO <sub>2</sub> system at specific pump (490 nm) and probe (510 nm). Time constants are derived using a double exponential fit.....	128
6.22 Schematic summarizing results of Ultrafast spectroscopy for FeS/TiO <sub>2</sub> .....	129
7.1 A) SEM of as grown SnO <sub>2</sub> nanowire array. B) Detail SEM showing smooth, faceted surface of an individual SnO <sub>2</sub> nanowire. C) HRTEM and D) SAED of individual SnO <sub>2</sub> nanowire.....	132
7.2 A) SEM image of branched SnS <sub>x</sub> nanowire array. B) BFTEM of tin sulfide nanowire branches on tin oxide core.....	133
7.3 TEM of single SnS <sub>x</sub> nanowire branch. B) HRTEM of the Sn <sub>2</sub> S <sub>3</sub> nanowire branch.....	134
7.4 SAED of multiple tin sulfide nanowires branches.....	135
7.5 BFTEM of single SnS <sub>x</sub> shell/core interface, with SAED.....	136
7.6 UV Vis absorption spectrum of Sn <sub>2</sub> S <sub>3</sub> /SnO <sub>2</sub> nanowire array. B) Tauc's plot analysis showing indirect optical band gap.....	138
7.7 Cold (125 K) photoluminescence (PL) for Sn <sub>2</sub> S <sub>3</sub> /SnO <sub>2</sub> nanowire array.....	138
7.8 Raman spectroscopy of as grown SnO <sub>2</sub> nanowires, as well as Sn <sub>2</sub> S <sub>3</sub> /SnO <sub>2</sub> branched nanowire array.....	139
7.9 A) TEM of ZnS hollow nanowire with visible, randomly oriented voids. B) Electron diffraction of ZnS nanowire.....	142

## CHAPTER I: INTRODUCTION

Crystal phase transformation, *i.e.* chemical conversion a material from one crystal phase to another, is of fundamental interest both in research environments and commercial uses. One of the most common applications in which a phase transformation occurs regularly is the charging and discharging of lithium ion batteries. During charging and discharging, lithium ions are intercalated into the anode/cathode, which consists typically of a nano-structured semiconductor. This addition and removal of the lithium ion continually transforms the nanostructured semiconductor from one phase in to another and this directly leads to degradation of the electrode. This is clearly illustrated in an investigation involving MoS<sub>2</sub>. The bulk MoS<sub>2</sub> particles start as crystalline, but the intercalation of lithium, *i.e.* the phase transformation from MoS<sub>2</sub> to Li<sub>x</sub>MoS<sub>2</sub>, eventually destroyed the ordered structure.[1] This same degradation is observed in layered transition metal oxide materials, such as metal doped (Ni, Fe, Co) MnO<sub>2</sub>, and even organic electrodes.[2, 3] Understanding how to change, and more importantly, maintain crystallinity and morphology during crystal phase transformation will facilitate the design of improved and more robust electrodes.

Similar crystal transformations occurring during normal processing is observed in transition metal catalysts and absorbents. Catalysts operate by the absorbing of chemicals onto active sites and then reacting; this affects the crystal and chemical properties of many catalysts. This transformation and changing of crystal structure leads to the degradation of the catalysts. Common applications where this degradation is problematic is in metal oxide

supports in automotive catalytic converters, or metal oxide nanostructures in fuel desulfurization. When adsorbing compounds, whether organics from exhaust or sulfur from a fuel stream, the metal oxide framework reacts and loses crystallinity, degrading the active surface area and, eventually destroying the catalyst. [4, 5] Phase transformation studies can lead to the creation of new, longer lasting catalyst materials, as well as facilitating the regeneration of a spent, degraded catalyst.

An emerging technology that relies heavily on understanding and controlling crystal phase transformations is solid state memory applications, in which two different crystal phases of the same material acting as the data storage medium. The current form of large data storage, digital versatile discs (DVDs) operate on a simple binary phase transformation model, converting a pseudobinary compound ( $\text{GeTe} (1-x)\text{-Sb}_2\text{Te}_3 (x)$ ) from an amorphous state to a metastable cubic NiCl crystal structure using laser annealing. These amorphous and crystalline phases have different optical absorption/reflectivity properties, therefore allowing for optical recording of data onto the disc.[6, 7] This is a widely used technology, but requires exotic and relatively expensive materials. Exploiting the properties of different crystal structures, whether that is difference in optical, thermal, or magnetic properties, has been demonstrated in more earth abundant materials, particularly transition metal chalcogenide compounds, such as  $\text{FeS}_x$ [8],  $\text{InSe}$ [9], and doped  $\text{In}_2\text{O}_3$ [10, 11]. Despite the success in some commercial applications, there is still a large knowledge gap in fundamental understanding of the materials science aspects of crystal phase transformations. This emerging class of materials, transition metal chalcogenides, have potentially interesting electronic and optical properties, which make them a prime material system to be optimized with nano-structuring and chemical modification, for a

variety of applications. One of the only hindrances to implementation of chalcogenides is the inability for scalable and controllable synthesis. Crystal phase transformation, particularly conversion of one chemical structure to another, *i.e.* metal oxide to metal sulfide, seems to be an optimal solution to the synthesis issues.

Transition metal chalcogenides (TMCs) are an interesting class of materials, which consist of transition metal cations (Group 3 through 12 elements) forming a chemical compound with chalcogen anions (Group 6), which include sulfur, selenium, and tellurium. This class of materials consist predominantly of earth abundant elements and possess desirable optical and electronic properties for a variety of applications, many notable for energy generation and storage. At a time when global energy demands are increasing and rising concentrations of CO<sub>2</sub> and other greenhouse gases are leading to global climate change[12], there is a necessity for carbon free, renewable, and efficient energy generation using inexpensive, non-toxic, and scalable materials. TMCs have the potential to fulfill these requirements and be the energy source of the future, but the largest drawback is the synthesis of these materials is control of crystallinity and morphology. Creation of these materials using scalable methods is very important for future implementation in commercial devices.

Many TMCs with high surface nanomorphologies show promise as an inexpensive yet efficient alternative to traditional photoabsorption and hydrogen production. The production of hydrogen by water splitting allows for a storable chemical fuel, which is carbon free and environmentally friendly. Currently, the most common form of hydrogen production by water splitting involves the use of platinum or platinum composites as an electrocatalyst [13-15], which is very expensive and easily “poisoned” by contaminants in

the system. Other methods of hydrogen production involve thermal reforming of coal and fossil fuel[16-18], which is very cheap, but creates greenhouse gases, electrolysis of water[19], and photolytic water splitting[20], which are not efficient and expensive. Inexpensive alternatives, such as metal oxides [21, 22] are not efficient or stable for long periods, and rare earth materials[23, 24] are efficient, but economically unfeasible for large scale production. Transition metal chalcogenides, particularly MoS<sub>2</sub> and WS<sub>2</sub>, are earth abundant and efficient, with electrocatalytic performances near platinum and are most likely to be the solution to efficient hydrogen production.[25-40] The primary limitation for first, optimization of TMCs catalytic performance, then implementation into large scale devices is a fundamental understanding in the crystallographic properties of the these materials on the nanoscale, as well as scalable material creation. One dimensional nanomorphologies, referred to as nanowires, provide an optimal architecture for absorption and catalytic applications, allowing for a high surface area crystalline structure which facilitates improved charge transfer kinetics. Metal oxide nanowire synthesis is well understood and very accessible, but creation of more complex compounds, *i.e.* TMCs, is much more challenging. This dissertation seeks to investigate crystal phase transformation processes in the post-synthesis gas solid reaction to convert metal oxide 1D structures to more desirable chalcogenides.

Currently, the prevailing methods of chemical phase transformation are performed using liquid phase reactants, typically organic molecules with dispersed 0D particles with very small size scales (1 – 10 nm). These larger reactant molecules encounter significant diffusion limitation during the chemical reaction of solid particles with liquid species, which necessitates the small dimensioned particles. Solid state reactions require high

pressures and high temperatures, due to the even larger diffusion limits. A representation of the limitations in current technologies using 0D materials and how 1D structure can overcome these limitations is outlined in Figure 1.1. Here, we propose that using a gas phase anion reactant species, like  $H_2$ ,  $N_2$ ,  $H_2S$ , etc. will have a diffusive advantage, capable of longer diffusion lengths into the solid system, so more favorable conversion and crystal transformation. Further, as the size of the particle increases in 0D systems, there is less control over the resulting crystallinity and morphology, typically forming highly polycrystalline structures. Using 1D structures having micron scale lengths with nanometer scale diameters, should not only help overcome diffusion limits, but will also provide support and control over the crystallinity of the reacted material, whether this be single crystal to single crystal conversion, or nucleated polycrystalline growth. One benefit of single crystal 1D nanowires, compared to 0D particles for chemical conversion, is uniformity in exposed surface crystal planes; crystal lattice planes are consistent in most 1D single crystal nanowires along the growth direction, while the lattice planes vary with the curvature of 0D spherical particles. This will favor epitaxial growth/orientation during chemical reactions with 1D nanowires. From a material science perspective, it is not clear if reaction processes follow the same “rules” (diffusion, kinetics, nucleation, and growth) in nanoscale 0D particles when compared to 1D structures, so the reactions in 0D particles are not necessarily applicable to 1D systems. This motivates this fundamental investigation of gas-solid reactions in nanowires; how different are 0D, 1D, and even 2D architectures? An understanding of how crystal structures change and interact, during both reaction of one material system to form another, as well as crystal transitions in the same material, *e.g.*

hexagonal to cubic structure, has never been adequately explored and will have profound implications in fundamental material science on the nanoscale.

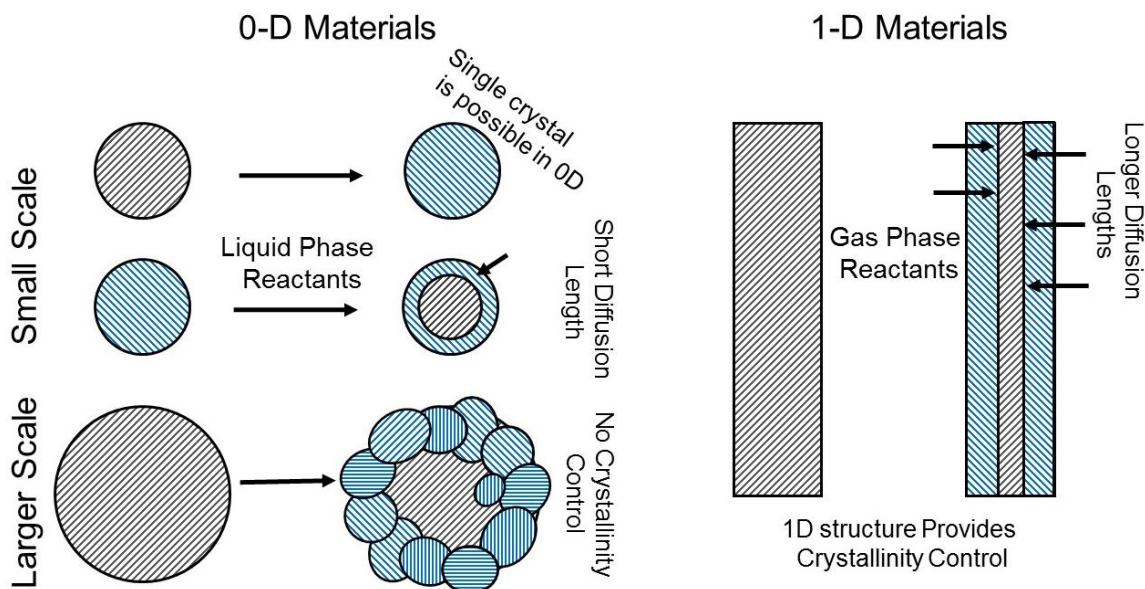


**Figure 1.1.** Representation of the limitations in current techniques for phase transformation in 0-D material systems, which typically suffer from poor crystallinity control and diffusion inhibitions. It is proposed that 1-D morphologies, along with gas phase reactants, can overcome this limitations.

The primary objectives put forth in this dissertation are:

- Develop a fundamental understanding of phase transformation and diffusion processes occurring in gas-solid reactions of metal oxide nanowires with chalcogen sources to synthesize sulfide and selenide compounds with 1D morphologies. This involves extensive crystallographic and spectroscopic characterization
- After optimization and understanding of the TMCs nanomorphology synthesis, these materials are implemented in photoelectrochemical and electrocatalytic device application to demonstrate the increased performance resulting from the 1D

structure resulting from phase transformation. This not only involves understanding the performance of the as-synthesized nanowires, but also using chemical modification techniques to further exploit this optimal architecture.

Understanding phase transformation on the nanoscale, particularly in post-synthesis metal oxide gas solid reactions to form these chalcogenides provides not only the opportunity for novel material synthesis, which may be impossible using other techniques, but also tailoring the nanomorphology to optimize the material for the desired applications.

Chapter II begins by laying a foundation with a strong review of phase transformation in 0D nanoparticles, then expanding to chalcogen phase transformation in 1D materials and 2D sheets. The favorable electronic and optical properties of select TMCs are discussed along with materials possessing a unique 2D layered structure, with focus on the current methods of synthesizing TMCs in nanoscale morphologies.

Chapter III describes the synthesis techniques used in the creation of metal oxide nanowires for this research and the reactor designs for the sulfurization reaction. Crystallographic and spectroscopic characterization techniques are explained, along with a thorough description of electrochemical techniques used in electrocatalysis of the hydrogen evolution reaction.

Chapter IV describes the synthesis of  $\text{MoS}_2/\text{MoO}_x$  shell/core nanowires using sulfurization of  $\text{MoO}_3$  nanowire arrays and the strong applications in electrocatalysis. A brief review of the state of the art in  $\text{MoS}_2$  for electrocatalysis highlights the novelty and improved performance following phase transformation. Due to the strong catalytic performance of these nanowires, further chemical modification is pursued, involving both the intercalation of lithium to attempts to induce a crystal phase change to a metastable



MoS<sub>2</sub> structure, as well as using strong electron donors and reducing agents to electrochemically modify the nanowire surface, discussed in Chapter V.

Chapter VI describes the phase transformation of Fe<sub>2</sub>O<sub>3</sub> single crystal nanowires to FeS<sub>x</sub> hollow crystalline nanotubes and the extensive characterization, both experimental and theoretical, for application in photo energy generation. Preliminary results of “hot” electron injection from the FeS nanotubes into a wide band gap semiconductor, detected using Ultrafast pump-probe spectroscopy, are briefly discussed.

Chapter VII details other phase transformation of transition metal oxides nanowires to transition metal chalcogenides, with strong characterization of SnS<sub>x</sub>/SnO<sub>2</sub> branched nanowire growth, as well as observation of hollowing in ZnS/ZnO nanowires. These observations, together with literature reports of other cation and anion systems, are used to provide insight into the effects of differing diffusion rates and material properties. Chapter VIII outlines the conclusions that can be drawn from this work and further confirmation of the scientific and technological merit of understanding phase transformation on the nanoscale. Chapter IX briefly outlines recommendations for future work.

## CHAPTER II: BACKGROUND

This chapter provides a review of nanoscale materials and their transformations from one composition to another using various methods. Of the nanoscale materials, 0D materials have been extensively studied with respect to transformations through chemical reaction. Significantly less research has been shown for phase transformations 1D nanostructures, “nanowires” and even less in 2D layered materials. The final section reviews the appeal and desired properties of transition metal chalcogenide and the difficulties associated with their synthesis. A strong review of crystal phase transformation in multiple nanoscale geometries will not only determine the areas open for innovation and further study, but will provide insight for the proposed experiments and multiple chemical and crystallographic factor which must be taken into account when synthesizing and optimizing phase transformed nanomaterials.

### 2.1. Phase Transformation in 0D Chalcogenides

Methods for making colloidal suspensions of transition metal chalcogenides using organic chemistry methods involving metallic precursors and chalcogen rich solutions are fairly well known. The chalcogen concentration is achieved by either injection of sulfur or selenium powders into hot organic solvents, known as “hot injection”, but more commonly involves a soluble chalcogen compound, such as  $\text{Na}_2\text{S}$ , thioacetamide ( $\text{C}_2\text{H}_5\text{NS}$ ) and thiohydracrylic acid ( $\text{C}_3\text{H}_6\text{O}_2\text{S}$ ), commonly referred to as “solvothermal”. These liquid processing synthesis have been shown in a plethora of transition metal chalcogenides,

including GeTe[41, 42], ZnS[43], Bi<sub>2</sub>S<sub>3</sub>[44, 45], Bi<sub>2</sub>Te<sub>3</sub>[46, 47], Ag<sub>2</sub>(S, Se, Te)[48], FeSe<sub>x</sub>[49], In<sub>2</sub>Se<sub>3</sub>[50, 51], SnSe[52, 53], CuS<sub>x</sub>[54], GaSe[55], Sb<sub>2</sub>S<sub>3</sub>[56], and others.

While the understanding of direct liquid synthesis of metal chalcogenide structures has been well established, these methods lack any significant control over morphology and chemistry. To overcome this, chemical reaction of metal and metal oxide nanostructures to serve as a template for chalcogenides through crystal phase transformation has been pursued. One of the earliest reports of the formation of 0D nanoparticles *via* the phase transformation from metal to metal chalcogen is from Paul Alivisatos at Berkeley National Laboratory in 2004.[57] These studies used cobalt nanoparticles formed by solvothermal methods. The resulting nanoparticle solution was heated to ~455 K and a sulfur solution was injected to quickly form cobalt sulfide nanoparticles in solution. HRTEM analysis showed that the resulting nanoparticles were actually hollow nanospheres on the scale of 15 nm. This hollowing effect was repeated by oxidation of the cobalt nanoparticles, as well as exposure to selenium. Time resolved formation of these hollow cobalt selenide nanospheres can be seen in Figure 2.1.

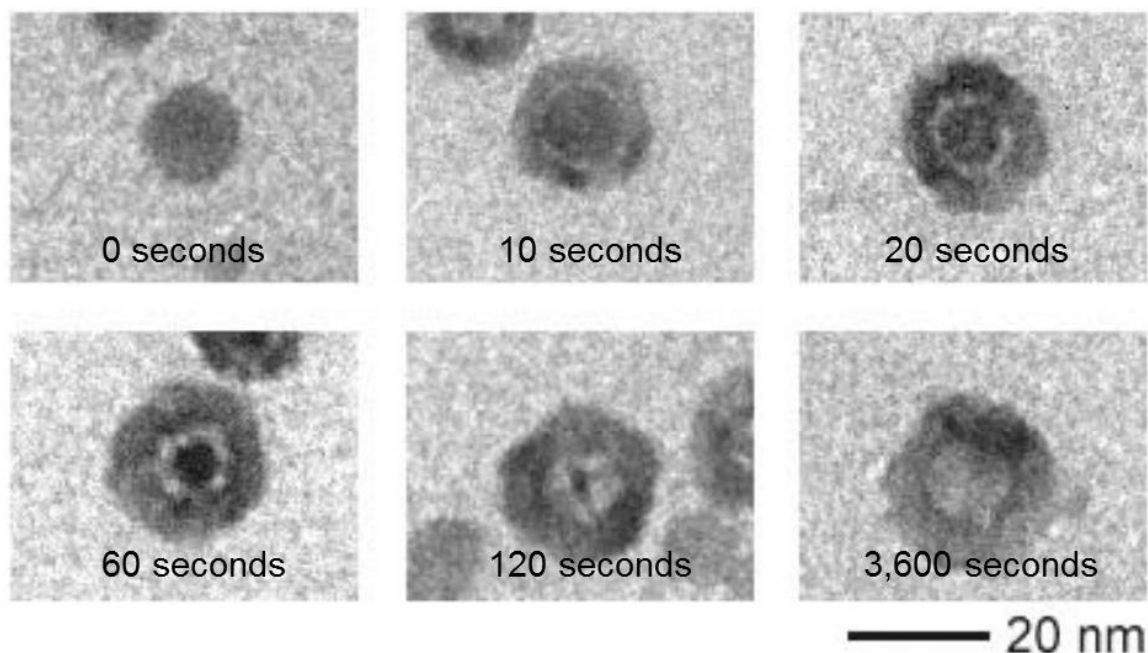


**Figure 2.1.** HRTEM showing the progressive reaction of a single crystal cobalt nanoparticle (zero seconds) with selenium in solution. The accumulation of vacancies at the core, as well as the selenide/metal reaction interface begin to appear, until the cobalt core is completely depleted, forming the hollow CoSe nanosphere. Adapted from Yin, *et al.* 2004.[57] © AAAS, 2004.

The formation of these chalcogenide nanoparticles, and more specifically hollow nanospheres, paved the way for many different material systems to be formed by chemical reactions and phase transformation. To fully understand the mechanisms underlying the phase transformation of nanoscale morphologies, it is important to look at the atomic diffusion processes occurring during reaction. The first experimental evidence that atomic diffusion occurs predominantly by movement and exchange of vacancies as opposed to direct exchange of cations and anions, reported by Smigelkas and Kirkendall in 1947.[58] In this experiment, a brass rod (alloy of copper and zinc) was heated to varying

temperatures and the formation of voids at zinc-copper interfaces was observed. It was found that the diffusion of zinc is significantly faster than the diffusion of copper in the brass alloy, which thermodynamically necessitate that cationic vacancies diffuse in the opposite direction of the net diffusion flow. Due to the large difference between the copper and zinc diffusion rates, these vacancies will either annihilate at crystal defects and/or grain boundaries or will accumulate to form macroscopic voids. This accumulation of vacancies in systems of two materials with different diffusion rates is now known as the Kirkendall Effect. This effect is most noted in electronic applications and the formation of voids in lead-tin solder. The formation of voids is seen as a detriment in many material applications, but has recently been exploited in nano materials to control the void formation and create interesting nano morphologies.

The exploitation of the Kirkendall Effect in phase transformation has, predominantly, been shown in 0D metal and metal oxide nanoparticles and nanostructures reacted in solutions concentrated with the chalcogen anions.[59, 60] This has been shown heavily in  $\text{CuS}_x$ ,  $\text{CuSe}$ , and  $\text{CuTe}_x$  nanoparticles and nanostructures, due to the fast diffusion kinetics of copper cations, as well as established crystallinity.[61-63] Understanding the effects of liquid reactants on nanoscale phase transformations has been demonstrated in non chalcogen systems as well, including formation of hollow platinum particles and spheres[64, 65], hollow Fe-Cr alloys[66], nickel phosphides[67], and many more.

This Kirkendall Effect induced formation of hollow structures, typically, has been observed only in small size scales,  $< 20$  nm. This is due to the preference for the diffusing vacancies to annihilate at defects in the crystal structure and grain boundaries in

polycrystalline materials, rather than agglomerating to form voids; the occurrence of these annihilation sites obviously increases as the size of the system increases.[68] Also, due to the necessity of small size scales, liquid phase processing dominates the current field. Using gas phase processing helps to overcome some of these limitations, but is also scalable and provides some control over morphology and chemical composition. The gas-solid reaction induced phase transformations in 0D materials has been confined almost entirely to thermal oxidation and hollow, polycrystalline spheres. This technique has been demonstrated in many transition metals.[69-77]

## 2.2. Phase Transformation in 1D Structures.

One dimensional nanomaterials, *i.e.* having a high aspect ratio and a primary size on scale of 10-100 nm, allow for unique properties in the areas of energy generation, energy storage, catalysis, and many other applications. Semiconductors with these 1D morphologies allow for small diffusion lengths in devices for minority carriers, leading to improved charge transfer kinetics, while having a large surface area, especially when compared with nanoparticles or thin films. These single crystal nanowires have many interesting properties, but one bottleneck is the synthesis methods. Unlike 0-D morphologies, the one-dimensional growth of nanostructures needs additional control, *i.e.*, enhanced crystal growth in one-dimension. Metal oxide nanowires can be efficiently and easily grown using various CVD techniques, templating, and solvothermal approaches. However it is much more difficult to directly grow metal chalcogenide (sulfides and selenides) nanowires, while maintaining crystallinity and optimize electrochemical properties. Due to the ease of synthesis of metal oxides, it stands to reason that the

“simplest” approach to chalcogenide synthesis is conversion, or phase transformation, of the metal oxide nanowire by chemical reaction.

Recently, the area of post-processing of metal or metal oxide nanowires to create new materials *via* phase transformation has gained interest, but there is still little work in the effects and mechanism of phase transformation on the nanoscale. In addition to conversion from one composition to another, there is a generic interest in phase transformation of one phase to another within 1-D. One of the first reports of crystal phase transformation in nanowires is the conversion of hexagonal GaN nanowires to a metastable cubic phase. Hexagonal wurtzite GaN nanowires were synthesized by CVD then bombarded by  $\text{Ga}^+$  ions using focused ion beam (FIB) ion implantation, which caused the phase transformation to a more stable cubic GaN, with improved electronic properties.[78] This metastable phase is difficult to form in thin films, but the unique size scale of 1D nanowires allowed for the synthesis.

The majority of phase transformation in synthesis of 1D TMCs is performed by liquid phase processing, primarily anodic exchange, but also some cationic exchange. The use of phase transformation in solutions helps to facilitate diffusion, but typically require high processing temperatures and/or long processing times. Reports of cationic exchange to form hybrid CdS/Ag<sub>2</sub>S and CdSe/Ag<sub>2</sub>Se nanowires has also been shown, but require liquid processing methods.[79, 80] This cationic exchange mechanism, however, has led to some interesting compounds, such as formation of 1D ternary compounds, such as CuInSe<sub>2</sub> nanowires by cationic reaction between In<sub>2</sub>Se<sub>3</sub> nanowires and a copper rich solution.[81] The large disadvantage for liquid processing is the lack of scalability, as well as loss of the original crystallinity and, therefore, any control on the resulting crystal

structure and morphology. The majority of liquid reaction phase transformed materials are heavily polycrystalline.

Research in phase transformation of 1D transition metal nanowires using gas-solid reactions is dominated by oxidation of metal nanowires. Nanowires have the unique properties of, predominantly, being composed of single crystal and having very few defects.[82] One of the earliest reports of metal oxide nanotube formation is in the Ni/NiO nanowire system. The single crystalline metal nickel nanowires (80 nm) are synthesized using electrodeposition in an anodic aluminum oxide template.[83-86] When exposed to oxygen at elevated temperatures, a ~10 nm NiO shell on a hollow core starts to form. This small diameter nanowire allows for the nickel cation to diffuse out much more quickly than the oxygen can diffuse into the nanowire, which forms the hollow nanotube using the Kirkendall Effect.[87] As the oxidation reaction occurs, the nickel cations diffuse quickly to the nanowire surface and of the nanowire, these vacancies accumulate at the metal/oxide interface to form voids, which agglomerate to form larger voids and, eventually, a completely hollow structure. This phase transformation using thermal oxidation has been demonstrated in formation of other metal oxide nanowires and nanotubes, such as  $\text{CuO}_x$ [88-91],  $\text{Co}_3\text{O}_4$ [92],  $\text{Nb}_2\text{O}_5$ [93],  $\text{TiO}_2$ [94],  $\text{FeO}_x$ [95],  $\text{MnO}$ [96],  $\text{MgO}$  and  $\text{ZnO}$ [97]. The understanding of the effects of thermal oxidation on 1D metallic structures can be expanded to form more complex compounds, such as nitrides and chalcogenides.

One of the first demonstrations of non-oxide formation by gas phase reaction is exposure of pseudo-1D cadmium “nanorods” to  $\text{H}_2\text{S}$  to form polycrystalline, hemispherical CdS.[98] These resultant nanowires were highly polycrystalline and were restricted to patterned substrates. Phase transformation of free standing 1D nanowires was observed in



nitride formation, creating boron nitride[99] by reaction with metallic boron nanowires with nitrogen at very high temperatures. Phase transformation of metal oxide nanowire, which are most often more thermodynamically reactive, using post synthesis gas phase reaction was first described in the conversion of  $\text{WO}_3$  nanowires to  $\text{W}_2\text{N}$  by exposure to  $\text{NH}_3$  gas.  $\text{WO}_3$  nanowires were grown by hot filament CVD, then reacted with ammonia gas at high temperatures ( $\sim 750^\circ\text{C}$ ). This resulted in a diameter dependent phase transformation; smaller diameter nanowires showed complete anion exchange with single crystal  $\text{WO}_3$  to single crystal  $\text{W}_2\text{N}$  conversion, while large diameter nanowires showed polycrystalline nucleation throughout the whole bulk of the wire, forming randomly oriented  $\text{W}_2\text{N}$  grains, which maintained the overall 1D morphology.[100]

In the area of metal chalcogenide nanowires, the zinc oxide to zinc sulfide nanowire transformation is one of the most well studied, due in part to the ease of synthesis of ZnO nanowires. The earliest report involves exposing ZnO “nanocolumns” grown by electrodeposition in a chemical bath, to  $\text{H}_2\text{S}$  gas at elevated temperatures at atmospheric pressure. The ZnO nanowires are quickly converted to polycrystalline ZnS nanocolumns, which maintain the same over hexagonal 1D morphology as the starting nanowires.[101] This work was built upon to form polycrystalline ZnS hollow nanotubes by phase transformation.[102] This hollowing effect is due to unequal cation and anion diffusion rates, resulting in the accumulation of voids, known as the Kirkendall Effect. Understanding the Kirkendall Effect and the processes taking place in the phase transformation allowed for optimization to form single crystalline hollow ZnS nanotubes.[103] Despite the success of the ZnO/ZnS system, very little work has been

done in phase transformation of nanostructures using gas-solid reactions, or the even in understanding gas-solid processes on a nanoscale.

In many applications, the transition metal chalcogenide must be single crystalline and phase pure, which cannot be accomplished using liquid methods and is unlikely using gas phase reactants. Iron sulfide, the merits of which will be discussed later in this chapter, requires absolute phase purity and crystallinity to effectively manifest its desirable properties. The most obvious morphology to achieve this is a 1D nanowire array; the first published claim of FeS<sub>2</sub> nanowires was reported by Wan, *et al.* in 2005. This method utilized an anodized aluminum oxide template, into which iron was electrodeposited, then subsequently exposed to sulfur.[104] However, the crystallographic characterization of these “nanowires” was very limited and there is almost no evidence of crystal phase identification, crystallinity, or purity provided. Single crystal pyrite nanowires were claimed by Sunkara, *et al.* in 2011, as a part of a review of inorganic nanowire synthesis and application, but there is no provided crystallographic evidence to support the claim.[82] A credible and substantiated claim to single crystal FeS<sub>2</sub> nanowires was reported by Caban-Acevedo, *et al.* in 2013. This was achieved by thermal sulfurization of an iron foil. Exposure of the iron foil at 200°C for 2 hours in a sulfur vapor atmosphere lead to direct growth of single crystal FeS<sub>2</sub> nanowires, with diameters of 4 to 10 nm and long lengths of 2 to 6 μm.[105] Extensive TEM, Raman, and optical characterization were used to confirm the cubic pyrite FeS<sub>2</sub> phase. The growth mechanism, as well as morphological control, is not well described in these reports. Other groups claim to have utilized phase transformation of 1D iron oxide nanostructures to synthesize pyrite, but typically have poor characterization and most like, lack phase purity and proper

crystallinity.[106] There is a large gap, which systematic experiments can be used to provide understanding of iron-sulfur chemistry and phase transformation to provide crystallinity and morphology control. Not only for iron sulfide, but many other sulfides have not, to date, been successfully synthesized in 1D single crystalline morphologies, especially using scalable methods.

### 2.3 Phase Transformation in 2D Layered Materials.

Phase transformation, *i.e.* chemical conversion of one compound to another, is severely understudied, due in part to the limited materials capable of forming atomically thin layered structures. Of these 2D layered materials, the most researched is graphene, composed of single atom thick two dimensional layer of carbon. These layers are weakly held together by van der Waals forces to form bulk graphite, which can be chemically or mechanically separated to form these single graphene layers. The unique properties of this single layer graphene is well studied and understood.[107-109] Individual sheets of graphene are, relatively, chemically inert and must be doped or be used as a support for some other, more active material system for real effectiveness in electrochemical or electrocatalytic applications. Since the majority of 2D materials research focuses on graphene, studies of phase transformation in 2D sheets, especially inorganic, is very limited. Boron nitride (BN) has a very similar structure to graphene and is commonly referred to as “white graphite”, not only for its layered structure, but similar hexagonal lattice. Due to these similarities in lattice structure, *h*-BN is used as a support for graphene growth and *vice versa*.[110] One of the few reports of actual phase transformation in 2D sheets involves doping graphene with boron and nitrogen, forming BCN 2D sheets, which allows for tunable mechanical properties and electronic band structure.[111]

The majority of research in crystal transformation of 2D sheets is concerned not with anion or cation exchange, but transitioning between polymorphs of the same material. This type of crystal transition is shown in carbon chemistries, transforming layers of graphene to a diamond-like structure [112] and has been researched extensively in boron nitride, converting from hexagonal, layered BN to cubic BN, which has a diamond structure and similar hardness properties. [113-118] Investigation of these crystal phase transitions, while maintaining the same material composition, has to other inorganic layered structures, including metallic bismuth[119] MoO<sub>x</sub> [120], In<sub>2</sub>Se<sub>3</sub> sheets[121], Zinc sulfates (ZDHS)[122], Ge<sub>2</sub>Sb<sub>2</sub>Te<sub>5</sub> 2D films[123], and many other transition metal chalcogens with layered structures[25].

Many transition metal dichalcogenides (TMDCs) have a similar layered structure to graphene and boron nitride, but maintain chemical functionality when exfoliated, leading to many interesting applications. TMDCs with a layered structure (LTMDs) are composed of cations, predominantly, from Group 4 – 7 metals. The oxidation state of the cation in these systems is typically 4<sup>+</sup>, while the anion has an oxidation state of 2<sup>-</sup>. In most cases, the pair of electrons contributed by the chalcogen anion are terminated at the surface of the layers, which means there are no dangling bonds on the surface, making the surface resistant to oxidation, corrosion, etc., but also typically leaves the larger, basal plane surface of the LTMDs electrochemically inert. In a single LTMD crystal layer, while the metal cation is covalently bonded to the chalcogen anion, each layer is bonded to one another only by weak van der Waals forces. The cation and anion are typically oriented in a trigonal prismatic orientation or an octahedral orientation. This octahedral orientation is, essentially, a distortion of the trigonal structure, so it is also known as trigonal

antiprismatic. Due to the multitude of transition metals which can compose LTMDs, there are a variety of polymorphs which can be formed by different stacking orientations of the individual layers, each consisting of three atomic layers (anion-cation-anion). The most common crystal stacking polymorphs are 1T, 2H, and 3R. The letters stand for the crystal orientation, *i.e.* trigonal, hexagonal, and rhombohedral respectively, while the numbers indicates the number of “layers” in each unit cell.[25] Typically, bulk LTMDs are a combination of multiple crystallographic polymorphs. One of the most interesting layered semiconductors is molybdenum disulfide, and understanding its crystal phase transformation has been shown to dramatically affect its electronic and catalytic properties.

Bulk MoS<sub>2</sub> layered can be separated to form single sheets by either chemical intercalation[124-128] or mechanical layer exfoliation.[129, 130] Specifically, during the intercalation of lithium and other alkali metals to the interlayer spacing of the MoS<sub>2</sub> not only separates the sheets, but also induces a crystal phase change from the stable trigonal 2H-MoS<sub>2</sub> to a metastable octahedral 1T-MoS<sub>2</sub>. [25, 27, 28, 124, 131] Typically the intercalation of lithium is performed by exposure to ionic liquids such as lithium borohydride (LiBH<sub>4</sub>) or n-butyllithium.[132] During the intercalation of lithium, an electron is donated to the trigonal prismatic MoS<sub>2</sub>, causing a tension in the lattice leading to a 60° rotation of the basal plane, forming the trigonal antiprismatic, or octahedral 1T-MoS<sub>2</sub> phase. Bulk 2H-MoS<sub>2</sub>, consisting of a minimum of several layers, has an indirect band gap of 1.2 eV and has semiconducting properties.[133] This metastable strained 1T-MoS<sub>2</sub>, typically consisting of only a single to a few layers, exhibits highly conducting, almost metallic properties with a direct band gap transition of ~1.9 eV.[25, 129, 131] A

molecular model showing this electron strained induced phase transformation schematically is shown in Figure 2.2.

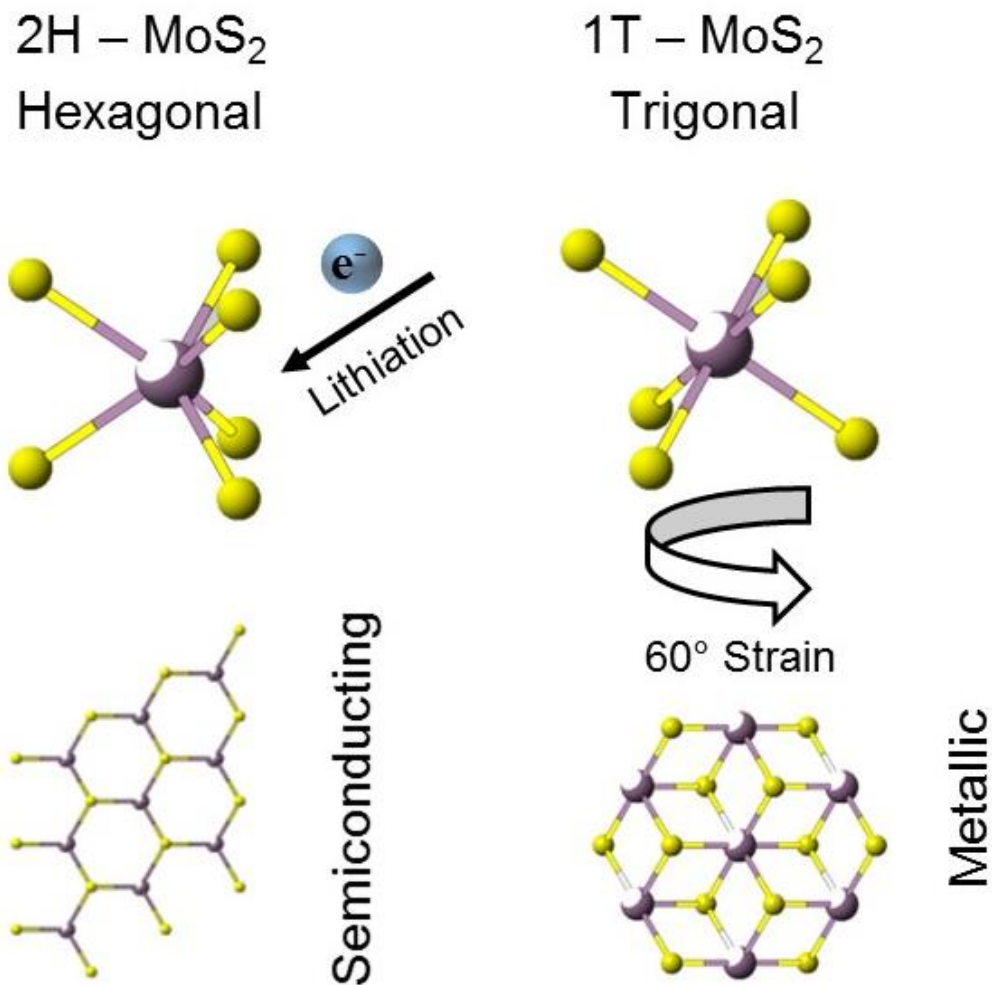


**Figure 2.2.** Molecular schematic demonstrating the strain induced phase transformation from hexagonal MoS<sub>2</sub> to trigonal MoS<sub>2</sub>. The intercalation of lithium donates an electron to the 2H lattice, causing strain to form an octahedral molecular orientation and a metastable, metallic phase.

This phase transformed 1T-MoS<sub>2</sub> has significantly different electronic, as well as chemical properties than the bulk 2H-MoS<sub>2</sub>. This plays an important role in

electrocatalysis, especially when coupled with a 1D nanowire architecture, which will be discussed in depth in Chapter 5. This 2H to 1T formation due to strain in the lattice following chemical intercalation is also observed in molybdenum selenides, as well as tungsten sulfide and selenides, which have similar layered structures.

#### 2.4. Transition Metal Chalcogenide Materials Systems

In most applications with earth abundant materials, transition metal chalcogenides present the best material system for a variety of electronic and catalytic applications. Transition metal dichalcogenides have the chemical structure  $\text{MX}_2$ , where M is a transition metal in the groups 4 – 10, and X is a chalcogen. Chalcogens are the Group 16 anions, sulfur (S), selenium (Se), tellurium (Te), and polonium (Po). Oxygen is technically a member of the chalcogen family, but since transition metal oxides are incredibly abundant and have significantly different properties than other, more active sulfide/selenide/telluride compounds, oxides are not considered TMCs. The chalcogen anions have six electrons in the valence shell, so when bound to a transition metal cation, there are two unbound electrons exposed, which makes these compounds particularly reactive. These interesting properties are most applicable and interesting as a solar absorber material for photoelectrochemical cells, as well as electrocatalytic materials.

#### **Photoabsorption**

Many transition metal chalcogenides are desirable for solar energy generation due to high optical absorption elevated charge carrier concentrations. Many of these materials are earth abundant and, due to the variety of TMCs, cover a large range of band gaps in the visible region. This variety of band gap has applications not only in thin film solar devices, but also designing photoelectrochemical devices. A plot showing a literature review of

many TMCs with band gaps in the visible region versus their respective absorption coefficient, is shown in Figure 2.3. For comparison, the absorption characteristics of crystalline silicon, the predominant material current used in commercial photovoltaics, along with amorphous silicon and gallium arsenide, used in high efficiency PV. As is clearly evident, a large amount of TMCs have absorption coefficients orders of magnitude greater than crystalline silicon, but possessing very similar band gap transitions. Transition metal sulfides (red circles), selenides (blue circles), layered structures (triangles), ternary chalcopyrites (diamonds) all share desirable properties for solar absorption.

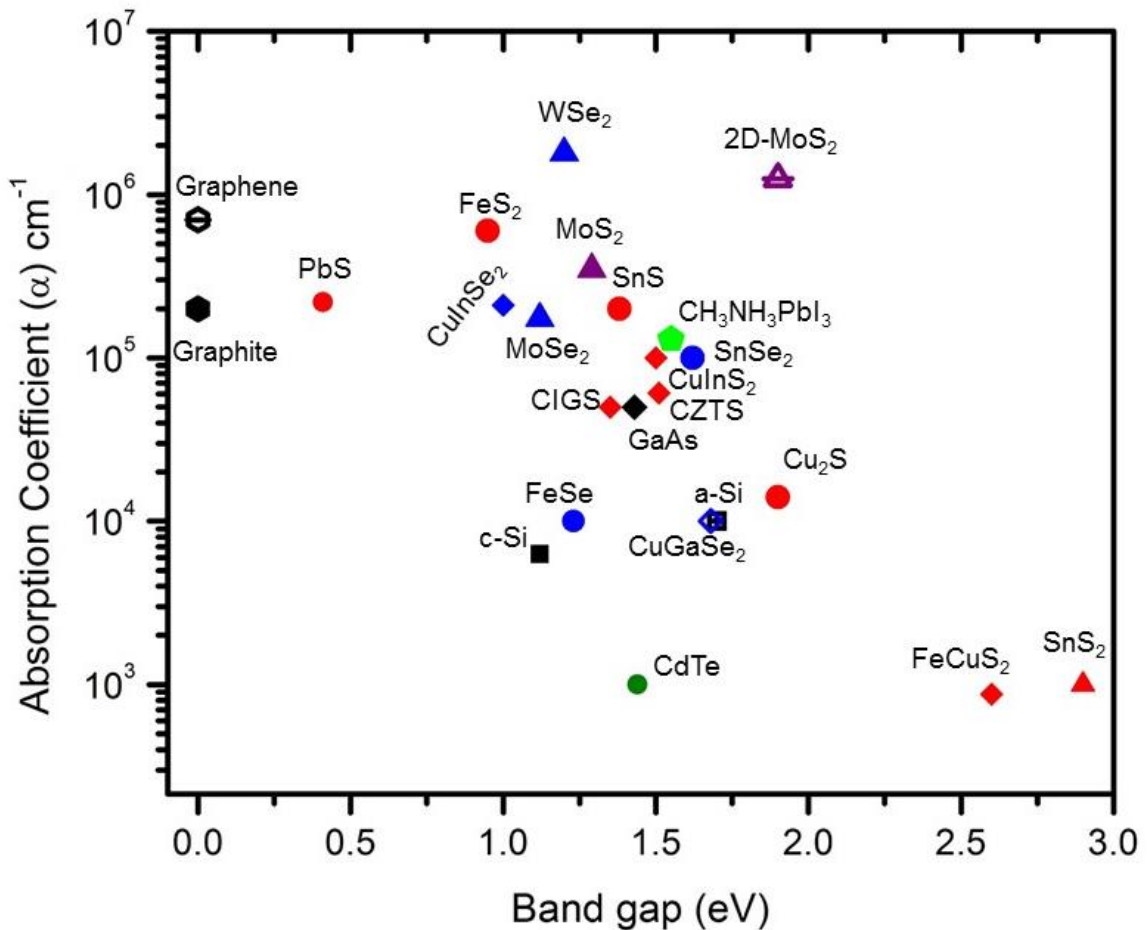




**Figure 2.3.** Review of literature reports of absorption coefficients and optical band gaps for common TMCs for thin film solar energy and photoelectrochemical applications. [129, 134-157]

Combining these properties with earth abundance and appropriate electronic band structure, materials such as iron sulfides and tin sulfides show promise for implementation in solar energy conversion. Theoretical calculations by Wadia, *et al.* shows that FeS<sub>2</sub>, cubic pyrite has the greatest potential, from an economic stand point together with its desirable band gap and optical properties, is the most desirable material for large scale photovoltaic applications.[158] Unfortunately, iron sulfides have an incredibly complicated phase diagram, with 100's of possible crystal morphologies and iron/sulfur ratios, even multiple, stable structures for the same stoichiometries.[159] It should be noted that the most desired phase, cubic FeS<sub>2</sub>, only occurs in sulfur concentrations between 50 and 52% and in a narrow synthesis temperature window, which leads to its difficult synthesis parameters.

Cubic FeS<sub>2</sub> pyrite has an indirect band gap of ~0.95 eV and a high absorption coefficient in the visible region ( $6 \times 10^5 \text{ cm}^{-2}$ ).[160] Despite the difficulty in synthesizing FeS<sub>2</sub> pyrite, especially without phase impurity, there are many reports of using nanoparticles for solar energy applications. The first report of using FeS<sub>2</sub> thin films to “sensitize” a wide band gap semiconductor (TiO<sub>2</sub>) is by Ennaoui, *et al.* The TiO<sub>2</sub> thin film is grown by a sol-gel method and an “FeS<sub>2</sub>” thin film was electrochemically deposited on the surface. This set up generated a solar to energy efficiency of ~ 1 %, which is due in a large part to the very poor quality of the deposited FeS<sub>2</sub> film.[161] The film was polycrystalline and almost certainly not phase pure. There is little evidence that the

deposited film was actually composed of cubic crystal FeS<sub>2</sub> pyrite. This, as well as other studies, details the importance of not only single crystallinity in the pyrite structure, but also phase purity.

There have been many attempts to synthesize nanoparticles and thin films of iron sulfide using MOCVD[162-164], sulfurization of iron and iron oxide films[165], reactive sputtering, spray pyrolysis[161], hydrothermal[160], solvothermal[166, 167], surfactant assisted hot injection[168], *etc.* Many of these methods reported have poor phase characterization and have many defects and chemical impurities. As mentioned previously, there have been many claims to pyrite 1D nanowire synthesis [82, 104-106], some more credible than others, but there is a lack of understanding of this complex material and extensive characterization is necessary. The proposed work for this dissertation asserts that gas-solid reaction of single crystal iron oxide nanowires with H<sub>2</sub>S gas will allow for phase purity and morphological control of the resulting iron sulfide structure.

### **Electrocatalysis**

As briefly discussed earlier in this chapter, layered TMCs have the unique property being able to be exfoliated into 2D single crystal sheets, the properties of which are drastically different than the bulk semiconductor. This section will look more in depth at the characteristics, and more importantly, the synthesis difficulties for molybdenum disulfide.

Of the multitude of layered transition metal chalcogenides, MoS<sub>2</sub> is by far the most researched, since it is earth abundant and very chemically active. Typical of layered chalcogenides, bulk MoS<sub>2</sub> has a hexagonal crystal structure with a trigonal prismatic orientation, having each Mo cation tightly bound to six sulfur anions. To form the bulk

crystal, the S-Mo-S sheets are weakly bound to one another by van der Waals forces, with an average interlayer spacing of 6.2 Å. A ball and stick model of the 2H-MoS<sub>2</sub> crystal can be seen in Figure 2.4.

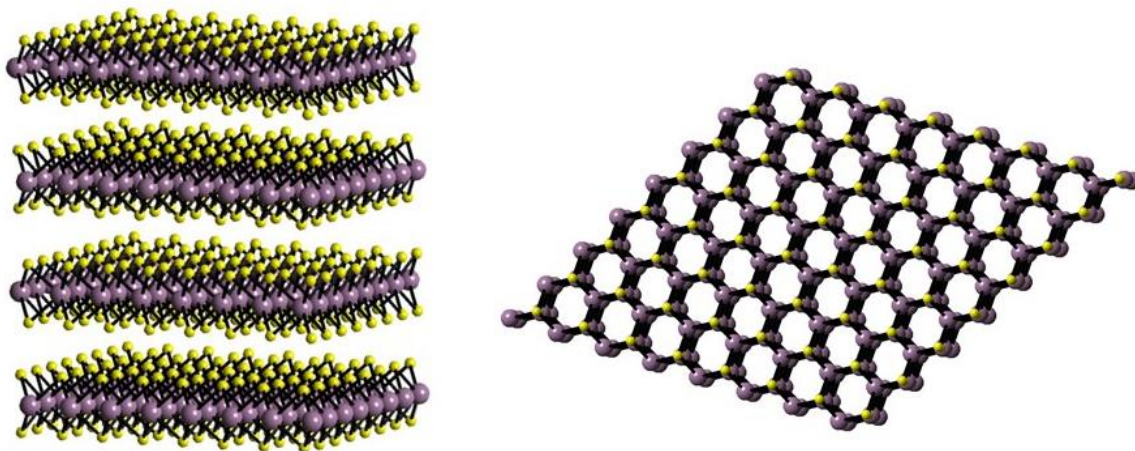


**Figure 2.4.** Ball and Stick model (Crystal Maker ®) of 2H-MoS<sub>2</sub> with the Mo cation represented by the purple sphere and the sulfur anion represented by a smaller, yellow sphere. The left hand model highlights the layered structure of the MoS<sub>2</sub>, as well as showing the chemically inert basal plane. The right hand model showcases the hexagonal structure, when observing the crystal from the (100) direction.

In a single crystal sheet, each sulfur atom is bound strongly to three molybdenum atoms to form the basal plane, which makes this plane almost completely chemically inert. Any chemical activity, whether it is reactions or catalysis, must therefore occur at sulfur vacancies, which thermodynamically, occur very rarely on the large basal surface, but instead on concentrated at the crystal edges [169-172]. During oxidation of the MoS<sub>2</sub> crystal, the crystal edges will oxidize much more quickly than the larger basal planes. Also, when dopants, such as cobalt ions, are introduced into the system, they will preferential

accumulate at these edge sites; this is further evidence that these edge sites are very chemically active compared to the larger basal crystal plane.[169] Density functional theory, along with microscopy of a single MoS<sub>2</sub> sheet shows that the S – Mo dimer which occurs at the edge sites of the 2H-MoS<sub>2</sub> crystal have highly conducting, almost metallic properties, which differ significantly from the adjacent basal plane.[173] The significantly different chemical properties of the crystal edges have the largest impact in the catalytic applications of MoS<sub>2</sub>. Jaramillo *et al.* experimentally demonstrated the significance of the catalytically active edge sites of MoS<sub>2</sub> for catalysis of the Hydrogen evolution reaction (HER). [33]

Once it was well understood that the chemical and catalytic activity of hexagonal 2H-MoS<sub>2</sub> was dependent on the exposure of the crystal edge sites, a multitude of morphologies and synthesis techniques were proposed to optimize the MoS<sub>2</sub> structures for HER electrocatalysis. Not only is the chemical reactivity highly anisotropic, but the electron transfer kinetics and chemical diffusion properties are also very dependent; electrons diffuse much more quickly along the basal plan, while even a few layers thick will inhibit any inter-layer flow. [174] The primary approach to both optimize the exposure of edge sites, as well as decrease the impediment to charge transfer is nanostructured MoS<sub>2</sub> morphologies. MoS<sub>2</sub> nanoparticles have been synthesized chemical reduction of molybdenum sulfide particles[175], as well as thermal sulfurization and decomposition[176] of molybdenum and sulfur precursors.[32] Synthesizing these layered chalcogenides has many of the same challenges as traditional bulk crystal TMCs, but now also include consideration of additional diffusion and reactivity limitations, as well as overcoming the anisotropic properties to make a functional device. Phase transformation,

from oxide to sulfide using gas reactant, can mitigate these difficulties, not only assisting in chemical conversion, due to the thermodynamic favorability of oxide to sulfide reaction, but also the nanostructure architecture opens the possibility for tailoring the anisotropic properties to optimize desired effects. Understanding phase transformation will help to overcome these limitation or use these limitations in an advantageous way, using metal oxide nanostructures to provide high surface area support for the layered materials. Understanding phase transformation in these 2D layered semiconductors, both in conversion of one material to another, as well as phase transitions from one crystal structure to another in the same compound can lead to new materials creation and optimal nano-architectures.

## 2.5 Summary

Transition metal chalcogenides have garnered a great deal of attention for their desirable electronic and chemical properties. Many of these materials have complicated phase diagrams and crystal structures, so cannot be synthesized easily, if at all, in a phase pure, nanoscale morphology by conventional chemical methods. What progress has been made uses long reaction times, high temperatures and complicated liquid techniques. More importantly, liquid processing techniques are not scalable and limit the impact of the initial starting material on morphology. Using phase transformation by gas-solid reactions of 1D metal oxides provides for a scalable method of creating transition metal chalcogenides in 1D morphologies with phase purity, improved crystallinity, and morphological control. While some initial work has been done, there are still many, very fundamental questions which have not been addressed, not limited to just 1D systems.

- Can single crystal chalcogenide nanowires be formed using gas-solid reactions with single crystal metal oxide nanowires?
- What role does the metal cation play in the resulting phase transformation and the morphology?
- How do 2D layered materials function and interact when synthesized using 1D morphologies as a template?
- The properties of the resulting 1-D materials systems and the methods for their integration into devices still needs to be studied.

Understanding the many factors which occur in nanoscale phase transformation, such as cation and anion diffusion rates, epitaxial relationships, and crystallographic properties of the reacted material will lead to synthesis of new materials, but determining which characteristics are important to the resulting structure and properties will allow for tailoring and optimizing morphologies for desired applications. This will involve extensive crystallographic and electrochemical characterization, as well as implementation in electrochemical device applications, in order to show the improved properties of the phase transformed nanowires.

## CHAPTER III: EXPERIMENTAL AND CHARACTERIZATION TECHNIQUES

This dissertation focuses on a variety of chemical reactions to first, create the transition metal oxide nanowire arrays and second, the reaction of these metal oxides, which undergo a phase transformation to create metal chalcogenide structures. This chapter provides an in depth discussion of the CVD processes used to synthesize the original metal oxide nanowire arrays, as well as the reactor chambers designed to perform the phase transformation experiments. Also discussed is the theory and working principles of the variety of crystallographic and spectroscopic materials characterization techniques used in this research, along with explanation of the electrochemical and electrocatalytic properties testing, both theoretical and practical.

### 3.1. Metal Oxide Nanowire Synthesis

#### **3.1.1. Fe<sub>2</sub>O<sub>3</sub> Nanowire Synthesis by Atmospheric Plasma Oxidation**

1D nanowires of single crystal  $\alpha$ -Fe<sub>2</sub>O<sub>3</sub> have been synthesized previously by a variety of techniques including electrodeposition in an alumina template[177, 178], hydrothermal reactions[179, 180], sol-gel and solvothermal techniques[181-183], thermal oxidation[184-186], chemical vapor deposition[187], as well as CVD assisted by plasma.[188] Many of these techniques are limited by long reaction times, especially thermal oxidation, or are limited in scalability. To overcome this, plasma oxidation of an iron foil was discovered to directly nucleate hematite nanowires from the substrate. This was first reported in vacuum oxidation by a low temperature RF plasma[189]. It is proposed that these nanowires start by nucleation of iron oxide on the foil surface, then the

oxygen radicals in the plasma react to grow this nucleus in one direction in a modified VLS mechanism, using the iron foil as a metal cation “sink”. Further optimization of this plasma oxidation led to the use of an atmospheric plasma set up to react iron foils, producing  $\text{Fe}_2\text{O}_3$  nanowires. A schematic of the plasma set up is seen in Figure 3.1. A Magnetron emits microwaves, which are focused by other physically and electronically by wave guides to a small chamber where the reactive gases, in this case  $\text{O}_2$ ,  $\text{N}_2$ , and Ar, enter the reactor. Based on the entry gas valve orientation, the gases are “sparked” to form a plasma, which is ejected upward from the reactor as a flame.[190] When an iron foil is exposed to the atmospheric plasma, it quickly reaches temperatures of  $700 - 800^\circ\text{C}$  and after  $\sim 10$  to 15 minutes of exposure, single crystal nanowires have grown from the surface. These nanowires have a large range in diameter, from 10 nm to 500 nm and lengths of  $1 - 3 \mu\text{m}$ .[191, 192] These single crystal nanowires are further discussed in the phase transformation experiments to  $\text{FeS}_x$  in Chapter VI.

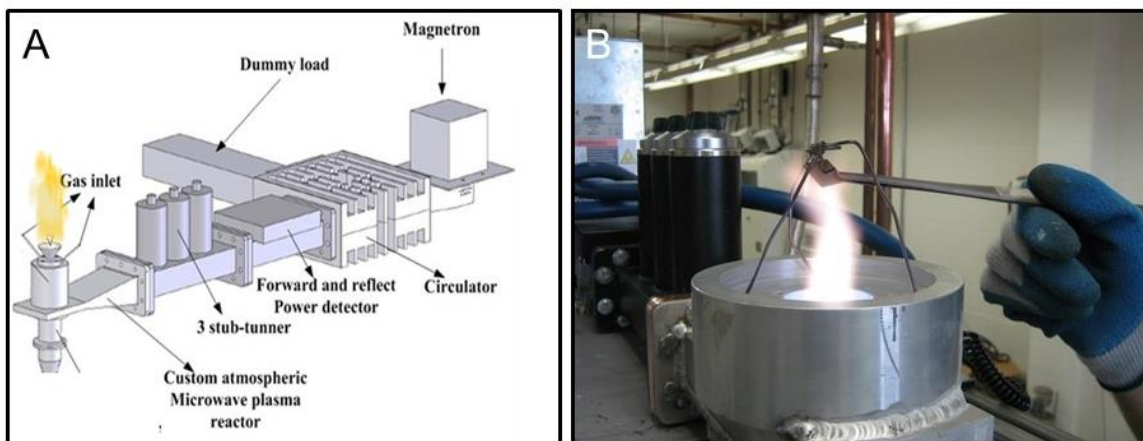


**Figure 3.1.** A) Schematic of “upstream” atmospheric plasma flame set up. B) Photograph of metallic iron foil being exposed to atmospheric oxygen plasma. Schematic was modified from Kumar, *et al.* 2008[190] by Ben Russell.



### 3.1.2. MoO<sub>3</sub> Nanowire Synthesis by Hot Filament CVD

The synthesis of MoO<sub>3</sub>, as well as WO<sub>3</sub> nanowires on a relatively bulk scale is performed by hot filament chemical vapor deposition (HF CVD). This reactor was first designed as a Master's of Engineering thesis for the bulk production of WO<sub>3</sub> nanowires.[193] 6 ft. of metal filament, typically 0.5 mm in diameter, is wound around 2 7" ceramic boron nitride cylinders and connected to 2 electrical contacts in order to apply an external voltage. This hot filament set up is placed into a 2" diameter quartz tubes vacuum reactor (32" in length). Substrates consisting of quartz, FTO, silicon, *etc.* are placed in a smaller, 1.75" quartz tube and inserted to be directly underneath the metal filament coils, with ~0.5" of separation between the filament and the growth substrates. A photograph of the HF CVD reactor set up, as well as a detail showing the coiled metal filament around the boron nitride cylinders. In the case of WO<sub>3</sub> nanowire synthesis, the tungsten metal filament is heated to ~1,650°C by an applied voltage of 25 to 30 V, in a low oxygen atmosphere, which produces vertically oriented WO<sub>3</sub> nanowire arrays on the substrates.[193, 194] To modify this process to synthesize MoO<sub>3</sub> nanowires, the reactor was modified and conditions optimized. Obviously, the tungsten source wire is replaced with molybdenum metal filament. A lower voltage is applied (17 to 22 V), yielding a lower filament temperature of ~775°C, which in a lean oxygen environment leads to a glass substrate temperature of ~450°C, facilitating the deposition and growth of single crystal, vertically oriented MoO<sub>3</sub> nanowires.[195, 196] A schematic showing the operating principles of the HFCVD are shown in Figure 3.2A, while a photograph details the metal filament coil and its electrical connection to the conducting molybdenum rod is seen in Figure 3.2B.

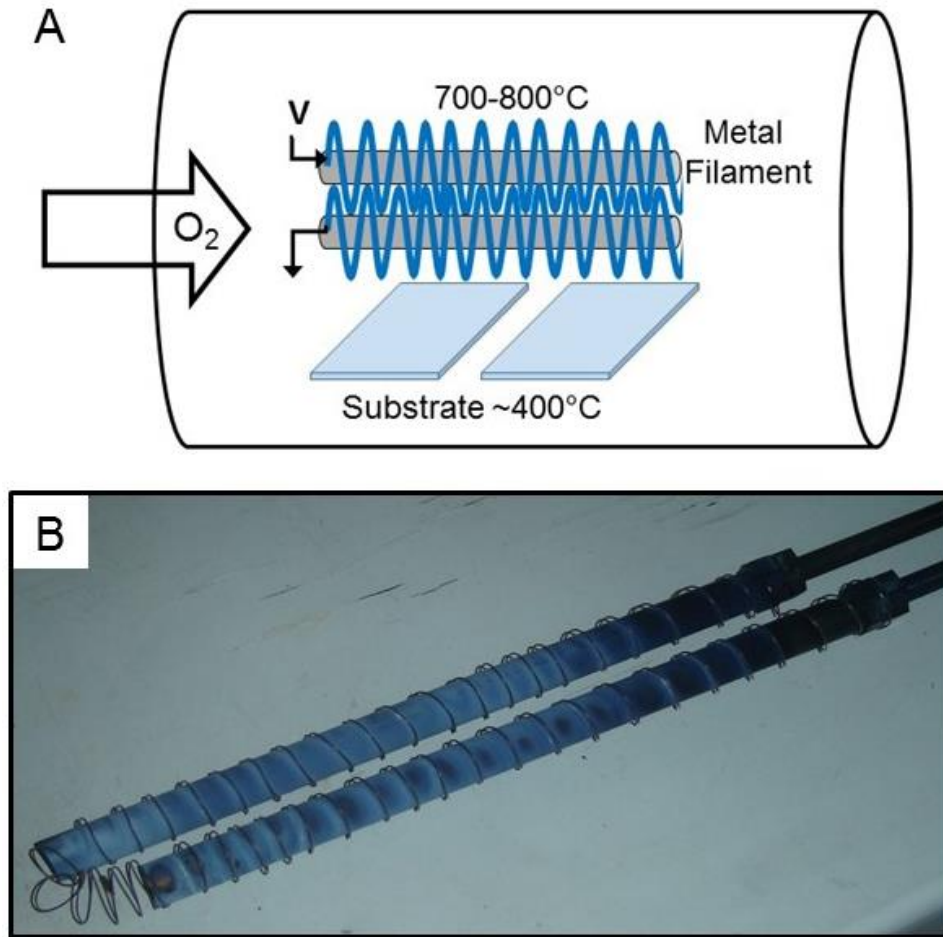


**Figure 3.2.** A) Schematic of the HF CVD quartz tube vacuum reactor highlighting the reactor setup and orientation. B) Detail showing metal filament coiled around boron nitride cylinders and electrically connected at the end of molybdenum rods. Adapted from Cummins, 2009 [195]

### 3.1.3. SnO<sub>2</sub> Nanowire Synthesis by Hot Cup CVD

Tin oxide nanowires are formed by vaporization of tin metal in a CVD reactor. The tin metal powder is placed in a funnel shaped alumina coated tungsten heater. A quartz substrate is placed over the opening of the funnel and a DC voltage of ~40 V is applied to the heater. The resistive heating quickly heats the tin metal to 1200°C causing the vaporization of the tin. In a lean oxygen reducing environment, typically 5 sccm O<sub>2</sub>

and 350 sccm of  $H_2$ , the tin vapor nucleated on the substrate and stimulates the growth of  $SnO_2$  nanowires on the quartz surface. These nanowires range in diameter from 10 nm to 300 nm and have lengths of 10's of microns. A schematic showing the operating principles of the "hot cup" reactor is shown in Figure 3.3A, and a detail of the alumina coated tungsten funnel "cup" is shown in Figure 3.3B.

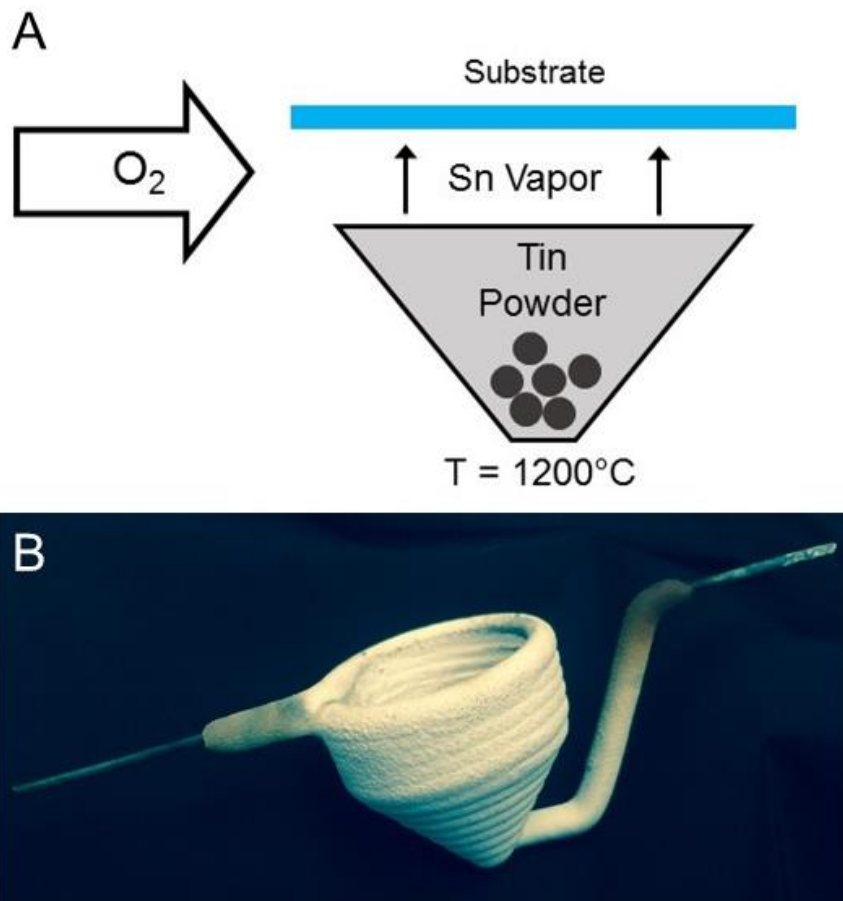


**Figure 3.3.** A) Schematic of "hot cup" CVD vacuum reactor used in  $SnO_2$  nanowire synthesis. B) Photograph of alumina coated tungsten funnel cup which acts as heater for tin metal powder.

#### 3.1.4. ZnO Nanowire Synthesis by Bulk Plasma Oxidation

ZnO nanowires were made by utilization of unique high throughput microwave atmospheric plasma flame oxidation of zinc metal nanoparticles. An  $H_2/O_2/Ar$  microwave plasma is initiated at the top of a vertically oriented 2" quartz tube. This plasma is pulled down into the tube by a combination of vacuum pumps and oriented gas flows, leading to a 12 to 15" highly reactive plasma flame. A schematic and photograph of the plasma flame reactor can be seen in Figure 3.4. The zinc metal powder is fed into the top of the plasma flame; these particles react quickly to nucleate zinc oxide nanowire powders by the time the bottom of the flame is reached (1 second). For zinc oxide nanowire and nanoparticle formation, typically a plasma power of 1400 to 1700 W is applied to spark the gases.[190] These nanowires formed are single crystal hexagonal wurtzite ZnO, with long lengths (1 – 10  $\mu m$ ) and diameters of 10 to 200 nm. For phase transformation experiments, small amounts of the ZnO nanowire powder is dispersed on carbon tape, which is mounted on thin iron foil for stability.

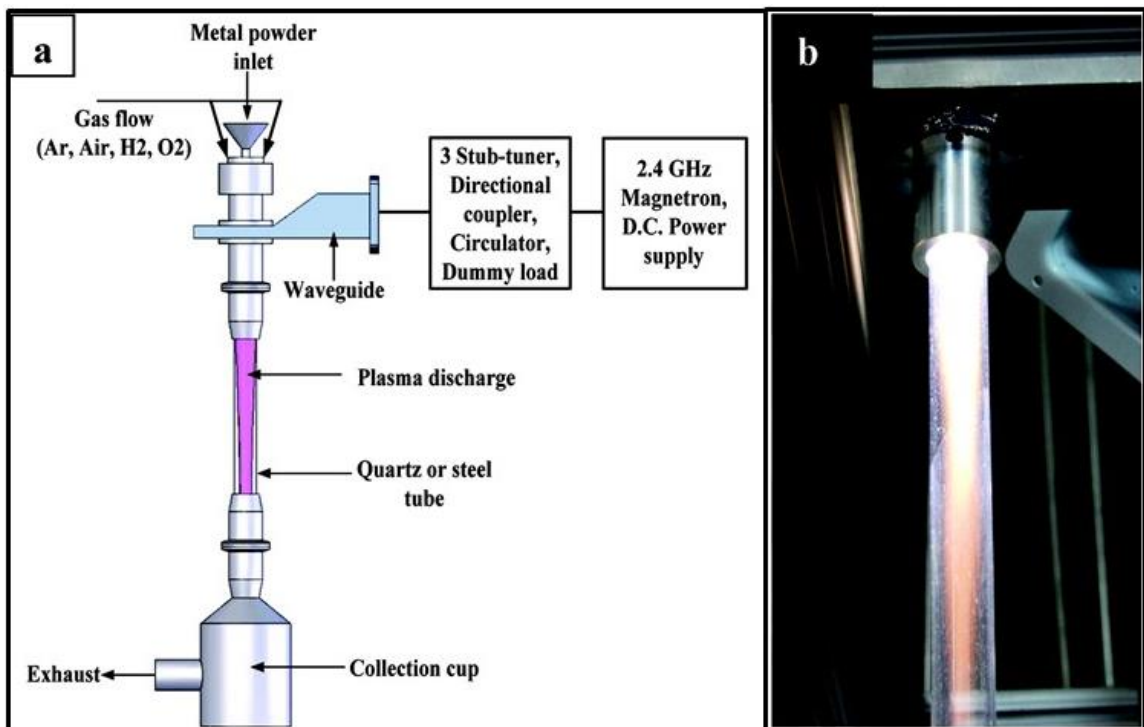


**Figure 3.4.** A) Schematic of the microwave plasma jet reactor, showing the essential components. B) Photograph of high density plasma jet at 2,000 W power in 1.5” quartz tube. Figure published by Kumar *et al.* 2008 [190] © American Chemical Society, 2008.

## 3.2. Sulfurization and Selenization Reactor

### **3.2.1. H<sub>2</sub>S Reactor**

To perform the reaction of metal oxides with H<sub>2</sub>S gas, a sulfurization reactor was designed from stainless steel ConFlat components. The primary body of the reactor is composed of a stainless steel 6 point cross with 2.75” flanges, providing an approximate total reactor volume of 22.5 cm<sup>3</sup>. 0.25” Teflon tubing is used to introduce 99 % H<sub>2</sub>S (stored in a 3 lb. lecture bottle) using a Type 1660 Metal ZSeal™ Mass Flow Controller (MFC) calibrated to 25 sccm. The substrate is placed on a boron nitride resistive heater, connected to an outside voltage source by two copper contacts. The sample is lowered onto the heater through the top flange. Figure 3.5A shows a schematic highlighting the operating principles for the stainless steel sulfurization reactor, including key reactor dimensions, accompanied by a photograph of the reactor (Figure 3.5B). The front facing flange connection once, during initial construction, housed a thermocouple for *in situ* reaction temperature measurement, but due to the uniquely corrosive conditions in the reactor, the thermocouple decomposed completely and was not practical.

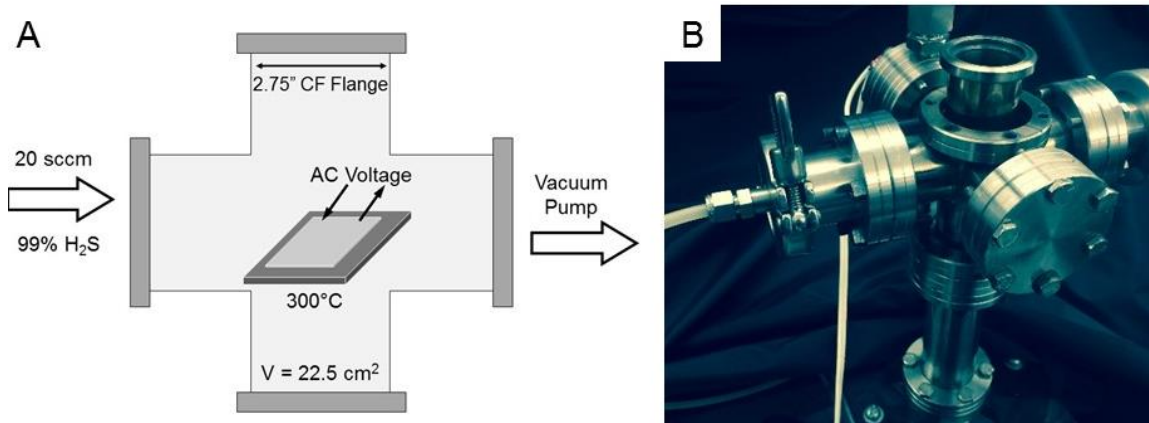


**Figure 3.5.** A) Schematic of H<sub>2</sub>S sulfurization reactor. B) Photograph showing typical reactor set up.

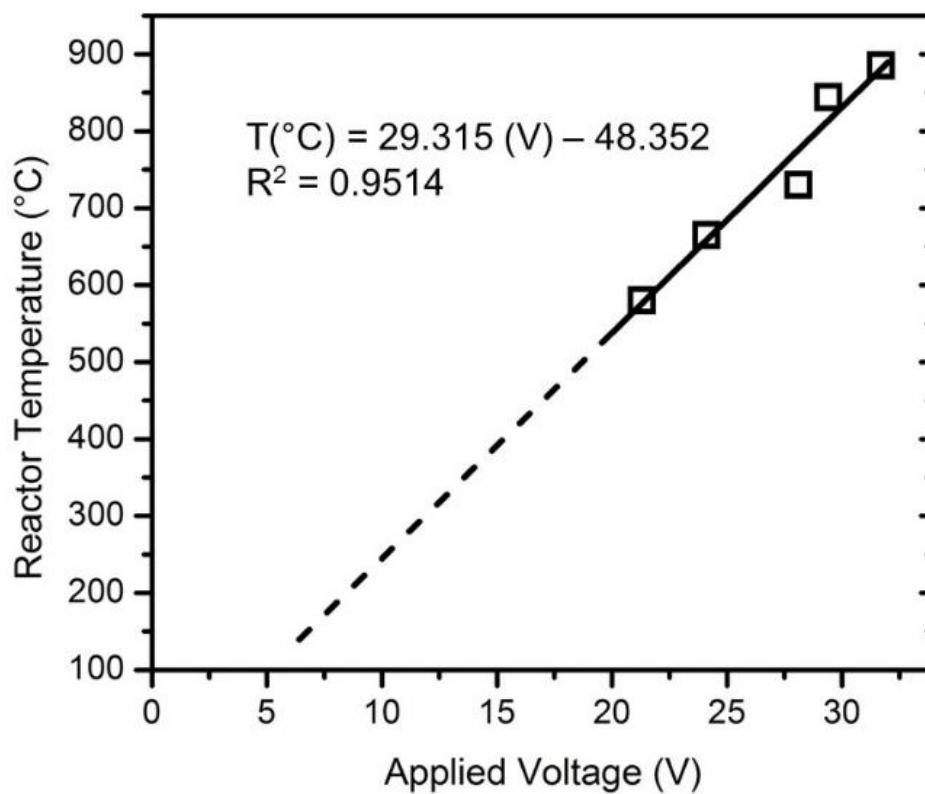


**Figure 3.6.** Correlation curve of spectroscopically measured heating stage temperature at incremental applied voltages, shown by black squares.

In order to calibrate the reaction temperature and accurately set the required applied voltage, a spectrometer was used to correlate the fluorescence emission of the heated stage to the stage temperature, and then related to the voltage. The calibration curve is shown in Figure 3.6. This curve is extrapolated to give an accurate correlation of applied voltage to reactor temperature. For the sake of example, for an average reaction temperature of  $\sim 300^{\circ}\text{C}$ , the applied voltage is set to  $\sim 13.6$  V. This provides a consistent method of standardizing reaction temperatures, regardless of thermocouple degradation. This reactor is frequently leak checked, due to the corrosive and highly toxic nature of  $\text{H}_2\text{S}$  gas.

### **3.2.2. Two Zone Furnace**

In order to study the effects of vaporized reactive solids, in this case sulfur and selenium powders, a two heated zone quartz tube vacuum reactor is designed. A 2” diameter quartz tube is placed into a Model OTF1200X-II Two Zone Tube Furnace manufactured by MTI Corp. Ceramic insulation is placed around the quartz reactor tube at the approximate separation between the two heating zones, allowing for some amount of temperature isolation. In typical phase transformation experiments, the metal oxide nanowires or nanoparticles are placed in the second zone, while the sulfur or selenium powder is placed in an alumina or iron boat in the first zone. The carrier gas, either inert Argon or Hydrogen are flowed into the reactor from the first zone to the second zone. The first zone is heated to a lower temperature ( $\sim 100^{\circ}\text{C}$ ) to allow for the slow sublimation of the sulfur powder, whose vapors are then carried by the carrier gas flow to the second zone, heated to  $300^{\circ}\text{C}$  to  $500^{\circ}\text{C}$ , where the phase transformation reaction takes place. A schematic of this reactor set up is shown in Figure 3.7. For practical reasons, a cold moist towel is placed on the outlet of the tube furnace, just before the entrance to the main vacuum

control valve and pumping equipment. This allows the vaporized selenium or sulfur to deposit on the quartz tube, rather than accumulate in the valves and pump, potentially leading to catastrophic failure.

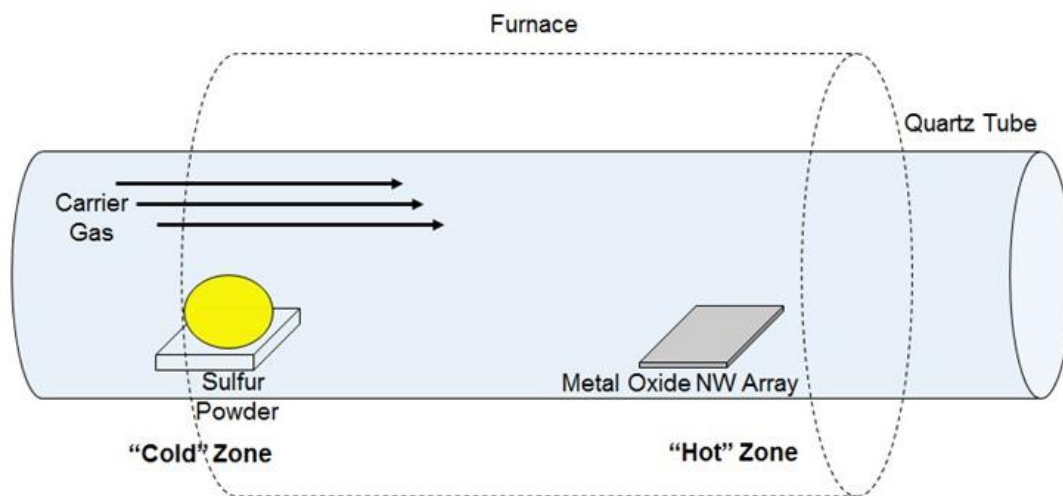


**Figure 3.7.** Schematic showing the reactor layout involving vaporization of sulfur powder in the first, cold zone, which is then carried to the second, “hot” zone where the reaction takes place.

### 3.3. Characterization Techniques

#### **3.3.1. Crystallographic Techniques**

The characterization of the material is almost as important as the actual synthesis. The physical and electrochemical properties of the nanowire arrays were determined by scanning electron microscopy (SEM), X-Ray diffraction (XRD), UV- Visible spectroscopy, and also Raman Spectroscopy and Photoluminescence (PL).

#### Scanning Electron Microscopy



Scanning Electron microscopy (SEM) is a vital instrument in the characterization of nanoscale morphologies. SEM works by bombarding the sample surface with electrons. When the electron interacts with the sample, some of the electrons are elastically scattered and reflected back, known as “back scattered” electrons, but it can also inelastically interact with the sample and cause the emission of a secondary electron, an Auger electron, or an X-ray.

The topographical surface imaging ability of the SEM is due to the detection of secondary electrons from the sample. The incident electron beam interacts with the conduction band electrons, weakly bound to the atoms on the sample surface; these secondary emitted electrons typically have an energy of only 3 eV to 5 eV. When the electron beam interacts with a sample, secondary electrons are actually produced in the whole area of the beam/sample interaction, but since these conduction band electrons have such low energy, they are quickly and easily absorbed by the sample, except for those emitted at surface. In metals, the calculated “escape depth” of secondary electrons is ~5 nm, which makes the imaging produced by secondary electron detection surface sensitive, leading to the sensitivity of SEM imaging. The secondary electrons provide the strongest resolution of the topography of the sample surface, compared to other emissions.[197] SEM imaging is used in this dissertation to characterize the external nanowire morphologies of the metal oxides and sulfides.

### **Characteristic X-Rays.**

In some cases, the incident electron beam interacts with the sample, causing an electron from an inner orbital of an atom to be emitted. This causes a vacancy, which an electron from a higher energy shell will “fall down” to occupy. The difference in energy

from this electron shell mobility could lead to the emission of an x ray. The x ray emitted is described by the name of the shell where vacancy was created, *e.g.* K, L, M, *etc.* and the number of shells the higher energy electron had to transfer from in order to fill that vacancy. A one shell jump is denoted by “ $\alpha$ ”, two shells by “ $\beta$ ”, and a three shell jump by “ $\gamma$ ”. As an example, if a vacancy is caused in the K shell of an atom and is filled by an electron from the L shell, the x ray emitted would be labeled  $K_{\alpha}$ ; if the vacancy filling electron originated from the M shell, then the resulting x ray would be labeled  $K_{\beta}$ . Since electron shell contains orbitals (s, p, d *etc.*), subshells, spin differences, and quantum interactions, the labeling of an emitted x ray by source can become complicated with multiple subscripts and numerals, but in practice, only one Greek letter subscript is use.[197] A schematic showing the most common electron shell transitions for EDS analysis and their corresponding characteristic x ray emission can be seen in Figure 3.8.

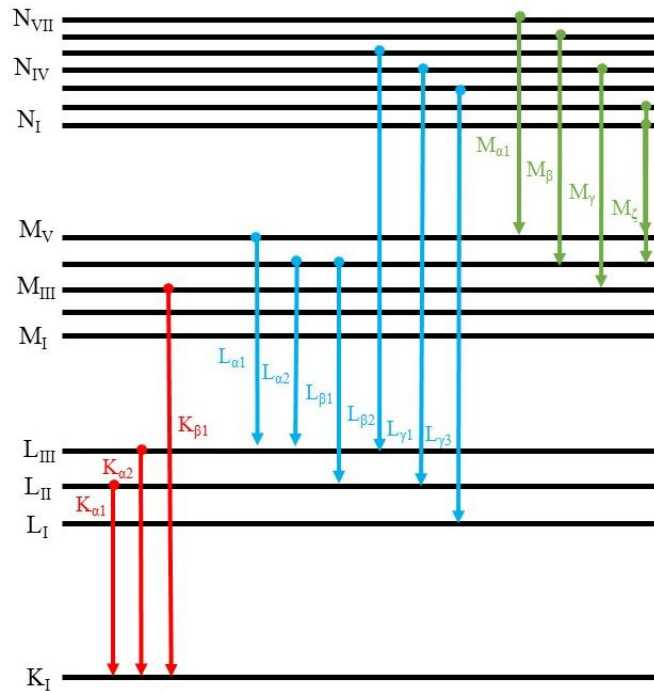


**Figure 3.8.** Schematic of the most common electron shell transitions during EDS analysis and emission of a characteristic x ray. The red arrows show electron transitions to vacancies in the K shell, blue arrows for transitions to L shell vacancies, and green arrows for M shell vacancy transitions.

Energy Dispersive x ray spectroscopy (EDS), also known as EDAX, is a technique where these emitted characteristic x rays can be used to determine the elemental composition of a sample. The incident electron beam must have sufficient energy to remove an electron from an energy shell and cause an x ray emission. This binding energy of shell electrons is unique to each element. For example, 25.517 keV of energy is required to remove an electron from the K shell of silver. This energy is known as the “critical excitation energy”. If the incident electron has an energy less than the critical excitation, then no characteristic x ray will be emitted. If the incident electron energy is larger than critical excitation energy, then the electron shell will be disrupted and one or more characteristic x rays will be produced. EDS provided elemental analysis, both in SEM and TEM imaging, to characterize the extent of phase transformations and estimate stoichiometric ratios of the reacted species.

The SEM used for these experiments was the Nova 600 NanoSEM by FEI with a field emission gun. The secondary electron detector used was a TLD detector in immersion mode for high resolution images.

#### Transmission Electron Microscopy (TEM)

While scanning electron microscopy is surface sensitive and characterizes the topography of a sample using the “reflection” of secondary electrons, transmission electron

microscopy characterize the internal structure of a sample by detecting the electrons which are transmitted through the sample. The most common form of imaging using a TEM is known as bright field TEM, where a narrow electron beam with an average spot size of 1 to 10 Å is rastered across the sample, transmitting electrons through the sample, which are collected by an aperture on the back, projecting the image onto a detector. Using high resolution TEM mode (HRTEM), the phase of the diffracted electron wave is maintained which allows for constructive and destructive interference. This forms the “phase contrasted” image, which shows fringes forming atomic columns and rows. Measurement of the spacing between these diffraction fringes gives the characteristic “d spacing” of the crystal structure in multiple geometric crystal planes.[198] These d spacing analysis were used in this dissertation to identify crystal lattice structure and analyze epitaxial relationships formed in core/shell structures during phase transformation reactions.

### X-Ray Diffraction

X-Ray Diffraction (XRD) is a characterization technique to determine the crystal structure of a material. X-rays are produced by a tungsten filament, which is heated and bombards a target, usually copper to produce x-rays. The x-rays hit the sample and, if the sample is crystalline and has the proper atomic spacing, then constructive and destructive interference occurs. In order for the incident x-ray to be diffracted, the scattered ray must satisfy Bragg's Law, which is

$$n\lambda = 2d \sin \theta \quad (10)$$

The wavelength of the monochromatic incident x-ray,  $\lambda$ , must strike penetrate the sample to a certain depth,  $d$ , and at a specific angle,  $\theta$ , to be diffracted.[199] The XRD apparatus involves two movable arms that revolve around a stage. One arm is the x-ray emitter,

while the other is a collector. The angle between the emitter and the detector is measured as  $2\theta$ . The intensity of the diffracted x-ray is plotted versus  $2\theta$ , and the spectrum can be used to determine chemical composition and crystal structure. When the x ray diffracts off the crystal plane ( $hkl$ ), that diffraction peak will occur at an angle  $2\theta_{hkl}$ , specified by:

$$2\theta_{hkl} = 2 \sin^{-1} \left( \frac{\lambda \sqrt{h^2 + k^2 + l^2}}{2a_0} \right)$$

Where  $h, k, l$  are the miller indices of the crystal plane and  $a_0$  is the crystal lattice spacing. The combination of crystal planes which allow for a diffraction peak and its relative intensity provide a “fingerprint” for a compound and, using databases, can easily identify the composition and crystal structure.[198]

The XRD used for these experiments is the Bruker AXS D-8 HR XRD

### 3.3.2. Spectroscopic Techniques: Optical and X Ray

#### UV- Visible Spectroscopy

UV- Visible Spectroscopy (UV-Vis) is a technique to determine the band gap of a material by exposing the sample to light ranging from Ultraviolet to the near Infra-Red and measuring the adsorption of each wavelength.

For UV-Vis spectroscopy, the following equations can be used to calculate important parameters such as band gap.

For direct band gap semiconductors:

$$\alpha(\hbar\omega) \propto \frac{\sqrt{\hbar\omega - E_{gap}}}{\hbar\omega} \quad (11)$$

where  $\alpha$  is the absorption coefficient,  $h\omega$  is the energy of incident photons, and  $E_g$  is the electronic band gap of the semiconductor.  $E_g$  is the intercept of the straight line obtained by plotting  $(\alpha h\omega)^2$  vs.  $h\omega$ .

For indirect band gap semiconductors:

$$\alpha(\hbar\omega) \propto \frac{(\hbar\omega - E_{gap})^2}{\hbar\omega} \quad (12)$$

$E_g$  is the intercept of the straight line obtained by plotting the **square root of  $(\alpha h\omega)$**  vs.  $h\omega$ .

The UV-Vis spectrometer used in these experiments was Perkin Elmer Lambda 950 UV/Visible/NIR Spectrophotometer.

### Raman Spectroscopy

Raman spectroscopy is a spectroscopic technique useful in characterizing the vibrational, rotational properties of a material system and investigate the internal structure of molecules and crystals. When light interacts with a material, it can either be absorbed, scattered, or could pass through the material. If the photon interacts with the electron cloud of the material, it will be scattered. If the electron cloud distortion is the only interaction with the photon, then the frequency change of the photon will be very small, as the electrons in the cloud are relatively smaller and lighter. This is known as elastic scattering, or Rayleigh scattering. Rayleigh scattering is the dominant process in most photon/atom interactions. However, if the photon passes through the electron cloud and interacts with the nucleus, then energy is transferred from the photon to the molecule, or from the

molecule to the photon. This is inelastic scattering, and is known as Raman scattering. The signal from Raman scattering is significantly weaker than Rayleigh scattering, as only one photon in every  $10^6$  to  $10^8$  will exhibit Raman scattering[200].

There are two mechanisms by which Raman scattering can occur. If the photon transmits energy to the molecule and excites it from the  $m$  vibrational ground state to an excited  $n$  state, then the scattering is known as Stokes scattering. However, if the molecule is already in an excited vibrational state, due to thermal energy or some other excitation, then the molecule will relax back to the ground state,  $m$ , and that excess energy will be transferred to the scattered photon. This is known as anti-Stokes scattering. Anti-Stokes scattering is significantly less intense than Stokes scattering and the Anti-Stokes transitions tend to diminish as the excitations are conducted at lower temperatures. Typically, in Raman spectroscopy, Stokes inelastic scattering is the dominant process and contributes to the measured signal [200]. A comparison of the excitations involved during Rayleigh, Stokes, and anti-Stokes scattering can be seen in Figure 3.9.

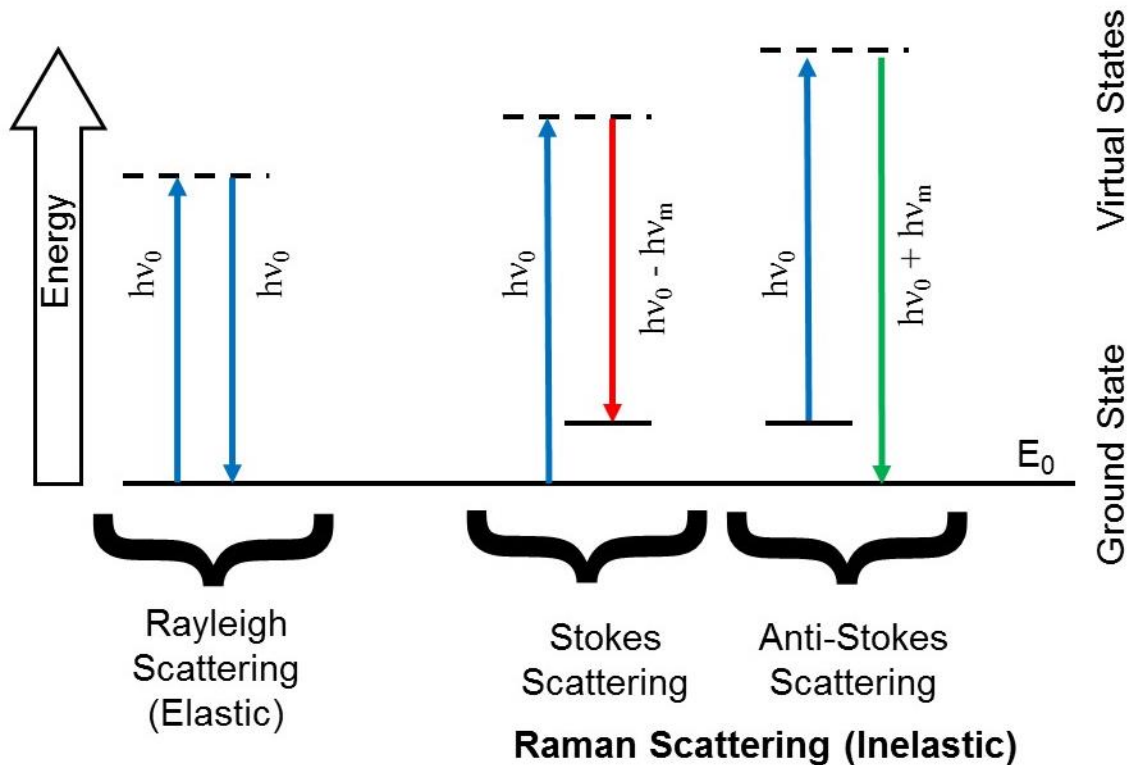


**Figure 3.9.** Summary of elastic and inelastic scattering processes observed during Raman spectroscopy.

A monochromatic laser source is most typically used to provide photons to induce Raman scattering in a material. This laser could be Visible wavelengths (most commonly 632 nm or 535 nm), UV (325 nm) or near infrared (nIR). The frequency of the Raman scattered photon is shifted with respect to the frequency of the original excitation phonon, but the magnitude of the shift is independent of the excitation frequency. This "Raman shift" is therefore an intrinsic property of the material in which the scattering occurs. Since the Raman scattered photon has undergone a change in frequency, the conservation of energy mandates that some energy is transferred to the material system. A definite Raman shift corresponds to excitation energy of the sample (such as the energy of a free vibration of a molecule). For most materials, only a few vibrations and excitations are considered



"Raman active," meaning that some vibrations will contribute to the Raman scattering process. The Raman spectrum obtained during spectroscopy is plotted as the intensity of the Raman scattered photons as a function of the frequency shift from the original excitation radiation, which is represented by wave number or inverse wavelength ( $\text{cm}^{-1}$ ). The Raman peaks allow for detection of different bond energies in the material lattice, which is very helpful in understanding phase transformations in some material systems.

The Renishaw inVia Raman Microscope is used to obtain all the Raman spectra reported in this work and, most commonly, the excitation radiation source is a 633 nm HeCd red laser.

#### Photoluminescence.

Photoluminescence (PL) spectroscopy analyzes the polarized emissions of a semiconductor when excited by an optical source. If the energy of the incident photon source is above the band gap of the semiconductor, this causes the formation of an exciton, with the electron and hole forming in the valence and conduction band at the same momentum space. The exciton relaxes, in both energy and momentum, to the band gap minimum and emits a photon with the energy at this point. This photon is detected in the spectroscopy system and gives the value of the minimum band gap transition. The momentum and energy relaxation occurs by Coulombic scattering or phonon interactions. Coulombic scattering is more commonly known as Rutherford scattering and causes the dissipation of atomic energy by elastic collisions with neighboring particles.[201] The other means of energy dissipation/relaxation is by vibrations of the crystal lattice, *i.e.* phonons. This phonon mechanism necessitates a semiconductor with a direct band gap transition for room temperature PL; indirect band gap transitions rely upon phonons to

transition from the valence to the conduction band, therefore the photo induced exciton formed in PL will not have the same momenta and, therefore will not emit a characteristic luminesced photon, at least at room temperature. “Cold PL” cools the semiconductor to sufficiently low temperatures (typically using liquid nitrogen) to restrict the phonons and allow for a photon to be emitted by the indirect band gap transition. PL spectroscopy was attempted for many of the materials discussed in this dissertation, but was only significantly observed in tin sulfide nanowires.

### X-Ray Photoelectron Spectroscopy

X Ray Photoelectron Spectroscopy (XPS) is a surface sensitive technique which measures the chemical composition of a compound and, most notably, the electronic state of each element. This is done by irradiating the compound with x-rays, which interact with the atoms, leading to the emission of high energy electrons from the core levels. The most common x-ray sources are Magnesium K $\alpha$  (1253.6 eV) and Aluminum K $\alpha$  (1486.7 eV). The energy of the emitted electrons can be described by the equation:

$$KE = h\nu - BE - \varphi_s$$

where KE is the kinetic energy of the electron,  $h\nu$  denoting the excitation energy of the electron, BE the binding energy of the atomic orbital from which the emitted electron originated, and  $\varphi_s$  is the work function of the spectrometer. Each element has its own unique set of ionization energies, which allows for elemental analysis. Interestingly, the ionization resulting from the x-ray excitation leads to the separation of the  $p$ ,  $d$ , and  $f$  orbitals. This leaves vacancies in the  $p_{1/2}$ ,  $p_{3/2}$ ,  $d_{3/2}$ ,  $d_{5/2}$ ,  $f_{5/2}$ , and  $f_{7/2}$  orbitals. These split orbitals, due to spin, have the ratio of 1:2 for the  $p$  orbitals, 2:3 for  $d$  orbitals, and 3:4 for  $f$  orbitals. Shifts in these ionization peaks can show the chemical potential or oxidation state

of the element in the compound from which it originated. A schematic of a typical XPS measurement apparatus can be seen in Figure 3.10.

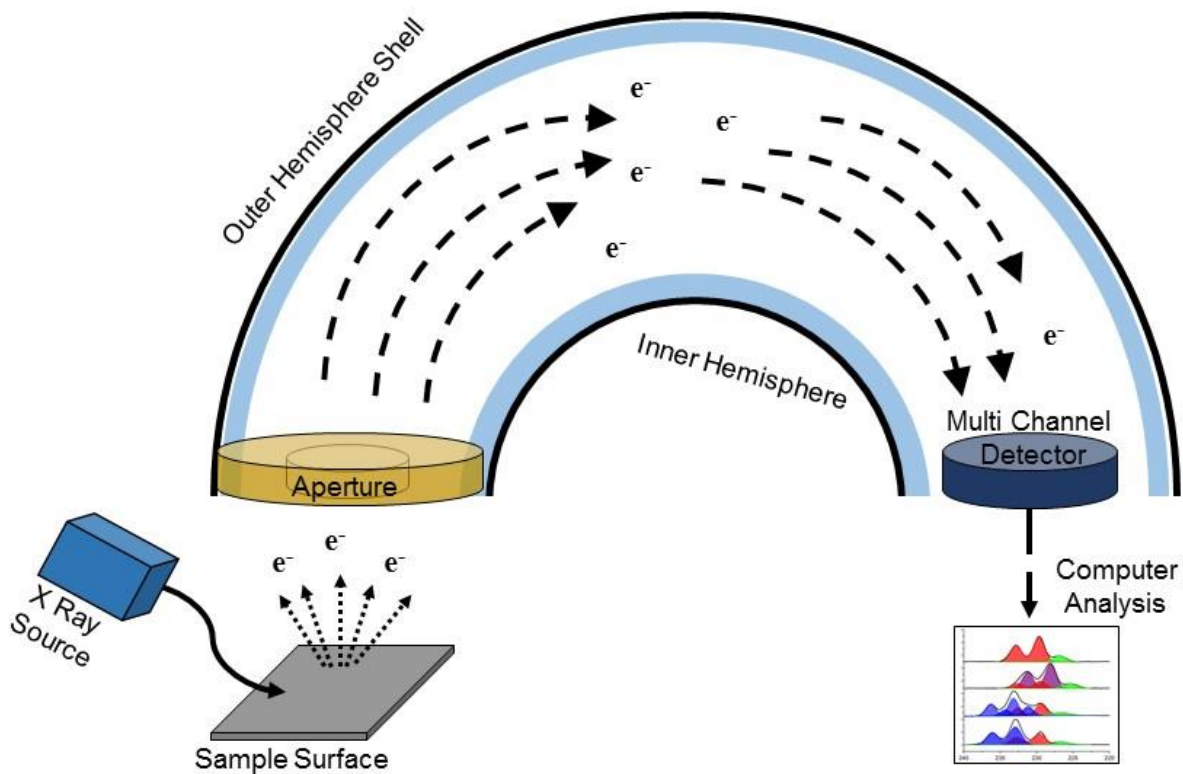


**Figure 3.10.** Schematic showing the typical set up and operating principle of an XPS. The sample is bombarded with an x ray source, causing the emission of photo-electrons. These electrons pass through an aperture into a hemispherical detector, which is composed of an inner and outer shell with a potential difference between each other. These biases hemispheres act to guide the photo-emitted electrons to a multi-channel detector, which communicates with software to create the experimental spectrum. The example spectrum used in the schematic is adapted from Cummins, et al.[202]

The large hemispherical detector actual consists of an inner and outer hemisphere shells, which are biased so that a potential difference exists between them, known as the

pass voltage. The potential difference acts to guide the emitted electrons through the hemisphere and to the detector, rather than the electrons colliding with the shells. This is similar to the XPS system used in these measurements, the MultiLab 3000 by VG technologies and Al K $\alpha$  radiation was used. In this dissertation, XPS is most utilized in characterization of MoS<sub>2</sub> and the effects of phase transitions from hexagonal to trigonal during chemical modification.

### 3.4 Electrochemical and Electrocatalytic Characterization

The predominant method of analyzing the electrochemical and electrocatalytic performance of a material is by cyclic voltammetry sweeps in a three electrode electrochemical test cell.[203-206] A schematic showing a typical electrochemical, three electrode setup is shown in Figure 3.11. In the case of the majority of electrochemical analysis presented in these experiments, a 3 mm diameter (.070686 cm<sup>2</sup>) glassy carbon electrode acted as the conducting substrate on which the catalyst material was dispersed; this is referred to as the working electrode. Other conducting substrates, such as stainless steel or fluorine doped tin oxide (FTO) or indium doped tin oxide (ITO) coated glass are commonly used as the working electrode substrate, but it is important that the substrate must be stable in the electrolyte chosen, as well as does not contribute any electrochemical or electrocatalytic activity, which is possible in FTO under certain conditions. A unique consideration in these experiments, which focus on the exposure of metal oxide nanowires to reactive, sulfurizing environments, is the chemical stability of the substrate. FTO reacts with H<sub>2</sub>S to form a tin sulfide layer, which is more resistive than the manufactured FTO and may impede the measurement of generated current.[196] To normalize the effects of the working electrode substrate in the analysis of electrocatalytic activity of MoS<sub>2</sub>/MoO<sub>x</sub>

shell/core nanowires (discussed in Chapters 6 and 7), the nanowires were synthesized and subsequently chemically modified on stainless steel substrates. The nanowires were then dispersed in  $\sim 5 - 10 \mu\text{L}$  of DI water and transferred to the glassy carbon electrode by drop casting. In order to prevent delamination of the nanowires into the  $0.5 \text{ M H}_2\text{SO}_4$  electrolyte during testing, a thin layer of 5% Nafion was applied to the working electrode surface. Nafion is a fluorinated polymer which facilitates proton exchange with the solution and provides mechanical support to the sample. The Nafion coating has no effect on the overpotential to catalyze the HER reaction and, actually, decreases the measured current density generated by the catalyst.

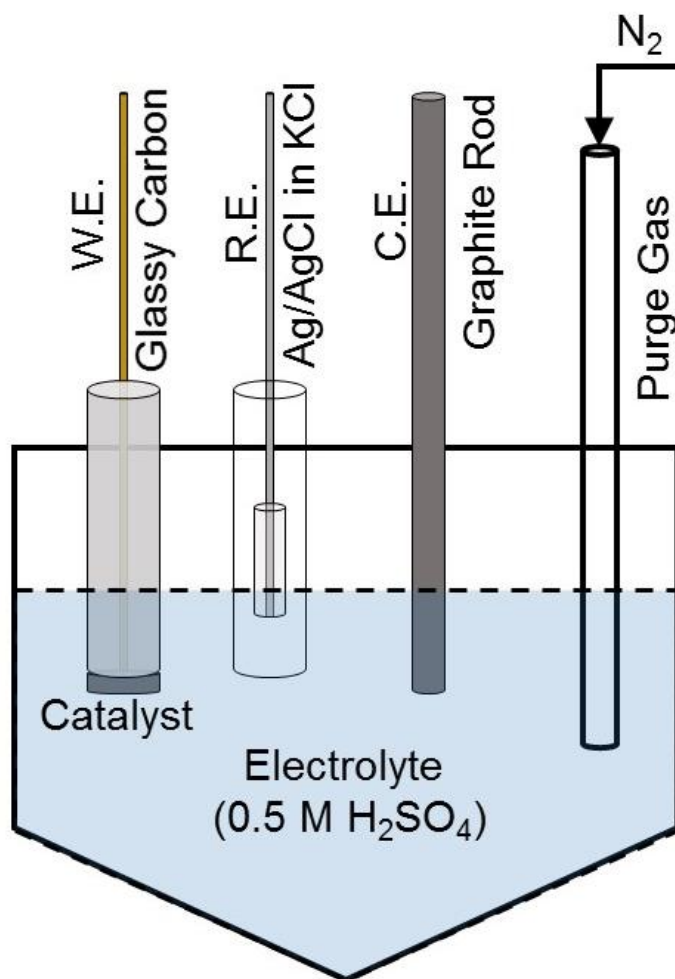
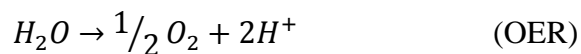


**Figure 3.11.** Schematic showing typically set up of three probe electrochemical/electrocatalytic testing set up. The active catalyst material is loaded on the glassy carbon electrode (working electrode). The silver chloride coated silver wire acts as the reference voltage (reference electrode) and the graphite rod acts as the counter electrode. Nitrogen is bubbled into the system to purge oxygen.

It is important to select a counter electrode which can efficiently accept all the current generated by the electrochemical activity of the working electrode/catalyst material. In the case of hydrogen evolution, platinum mesh is the most common counter electrode, as it provides high surface area for current collection, but also facilitates the half reaction for hydrogen evolution. In a p type semiconductor, platinum would not be an ideal counter electrode, as the oxygen evolution reaction (OER) would have to be facilitated by the counter electrode and platinum is not desirable for that application. In these experiments, a large conducting graphite rod is used as the counter electrode. Since we are analyzing the changes to catalysis of the HER, it is not appropriate to have an optimized HER electrocatalyst (platinum) in the system. It is possible for platinum to be leached into the solution, adsorbed onto the working electrode, or there is the possibility that the working electrode material may become absorbed onto the platinum mesh, potentially permanently poisoning the counter electrode. For these reasons, electrocatalytic measurements typically used graphite as the counter electrode.

The reference electrode used in the majority of the electrochemical measurements in this dissertation is a silver chloride (AgCl) coated silver (Ag) wire in a 3 M potassium chloride (KCl) electrolyte. This voltage reference set up has a potential of +0.210 V vs.

the reversible hydrogen electrode, which was calibrated against platinum coated carbon saturated with Hydrogen gas (SHE). This forms the thermodynamic scale for the splitting of water, which is the production of hydrogen by reduction and molecular oxygen by oxygenation of the water. The reactions are summarized as:



The Gibbs energy of the total water splitting reaction is +237.2 kJ/mol, meaning that it is significantly non-spontaneous and requires an energy input to proceed. This energy is calculated to be ~1.23 V using the Nernst Equation. In photoelectrochemical water splitting, the valence band maximum and conduction band minimum must be separated by at least 1.23 V, *i.e.* the minimum band gap of the semiconductor to drive both the HER and OER. In the case of electrocatalysis, the band edges are not necessarily important, as the semiconductor crystal acts as the site for catalysis of the hydrogen or oxygen evolution reaction.

Cyclic voltammetry in the three electrode set up helps to establish the onset potential of the electrochemical reaction. In a completely catalytic inactive system, *e.g.* bare glassy carbon, a cyclic voltammogram (CV) will only exhibit capacitive current between the working electrode and the counter electrode. A typical CV of a blank glassy electrode in 0.5 M H<sub>2</sub>SO<sub>4</sub> in the three electrode set up with a graphite counter electrode is shown in Figure 3.12.

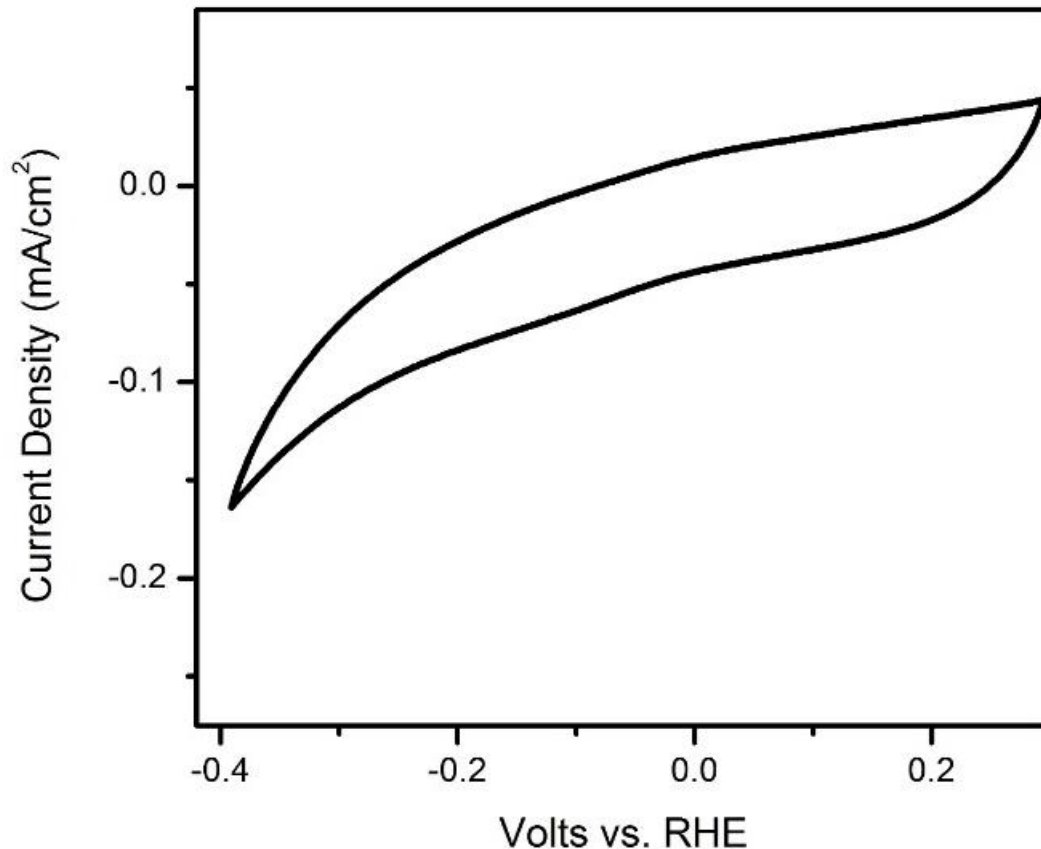


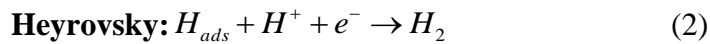
**Figure 3.12.** Cyclic voltammogram of blank glassy carbon, demonstrating capacitance between the working electrode and the counter electrode.

When there is electrochemical or electrocatalytic activity at the working electrode surface, *i.e.* the active material, then that capacitance is superseded and the generated current density increases dramatically. The voltage required to overcome this capacitance is the electrochemical “on set” potential, also referred to as the overpotential to drive the reaction. The generated current density is calculated based on the exposed geometric surface area. In the case of nanowire arrays, the geometric area is not equal to the electrochemically active surface area, but it simplifies analysis and standardizes the generated density. In most electrochemical and electrocatalytic materials for the HER, typically the voltage



required to drive 10 mA/cm<sup>2</sup>, which corresponds to an optimal efficiency to operate large scale water splitting operations. However, since the actual amount of material used in the catalysts measurement, as well as the actual surface area is different for every literature report, the “mA/cm<sup>2</sup>” parameter is subjective in many cases.

An important analytical tool which can be extracted from an electrochemical CV curve, especially in HER catalysis is the Tafel slope. This is calculated by plotting the logarithm of the current as the *x* axis and the overpotential (voltage) as the *y* axis. The measured slope of the CV after the catalytic on set, with units of mA/decade, gives insight into which reaction component of water splitting is the rate limiting step. Typically, there are three elementary rate-determining reactions involved in hydrogen catalysis at an active catalyst surface. Specifically, the proton adsorption (known as the Volmer (eq. 1) step), followed by either (a) the evolution of molecular hydrogen by the combination of an adsorbed proton and a proton from solution (Heyrovsky (eq. 2) step), or (b) the combination of two adsorbed protons (Tafel (eq. 3) step).<sup>[207, 208]</sup> Reaction pathways are either Volmer-Heyrovsky (1-2) or Volmer-Tafel (1-3).



Experimental observation and kinetic modeling show that if the adsorption of a proton, *i.e.* the Volmer step, is the rate-determining step, then a Tafel slope of ~120 mV/decade should be observed. However, if the evolution of molecular hydrogen is the rate-determining step, then a Tafel slope of ~40 mV/decade or ~30 mV/decade should be observed, indicative of the Heyrovsky or Tafel steps respectively.[15, 207, 208] It is

important to understand that these values will only hold if the same rate-determining step is homogeneous throughout the catalyst. However, this is rarely the case. Multiple reactions occur at any given applied potential as a consequence of different reaction sites. Due to this convolution of reactions, a higher Tafel slope, nearer to 120 mV/decade, indicates predominantly adsorption limited, while a lower Tafel slope is indicative of an evolution limitation.

The combination of all of these characterization techniques, both crystallographic and electrochemical, assists in providing a clear understanding of the processes occurring in crystal phase transformation, both the change in crystal morphology, as well as the effects of this transformation on the electronic and chemical material properties.

## CHAPTER IV: MOLYBDENUM OXIDE TO MOLYBDENUM SULFIDE

As mentioned earlier in this dissertation, one of the key parameters in the design of a strong catalytic material is optimization of the exposed surface area. Especially with a material such as MoS<sub>2</sub>, which has very anisotropic properties, *i.e.* only active at crystal edge sites[169, 209], the need for carefully synthesized morphologies is great. This edge site dependent chemical activity is very applicable to electrocatalysis of the hydrogen evolution reaction; the edge sites provide very efficient catalytic sites at the crystal edges, while the larger basal is completely chemical and catalytically inert.[33] A multitude of different morphologies have been attempted to optimize the anisotropy of MoS<sub>2</sub> for electrocatalysis, typically involving dispersions of particles[31], complex gyroid structures[34], CVD grown single crystals[33], vertically oriented sheets[35-37], carbon co-catalysts and graphene supports[32], *etc.* Many of these morphologies suffer from low surface area and are only available on small scale. The use of 1D morphologies, formed by phase transformation, creates a high surface area for catalytic material using scalable methods. The effectiveness of 1D morphologies for improved catalysis has been shown in silicon microwires[210, 211] and, by design, are the ideal catalytic architecture.[82] This motivation lead to experiments with synthesis of MoS<sub>2</sub> in a one dimensional nanowire structure. This is achieved by phase transformation of MoO<sub>3</sub> nanowire arrays by reaction with H<sub>2</sub>S gas. The result is a MoS<sub>2</sub> crystalline shell on a reduced conducting MoO<sub>x</sub> core, which exhibits strong HER catalytic properties and excellent stability in acid. Figure 4.1

shows a summary schematic and this chapter will discuss in detail the synthesis and characterization.

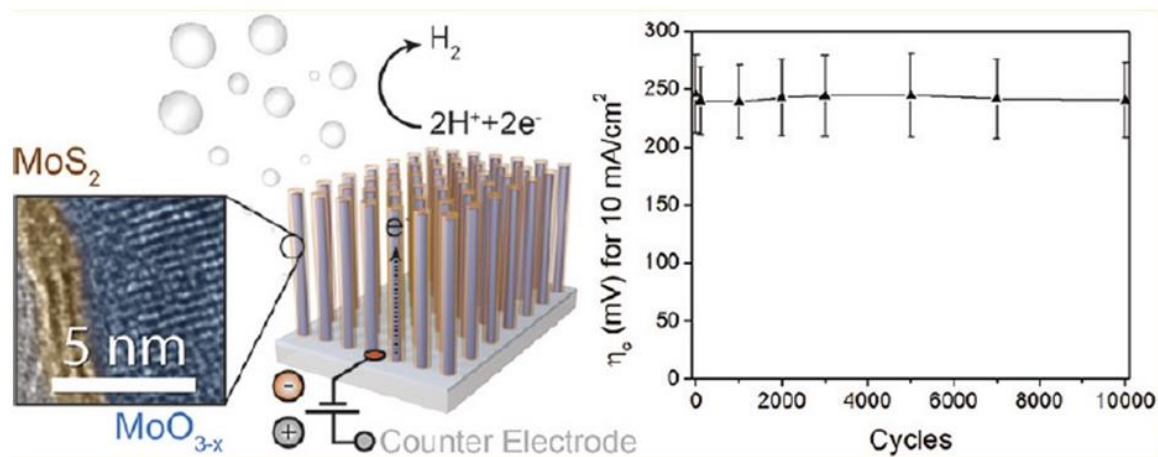


**Figure 4.1.** Summary schematic of the  $\text{MoS}_2/\text{MoO}_x$  shell/core nanowires, highlighting by HRTEM the crystal structure. The plot shows the normalized current and strong stability in acidic media. Published by Chen, et al., 2011[212] © American Chemical Society, 2011.

First, the  $\text{MoO}_3$  nanowire array is grown using Hot Filament Chemical Vapor Deposition (HFCVD), which has been used in the synthesis of other metal oxide nanowire arrays.[100, 194] A 6 foot molybdenum metal wire is coiled around two, 6.5” ceramic cylinders, which is placed in a 2” diameter quartz tube reactor, with a base pressure of  $\sim 10^{-3}$  Torr. Due to the almost “sputtering” effect of the HFCVD and no need for a catalyst, practically any substrate, under the right conditions, can be used as a growth platform for the metal oxide nanowire arrays, but most commonly quartz, stainless steel,  $\text{SiO}_2/\text{Si}$  wafers, or fluorine doped tin oxide (FTO) coated glass ( $15 \Omega/\square$ ) were utilized. In order to convert these nanowires to  $\text{MoS}_2$ , at least in these initial experiments done in collaboration with Zhebo Chen and Tom Jaramillo at Stanford University, the  $\text{MoO}_3$  nanowire arrays were

reacted in 10% H<sub>2</sub>S / 90% H<sub>2</sub> for 1 hour. These experiments were carried out at incremental temperatures in order to optimize the HER catalytic performance. A schematic showing the reactor set up for HFCVD, as well as reaction scheme can be seen in Figure 4.2.

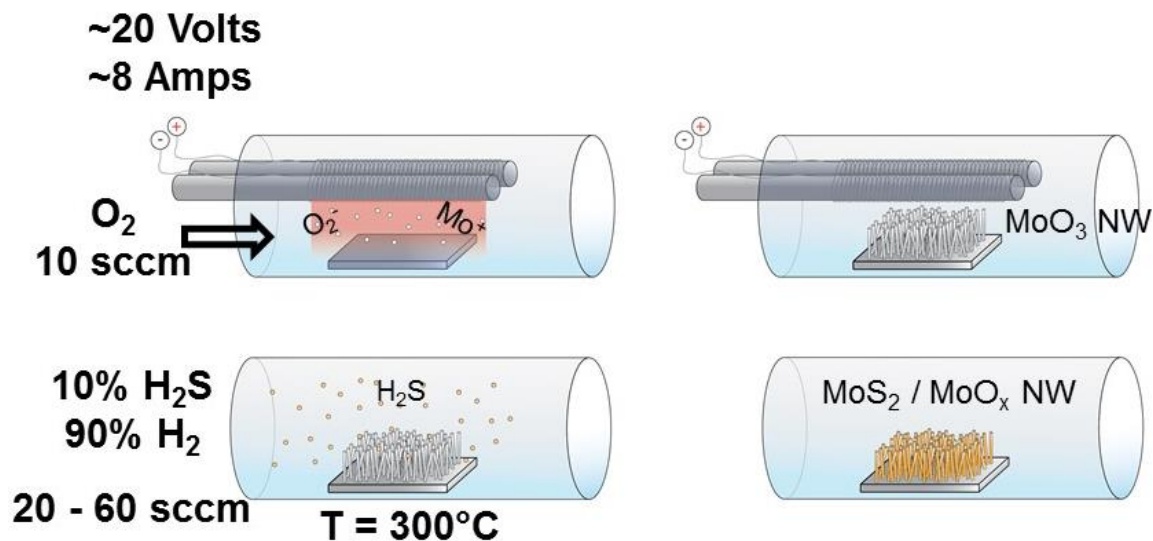


**Figure 4.2.** Schematic showing reaction scheme of, first, MoO<sub>3</sub> nanowire arrays by HFCVD, then exposure to H<sub>2</sub>S to form MoS<sub>2</sub> shell on a reduced MoO<sub>x</sub> nanowire core. This image was adapted from figure appearing in a presentation by Zhebo Chen.

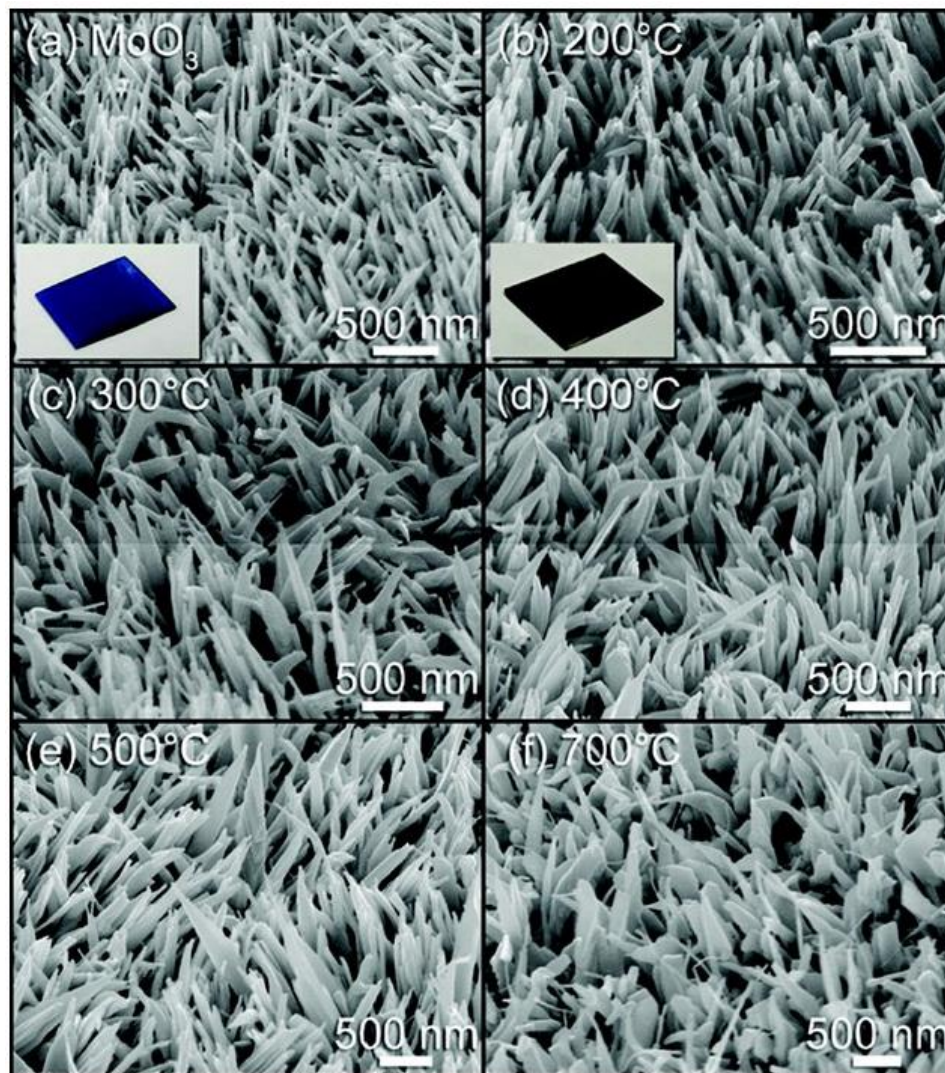


**Figure 4.3.** SEM imaging showing the external morphology of the nanowires array. A) shows the as grown MoO<sub>3</sub> nanowires, then the morphology at sulfurization of B) 200°C, C) 300°C, D) 400°C, E) 500°C, and F) 700°C. There is some slight thinning of the nanowires at higher temperatures, as well as some evidence sintering/agglomeration.[196] Published by Chen, *et al.* © American Chemical Society, 2011.

The incremental temperature of reaction between the MoO<sub>3</sub> nanowires in the 10% H<sub>2</sub>S atmosphere helps to determine the optimal temperature for MoS<sub>2</sub> shell formation. The

reaction was performed in 100° intervals beginning at 200°C. Even at temperature as high as 700°C, the nanowire morphology is still maintained, due in part to the low reaction pressure. Bulk MoO<sub>3</sub> typically sublimates at 600° to 700°C[213], but in the case of the low pressure, reducing atmosphere, the MoO<sub>3</sub> nanowires tend to agglomerate, but also may be thinning at higher temperatures. SEM images showing the maintenance of the nanowire morphology at various temperatures of sulfurization are shown in Figure 4.3.

HRTEM analysis of the H<sub>2</sub>S exposed nanowires shows that a conformal epitaxial layer of crystalline MoS<sub>2</sub> has grown on the surface of the MoO<sub>3</sub> nanowire, which maintains its single crystallinity (Figure 4.4). The MoS<sub>2</sub> shell grows with the basal plane (100) parallel to the nanowire growth direction. The thickness of the MoS<sub>2</sub> shell increases with the increase in reaction temperature, as expected. At 200°C, ~ 3 nm MoS<sub>2</sub> shell is formed, which maintains a single crystalline nature (Figure 4.4B). As the H<sub>2</sub>S reaction temperature increases, the actual thickness of the nanowire shell does not increase quickly, ~3 nm at 200°C, ~5 nm at 300°C, ~ 7 nm at 400°C, ~10 nm at 500°C, and ~12 nm at 700°C (Figure 4.4 B – F). This slow increase in reaction progression is due to the strong diffusion limits of the layered MoS<sub>2</sub> structure; these diffusion limitations continue to increase with shell thickness. Interestingly, the polycrystallinity of the MoS<sub>2</sub> shell increases with reaction temperature, with the grain boundaries increasing from practically nonexistent at 200°C, to the formation of large grains at 700°C, which exhibit a polycrystalline nature, but still maintain the oriented growth of the basal plane parallel to the nanowire length.

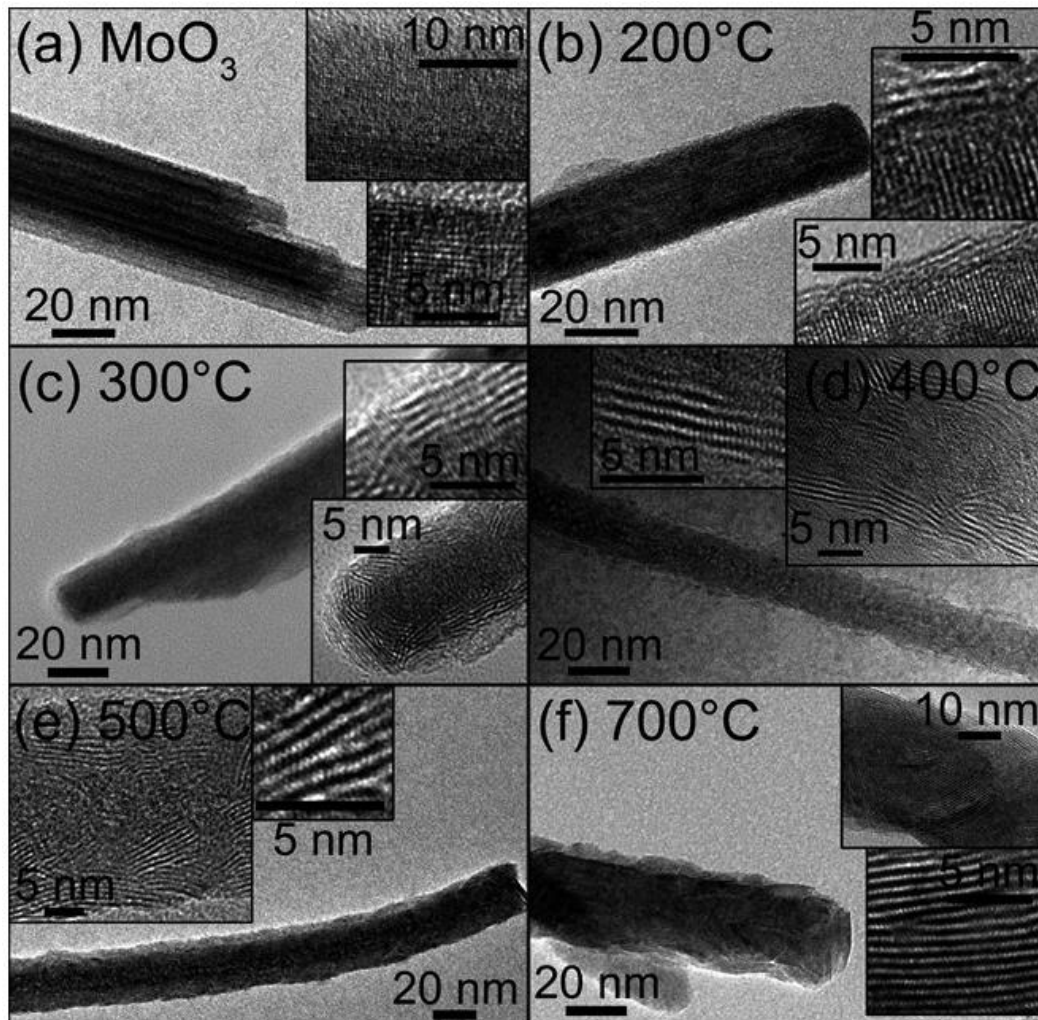


**Figure 4.4.** HRTEM imaging of the internal morphology of the  $\text{MoS}_2/\text{MoO}_3$  shell/core nanowires. A) As grown, single crystal  $\text{MoO}_3$  nanowire. Reaction with  $\text{H}_2\text{S}$  at incremental temperatures B) 200°C, C) 300°C, D) 400°C, E) 500°C, and F) 700°C shows the increase in shell thickness, as well as formation of grain boundaries in the crystalline shell with increased temperature.[196] Published by Chen, *et al.* © American Chemical Society, 2011.

X ray diffraction (XRD) analysis (Figure 4.5) of the nanowires grown at  $\sim 300^\circ\text{C}$  shows that the  $\text{MoO}_3$  nanowire core has been partially reduced to form tetragonal  $\text{MoO}_2$



(PDF 00-002-0422), as well as other molybdenum sub oxides, shown by prominent XRD peaks from (100), (101), and (211) MoO<sub>2</sub> crystal planes. Signal from 2H-MoS<sub>2</sub> (PDF 00-02-0132) is generated from the MoS<sub>2</sub> shell. For comparison, the as grown MoO<sub>3</sub> nanowires show phase purity of orthorhombic MoO<sub>3</sub> (PDF 00-001-0706). While MoO<sub>3</sub> has a band gap of ~ 3 eV[214], the reduced molybdenum oxide shows conducting, almost metallic properties from the high concentration of oxygen vacancies.[215, 216] This reduced molybdenum oxide core provides for a “metallic”, high surface area support for the MoS<sub>2</sub> electrocatalyst.

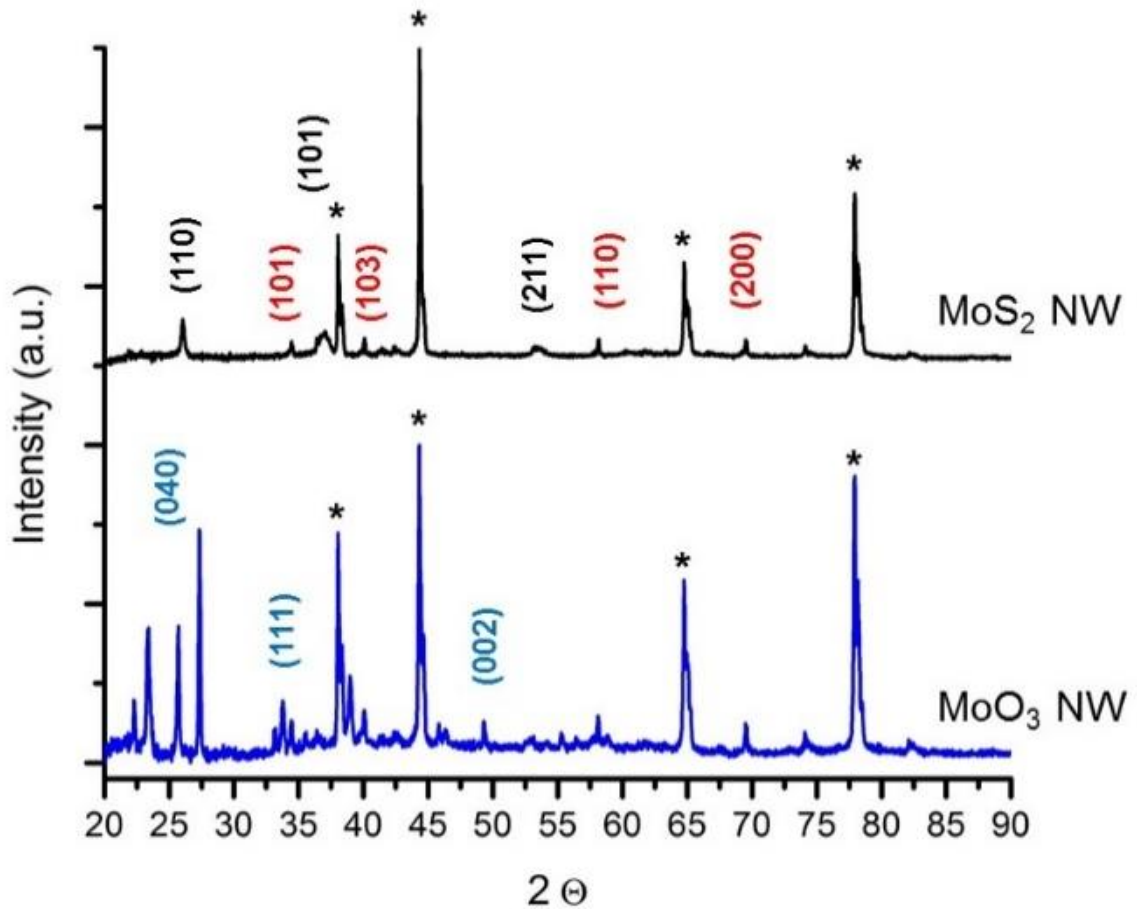


**Figure 4.5.** XRD analysis of the as grown MoO<sub>3</sub> nanowire array (blue curve) on amorphous quartz, showing phase purity of orthorhombic MoO<sub>3</sub> (blue). After sulfurization

(black curve), there is no signal from MoO<sub>3</sub>, but instead MoO<sub>2</sub> (black) and MoS<sub>2</sub> (red). The asterisks at ~38, ~45, ~65, and ~77 2θ correspond to metallic Aluminum from the XRD instrument substrate. Modified from Cummins, *et al.* [195]

The reaction of MoO<sub>3</sub> in a reducing H<sub>2</sub>S reactor has multiple reaction pathways to form MoS<sub>2</sub>, by either direct conversion of the oxide, or that the molybdenum oxide is first reduced, then reacted. The two most common reaction pathways are:



Thermodynamically, there is no limitation to the complete conversion of the molybdenum oxide to 2H MoS<sub>2</sub>. However, experimentally, there seems to be a limitation on the thickness of the MoS<sub>2</sub> shell formed. Since these limitations are not due to the reaction thermodynamics, they must be diffusion and kinetics based. As mentioned previously, there are strong diffusion limits for species to diffuse between the 2D MoS<sub>2</sub> layers through the chemically inert MoS<sub>2</sub> basal planes. Typically, sulfur has a low diffusion coefficient in many metal oxides, which further contributes to the diffusion limitations of the MoO<sub>3</sub>/MoS<sub>2</sub> conversion. The average rate of diffusion (D) for sulfur through an oxide, as well as a sulfide, is very low, while the kinetics of the reaction (k) tend to be significantly higher. The length of the reaction, which is a measure of how far the reaction can proceed and is defined as:

$$\left(\frac{D}{k}\right)^{0.5}$$

It is these diffusion and kinetic limitations inherent in the formation of a layered chalcogenide which leads to the shell/core structure, compared to complete conversion of Kirkendall-induced hollowing.

The electrochemical activity of the MoS<sub>2</sub>/MoO<sub>x</sub> nanowire arrays is tested using a three probe electrocatalytic set up in 0.5 M H<sub>2</sub>SO<sub>4</sub> (pH = 0), with a graphite counter electrode and a saturated mercury electrode (Hg/HgSO<sub>4</sub> in saturated K<sub>2</sub>SO<sub>4</sub>) and subjected to cyclic voltammetry; this is reported in Figure 4.6. As expected, the bare MoO<sub>3</sub> nanowires are not stable in acid and degrade during electrochemical testing.[217] As soon as a very thin layer of MoS<sub>2</sub> is grown on the surface (at 150°C), the degradation of the molybdenum oxide is significantly reduced and evolution of molecular hydrogen is observed, shown in Figure 4.6A. It is found that the optimal HER electrocatalytic activity is found for the nanowires grown at 200°C (in this particular study). As the temperature increase, the grain boundaries in the MoS<sub>2</sub> shell increase, as well as agglomeration of the nanowires begins to occur, which lowers the surface area exposed for catalysis, shown in Figure 4.6B. The resistance of the solution and measurement set up (~ 14 Ω) is accounted for by *iR* correction, *i.e.*

$$V_{corrected} = V_{exp} - iR_s$$

where  $V_{exp}$  is the experimentally obtained voltage,  $i$  is the measured current and  $R_s$  is the solution resistance.

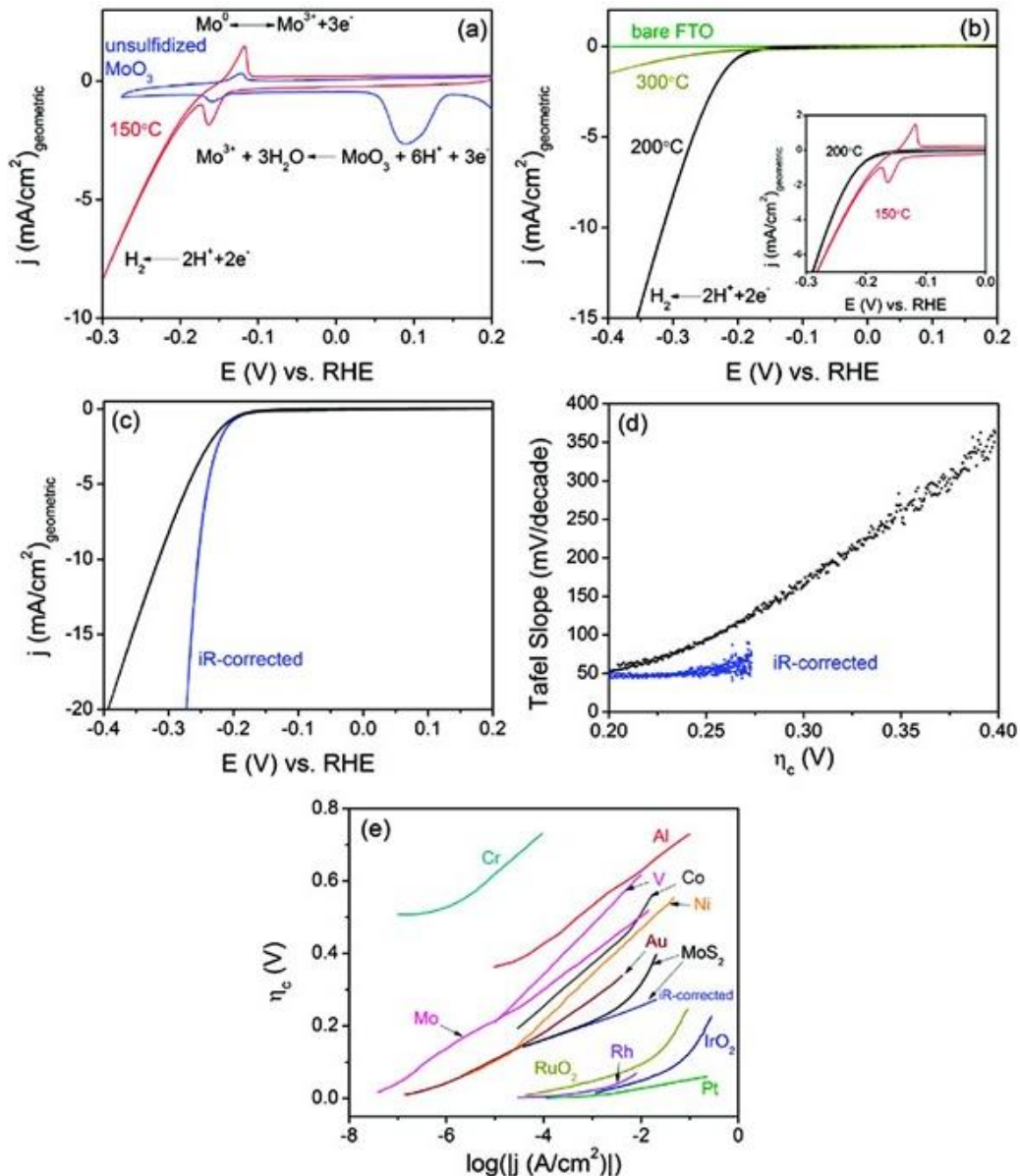


**Figure 4.6.** A) Cyclic voltammogram of MoO<sub>3</sub> nanowire array as grown (blue) and after exposure to H<sub>2</sub>S at 150°C (red curve). B) Voltammetry of the sulfurized nanowires at 200°C (black curve) and 300°C (yellow curve). The electrochemical activity of bare FTO coated glass is shown (green) for comparison. The inset highlights an electrochemical degradation reaction from the MoO<sub>3</sub> core, which occurs at 150°C, but is not observed at 200°C. C) Effects on the electrochemical voltammogram after iR correction. D) Tafel slope analysis of the MoS<sub>2</sub>/MoO<sub>x</sub> shell core nanowires after iR correction. E) Comparison

of the MoS<sub>2</sub> nanowire structure's Tafel slope to other literature reported electrocatalysts.[196] Published by Chen, *et al.* © American Chemical Society, 2011.

This iR correction allows for accurate determination of the Tafel slope and the rate limiting mechanism of hydrogen catalysis at the sample surface (Figure 4.6C). After iR correction, the Tafel slope of the MoS<sub>2</sub>/MoO<sub>x</sub> shell/core nanowire arrays is ~50 mV/decade, which is sufficiently low when compared to other catalytic metals (Figure 4.6 F). At the optimized reaction conditions, the shell/core MoS<sub>2</sub> coated MoO<sub>x</sub> core nanowires show a favorable HER onset potential of ~150 mV vs. RHE and a geometric current density of 20 mA/cm<sup>2</sup> at < -0.3 V vs. RHE.

These MoS<sub>2</sub>/MoO<sub>x</sub> nanowires show the potential to be a great architecture for electrocatalytic water splitting, but there are some limitations to this architecture. As grown, the basal plane of MoS<sub>2</sub>, which has been shown to be catalytically inert, grows parallel to the nanowire growth direction, which means that relatively few catalytically active crystal edge sites are available for water splitting. If these nanowires can be modified in order to expose more catalytic sites or chemically altered to make the basal plane effective for catalysis, as shown in 1T – MoS<sub>2</sub> 2D sheets[28, 37], the shell/core nanowire architecture (highly conducting with high surface area) could be an optimal morphology for an electrocatalyst material. In this dissertation, lithium intercalation is used to attempt a crystal phase transformation in the MoS<sub>2</sub> nanowires, along with attempts to electrochemically “activate” the MoS<sub>2</sub> surface by using a strong reducing agent/electron dopant and these results are discussed in Chapter V.

## CHAPTER V. CHEMICAL MODIFICATION OF MoS<sub>2</sub> SHELL/CORE NANOWIRES

As discussed briefly in Chapter 2, the chemical modification of 2D layered materials has been well researched, at least from the point of view of experimental techniques. This is especially true in the lithium exfoliation of MoS<sub>2</sub> particles to form 2D, single layered sheets. The lithium intercalation is believed to apply a strain on the MoS<sub>2</sub> lattice, cause the crystal phase transformation from bulk hexagonal (2H) to a metastable trigonal (1T), which has dramatically different electronic properties. Voiry, *et al.* have recently shown experimentally that this metastable 1T phase does not seem to suffer from the anisotropic catalytic properties as bulk 2H; both the basal and edge planes seem to be electrocatalytically active for HER.[28, 29] This recent observation has led researchers to lithium intercalate various structures of MoS<sub>2</sub>, attempting to improve catalysis.[37, 38] Despite this preliminary work, there still remains a gap in the understanding of the actual mechanism of improved electronic properties and catalytic activity. In this chapter, the MoS<sub>2</sub>/MoO<sub>x</sub> shell/core nanowires are intercalated with lithium to attempt this 2H to 1T phase transformation, as well as provide insight into the actual mechanism of improved catalysis. In the second section, a strong reducing agent, hydrazine (N<sub>2</sub>H<sub>4</sub>) is used to study the effects of electron donation in this 1D shell/core system.

### 5.1. Lithium Intercalation of MoS<sub>2</sub> Nanowires.

As described in Chapter 4, MoS<sub>2</sub>/MoO<sub>x</sub> shell/core nanowires have been successfully synthesized by the reaction of MoO<sub>3</sub> with H<sub>2</sub>S.[196] The thickness of the MoS<sub>2</sub> shell, i.e. the progression of the reaction, can be manipulated by the pressure of the

H<sub>2</sub>S atmosphere. In these experiments, a thicker, 8 – 10 nm MoS<sub>2</sub> shell is grown on the single crystal MoO<sub>x</sub> core by reacting in a ~15 Torr 99% H<sub>2</sub>S atmosphere at 300°C for 2 hours. This ensures that the reduced oxide core is not exposed when the nanowires are testing in acidic media for HER catalytic activity. At the time of the writing of this dissertation, this work has been submitted and is under review. The majority of the figures in this section are taken from this manuscript.[202]

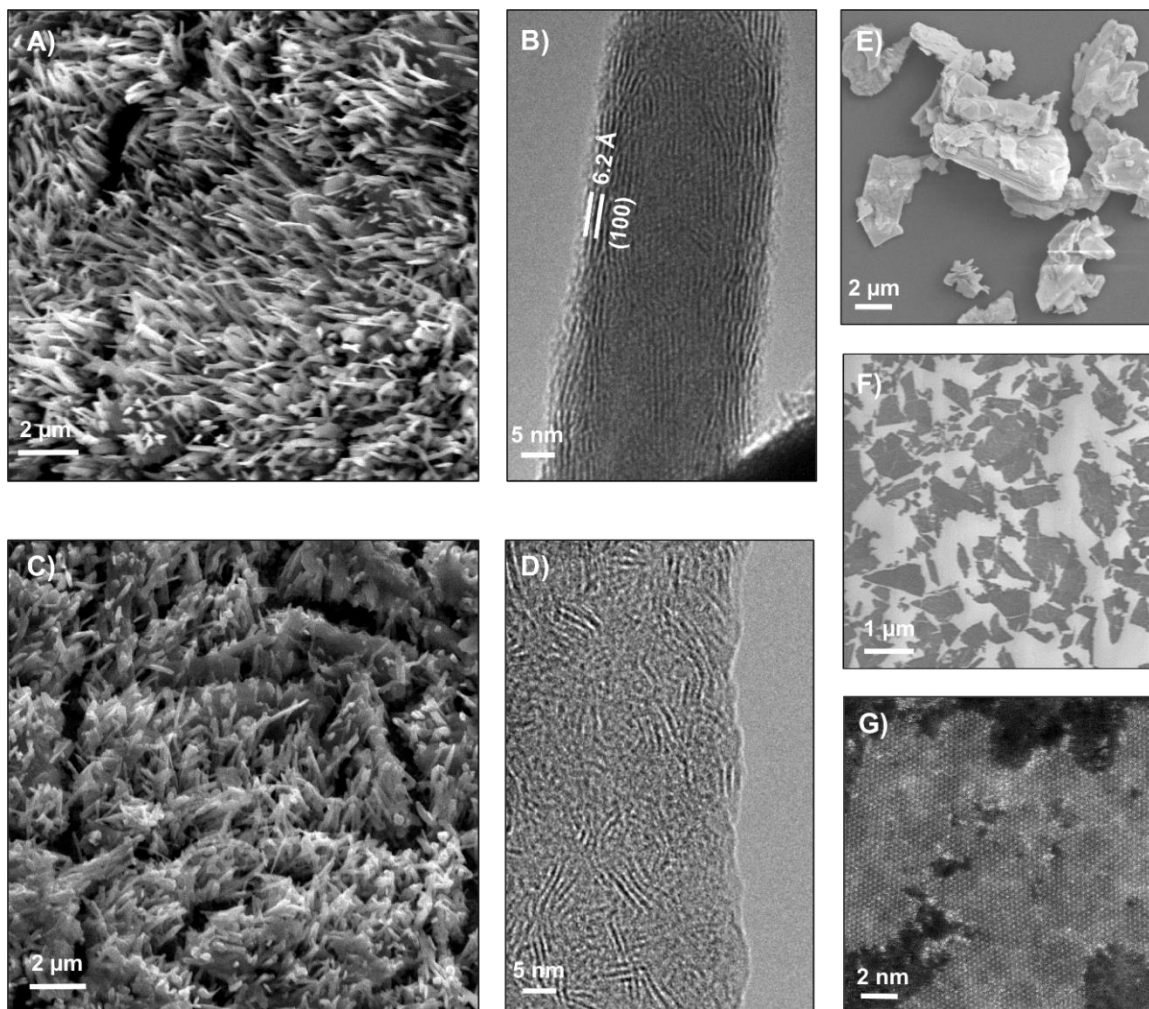


**Figure 5.1.** A) SEM of as grown MoS<sub>2</sub>/MoO<sub>x</sub> shell/core nanowire array. B) HRTEM of as grown nanowire, showing crystalline oriented MoS<sub>2</sub> shell on single crystal MoO<sub>x</sub> core. C) SEM of the MoS<sub>2</sub>/MoO<sub>x</sub> nanowires after lithium intercalation. D) HRTEM showing the

disordered MoS<sub>2</sub> shell after lithium intercalation. E) SEM image of bulk MoS<sub>2</sub> powder. F) SEM image of chemically exfoliated MoS<sub>2</sub> sheets. G) STEM imaging of 1T-MoS<sub>2</sub> chemically exfoliated 2D sheets.

The as-grown, “thick shelled” MoS<sub>2</sub> nanowires has a single crystalline shell (with some low angle grain boundaries) on a single crystal reduced MoO<sub>x</sub> core. At first glance, the nanowires do not seem to change their overall morphology, which can be seen by SEM in Figure 5.1A. HR-TEM (Figure 5.1B), however, shows that the shell/core morphology. It should be noted that the MoS<sub>2</sub> layers (interlayer spacing of 6.2Å) grow parallel to the growth axis of the nanowire. As discussed in Chapter 2, the larger, basal plane of MoS<sub>2</sub> is chemically inert, compared to the metallic, “edge” sites. In the as-grown nanowires, these edge sites are not well exposed to provide sites for the catalysis.

In an attempt to take advantage of the high surface area morphology of the nanowire array and also to increase the catalytic activity of the MoS<sub>2</sub> shell, the intercalation of lithium was proposed. The MoS<sub>2</sub> shell nanowires were soaked in *tert* butyl lithium solution from 12 to 24 hours, then rinsed vigorously in DI water to remove lithium. As seen in Figure 5.1C, the nanowire morphology is maintained after lithium intercalation. Due to the liquid processing, the entire nanowire film is delaminated from the substrate, but the individual nanowire structure is maintained. HRTEM analysis (Figure 5.1D), however, shows that the ordered MoS<sub>2</sub> shell has been severely disrupted, leading to polycrystalline domains with random orientations. This is due to the large volume expansions observed during lithium intercalation.[218, 219] As discussed previously, bulk MoS<sub>2</sub> particles (Figure 5.1E) has a hexagonal structure, known as 2H-MoS<sub>2</sub>. A metastable phase of MoS<sub>2</sub> with an octahedral crystal structure (1T-MoS<sub>2</sub>) has been shown to have significantly different



electronic properties than the stable, bulk 2H phase. For comparison, bulk MoS<sub>2</sub> powder was intercalated with lithium in the exact same manner as the nanowires, leading to single layer, 2D sheets composed primarily of 1T-MoS<sub>2</sub>, as seen in Figure 5.1 F and G.

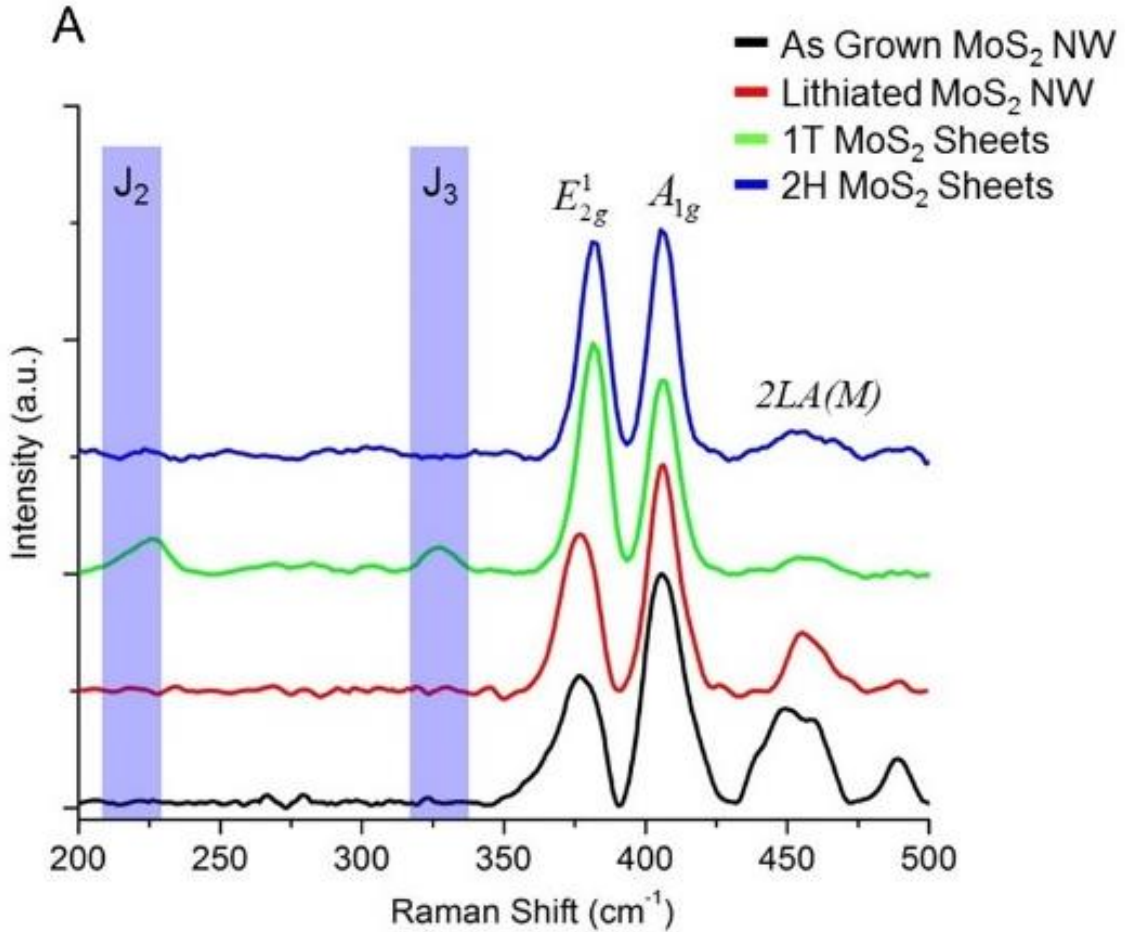


**Figure 5.2.** Raman spectroscopy for MoS<sub>2</sub> architectures: “as grown” MoS<sub>2</sub> nanowires (black curve), MoS<sub>2</sub> nanowires following lithium intercalation (red curve), chemically exfoliated 1T-MoS<sub>2</sub> sheets (green curve), and 2H-MoS<sub>2</sub> sheets (blue curves).

Since the intercalation of lithium has been shown to induce a phase change in MoS<sub>2</sub> from trigonal 2H to orthorhombic 1T, more characterization is necessary to determine whether any phase transition has occurred in the intercalated nanowires. Raman

spectroscopy is a reliable method to identify the predominant phase of MoS<sub>2</sub>. The stable 2H-MoS<sub>2</sub> has strong Raman shifts at ~382 and 407 cm<sup>-1</sup>, which correspond to the E<sup>1</sup><sub>2g</sub> and A<sub>1g</sub>, respectively. The broad peak at 454 cm<sup>-1</sup>, which is a convolution of a second order zone-edge phonon peak, 2LA(M), and a first order optical phonon, A<sub>2u</sub>. [220, 221] The metastable 1T-MoS<sub>2</sub> has unique vibrational modes at ~150 (J<sub>1</sub>), ~220 (J<sub>2</sub>), and ~325 cm<sup>-1</sup> (J<sub>3</sub>). [131] Figure 5.2 compares the Raman spectra of the MoS<sub>2</sub> nanowires, both as grown (black curve) and after lithiation (red curve), as well as chemically exfoliated 1T-MoS<sub>2</sub> sheets (green curve) and 2H-MoS<sub>2</sub> flakes (blue curve). The J<sub>2</sub> and J<sub>3</sub> Raman modes are clearly evident in 1T-MoS<sub>2</sub> sheets, but are not present in the nanowires, either before or after lithiation, which demonstrates that no detectable phase transition has occurred during the lithiation of the nanowires.

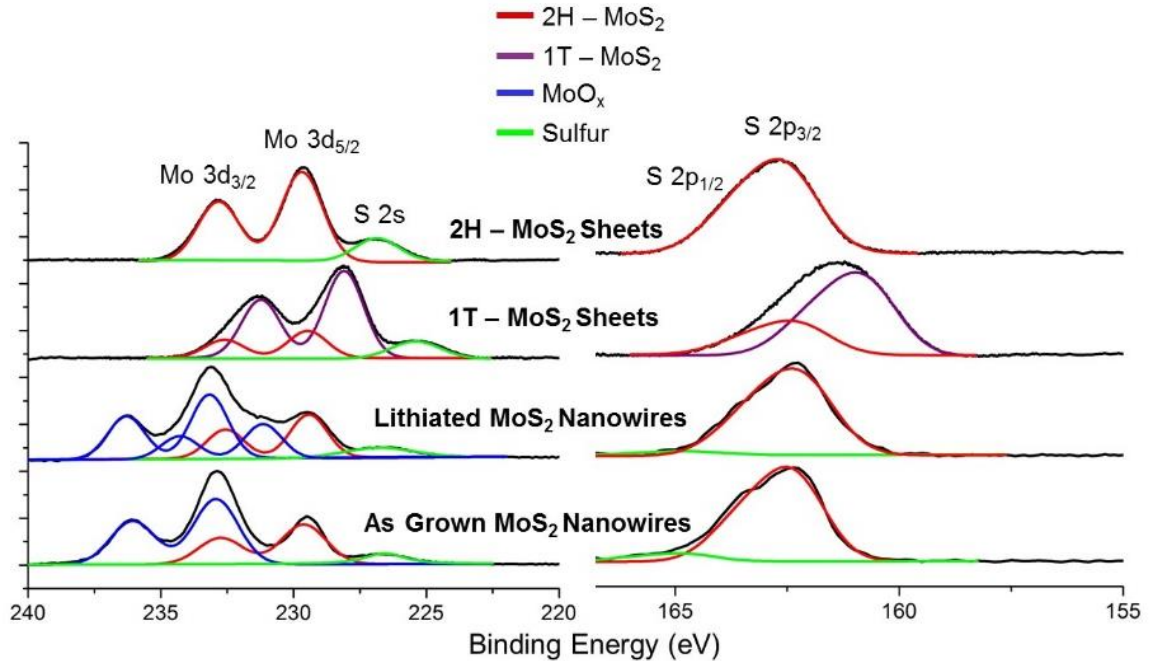


**Figure 5.3.** XPS analysis of various MoS<sub>2</sub> architectures, focusing on the core level binding energies for molybdenum and sulfur.

To further characterize the effect of lithium intercalation on the crystal structure of the MoS<sub>2</sub> nanowires, x ray photoelectron spectroscopy (XPS) is performed. Figure 5.3 clearly shows the core level binding energies of molybdenum, corresponding to trigonal prismatic 2H-MoS<sub>2</sub> with strong peaks at 229 and 232 eV, denoting Mo<sup>4+</sup> 3d<sub>5/2</sub> and Mo<sup>4+</sup> 3d<sub>3/2</sub>. Deconvolution shows the signal for Mo<sup>6+</sup> 3d<sub>5/2</sub> and 3d<sub>3/2</sub> at 232 and 236 eV, which arises from the reduced MoO<sub>x</sub> core. After exposure to lithium, the Mo<sup>4+</sup> binding energy is unaffected, but a new signal corresponding to Mo<sup>6+</sup> shows that the lithium has affected the MoO<sub>x</sub> core, further reducing it. Analysis of the sulfur core level binding energies shows the 2H-MoS<sub>2</sub> characteristic S 2p<sub>3/2</sub> and 2p<sub>1/2</sub> energies at 162.5 and 163.6 eV. The lithium intercalation of the nanowires shows no effect on the sulfur oxidation states. In contrast, XPS analysis of the chemically exfoliated 1T-MoS<sub>2</sub> shows a positive 0.9 eV shift in binding energies, in both Mo 3d and S 2p energies.[25, 131, 222] This is clearly evident in spectrum in Figure 5.3. This shows that no crystal phase transition has occurred during the lithium intercalation of the MoS<sub>2</sub>/MoO<sub>x</sub> shell/core nanowires.

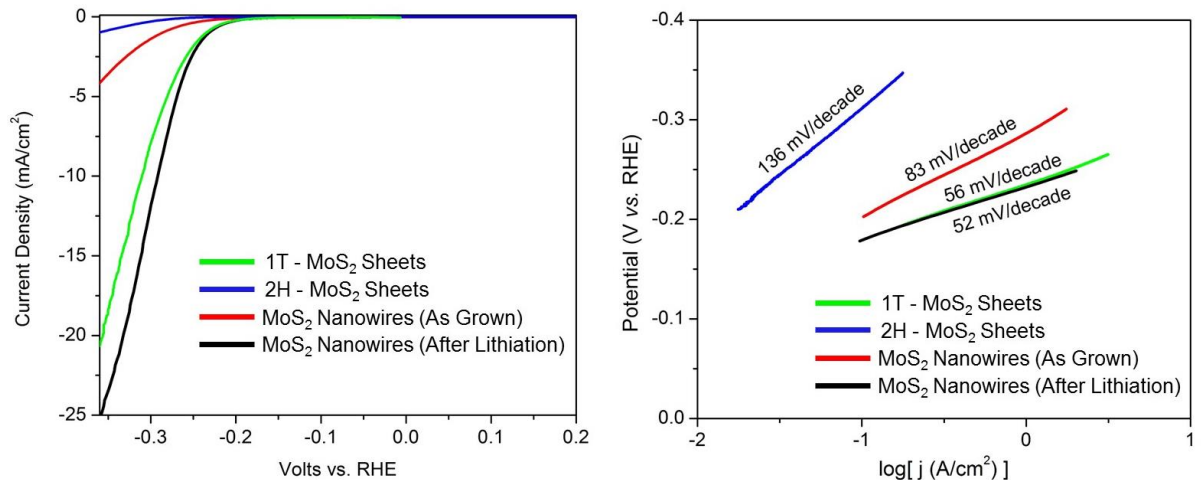


**Figure 5.4.** A) Linear voltammograms of MoS<sub>2</sub> architectures: 2H-MoS<sub>2</sub> sheets (blue curve), 1T-MoS<sub>2</sub> sheets (green curve), as-grown MoS<sub>2</sub>/MoO<sub>x</sub> shell/core nanowires (red

curve) and lithium intercalated MoS<sub>2</sub>/MoO<sub>x</sub> nanowires (black curve). B) Tafel slope analysis of the MoS<sub>2</sub> architectures.

To see the effect of the increased surface area of the intercalated nanowires, linear voltammetry is performed to gauge catalytic activity. The voltammograms can be seen in Figure 5.4A. The as-grown MoS<sub>2</sub> nanowires (red curve) show an on-set potential for the HER of -0.200 V vs. RHE and a current density of ~4 mA/cm<sup>2</sup> at -0.35 V. After the intercalation of lithium into the nanowires (black curve), resulting in the disruption of the ordered, MoS<sub>2</sub> crystalline shell, the overpotential necessary to drive the HER reduced to ~0.150 V vs. RHE and the generated current density increases six fold, ~25 mA/cm<sup>2</sup> at -0.35 V. This improvement in catalytic on-set potential is due directly to the increased exposure of active MoS<sub>2</sub> edge sites, but the catalysis is also improved by the continued reduction of the MoO<sub>x</sub> core, which provides greater conductivity of the nanowire array and allows for better carrier transport, which assists in the catalysis. 2D sheets of semiconducting 2H-MoS<sub>2</sub> sheets (blue curve), which have low conductivity, as well as low surface area, show poor catalytic activity, with an on-set potential of -0.250 mV vs. RHE and a current density of ~1.5 mA/cm<sup>2</sup>. The chemically exfoliated 1T-MoS<sub>2</sub> sheets (green curve) shows a favorable on-set potential of -0.150 mV vs. RHE, comparable to the intercalated nanowires, and a current density of ~20 mA/cm<sup>2</sup>. The metallic nature of the 1T sheets allows for better charge transport, which leads to the improved catalysis[28], but it is still inhibited by low surface area, which is overcome by the conducting, high surface area nanowire architecture.

Figure 5.4B shows the Tafel slope analysis for the various experimental MoS<sub>2</sub> architectures. The semiconducting 2H-MoS<sub>2</sub> flakes show a Tafel slope of ~136 mV/decade (blue curve), which denotes that the adsorption of protons onto the catalyst surface (*i.e.* the Volmer reaction) is the rate limiting step. The chemically exfoliated, 1T-MoS<sub>2</sub> sheets show a significantly lower Tafel slope (~56 mV/decade), which shows that the rate limiting step has changed from adsorption (Volmer step) to the evolution of hydrogen from the catalyst (Heyrovsky and Tafel steps). The chemical exfoliation and resulting crystal phase transformation has fundamentally changed the catalytic site. In contrast, the as grown MoS<sub>2</sub>/MoO<sub>x</sub> core shell nanowires show a Tafel slope of 83 mV/decade, which indicates a combination of hydrogen adsorption and evolution as the rate limiting step, but the adsorption onto the catalytic site is still the dominant rate limiting step. After the intercalation of lithium into the shell/core nanowire, the Tafel slope decreases to 52 mV/decade, similar to the 1T-MoS<sub>2</sub> sheets. This shows a change in the rate determining step, which shows that catalytically active site has changed, indicative of the freshly exposed active edge sites from the crystal disruption of the MoS<sub>2</sub> shell. For comparison, Figure 5.5A shows the catalytic activity of bulk MoS<sub>2</sub> powder, prepared for electrochemical testing in a similar method as the nanowires and 2D sheets. The bulk MoS<sub>2</sub> requires a significantly high overpotential to drive the HER, ~0.8 V vs. RHE and has poor conductivity, thus low current density. The high Tafel slope of ~155 mV/decade shows the poor kinetics.

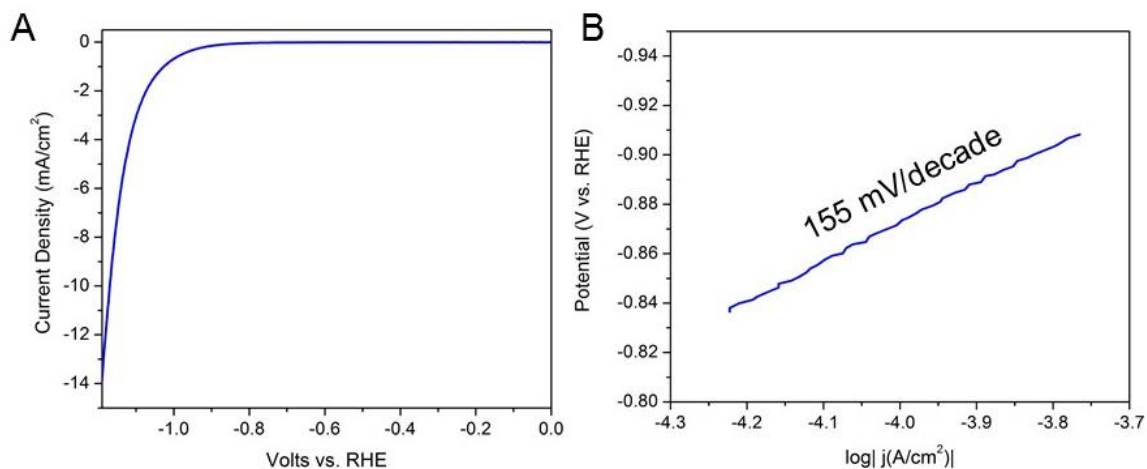


**Figure 5.5.** A) Linear Voltammogram of bulk MoS<sub>2</sub> powder. B) Tafel slope analysis of bulk MoS<sub>2</sub> powder.

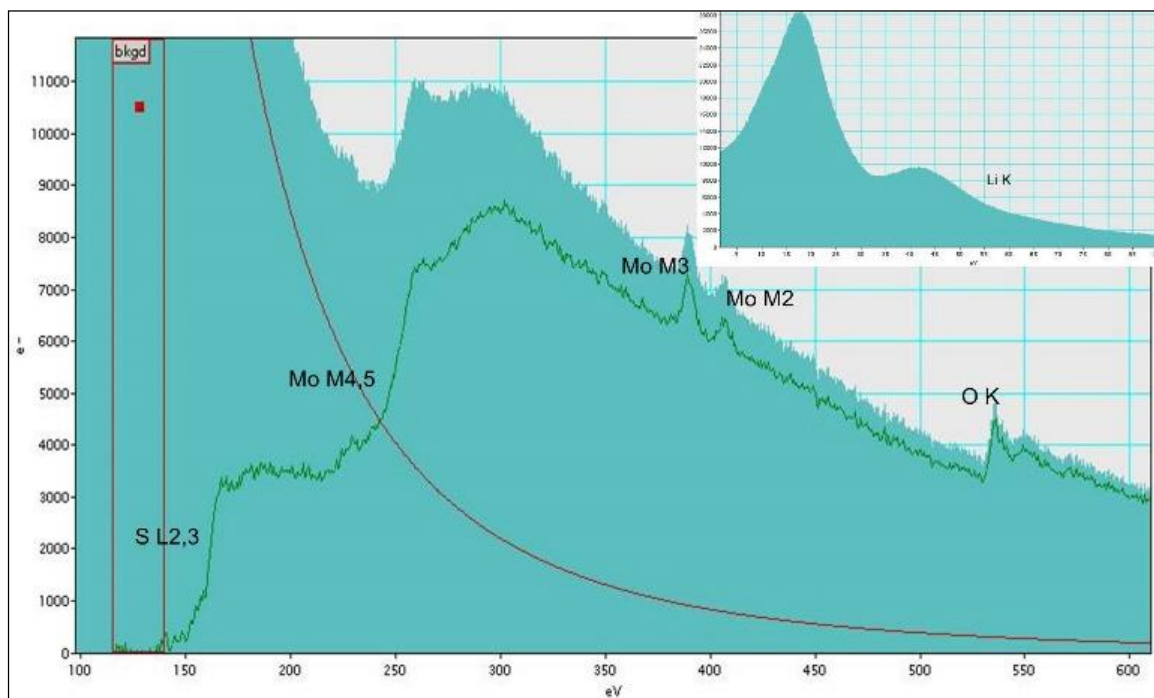


**Figure 5.6.** EELS spectrum of lithium intercalated MoS<sub>2</sub>/MoO<sub>x</sub> shell/core nanowires, showing strong signal for sulfur, molybdenum, and oxygen. The inset focuses on the location of the lithium edge (65 eV). This shows very minimal signal for the presence of lithium.

It is possible that some intercalated lithium may remain intercalated in the MoS<sub>2</sub> shell lattice of the nanowires, even after the vigorous water washing. To confirm that all the intercalated lithium has been effectively removed, electron energy loss spectroscopy (EELS) was performed. Figure 5.6 shows the strong signal resulting from the Sulfur edge (165 eV), Molybdenum edge (227, 392, and 410 eV), and Oxygen edge (532 eV). The inset focuses on the location of the Lithium edge (65 eV). The EELS spectrum was obtained in multiple spots on different nanowires and showed no trace of lithium signal. The spectrum shown reveals the weakest trace of lithium. This shows that, predominantly, the lithium has been removed from the nanowires and only trace amounts may remain in the lattice or adsorbed on the surface. The nanowires are essentially washed again when they are dispersed in DI water for transfer to the glassy carbon electrode, so it is virtually impossible that lithium is contributing in any way to the catalytic activity.

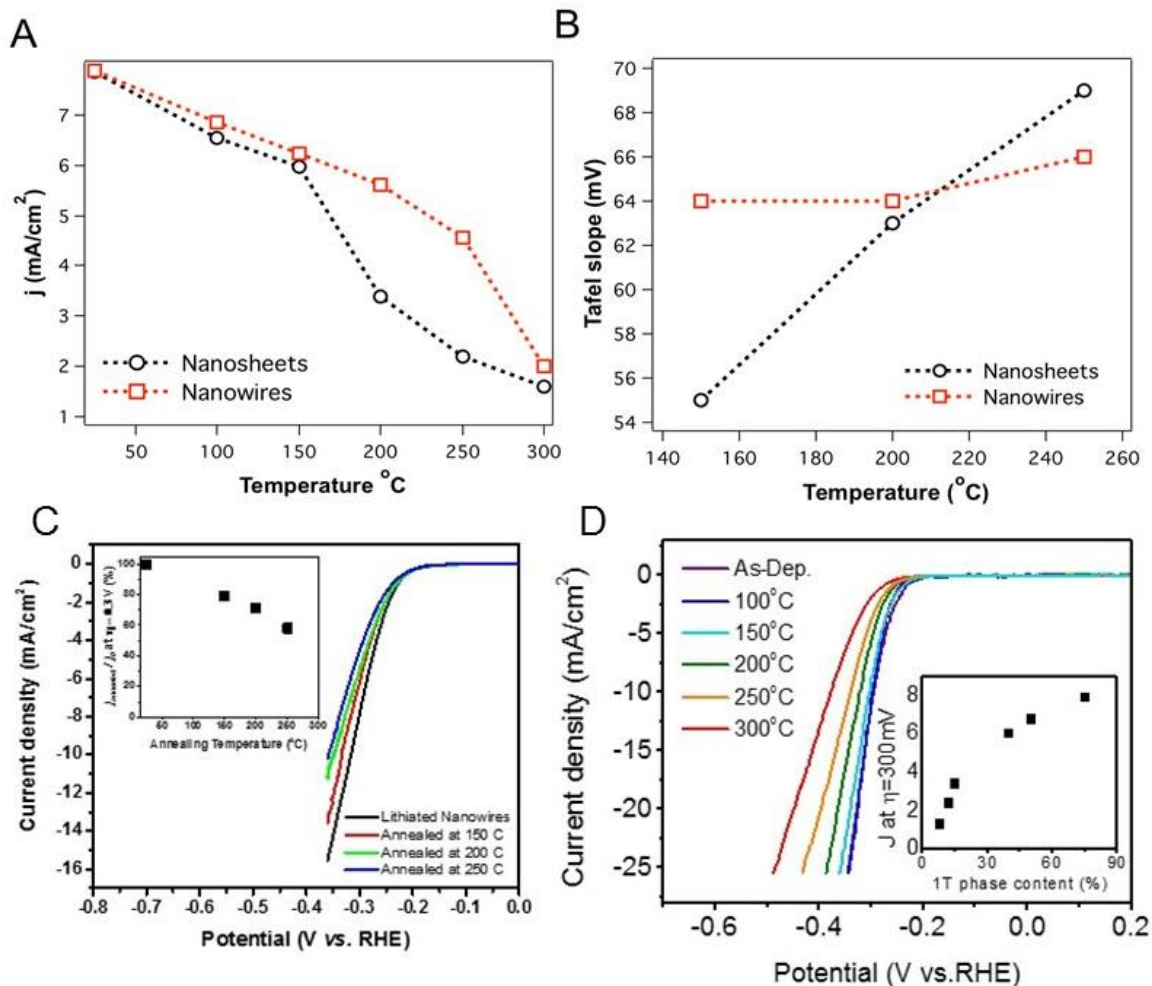


**Figure 5.7.** A) Normalized Current density of MoS<sub>2</sub> nanosheets and nanowires during step by step annealing. B) Change in Tafel slope of MoS<sub>2</sub> nanosheets and nanowires during step by step annealing. C) Linear voltammograms showing the HER catalytic activity of lithitated nanowires during step by step annealing. D) Linear voltammograms showing HER activity of 1T-MoS<sub>2</sub> during step by step annealing.

It is well known that metallic octahedral 1T-MoS<sub>2</sub> is a metastable phase and will convert back to stable, semiconducting trigonal 2H-MoS<sub>2</sub> under mild annealing. Step by step annealing was performed on the chemically exfoliated flakes and the lithiated nanowires and the effect on catalytic activity is measured and can be seen in Figure 5.7.



As expected, the catalytic activity of the 1T-MoS<sub>2</sub> changes significantly during the annealing process, due to the crystal phase transition from 1T to 2H phase. The overpotential required to drive the HER reaction increases linearly with increasing temperature while the current density decreases; similarly the Tafel slope increases with annealing temperature, showing a change in the catalytically active site. In contrast, the lithiated MoS<sub>2</sub>/MoO<sub>x</sub> nanowires show almost no change in HER on-set potential as the sample is annealed and the Tafel slope remains unchanged, demonstrating that there is no change in the catalytically active site. The current density of the lithiated nanowires slightly decreases as the sample is annealed, but not to the extent as the 1T-MoS<sub>2</sub> 2D sheets. This current density reduction, but no change in onset or Tafel slope in the nanowires is a result of physical agglomeration of the nanowires during annealing; there is no effect on the active site, but the actual surface area is reduced.

In conclusion, the goal of these experiments was, initially, to expose MoS<sub>2</sub>/MoO<sub>x</sub> shell/core nanowires to lithium solution in order to induce a crystal phase transformation from bulk trigonal prismatic 2H-MoS<sub>2</sub>, which has semiconducting properties and is relatively poor for catalysis to the metastable octahedral 1T-MoS<sub>2</sub>, which has metallic properties and has been shown to be highly active in catalyzing the hydrogen evolution reaction. After extensive characterization, it was observed that no crystal phase transition occurred during the lithium intercalation, *i.e.* the MoS<sub>2</sub> shell maintained its stable 2H-MoS<sub>2</sub> phase. The lithium intercalation instead caused a large volume change, which led to the large expansion of the MoS<sub>2</sub> shell and, upon relaxation, destroyed the ordered layered structure, leading to polycrystalline MoS<sub>2</sub> domains with random orientations. These random orientations dramatically exposed more “edge sites” of the MoS<sub>2</sub>, which increased

the active area for HER catalysis. While not being a crystal phase transformation, the crystal structure was modified to improve the overpotential required to drive the catalysis, as well as increasing the generated current density during electrocatalysis.

## 5.2. Exposure of MoS<sub>2</sub> Nanowires to Reducing Agents

It has been shown that lithiation of bulk MoS<sub>2</sub> causes the donation of an electron to the lattice, causing a 60° tension in the structure, changing the properties from semiconducting to metallic and improving the catalytic properties of the exfoliated sheets.[131] The molecular orientation shift from trigonal prismatic to octahedral is attributed to the donation of an electron from lithium, but no other electron donors have been investigated. In the production of graphene, hydrazine (N<sub>2</sub>H<sub>4</sub>) is a common reducing agent and “electron dopant” in conversion of graphene oxide (GO) flakes to reduced graphene oxide (rGO).[223, 224]. The effects of these reducing agents/electron donors in layered transition metal chalcogenides has not been reported.

In this section, hydrazine is used to chemically modify the surface of the 1D MoS<sub>2</sub>/MoO<sub>x</sub> shell/core nanowires. A brief exposure to N<sub>2</sub>H<sub>4</sub> significantly improves the HER catalytic activity of the nanowires, requiring a low onset potential of <100 mV vs. RHE and an exponential improvement in current density.

In the preparation of these nanowires to observe the surface effects, a thinner MoS<sub>2</sub> shell (1 – 3 nm) was grown on the MoO<sub>x</sub> core by reacting at low pressures (~100 mTorr) in 99% H<sub>2</sub>S at 300°C for the two hours. In order to treat the nanowires with hydrazine, a 1% by volume solution of N<sub>2</sub>H<sub>4</sub> in water was dropped (5 μL) directly on the nanowire array and allowed to dry in air (~10 – 15 minutes). For electrochemical testing, this array was dispersed in DI water and applied to a glassy carbon electrode; this second dispersion reduces the agglomeration of the treated nanowires.

Figure 5.8A shows SEM of the as-grown vertically oriented MoS<sub>2</sub>/MoO<sub>x</sub> nanowires. SEM images of the drop cast nanowire array merely shows the viscous N<sub>2</sub>H<sub>4</sub>

solution, which is what necessitates the second dispersion in DI water. SEM of the hydrazine treated nanowire array shows that the nanowire morphology is still maintained, as seen in Figure 5.8B.

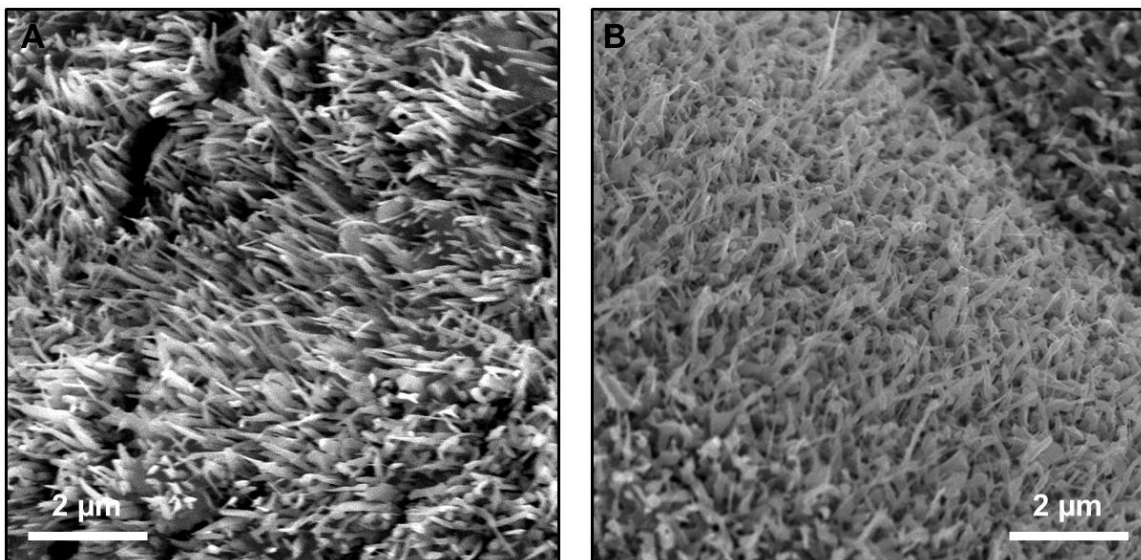


**Figure 5.8.** A) SEM image of the as grown  $\text{MoS}_2/\text{MoO}_x$  shell core nanowires grown on  $\text{SiO}_2$  substrates. B) SEM of the hydrazine treated nanowires, showing the maintenance of the 1D morphology.

Under HRTEM, the as grown nanowires show the shell/core structure, having a 1 – 3 nm  $\text{MoS}_2$  shell on the single crystal oxide core. The  $\text{MoS}_2$  shell exhibits the characteristic interlayer spacing of 6.2 Å for semiconducting 2H- $\text{MoS}_2$ , as seen in Figure 5.9A. Figure 5.9B shows the crystallographic structure after exposure to the 1% hydrazine. There is no noticeable disruption of the ordered  $\text{MoS}_2$  shell, as seen during the lithium intercalation.[202] Upon analysis of the interlayer spacing, the hydrazine treated nanowires show an average interlayer spacing of ~5.7 Å. This decrease of interlayer

spacing is not indicative of intercalation, which would lead to an increase in the spacing [37], even though it has been shown that it is possible for hydrazine ( $\text{N}_2\text{H}_4$ ) molecules to intercalate into bulk  $\text{MoS}_2$  [225]. Since the d spacing of the material decreased, simple intercalation cannot be the observed mechanism; the effects of hydrazine on the nanowires structure can be seen in Figure 5.9B.

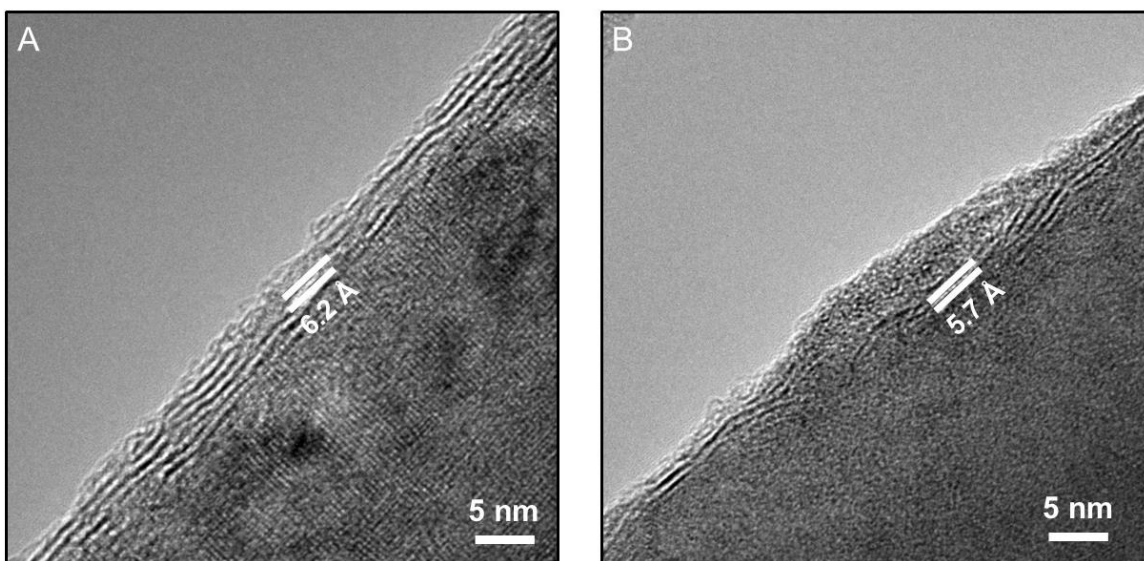


**Figure 5.9.** A) HRTEM of the as grown “thin shelled”  $\text{MoS}_2/\text{MoO}_x$  shell/core nanowire, with the thin 1 – 3 nm shell with interlayer spacing of  $\sim 6.2$  Å. B) HRTEM of the  $\text{MoS}_2/\text{MoO}_x$  shell/core nanowire after exposure to 1% Hydrazine. There is no significant disruption of the order  $\text{MoS}_2$  crystalline shell, but the average interlayer spacing has decreased to  $\sim 5.7$  Å.

Though it appears that there appears to be no significant modification of the  $\text{MoS}_2$  crystal structure, the electrocatalytic activity of the nanowires increases significantly, as seen in Figure 5.10. The nanowires were dispersed in DI water and applied to a glassy

carbon electrode for testing in a three-electrode electrochemical setup, with 0.5 M H<sub>2</sub>SO<sub>4</sub> as the electrolyte.

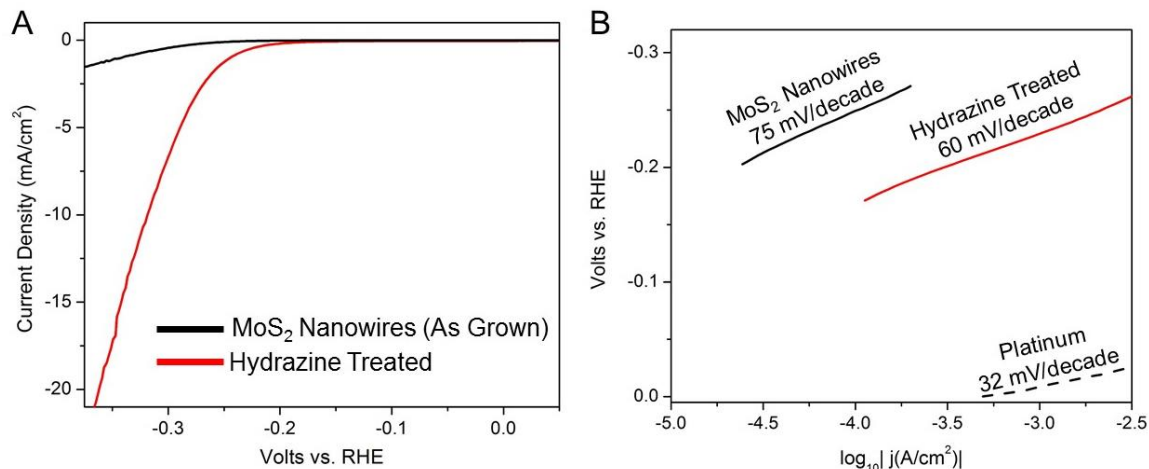


**Figure 5.10.** A) Linear voltammograms of the as grown MoS<sub>2</sub>/MoO<sub>x</sub> shell/core nanowire (1-3 nm shell) and after exposure to 1% hydrazine. B) Tafel slope analysis of the as grown and hydrazine treated nanowires. The Tafel slope of platinum wire is shown for comparison.

The thin shelled, as grown nanowires show an HER on set potential of -200 mV vs. RHE and a current density of ~ 2 mA/cm<sup>2</sup> at -0.4 V vs. RHE. After the 10 minute exposure to dilute hydrazine, the overpotential required to drive the HER is improved to < 100 mV vs. RHE. The Tafel slope of the nanowires decreases from 75 mV/decade, indicative of limited proton absorption sites (Volmer reaction)[15], combined with limited evolution of molecular hydrogen *via* the Hevrovsky mechanism. After the exposure to hydrazine, the Tafel slope decreases to 60 mV/decade. This is not a dramatic change in Tafel slope, but indicates that the adsorption of hydrogen has been facilitated by the hydrazine. This could

be indicative that more electrons have been accumulated on the surface, providing sites for protons. The Tafel slope of the hydrazine treated nanowires is nearing the ideal HER electrocatalyst, platinum, with a Tafel slope of 30 mV/decade.[207]

To further characterize the effect of hydrazine on the MoS<sub>2</sub>/MoO<sub>x</sub> shell/core nanowires, the crystal structure was analyzed using Raman and XPS spectroscopy to determine if the donated electron has induced a phase change from semiconducting 2H to metallic 1T. The Raman spectrum can be seen in Figure 5.11.

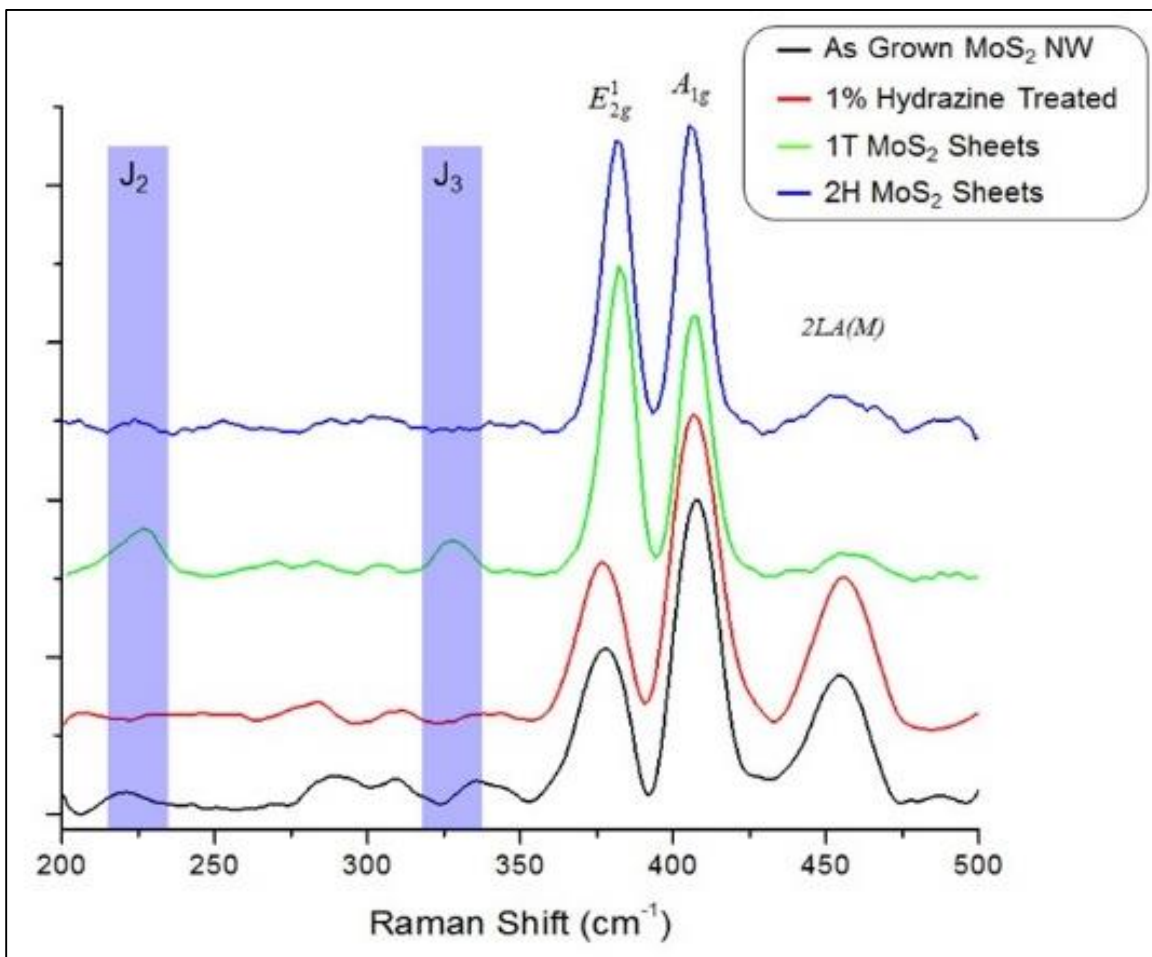


**Figure 5.11.** Raman spectroscopy of MoS<sub>2</sub> nanowire arrays as grown (black curve) and after the hydrazine treatment (red curve). For comparison, Raman analysis of chemically

intercalated 1T – MoS<sub>2</sub> 2D sheets (green curve) and 2H – MoS<sub>2</sub> sheets (blue curve) is included. Location of the J<sub>2</sub> and J<sub>3</sub> vibrational modes for 1T – MoS<sub>2</sub> are highlighted in blue.

The black curve shows the Raman spectrum for the as grown nanowires, with the characteristic MoS<sub>2</sub> Raman peaks at ~382 and 407 cm<sup>-1</sup>, indicative of the E<sub>2g</sub><sup>1</sup> and A<sub>1g</sub> vibrational modes. The broad Raman peak at ~453 cm<sup>-1</sup> corresponds to a second order phonon, 2LA(M).[220, 221]. The as grown nanowires corresponds to the 2H-MoS<sub>2</sub> spectrum (blue curve).[202] Raman analysis of the 1T – MoS<sub>2</sub> (green curve) shows the presence of unique J<sub>2</sub> and J<sub>3</sub> vibrational modes at 230 cm<sup>-1</sup> and 350 cm<sup>-1</sup>, which are unique to the metallic trigonal crystal phase. Raman analysis of the hydrazine treated MoS<sub>2</sub> nanowires (red curve) shows no evidence of a crystal phase transformation, indicating that the 2H-MoS<sub>2</sub> crystal structure is maintained.

To further confirm that the hydrazine treatment did not induce a crystal phase change, XPS analysis is performed and seen in Figure 5.12. The as grown MoS<sub>2</sub> / MoO<sub>x</sub> shell / core nanowires show the characteristic doublet peak at 229 and 232 eV, arising from the Mo<sup>4+</sup> 3d<sub>5/2</sub> and Mo<sup>4+</sup> 3d<sub>3/2</sub> from 2H-MoS<sub>2</sub>, denoted by the red curve. The peak at 230 eV is a convolution between Mo<sup>4+</sup> of MoS<sub>2</sub> and Mo<sup>6+</sup> from the reduced MoO<sub>x</sub> core. After exposure to hydrazine, there is no shift in the Mo binding energy for Mo<sup>4+</sup> at 2H-MoS<sub>2</sub>, but there was a slight shift in the Mo<sup>6+</sup> signal, indicating that the reduced Molybdenum oxide core was further reduced by the hydrazine. The sulfur 2p signal is very apparent at ~162.5 eV in the as grown sample and there is no observed shift in the S 2p binding energies



after hydrazine treatment, clearly indicating no crystal phase transformation from the 2H – MoS<sub>2</sub> phase.

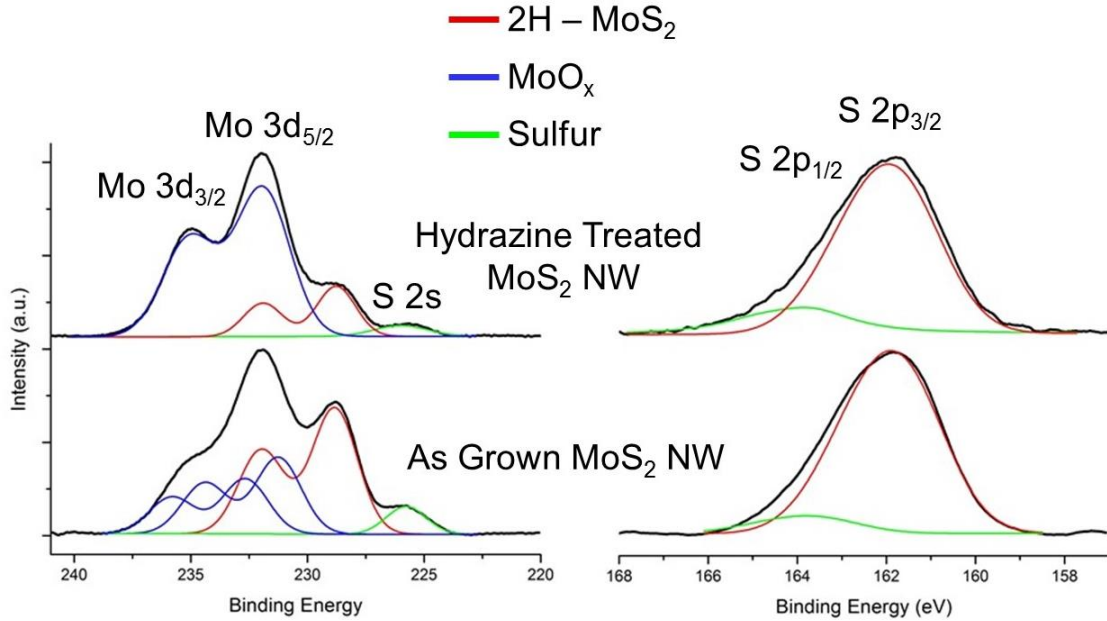
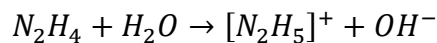
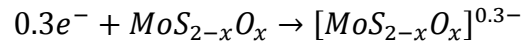
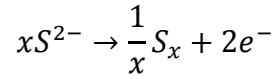
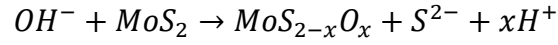


**Figure 5.12.** XPS analysis of the molybdenum 3d, sulfur 2s, and sulfur 2p core level binding energies in the MoS<sub>2</sub>/MoO<sub>x</sub> shell/core nanowires, both as grown and after exposure to 1% hydrazine.

Since the hydrazine electron dopant treatment does not induce a crystal phase transformation from semiconducting 2H to metallic 1T and the hydrazine does not appear to have intercalated between the layers, another mechanism must be considered. The relatively inert basal plane of the 2H-MoS<sub>2</sub> must be somehow “activated” by the hydrazine. One possibility is that the N<sub>2</sub>H<sub>4</sub> slightly reduces the MoS<sub>2</sub> surface. In aqueous conditions, hydrazine reacts to form a basic solution.



It has been shown in strong basic solutions, chalcogenide semiconductors, though chemically stable, can be pseudo “reduced” at surface sites.[226] Applying this reducing mechanism to the MoS<sub>2</sub> system, the following mechanism is proposed.[227]



This reducing effect gives an overall negative charge to the MoS<sub>2</sub> nanowires, effectively “electron doping” and activating the MoS<sub>2</sub> basal plane.

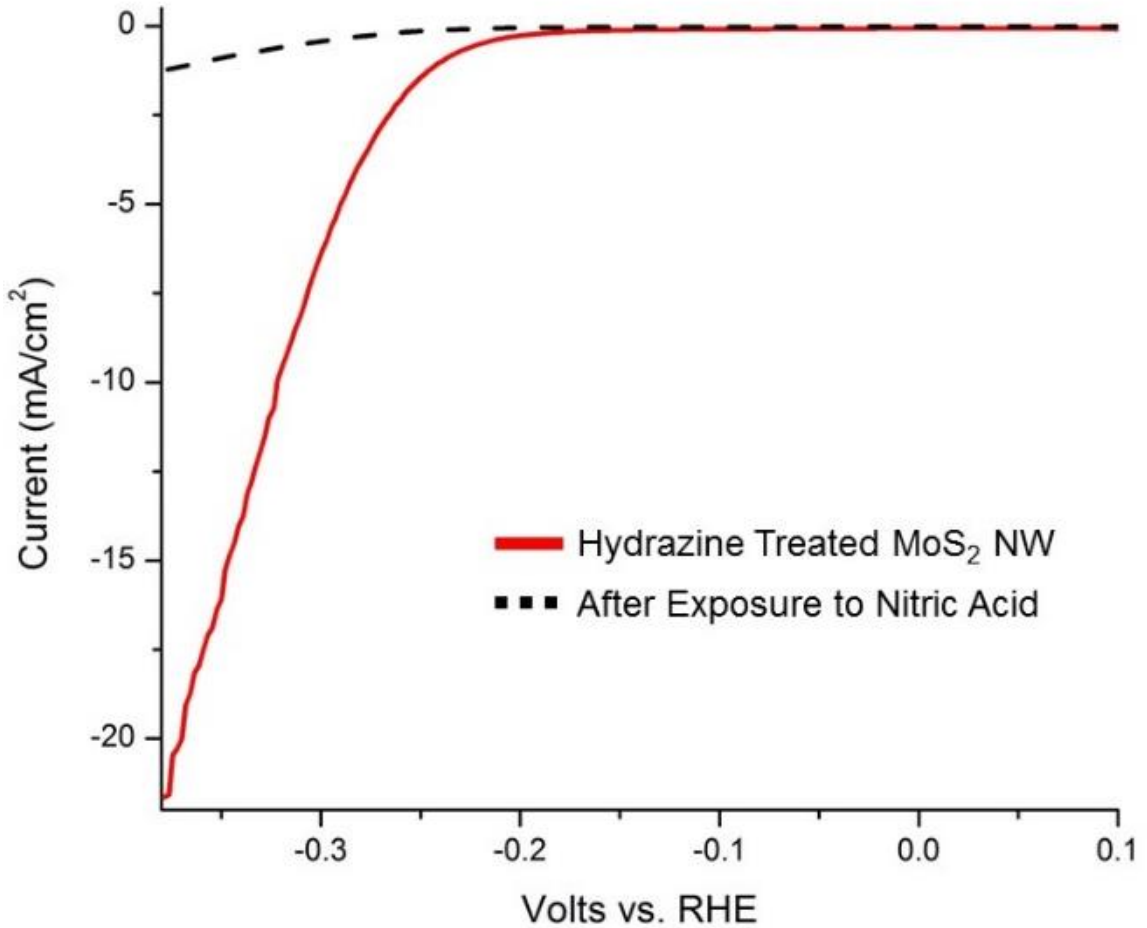


**Figure 5.13.** Linear sweep voltammetry of MoS<sub>2</sub> nanowire array first treated with dilute hydrazine (red curve), then exposed to dilute nitric acid (dashed black curve). The exposure of the hydrazine to a proton rich solution (acid) returned the electrocatalytic performance to as-grown properties.

The simplest method to test if charge carriers, whether they are electrons or hydroxyl groups are adsorbing onto the MoS<sub>2</sub> surface is to add protons to the system and observe the effects. The MoS<sub>2</sub>/MoO<sub>x</sub> shell/core nanowires were exposed to 1% hydrazine in the typical drop-cast method and the improved electrocatalytic activity was observed. Then, a 1% solution of nitric acid (HNO<sub>3</sub>) was drop-cast onto the hydrazine treated nanowires, essentially providing protons which will react with any negative charge carriers on the surface. The results of this experiment, shown in Figure 5.13, show the introduction of protons to the hydrazine treated system returns the nanowire to the as-grown activity. This helps build the argument that the hydrazine is causing the adsorption of negative charges on the MoS<sub>2</sub> surface.

Since the hydrazine is applied in aqueous form directly on the nanowires, it is possible that simply a monolayer of N<sub>2</sub>H<sub>4</sub>/H<sub>2</sub>O is absorbed on the surface of the nanowire and the actual activity of the MoS<sub>2</sub> is not affected. To disprove the presence of an aqueous layer, the nanowire array was treated with 1% hydrazine, then annealed at 150°C for 1 hour. As Figure 5.14 shows, there is no significant change in HER catalysis after annealing, proving that the improved electron concentration does not result from an aqueous physisorption. The increased activity is a result of electrochemical modification of the MoS<sub>2</sub> surface

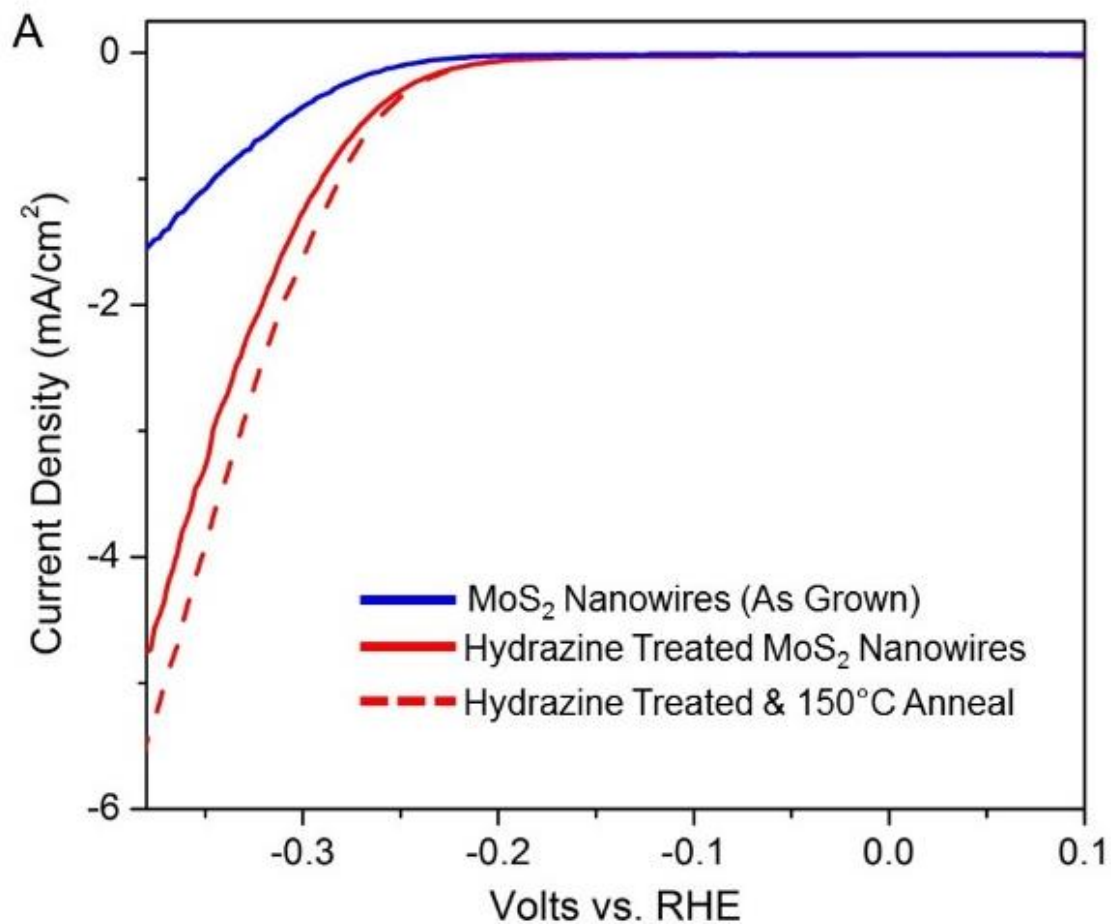


**Figure 5.14.** Linear voltammetry for as grown MoS<sub>2</sub> nanowires (blue curve), treated with Hydrazine (red curve), then annealed at 150°C for 1 hour (red dashed line).

To test the hypothesis that increasing the electron concentration on the basal plane of MoS<sub>2</sub> can effectively “activate” the material, an in-situ gate dependent HER catalysis experiment was set up. A mechanically exfoliated 2H – MoS<sub>2</sub> sheets is placed on a SiO<sub>2</sub> back gated substrate. E beam lithography is used to place gold contacts on the single sheet. The entire substrate is covered in a thick polymer PMMA coating and a window (~140 μm<sup>2</sup>) is opened, exposing only the basal plane of the 2H sheet, but covering the gold

contacts. An optical microscopic image of the device set up can be seen in Figure 5.13B. To measure the HER catalysis, a small droplet of 0.5 M  $\text{H}_2\text{SO}_4$  is applied to the flake and a thin platinum wire counter electrode and a AgCl coated Ag wire is placed into the droplet to act as a voltage reference. A schematic of the experimental set up is shown in Figure 5.15A. In this device set up, two different voltage sources were utilized. To perform the cyclic voltammetry and measure the actual electrochemical activity, the three-electrode system (working, counter and reference electrode) was controlled by an Autolab® Potentiostat. A voltage is applied between the working electrode ( $\text{MoS}_2$  flake) and the reference electrode (Ag/AgCl wire) and the generated current is measured between the working electrode and the counter electrode (platinum wire). A separate voltage source is used to apply a gate voltage to the doped silicon wafer, which leads to the  $\text{MoS}_2$  flake acting as the “channel” in the transistor device, the  $\text{SiO}_2$  layer acting as the oxide layer, and Si (n++) acting as the gate, which is grounded.[228]

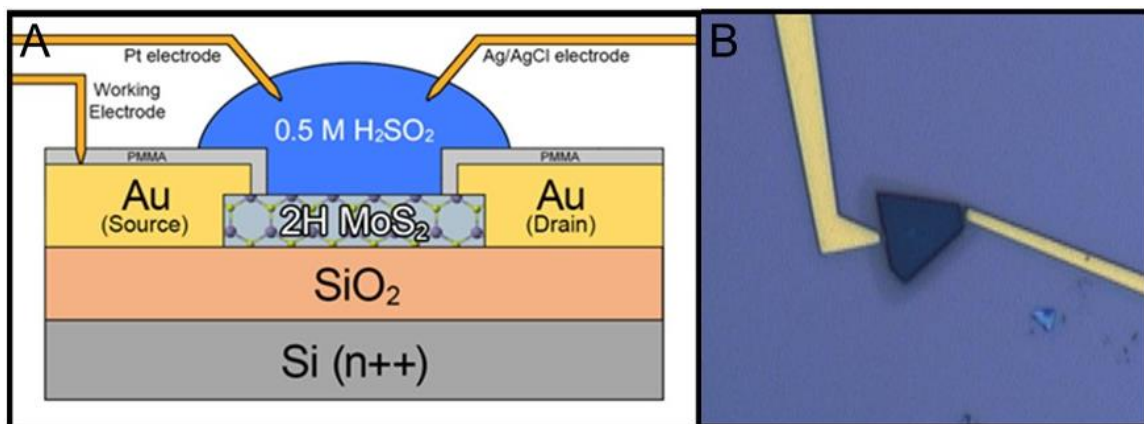


**Figure 5.15.** A) Schematic showing experimental set up for gate dependent HER catalysis measurements. B) Optical microscopic image of the exposed  $\text{MoS}_2$  flake.

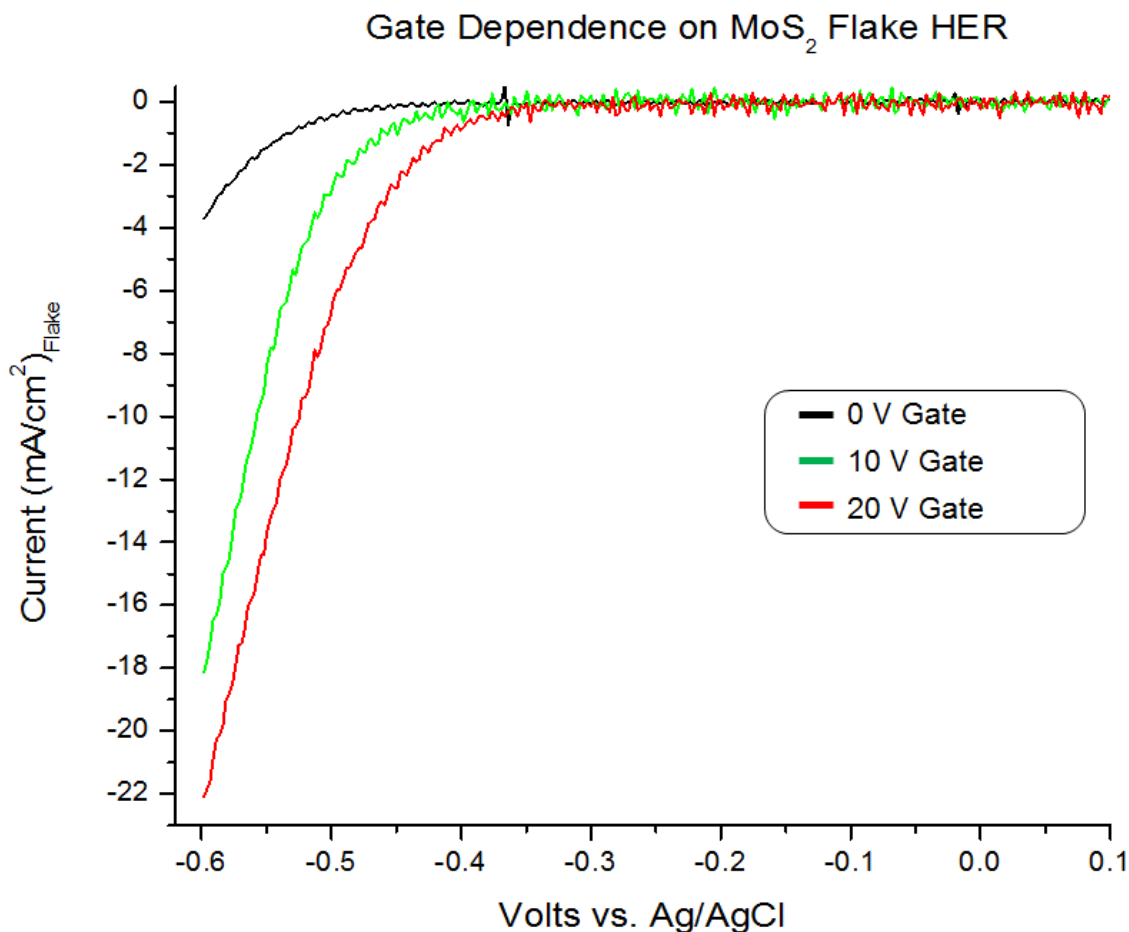


**Figure 5.16.** Linear sweep voltammograms showing the gate dependence of HER catalysis in a single MoS<sub>2</sub> sheet.

Figure 5.16 shows linear sweep voltammograms of the MoS<sub>2</sub> flake when a gate voltage is applied. The voltage is reported versus the arbitrary Ag/AgCl wire. It is not possible to establish a reference voltage for the electrode vs. RHE if there is no redox reaction. As expected, the 2H sheet with no gate voltage shows very poor electrocatalytic activity (black curve). When a positive 10 V gate is applied to the substrate, electrons are effectively forced to the material surface (green curve). The overpotential to drive the HER catalysis reduces dramatically and the generated current density improves. When the gate

bias is increased to 20 V, the on-set potential continues to improve, as well as the current density. This in-situ analysis shows that the inert basal plane of MoS<sub>2</sub> can be activated by increasing the electron concentration on the surface. The hydrazine treatment is causing a similar effect in the MoS<sub>2</sub> nanowires.

While the increased electron concentration has been shown to increase electrocatalytic activity, it is not clear if hydrazine actually has an effect on the electrochemical properties of MoS<sub>2</sub>. The MoS<sub>2</sub>/MoO<sub>x</sub> shell/core nanowire array was grown on a non-conducting substrate, glass, and was mounted on a ceramic holder and connected in a four point probe configuration using silver epoxy. A photograph of the nanowire array in the four point probe set up is shown in Figure 5.17.

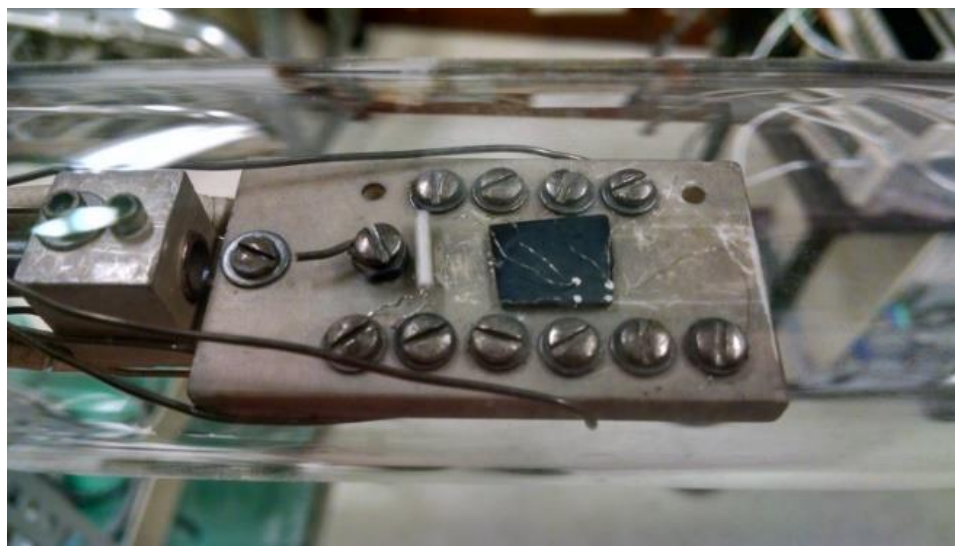


**Figure 5.17.** Photograph of MoS<sub>2</sub>/MoO<sub>x</sub> shell/core nanowire array in a four point probe configuration. The ceramic holder is in an evacuated quartz chamber.

The ceramic holder was placed in an evacuated quartz chamber, then placed inside a tube furnace. The initial four point resistance was measured at  $\sim 1.588 \text{ k}\Omega$ . The chamber was evacuated to a base pressure of  $\sim 10^{-5}$  Torr and the resistance decreased to  $\sim 1.064 \text{ k}\Omega$ , shown in Figure 5.18A. The sample was annealed at 450 K under vacuum in order to remove surface moisture and contamination. As the sample is annealed (Figure 5.18B), the resistance of the array decreases and reaches an equilibrium of  $\sim 706 \Omega$ .

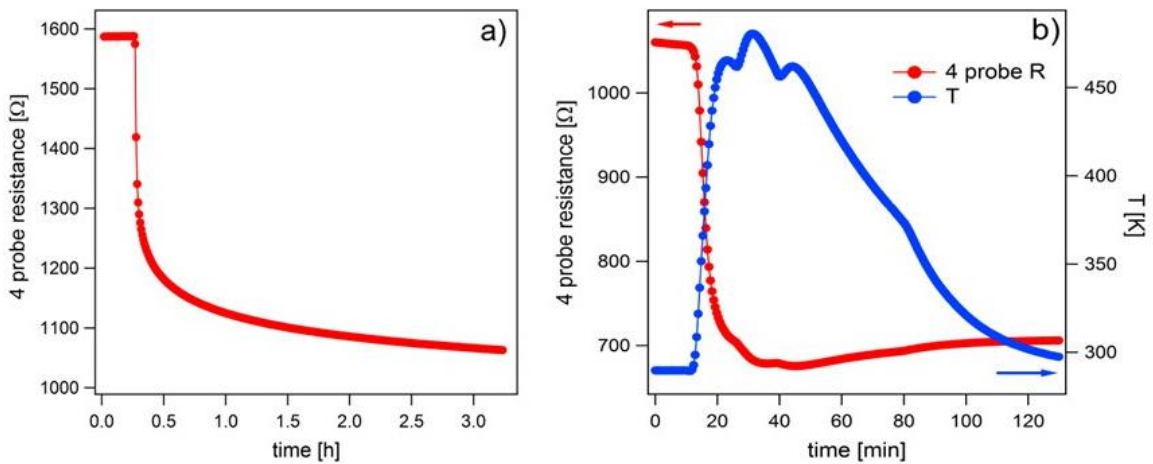


**Figure 5.18.** A) Change in four probe resistance as the chamber is evacuated. B) Effect of annealing on the four probe resistance of MoS<sub>2</sub>

Once the sample maintained a constant resistance ( $\sim 710 \Omega$ ), a maximum pressure of 350 Torr of ambient air was introduced to the system. The introduced air resulted in a very minimal increase in the MoS<sub>2</sub> nanowire array, from 706 to 708 Ω. The introduction of ambient air acts as a control experiment; this will isolate the effects of ambient air and moisture. The sample was annealed again, then 15 Torr of anhydrous hydrazine vapor was introduced. Almost instantaneously, the overall sample resistance decreased from 706 Ω



to  $\sim 495 \Omega$ . This dramatic decrease in resistance stabilized after approximately 30 minutes and the system was evacuated. Interestingly, there was no significant change in the hydrazine treated  $\text{MoS}_2$  nanowire array, even after the hydrazine vapor was removed. This experimentally shows that not only does hydrazine treatment lower the resistance, *i.e.* increase the conductivity of the  $\text{MoS}_2$  nanowires, but it is not just a temporary surface affect, but the nanowires are chemically altered. This seems to show that hydrazine acts as a reducing agent and electron “dopant” for the  $\text{MoS}_2$  and chemically modifies the material. The change in four probe resistance after hydrazine introduction is shown in Figure 5.19.

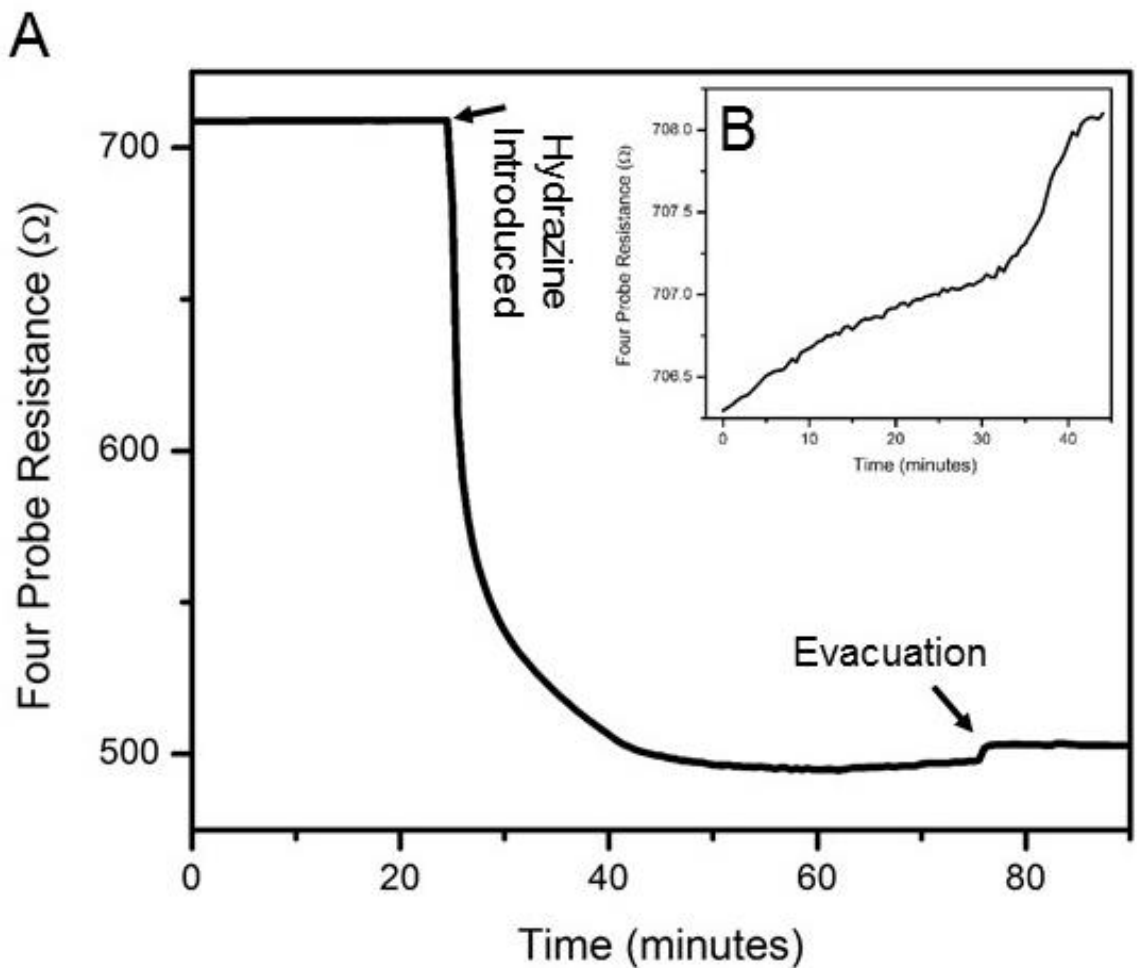


**Figure 5.19.** A) In Situ resistance measurement of MoS<sub>2</sub> nanowires after exposure to hydrazine vapor. B) Change in resistance when exposed to ambient air.

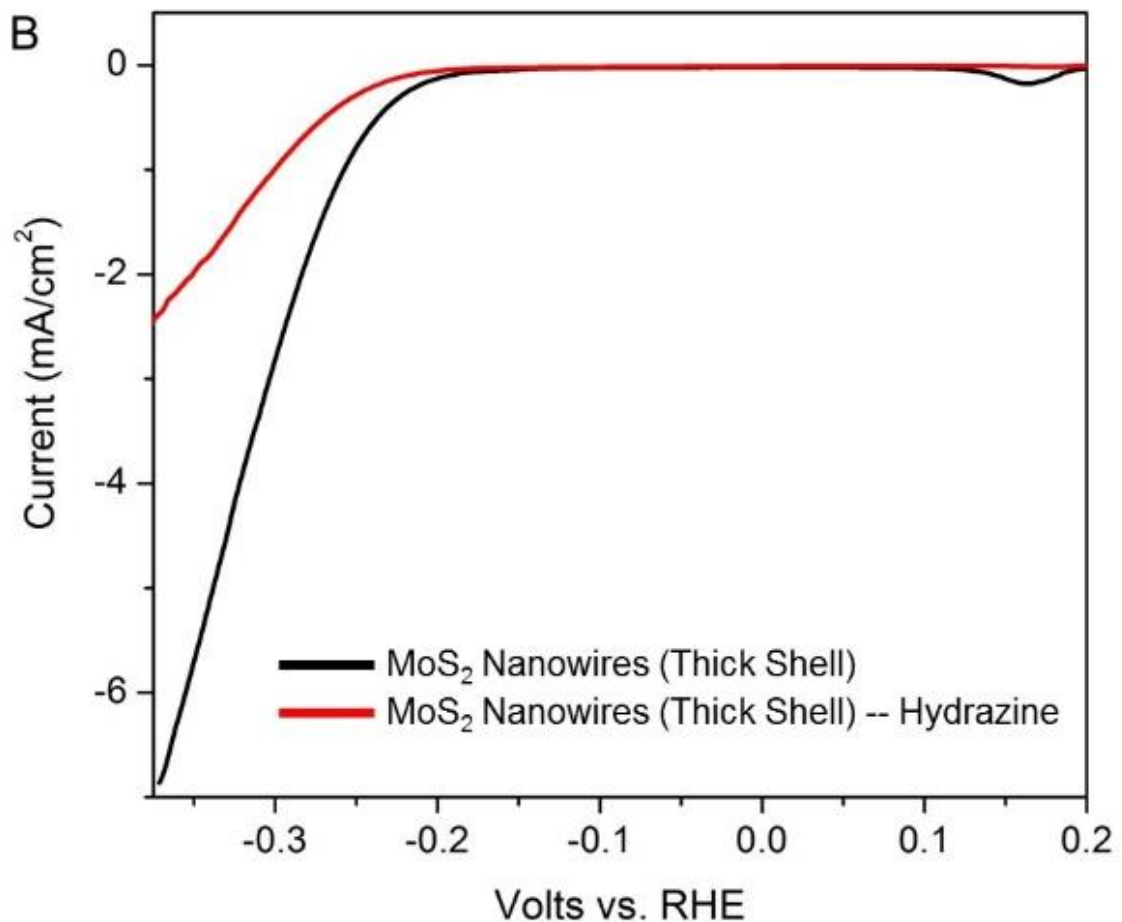


**Figure 5.20.** Linear voltammogram of thick shelled (8 – 10 nm) MoS<sub>2</sub>/MoO<sub>x</sub> nanowires as grown (black curve) and treated with 1% hydrazine (red curve).

The unique attribute of the shell/core nanowire is that the MoS<sub>2</sub> is grown epitaxially on the reduced MoO<sub>x</sub> core. The thin 1 – 3 nm MoS<sub>2</sub> shell used in the hydrazine treatment experiment may not be completely conformal and may allow some of the reduced oxide

core to be exposed to solution. To determine if the  $\text{MoO}_x$  core contributes to the catalysis, the same hydrazine treatment was applied to thicker, 8 -10 nm  $\text{MoS}_2$  shell nanowires.[202] Interestingly, the dramatic improvement in catalysis is not observed for the thicker shelled nanowires. The catalysis remains unchanged and, in some cases, is reduced by the hydrazine treatment, as seen in Figure 5.20. This seems to show that the molybdenum oxide core plays some role in the HER catalysis.

To ensure that the reduction of the molybdenum oxide core, *i.e.* the improvement in conductivity is not the primary reason for the improved electrocatalysis, simple calculations are performed to determine the voltage resistance of an individual  $\text{MoO}_x$  core ( $iR$ ). Assuming a 50 nm molybdenum oxide nanowire with 1 micron length, the average voltage drop from the nanowire, in this case  $\text{MoO}_2$ , is  $\sim 2.6 \times 10^{-4}$  mV. XRD analysis shows the core of the as-synthesized  $\text{MoS}_2$  shell/core nanowire is composed predominantly of  $\text{MoO}_2$ . For this calculation, the resistance of  $\text{MoO}_2$  is taken from thin films in literature ( $5.2 \times 10^{-3} \Omega\text{-cm}$ )[229]. In order for the core of the nanowire to impact the applied voltage for electrocatalysis even  $\sim 10$  mV, the hydrazine treatment would have to increase the conductivity of  $\text{MoO}_2$  by at least five orders of magnitude. Interestingly, under similar conditions, the resistivity of molybdenum metal is only three orders of magnitude lower than  $\text{MoO}_2$  ( $\sim 5 \times 10^{-6} \Omega\text{-cm}$ )[230]. So, even if the hydrazine reduces the molybdenum oxide core completely to molybdenum metal, which characterization shows is not the case, the impact on the applied voltage would be less than 1 mV. This confirms that the improved electrocatalytic activity is resulting from an electrochemical modification of the  $\text{MoS}_2$  surface, not merely improved conductivity of the electrode.

Pure MoO<sub>3</sub> is catalytically inactive and decomposes quickly in acid solutions. To see the true effect of hydrazine on the molybdenum oxide nanowire core, the bare MoO<sub>3</sub> nanowires were reacted with 1% hydrazine and subjected to electrochemical testing (Figure 5.21). As expected, the MoO<sub>3</sub> nanowires show no catalytic activity and strongly decomposes in the 0.5 M H<sub>2</sub>SO<sub>4</sub>. [217] When exposed to hydrazine, this electrochemical decomposition is diminished and even a weak HER catalytic on set potential develops. This seems to show that improved electron conductivity, synergistically combined with catalytic active site exposure, are very important parameters in designing an ideal electrocatalyst. The MoS<sub>2</sub>/MoO<sub>x</sub> shell core nanowire morphology, combined with the hydrazine treatment uniquely provides an architecture for an optimized electrocatalyst.

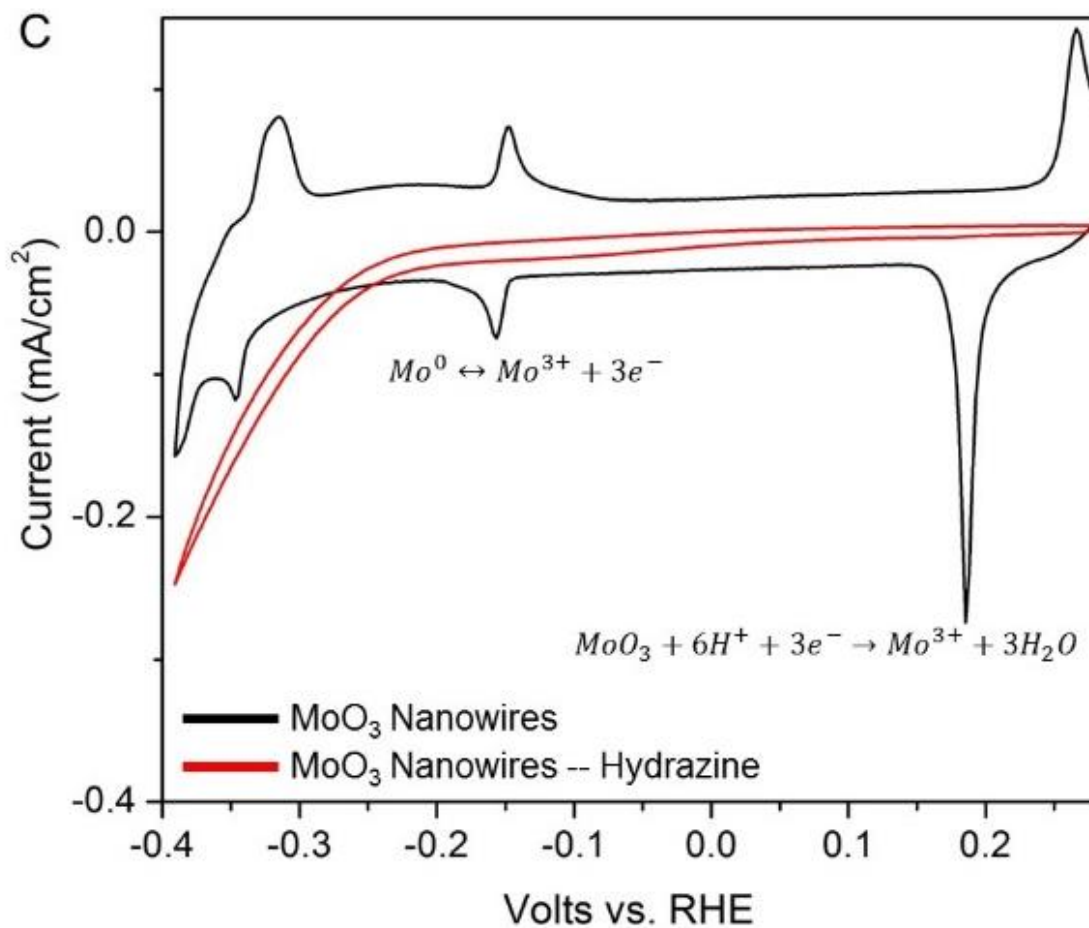


**Figure 5.21.** Linear voltammogram showing the effect of hydrazine treatment on MoO<sub>3</sub> nanowires.

In summary, the exposure of the MoS<sub>2</sub>/MoO<sub>x</sub> shell core nanowire arrays to dilute 1% aqueous hydrazine (N<sub>2</sub>H<sub>4</sub>) dramatically improves the HER electrocatalytic activity, leading to one of the best reported HER overpotentials for any MoS<sub>2</sub> architecture and an exponentially improved current density. The hydrazine acts as a reducing agent and, effectively, as an electron dopant, which increase the electron carrier concentration of the MoS<sub>2</sub> surface, activating the entire basal surface, while still maintaining the thermodynamically stable 2H – MoS<sub>2</sub> crystal phase. These charge carriers may be actual electrons or negative hydroxyl (OH<sup>-</sup>) groups, but may also be the result of pseudo-reduction of the MoS<sub>2</sub> surface by degradation in a basic solution. Gate dependent HER catalytic measurements confirm that the basal plane of MoS<sub>2</sub> can be activated by artificially increasing the electron surface concentration. *In situ* resistance measurements on the MoS<sub>2</sub>/MoO<sub>x</sub> shell core nanowire arrays shows that the electrochemical properties of the MoS<sub>2</sub> is altered by exposure to hydrazine, significantly increasing the overall conductivity. It seems that the hydrazine is affecting the nanowire structure in multiple ways; the MoS<sub>2</sub> surface is being electronically activated, the MoO<sub>x</sub> core is being further reduced, and it has been shown here that MoO<sub>3</sub> reduced in hydrazine can have a catalytic effect. The synergy of these processes leads to the dramatic electrocatalysis of the HER: activated material on a high surface area, highly conducting nanowire substrate. This shell core nanowire structure, especially with chemical modification, seems to be an ideal electrocatalytic architecture, not only applicable to MoS<sub>2</sub>, but many other catalyst systems. This is one of

the lowest overpotentials for the HER reported for any MoS<sub>2</sub> system and is one of the first reports of gate dependent HER catalytic measurements, as well as one of the first investigations of the effects of hydrazine on transition metal semiconductors.

## CHAPTER VI: IRON OXIDE TO IRON SULFIDE

### 6.1. Conversion of Iron Oxide Nanowires to Iron Sulfide Nanotubes

As discussed, there is considerable interest in transition metal chalcogenide nanostructures, due to their favorable properties for solar light absorption.[139] Particularly, pyrite phase  $\text{FeS}_2$  has an desirable band gap to absorb a large portion of the solar spectrum (0.95 eV) and a significantly high absorption coefficient ( $6 \times 10^5 \text{ cm}^2/\text{mol}$ ). It is a nontoxic, earth abundant material and is considered one of the least expensive semiconductors for implementation in a PV energy generation set up.[158] One inhibition to the use of iron sulfide in a variety of applications is the difficult synthesis of single crystal and phase pure compounds, which is due in large part to the complex phase diagram of iron-sulfur system and the multitude of possible stable crystal structures for iron sulfide.[159]

The approach used in this work involves the synthesis of single crystal,  $\text{Fe}_2\text{O}_3$ , hematite phase nanowire arrays and their subsequent exposure to  $\text{H}_2\text{S}$  in order to form single crystal iron sulfide nanowires, hopefully with the desired, pyrite  $\text{FeS}_2$  crystal structure. The hematite  $\text{Fe}_2\text{O}_3$  nanowires were first synthesized by Chen et al. using radio frequency, low temperature plasma oxidation of an iron foil.[189, 192] Other attempts have used the thermal oxidation of an iron foil, which after a few hours, grows vertically oriented  $\text{Fe}_2\text{O}_3$  nanowires by means of an “extrusion” process through a very thick amorphous iron oxide layer composed predominantly of hematite and magnetite ( $\text{Fe}_3\text{O}_4$ ), which forms on the iron foil surface.[191] This very thick amorphous iron oxide layer

prevents almost all electronic and chemical characterization of the nanowires themselves, so this technique is not favorable.

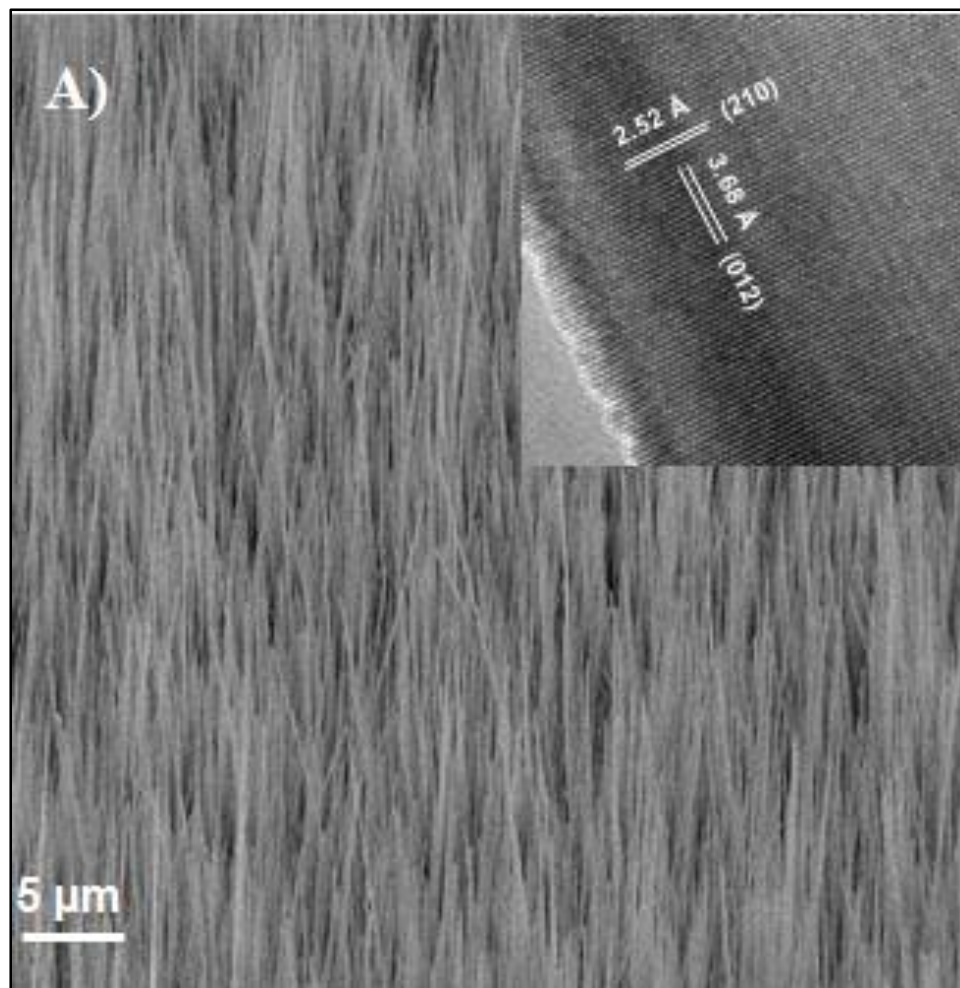


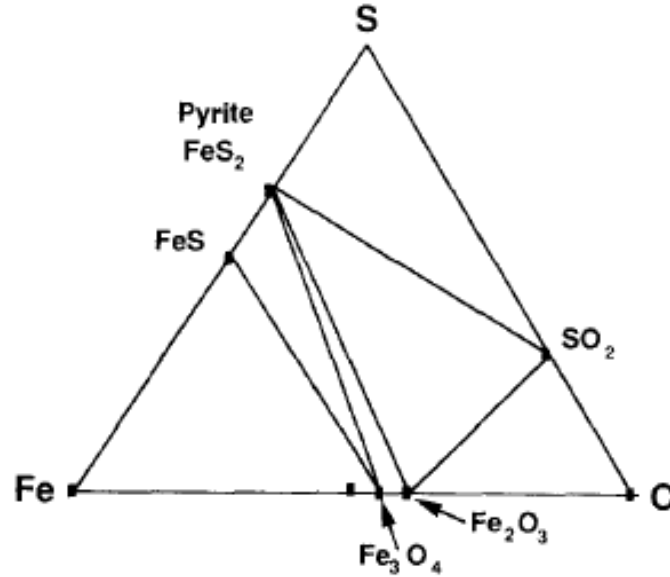
**Figure 6.1.** SEM imaging of as grown hematite, iron oxide nanowire arrays. The inset shows HRTEM imaging, confirming the single crystal nature of the nanowires.[231]

Published by Cummins, *et al.* 2013. © American Chemical Society, 2013

Chernomordik, et al. devised a method in order to quickly and efficiently grow phase pure, single crystal  $\text{Fe}_2\text{O}_3$  with a minimal interfacial amorphous oxide layer using atmospheric plasma oxidation of thin iron foil. The oxygen plasma flame quickly heats the iron foil to between  $580^\circ\text{C}$  and  $740^\circ\text{C}$  for short time scales (averaging 10 minutes) producing single

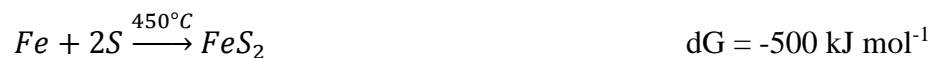
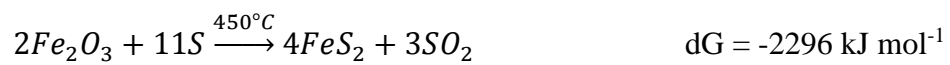


crystal nanowires with lengths ranging from 500 nm to 2  $\mu\text{m}$  and a wide range of diameters from 5 nm to 300 nm.[191] Each nanowire is single crystal and phase pure  $\alpha\text{-Fe}_2\text{O}_3$  with a rhombohedral crystal structure and lattice parameters of  $a = 5.038 \text{ \AA}$  and  $c = 13.772 \text{ \AA}$ .



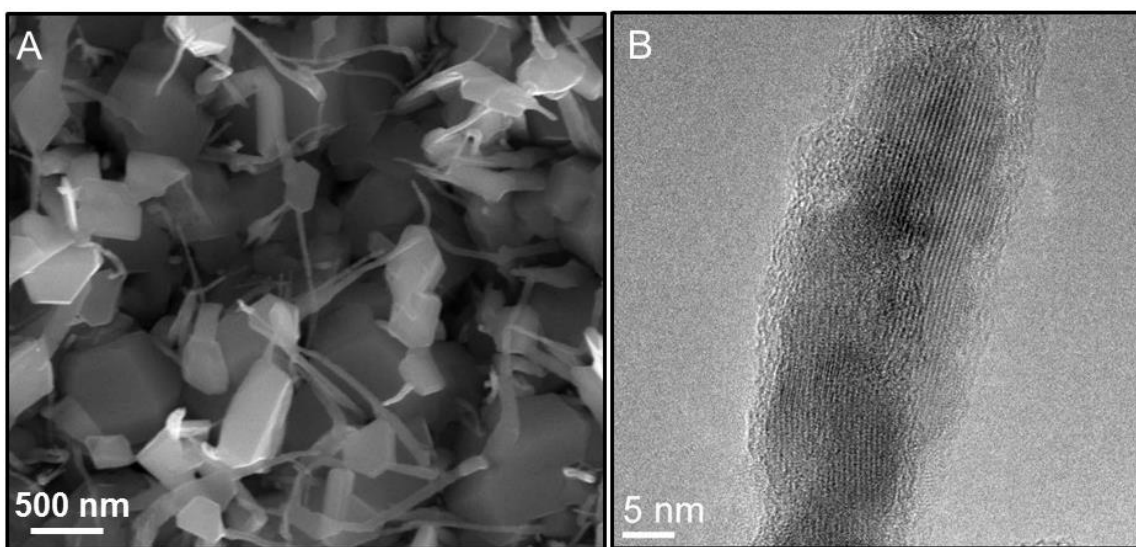
**Figure 6.2.** Gibbs phase triangle of conversion of iron oxides and iron sulfides in a Fe- O – S system. Published by Ennaoui, *et al.* 1993[161] © Elsevier Publishing, 1993.

Figure 6.1 shows the as synthesized hematite  $\text{Fe}_2\text{O}_3$  vertically oriented array with dense nanowire coverage on the iron substrate. The figure inset shows HRTEM imaging of a single nanowire, confirming the defect free, single crystal structure and hematite phase. Thermodynamically, it is much more favorable for iron oxide to convert to form  $\text{FeS}_2$  pyrite, compared to the reaction of iron metal.[139, 161, 232, 233] The two most pertinent reactions are, assuming the  $\text{H}_2\text{S}$  dissociates and hydrogen does not play a role:



Plotting the Gibb's energy of reaction, taking into account the phase diagram leads to a Gibb's phase triangle of the Fe – O – S system (Figure 6.2), graphically showing the thermodynamic advantage of exposing iron oxides to sulfur.

The first experiment for phase transformation of the  $\text{Fe}_2\text{O}_3$  nanowires to  $\text{FeS}_x$  involved the exposure in low pressure 99%  $\text{H}_2\text{S}$  at  $450^\circ\text{C}$  for 15 hours, in order to ensure complete conversion. Analysis by SEM (Figure 6.3A) shows long iron sulfide nanowires that appear to be single crystal segments, confirmed by HRTEM (Figure 6.3B). The crystallographic analysis shows that the crystals are non-stoichiometric  $\text{Fe}_7\text{S}_8$  pyrrhotite.[8] More interestingly, it appears that the original iron oxide nanowires decompose at these high temperatures, then the iron sulfide nanostructures nucleate directly on the foil and grow in 1D. The reaction temperature was lowered to prevent the destruction of the original nanowires, but also further investigation demonstrated that stoichiometric pyrite  $\text{FeS}_2$  will decompose at  $\sim 390^\circ\text{C}$ [159].



**Figure 6.3.** A) SEM image of  $\text{Fe}_7\text{S}_8$  nanowires grown at  $450^\circ\text{C}$ . B) HRTEM imaging confirming each segment of the nanowire is single crystal.

Decreasing the sulfurization reaction temperature to  $\sim 250^{\circ}\text{C}$  and the reactant pressure was maintained,  $\sim 100$  mTorr. Under these reaction conditions, the nanowire architecture is maintained, as shown in Figure 6.4A. However, it appears that the reaction proceeds only  $\sim 8 - 10$  nm, which typically results in a very thin  $\text{FeS}_x$  shell on the larger  $\text{Fe}_2\text{O}_3$  nanowire. Due to the range of hematite nanowire size scales, one nanowire with a small, 10 nm diameter was analyzed and showed complete single crystal transformation to an iron sulfide nanowire, evidenced by HRTEM (Figure 6.4B).[82]

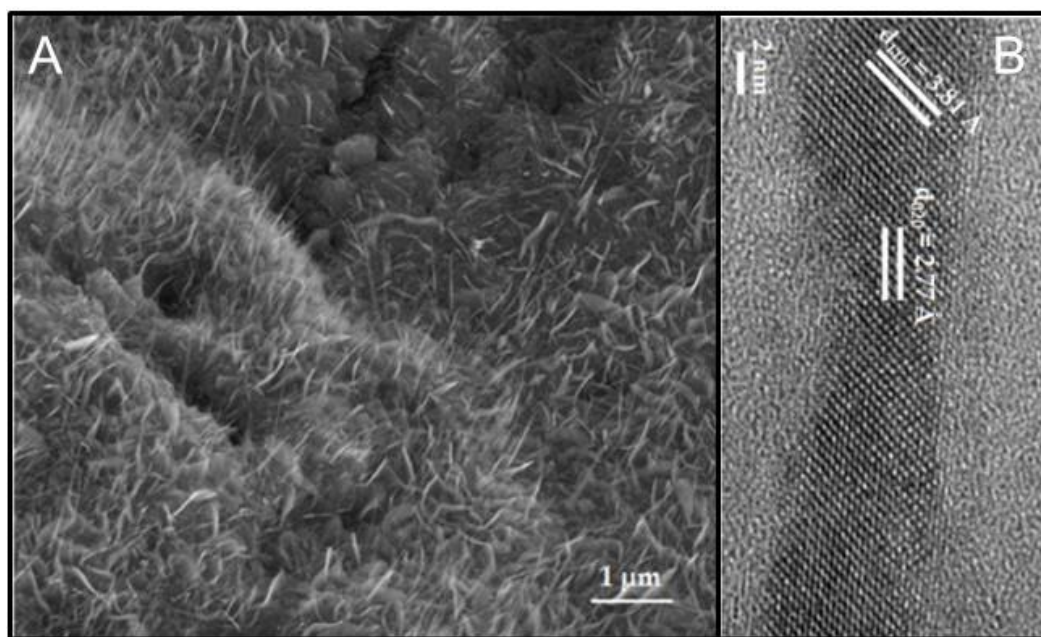


**Figure 6.4.** A) SEM of  $\text{FeS}_x$  nanowires with small diameters. B) HRTEM image of single crystal 10 nm  $\text{FeS}_x$  nanowire after phase transformation reaction. Adapted from Sunkara, *et al.*, 2011 [82] © IOP Publishing Ltd. 2011

The measured  $d$  –spacings of the nanowire are measured to be  $3.8 \text{ \AA}$ , with a perpendicular spacing of  $2.7 \text{ \AA}$ , which correspond to the dominant spacings of cubic  $\text{FeS}_2$ .

Unfortunately, there are hundreds of possible iron sulfide phases and structures, with very similar crystal d-spacings. Closer analysis of the relative angular orientation of the d spacings shows that this nanowire is not pyrite phase. The majority of the hematite nanowires synthesized have diameters of 100 nm to 300 nm, so duplication of this observed “thin” 10 nm wire has been impossible. This result, however, provides valuable insight into the size dependence of phase transformation.

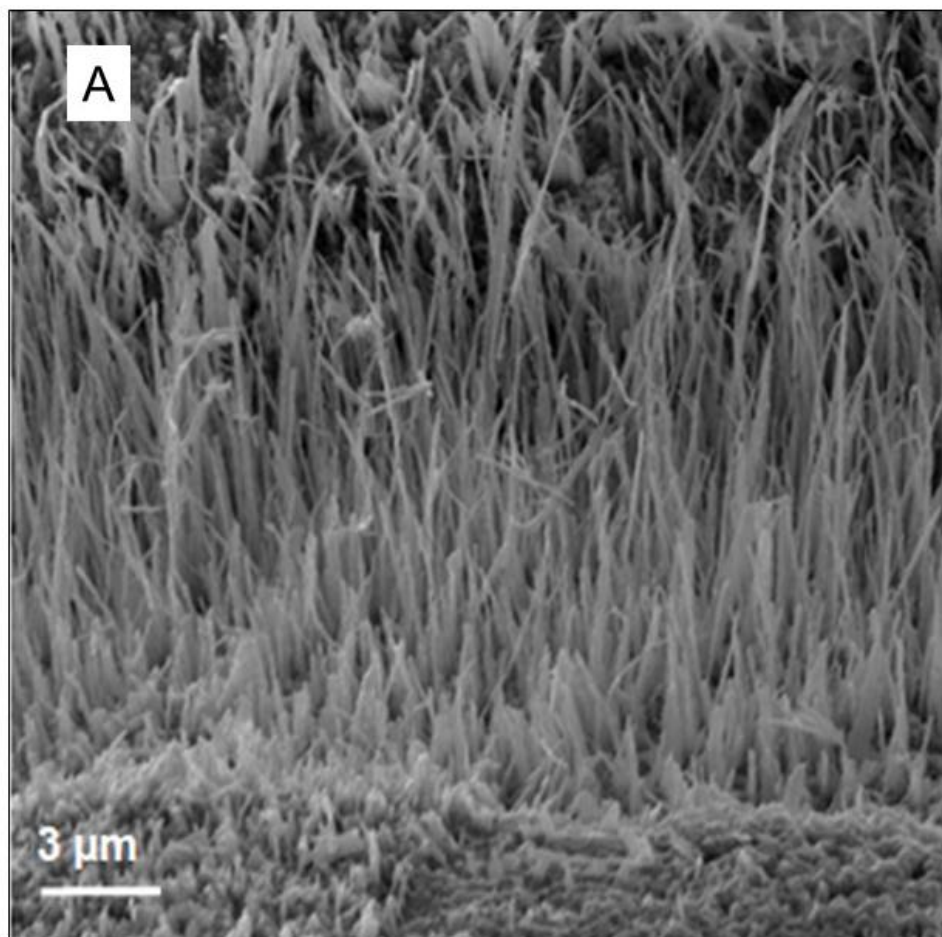


**Figure 6.5.** SEM of the  $\text{Fe}_2\text{O}_3$  nanowire array after exposure to 15 Torr  $\text{H}_2\text{S}$  at  $300^\circ\text{C}$  for 2 hours. Published by Cummins, *et al.* 2013[231] © American Chemical Society, 2013.

To overcome the strong diffusion limitations of the transformation of  $\text{Fe}_2\text{O}_3$  nanowires to  $\text{FeS}_x$  by post oxide synthesis reaction with  $\text{H}_2\text{S}$ , the reactant  $\text{H}_2\text{S}$  pressure was increased to 15 Torr and the temperature set at  $300^\circ\text{C}$ . After the reaction with  $\text{H}_2\text{S}$  for 2 hours, the external structure of the nanowires is maintained as shown by SEM imaging, seen in Figure 6.5.[231] However, using HRTEM and EDS analysis, the reacted nanowires have actually phase transformed to create hollow, single crystalline nanotubes composed of phase pure iron sulfide. This crystalline hollow nanotube structure can be seen in the Bright Field TEM image (BF-TEM) in Figure 6.6A. This BFTEM image shows that the nanotube walls are single crystal along the radius of the wire, but there appears to be low angle grain boundaries along the length of the nanowires between the crystal domains. Figure 6.6B shows a HRTEM image of a single crystal grain from the  $[1,-2,1,-3]$  zone axis with 3 measured d spacings of  $2.97 \text{ \AA}$ ,  $2.65 \text{ \AA}$ , and a perpendicular  $2.65 \text{ \AA}$ , indicative of a hexagonal structure. These d spacings correspond with less than 0.5% error with the reported d spacings of hexagonal iron monosulfide ( $\text{FeS}$ ) with a NiAs type structure (PDF 00-001-1247), having lattice parameters of  $a = 3.43 \text{ \AA}$  and  $c = 5.68 \text{ \AA}$ . Using this crystal database identification, the measure d spacings from the HRTEM,  $2.97 \text{ \AA}$ ,  $2.65 \text{ \AA}$ , and  $2.65 \text{ \AA}$  can be appropriately indexed to the  $(-1010)$ ,  $(-1101)$ , and  $(0-111)$  crystal planes respectively.[231]

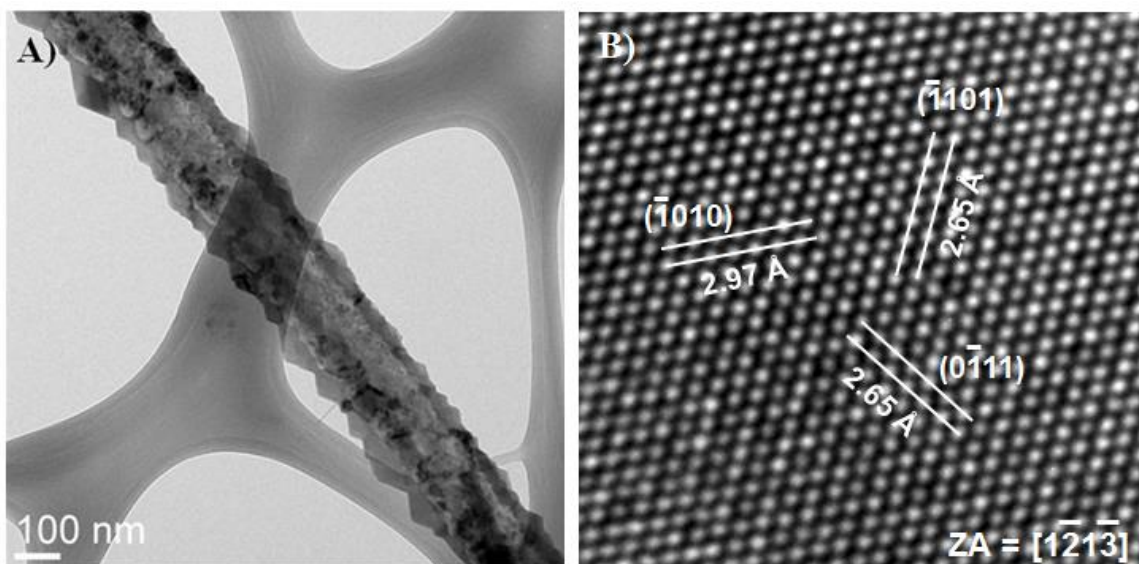


**Figure 6.6.** A) Bright Field TEM imaging of the hollow, crystalline, iron sulfide nanotube, formed by reaction of iron oxide nanowires with  $\text{H}_2\text{S}$ . B) HRTEM of a single crystal grain from the  $[1-21-3]$  zone axis, allowing for crystal phase identification as hexagonal  $\text{FeS}$  with  $\text{NiAs}$  structure.[231] © American Chemical Society, 2013

Raman spectroscopy is one of the predominant methods for quickly establishing the presence of cubic  $\text{FeS}_2$ . The Raman active modes in  $\text{FeS}_2$  are one symmetric mode ( $A_g$ ), a doublet degenerate mode ( $E_g$ ), and three triplet degenerate modes ( $T_g$ ). The  $A_g$  corresponds to the in-phase stretching of the S-S dimer.[234] The perpendicular displacement of S atoms on the dimer axes corresponds to the  $E_g$  mode. The triplet degenerate modes ( $T_g$ ) describe various librational and stretching vibrations, or a combination of these. Theoretical DFT calculations show that Raman shifts at  $\sim 340 \text{ cm}^{-1}$  and  $\sim 380 \text{ cm}^{-1}$  correspond to the  $E_g$  mode and  $A_g$  mode, respectively, of  $\text{FeS}_2$  pyrite.[235] Literature shows that a Raman excitation at  $\sim 320 \text{ cm}^{-1}$  corresponds to the  $A_g$  vibrational mode of orthorhombic  $\text{FeS}_2$  marcasite.[236].

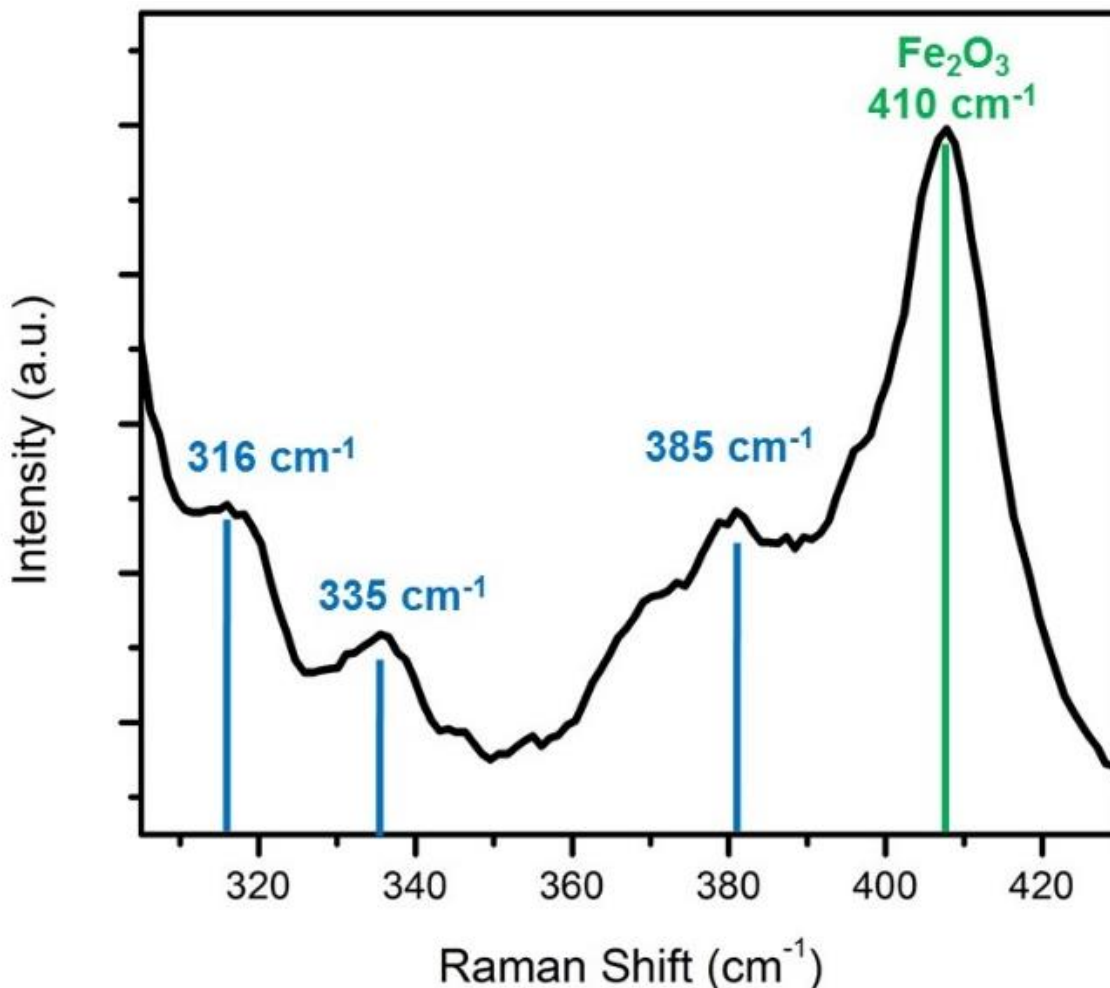


**Figure 6.7.** Experimental Raman spectrum for FeS nanowires grown on Fe/Fe<sub>2</sub>O<sub>3</sub> foil.

Due to the complex crystal structure and phase diagram for FeS<sub>2</sub>, a combination of multiple characterization techniques is necessary to confirm cubic pyrite. Common “contaminants” of pyrite are marcasite, which is FeS<sub>2</sub> with an orthorhombic crystal structure and a smaller band gap of ~.32 eV and FeS, troilite, which is commonly reported to have an almost metallic band gap of 0.04. Raman analysis of the phase transformed FeS nanowire array (Figure 6.7) shows a dominant signal for Fe<sub>2</sub>O<sub>3</sub>, resulting from the interfacial oxide layer on the substrate, but after full sulfurization of the nanowires, 3 unique peaks are observed at ~316, 335, and 385 cm<sup>-1</sup>. The strong peaks at 410 cm<sup>-1</sup> are

attributed to  $\text{Fe}_2\text{O}_3$ . [237] The peak at  $\sim 316 \text{ cm}^{-1}$  matches reports for  $\text{FeS}_2$  marcasite in literature, and 335 and  $385 \text{ cm}^{-1}$  match literature values for  $\text{FeS}_2$  pyrite. Some preliminary theoretical calculations for FeS with NiAs structure show that it possesses 3 Raman active modes at 295.8, 307.8, and  $308.2 \text{ cm}^{-1}$ , corresponding to the  $B_g^2$ ,  $A_g$ , and  $B_g^1$  vibrational modes, respectively. Further analysis of this system under strain, which exists in the phase transformed nanowires/nanotubes shows these Raman peaks are positively shifted, therefore matching more closely to the FeS experimental Raman spectra and easily misinterpreted for pyrite phase. A summary of these theoretical results are shown in Figure 6.8. [238] This confusion in characterization, especially in iron sulfide systems, necessitates multiple, in depth techniques.

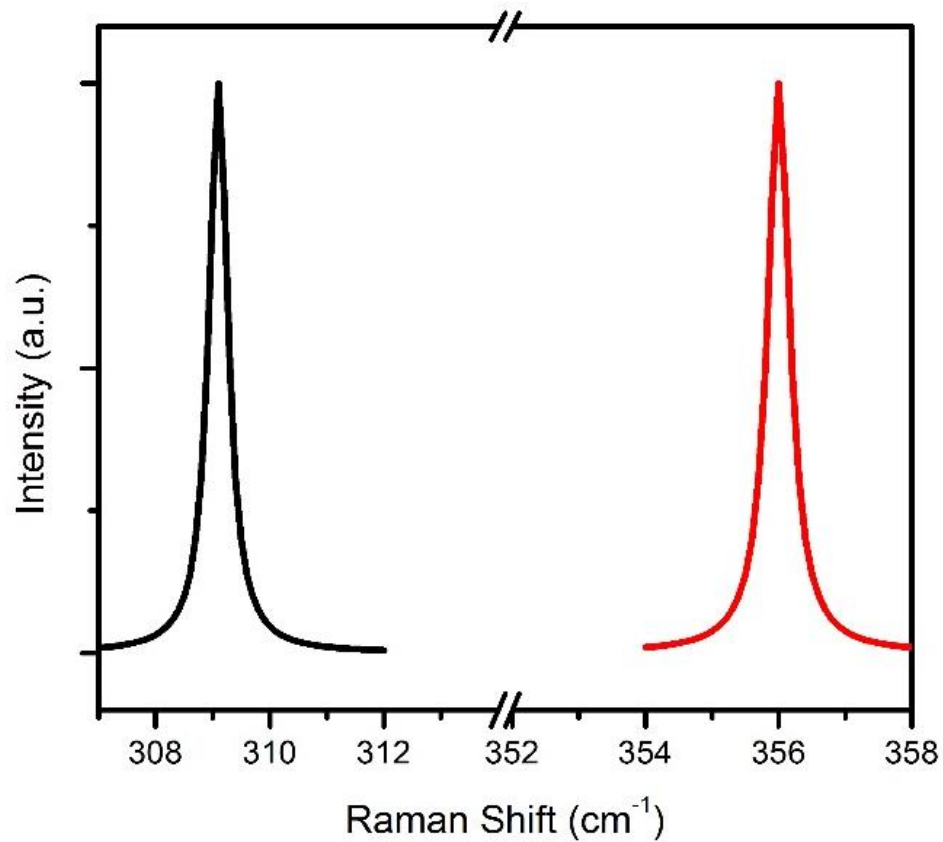




**Figure 6.8.** Raman spectra showing a theoretical vibrational mode of for single crystal FeS with NiAs structure (black curve) and after isotropic strain is applied (red curve) causing a  $\sim 50\text{ cm}^{-1}$  positive shift. Unpublished work in collaboration with Madhu Menon.

Since the iron/sulfur phase diagram is very complicated with hundreds of possible crystal structures, many of which having very similar d spacings, nano probe electron diffraction was performed on a single iron sulfide grain, tilted in order to allow diffraction from multiple zone axes. These three nano probe diffraction patterns can be seen in Figure 6.9 A, B, and C. The first diffraction pattern is observed from the  $[1\bar{2}1\bar{3}]$  zone axis, which is the same zone axis as the HR TEM image in Figure 6.6B. The sample was tilted appropriately to collect diffraction patterns from the  $[01\bar{1}0]$  zone axis, and then the  $[01\bar{1}1]$  direction. These zone axes are consistently indexed by both atomic spacing and angle to definitively prove the crystal phase as hexagonal FeS with NiAs structure.

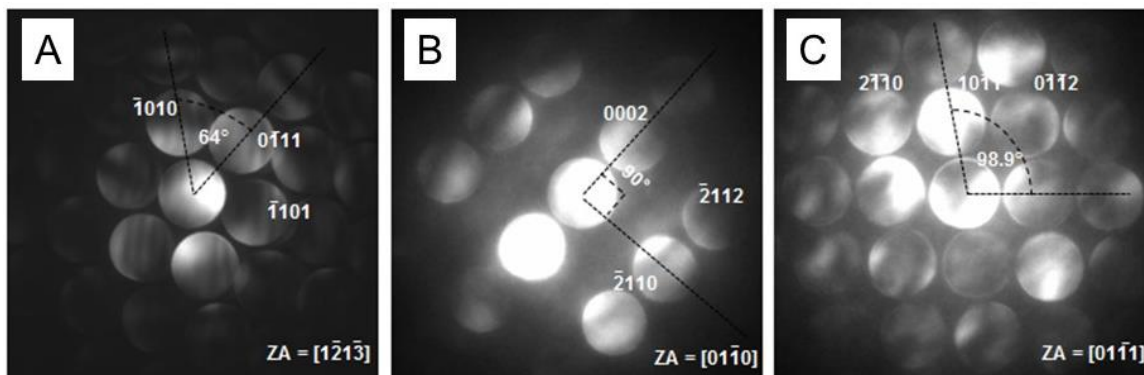


**Figure 6.9.** Nano probe electron diffraction from a single FeS crystal from multiple zone axes: A)  $[1\bar{2}1\bar{3}]$ , B)  $[01\bar{1}0]$ , and C)  $[01\bar{1}1]$ . [231] © American Chemical Society, 2013

Further characterization is used to both confirm the FeS with NiAs structure crystal phase identification, as well as investigate the growth mechanism of the iron sulfide

nanotubes. XRD characterization clearly shows the FeS with NiAs structure phase, along with crystalline Fe<sub>2</sub>O<sub>3</sub> and Fe<sub>3</sub>O<sub>4</sub> from the thick iron oxide interfacial layer on the substrate. Careful analysis of the XRD peak intensities shows a preferential orientation of the crystal growth. Literature database patterns for powder x ray diffraction report the relative peak intensities for randomly oriented, polycrystalline powders.

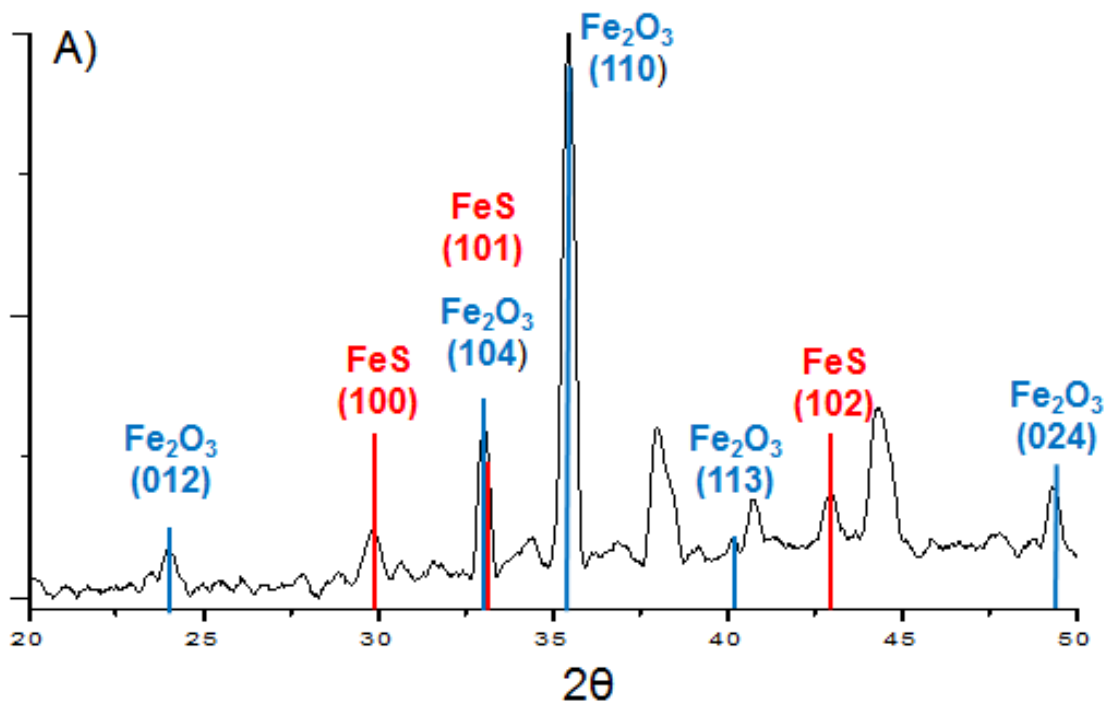


**Figure 6.10.** XRD pattern of vertically oriented iron sulfide nanowire/nanotube array on iron substrate with hematite and magnetite (iron oxide) interfacial layer.[231] ©American Chemical Society, 2013

PDF 00-001-1274 shows randomly oriented FeS crystals should have a ratio between the peak intensities of the (100) and (102) crystal planes of 0.33. Measurement of the actual XRD peaks of the iron sulfide array shows a diffraction peak ratio of ~1.2; this is indicative of a large preferential orientation of the (100) plane parallel to the substrate, compared to

random orientation. This same preferential orientation is observed in the (110) plane of hematite  $\text{Fe}_2\text{O}_3$ , showing that some of the vertically oriented iron oxide nanowires were unreacted on the substrate. This XRD pattern can be seen in Figure 6.10.

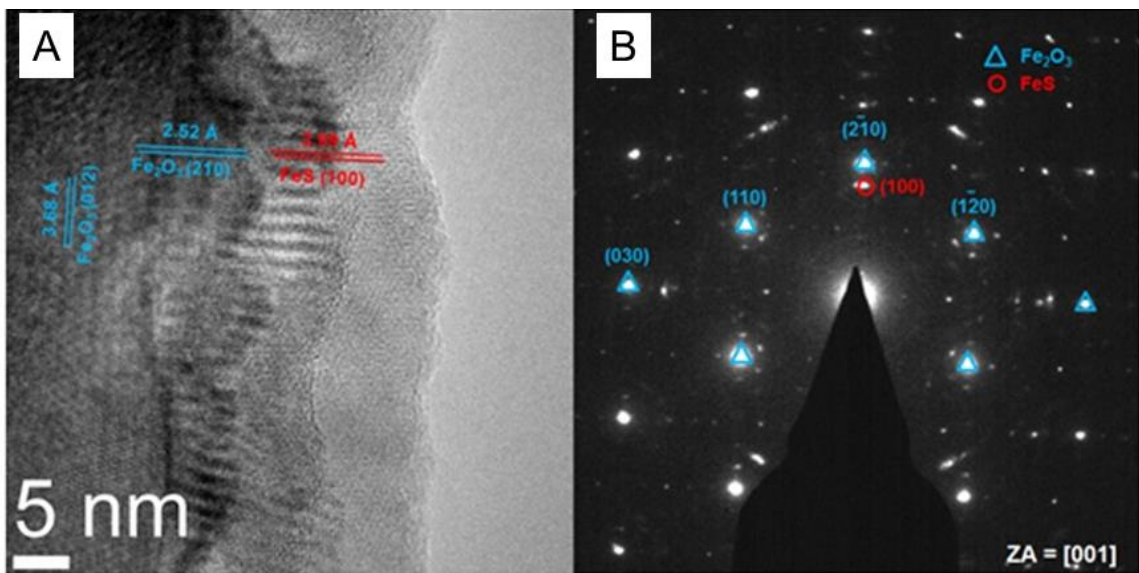


**Figure 6.11.** A) HRTEM imaging of the iron oxide core/ iron sulfide shell epitaxial interface. B) Selected Area electron diffraction showing the epitaxial relationship between the  $\text{FeS}(100)$  crystal plane (red circle) and the  $(210)$  hematite planes, denoted by blue triangles. [231] © American Chemical Society, 2013

To further confirm this epitaxial relationship between the  $(210)$  crystal planes of  $\text{Fe}_2\text{O}_3$  and the  $(100)$  planes of  $\text{FeS}$ , a single nanowire, reacted for 30 minutes, was observed in multiple zone axes using TEM and electron diffraction. As Figure 6.11 shows, this epitaxial relationship is maintained in multiple zone axes, showing this strong preferential growth and crystal orientation.

To understand this preferential orientated growth, growth studies were done at the same temperature and reaction pressure, but at incremental times. A thin iron sulfide shell

was grown on the surface of the oxide nanowire and that interface was investigated with HRTEM and electron diffraction. Figure 6.11A shows a HRTEM image of the oxide/sulfide interface. Most obviously are the Moiré fringes with the spacing of ~ 1.5 nm. Moiré fringes result from interfering periodicity from the diffraction from 2 crystals in series during HRTEM imaging. The fringe signal from the d spacing of the Fe<sub>2</sub>O<sub>3</sub>, interacts with the signal from the FeS at the interface, leading to a distortion and broadening of the observed d-spacing in the image. Since the crystals at the interface may have both interference from different d spacings, as well as interference from rotation of the crystal orientation, the observed Moiré fringe spacing can be described by:

$$D = \frac{d_1 d_2}{\sqrt{d_1 d_2 \theta^2 + (d_1 - d_2)^2}}$$

where d<sub>1</sub> and d<sub>2</sub> correspond to the parallel d spacings of “crystal 1” and “crystal 2” and  $\theta$  corresponding the angle of rotation between the two crystals.[198] For the sake of simplification, the rotational contribution of the Moiré fringe is assumed to be zero, reducing the relationship to:

$$D = \frac{d_1 d_2}{d_1 - d_2}$$

Using this Moiré fringe relationship in the FeS/Fe<sub>2</sub>O<sub>3</sub> system with d<sub>1</sub> = 2.52 Å from the (210) plane of Fe<sub>2</sub>O<sub>3</sub> and d<sub>2</sub> = 2.99 Å from the (100) of FeS, a theoretical Moiré fringe spacing of 1.60 nm, which matches very well to the experimentally measured spacing of ~1.5 nm, indicative of a close interaction between the FeS and Fe<sub>2</sub>O<sub>3</sub> lattice. Figure 6.11B shows selected area electron diffraction of the interface region. This diffraction clearly confirms that there is an epitaxial relationship between the hematite core (210) plane, marked by blue triangles and the (100) planes of the FeS shell, denoted by the red circle.

These crystal planes have a large lattice mismatch, which generates a large amount of strain and as the reaction continues the iron oxide core is depleted and defects form, leading to the observed low angle crystal boundaries.

UV-Visible Diffuse Reflectance Spectroscopy shows a high molar absorption coefficient in the visible region, on the order of  $10^4 \text{ cm}^{-1}$  (Figure 6.12), similar to that of pyrite,  $\text{FeS}_2$ .<sup>[104]</sup> The absorption coefficient was calculated using the Kubelka-Munk transformation of the diffuse reflectance data.<sup>[239]</sup> The Kubelka-Munk transformation, in its simplified form is:

$$F(R) = \frac{(1 - R)^2}{2R}$$

Figure 6.12A shows the absorption spectra for three separate samples of FeS nanowires, showing a consistent feature at  $\sim 1350 \text{ nm}$ . This data is unsmoothed, which is the reason for the noisiness of the signal, especially above  $\sim 1600 \text{ nm}$ . The absorption spectrum shows a broad, relatively uniform absorption, except for this “dip” in adsorption at  $\sim 1350 \text{ nm}$ , which is shown more clearly in Figure 6.12B.

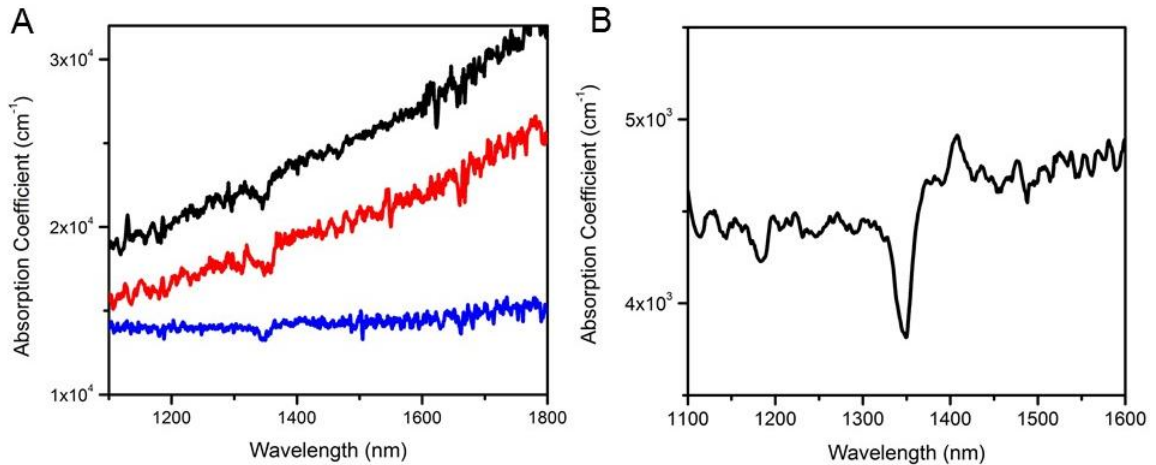


**Figure 6.12.** A) Absorption coefficient determination for FeS nanowire array by UV-Visible Diffuse Reflectance Spectroscopy for three separate samples. B) Zoomed spectrum highlighting the absorption feature.

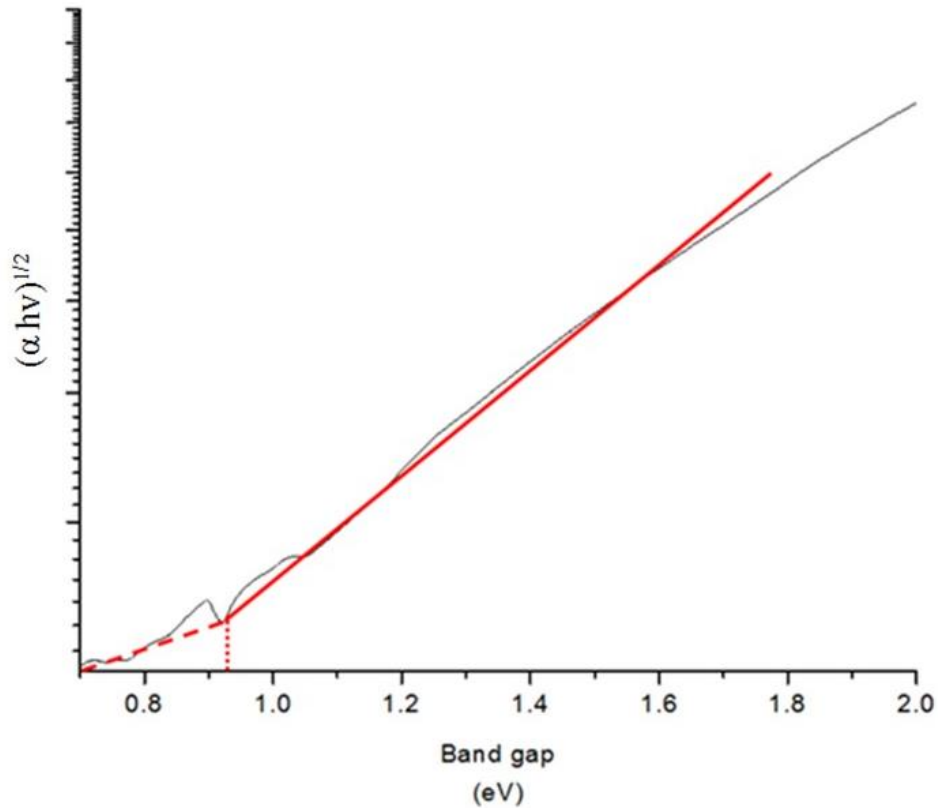


**Figure 6.13.** Tauc's plot analysis of absorption feature in FeS nanowires, showing the possibility of an indirect band gap transition.

Tauc's plot analysis of this feature (Figure 6.13) calculates an indirect band gap transition of  $\sim 0.9$  eV, which matches closely to reported values for FeS<sub>2</sub> pyrite (0.95 eV) and is slightly higher than the theoretical band gap transition of 0.6 eV, calculated from the DFT for FeS. It is tempting to label this feature as a band gap transition, but this is a very small decrease in adsorption, compared to typical "band edges" in other materials, which

essentially have no absorption signal below the band gap. Therefore, it is difficult to conclude much from the absorption spectra of FeS, other than a relatively uniform high absorption coefficient and this feature at  $\sim 0.9$  eV, which may be indicative of trap states, defects, etc. It is not clear if this feature corresponds to a band edge transition, which would be consistent with FeS<sub>2</sub> pyrite (0.95 eV), but could also correspond to a defect state in the crystal.

In literature, hexagonal FeS phase is known as troilite and is considered a detrimental contaminant in FeS<sub>2</sub> pyrite, with an almost metallic band gap of 0.04 eV. The phase achieved in these experiments, as stated earlier, is a more symmetric hexagonal FeS with NiAs structure. The band structure of this symmetric phase of FeS had not been researched; the only available literature shows a theoretical broadening of the band gap when troilite phase FeS is converted to the symmetric NiAs structure and may achieve a band structure similar to sub stoichiometric Fe<sub>7</sub>S<sub>8</sub>.<sup>[240]</sup> This lack of reliable data prompted our group to perform density functional theory (DFT) calculations to determine the band structure of this unique FeS phase. Using an idealized crystal structure (hexagonal  $a = 3.43$  Å,  $c = 5.68$  Å), we used first-principles DFT in the generalized gradient approximation (GGA) and the Perdew-Burke-Ernzerhof (PBE)<sup>[241]</sup> augmented by including Hubbard-U corrections (GGA+U formalism)<sup>[242]</sup> based on Dudarev's approach<sup>[243]</sup> as implemented in the Vienna Ab-initio Simulation Package (VASP).<sup>[244]</sup> The results can be seen in Figure 6.14, showing a direct band gap transition of  $\sim 0.6$  eV and high absorption in the visible region. This band gap determination may be consistent with the “feature” in the experimental absorption spectrum, occurring at  $\sim 0.9$  eV, but this is difficult to confirm. Interestingly, the theoretical calculations show a very high optical absorption at  $\sim 2.5$  eV,

allowing the possibility of excitation above the band gap, *i.e.* “hot” electron injection, which will be discussed in the next section.

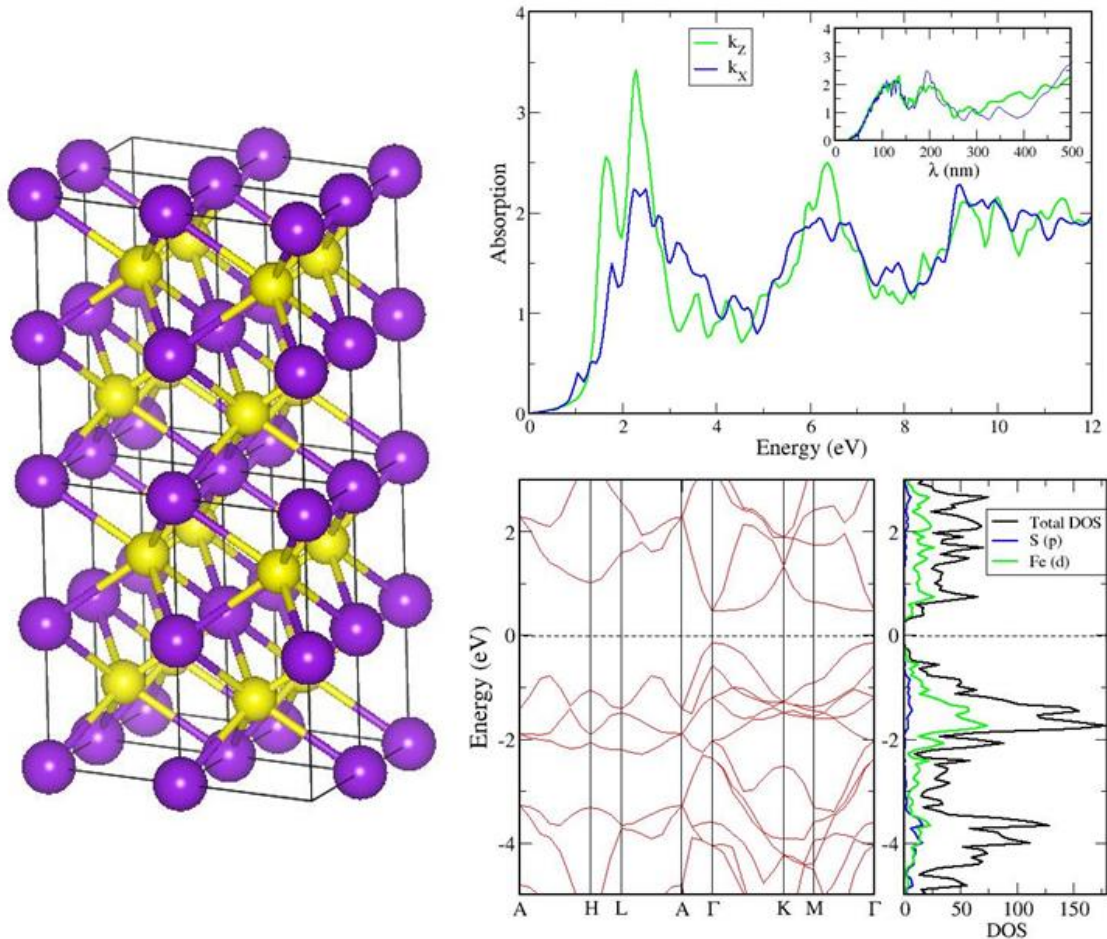


**Figure 6.14.** Results of first principles DFT calculations on FeS with NiAs structure. The band edge positions clearly show a direct band gap transition at  $\Gamma$  of 0.6 eV with slightly p type behavior, based on the density of states.[231]

In an effort to understand the mechanism by which the single crystal  $\text{Fe}_2\text{O}_3$  hematite nanowire is converted to a hollow, crystalline FeS shell, the sulfurization reaction was carried out at the same temperature and pressure for different time intervals. STEM and corresponding EDS line scans show the progression of the sulfurization reaction at 30



minutes, 1 hours, and 2 hours (Figure 6.15). After 30 minutes, the sulfurization has occurred epitaxially on the nanowire surface, proceeding only ~40 nm and the iron oxide core is maintained. After 1 hour, the iron sulfide shell thickness has increased to ~50 to 60 nm and there is a noticeable hollowing of the iron oxide core at the center, as well as void formation at the Fe<sub>2</sub>O<sub>3</sub>/FeS interface. After 2 hours at 300°C, the iron oxide core has been completely depleted, leaving only the hollow, FeS shell. This formation of hollow structures results from the Kirkendall Effect, *i.e.* the accumulation of voids due to different diffusion rates.

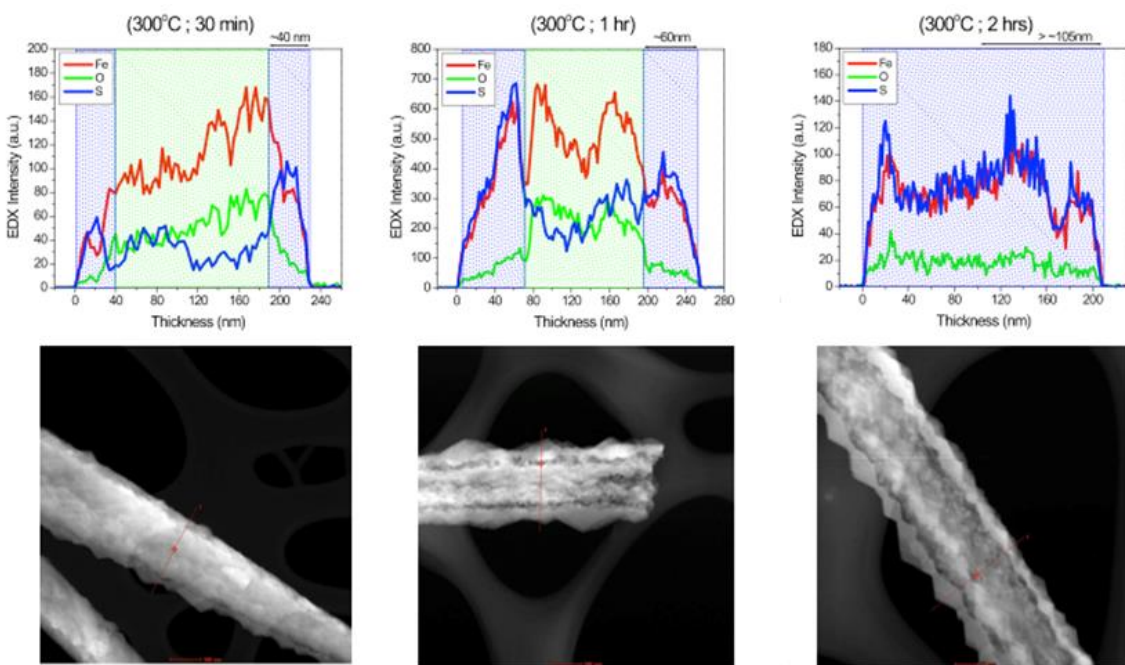


**Figure 6.15.** STEM and corresponding EDS line spectra showing the progression of the sulfurization reaction over time.[231] ©American Chemical Society, 2013

In order to claim the Kirkendall Effect as a medium for hollow structure formation, there should be a large difference between the diffusion of the cation and that of the anion within the lattice, in this case Fe and S. Since pyrite and other iron sulfides have large

application in the mining industry, the diffusion properties have been well researched. Using iron isotopes as a tracer, the self-diffusion of atomic iron was measured in sub stoichiometric iron sulfides. At 300°C (the reactor conditions), the average diffusion coefficient of iron cations in  $\text{Fe}_{1-x}\text{S}_x$  was measured to be on the order of  $9 \times 10^{-12} \text{ cm}^2 \text{ sec}^{-1}$ . [245] In these analyses, the diffusion of sulfur in the iron sulfide was assumed to be negligible, due to its diffusion rate being significantly less than iron. In more recent work, sulfur isotopes were used as radiotracers in natural pyrite [246] and experimentally calculated that the diffusion coefficient of sulfur anions in pyrite has a temperature dependence fitting an Arrhenius relationship, given by:

$$D_s = 1.75 \times 10^{-14} e^{-132,100/RT}$$

where  $D_s$  is the sulfur diffusion coefficient with units of  $\text{m}^2 \text{ sec}^{-1}$ ,  $R$  is the ideal gas constant ( $8.314 \text{ J mol}^{-1} \text{ K}^{-1}$ ),  $T$  is the absolute temperature (K). Extrapolating the data to the temperature of interest leads to a sulfur diffusion coefficient of  $1.6 \times 10^{-22} \text{ cm}^2 \text{ sec}^{-1}$  at 300°C. This is ten orders of magnitude slower diffusion than iron in a similar system, which is optimal conditions for the Kirkendall Effect and diffusion of vacancies and voids to dominate. To determine if these diffusion coefficients measured in bulk, polycrystalline iron sulfides are comparable to the  $\text{Fe}_2\text{O}_3/\text{FeS}$  nanowire system, the sulfurization reaction was carried out at various times and temperatures in order to develop a relationship, depending on the progression of the sulfur reaction. This relationship, shown in Figure 6.16, shows an Arrhenius dependence and an estimated activation energy can be extracted from the data. This experimentally found energy ( $59 \pm 7 \text{ kJ mol}^{-1}$ ) correlates very well with literature reports of vacancy diffusion of iron in iron sulfides. [245, 247] This not only confirms that the literature diffusion coefficients are applicable for this system, but also

that iron diffusion is the dominant process, further proof that the hollow nanowires are formed by unequal diffusion of iron and the Kirkendall Effect.

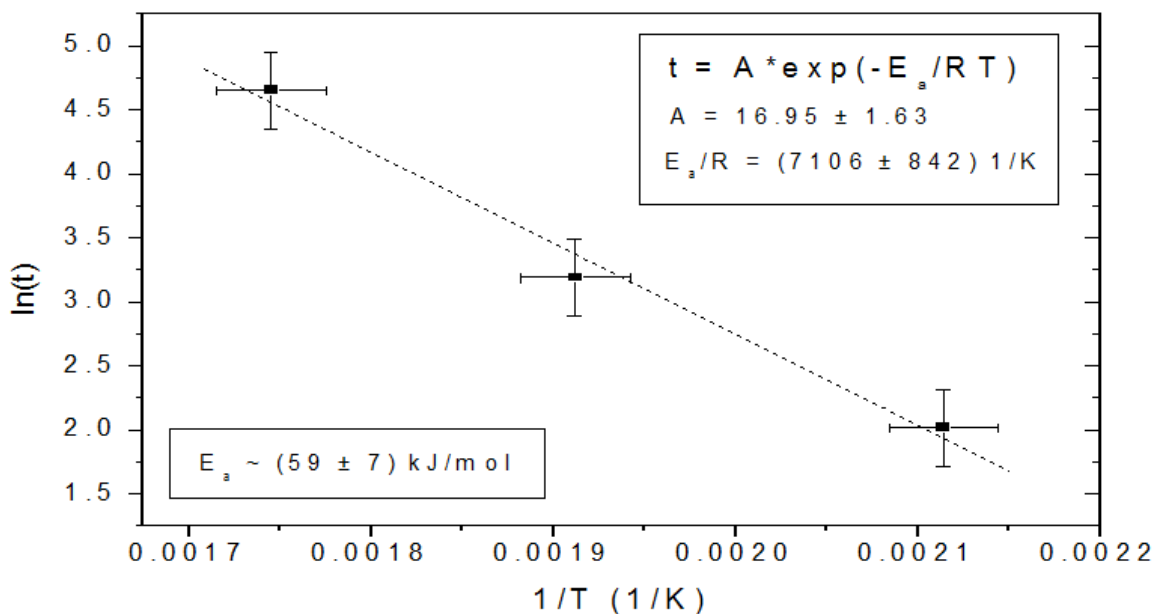


**Figure 6.16.** Experimental determination of the activation energy required for diffusion during the sulfurization reaction using an Arrhenius relationship. [231] ©American Chemical Society, 2013

In the system of reacting the  $\text{Fe}_2\text{O}_3$  nanowire with  $\text{H}_2\text{S}$  to form  $\text{FeS}$ , there are four diffusion processes occurring simultaneously. At the nanowire surface, at  $300^\circ\text{C}$ , the  $\text{H}_2\text{S}$  will spontaneously dissociate to form  $\text{H}_2$  and  $\text{S}^-$ . As these reactive hydrogen and sulfur species are beginning to diffuse into the nanowire, the iron and oxygen are both diffusing toward the surface, due to the diffusion gradient. The hydrogen reacts with the  $\text{Fe}_2\text{O}_3$  surface, removing the oxygen as  $\text{H}_2\text{O}$  vapor and reducing the Fe cation from the stable  $\text{Fe}^{3+}$  to reactive  $\text{Fe}^{2+}$ . These  $\text{Fe}^{2+}$  cations can diffuse much more quickly out toward the nanowire surface than the sulfur anions can diffuse into the wire, which causes the diffusion of vacancies opposite the iron diffusion, *i.e.* the Kirkendall Effect. As the iron cations

continue to diffuse to the surface/reaction interface, the vacancies are accumulating into voids at the center of the nanowire, as well as at the iron oxide/iron sulfide reaction interface. The iron cations from the iron oxide nanowire continue to diffuse to the surface and react to form iron sulfide, depleting the core and allowing more and more voids to accumulate. Once all of the iron from the iron oxide core has diffused out and reacted, the core has been completely depleted and “replaced” by voids, leaving only the FeS shell on a hollow core. Typically in larger scale systems, meaning larger than a few nanometers, the diffusing vacancies would be annihilated at grain boundaries and interfaces, so this uniform hollowing from the Kirkendall Effect is not observed. Using the unique system of single crystal nanowires, there are no crystal defects or grain boundaries, even on the order of 200 – 300 nm, so the vacancies have no impediment to their diffusion and easily accumulate to form voids and hollow structure. A schematic representation of the diffusion processes occurring in the  $\text{Fe}_2\text{O}_3/\text{FeS}$  conversion can be seen in Figure 6.17.

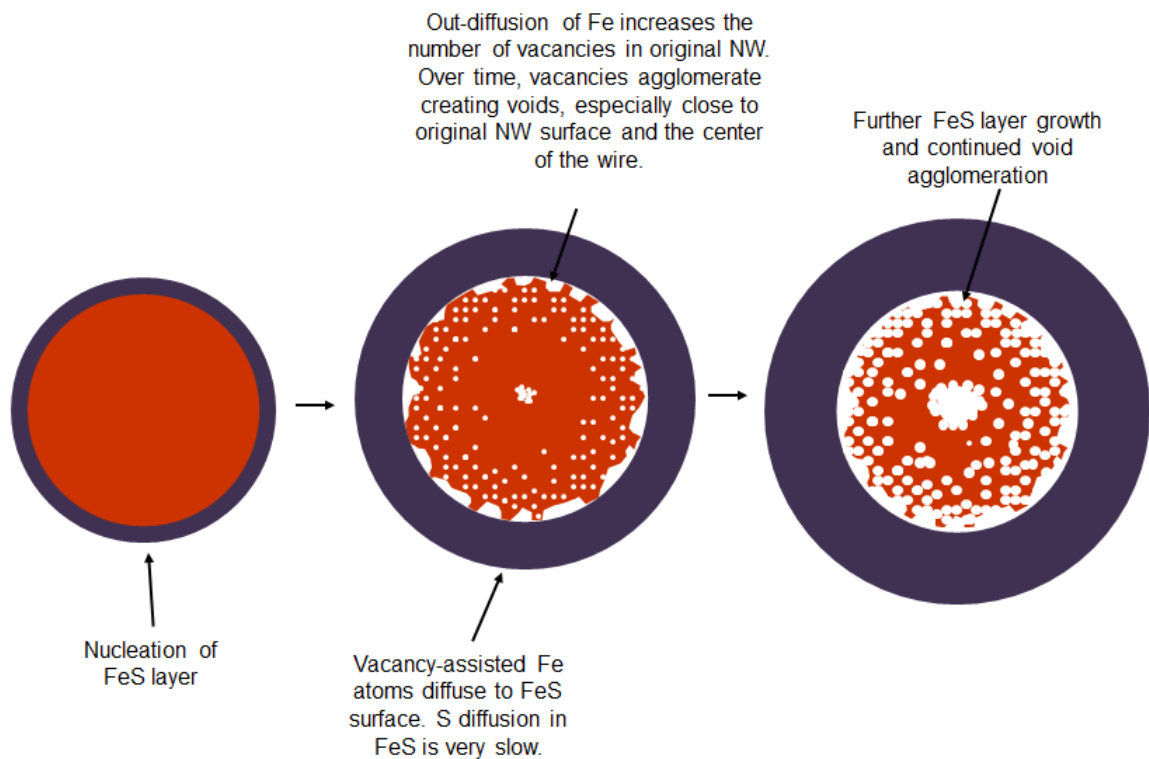


**Figure 6.17.** Schematic showing the progression of the reaction of  $\text{Fe}_2\text{O}_3$  nanowires with  $\text{H}_2\text{S}$ , detailing the diffusion processes. [231] ©American Chemical Society, 2013

These iron sulfide nanowires/nanotube have a beneficial and previously unexplored crystal structure, hexagonal FeS with a symmetrical NiAs structure. This FeS has a direct band gap transition and high absorption in the visible region. DFT calculations show that it is possible for very intense absorption at  $\sim 2.3$  eV, creating the possibility for electrons to be excited significantly more than the band gap of the material. In normal systems, these “hot” electrons would just relax down and cause the semiconductor to heat, but if coupled with a wide band gap semiconductor with appropriate band edges (such as  $\text{TiO}_2$ ,  $\text{SnO}_2$ , etc.), then this hot electron can be injected into the wide gap semiconductor before it has a chance to relax, allowing for the potential for a high energy solar absorption set up. This will be discussed in the next section.

## 6.2. Hot Carrier Injection of FeS Nanotubes

Based on the theoretical DFT calculations, it seems possible that electrons can be photoexcited above the band gap. By properly aligning the band edges, this “hot electron” can be injected into a wide band gap semiconductor. To test this theory, the FeS nanowires are coupled with a TiO<sub>2</sub> electrode. The conduction band of FeS is slightly below the conduction band of TiO<sub>2</sub>, so under normal conditions, the photoinduced electron in FeS cannot inject into TiO<sub>2</sub>, unless this excitation is above the band gap to a metastable state in the FeS conduction band. This band structure is schematically shown in Figure 6.18. The band edges for FeS are estimated from published band positions of Fe<sub>7</sub>S<sub>8</sub>, which has a very similar crystal structure.[240]

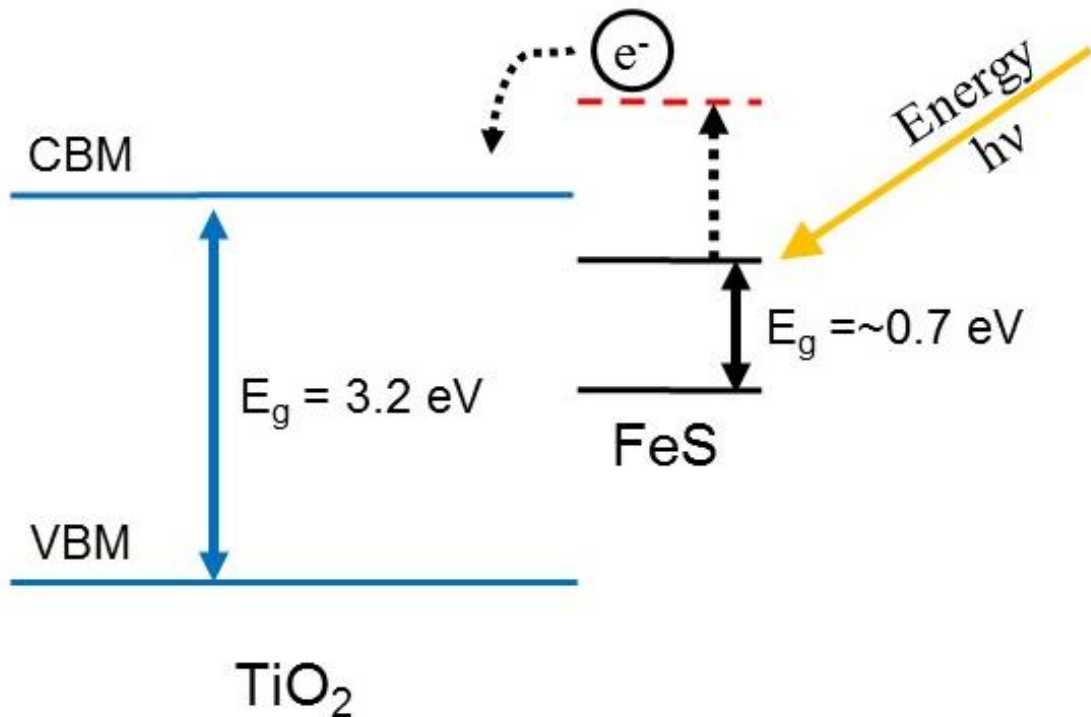


**Figure 6.18.** Schematic showing the theoretical band edge positions of TiO<sub>2</sub> for hot carrier injection from FeS.

To experimentally test this “hot” carrier injection, FeS nanowires were conformally coated with a ~10 nm shell of amorphous TiO<sub>2</sub> using atomic layer deposition (ALD). TEM imaging of this structure (Figure 6.19) shows the close contact relationship. The injection kinetics between the FeS nanowire and the TiO<sub>2</sub> was characterized using Ultra-Fast (femtosecond) Transient Absorption Pump Probe Spectroscopy (TAPPS).

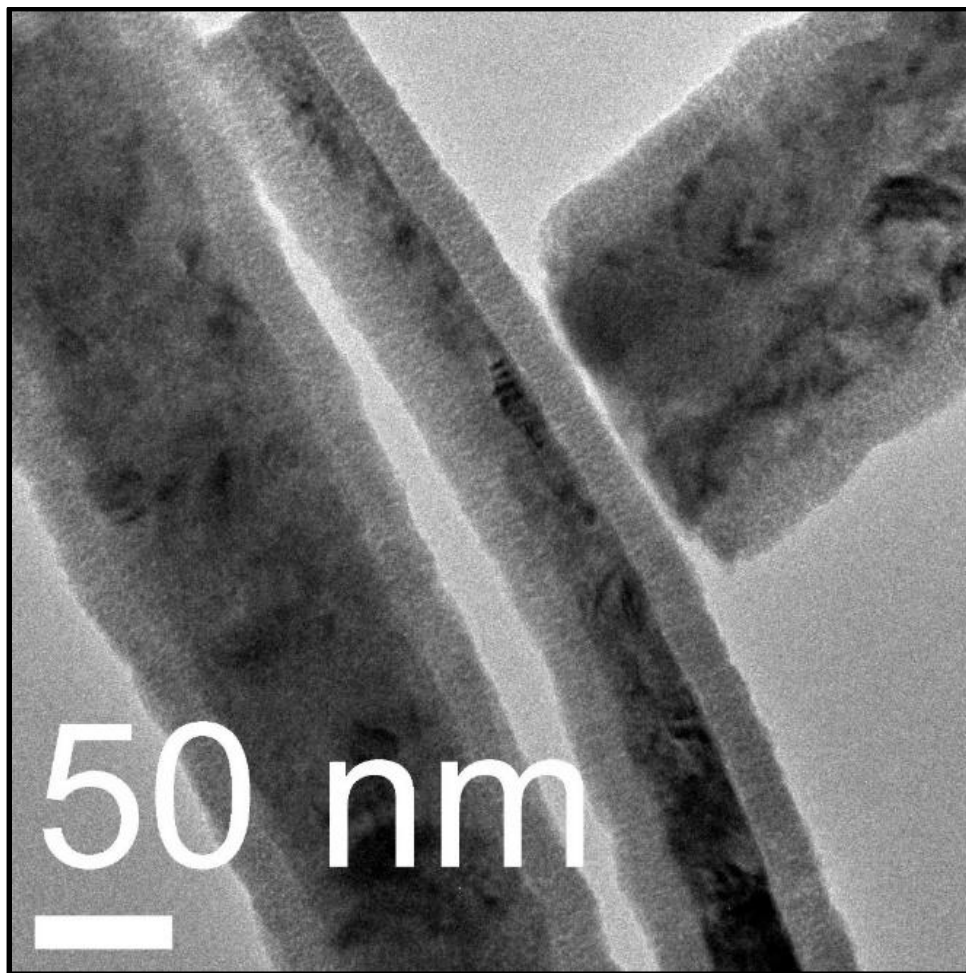


**Figure 6.19.** TEM image of FeS nanowire coated with TiO<sub>2</sub> *via* ALD.

To probe the electronic states of the FeS, the TiO<sub>2</sub>/FeS nanowires were suspended in dichloromethane and pumped and probed with various wavelengths. The pump

wavelengths used in these initial experiments were 388, 490, 530, 550, and 565 nm. The pulse width of the pump laser averaged  $<100$  fs. A white light laser (pulse width of  $\sim 150$  fs) was used as the probe beam. Figure 6.20 shows a contour plot of the transient absorption of the FeS/TiO<sub>2</sub> pumped with 388 nm and probed with white light. The delay time between the pump and probe beam is measured on the x-axis versus the probe wavelength. The color change describes the difference in optical density, indicative of photoabsorption processes.

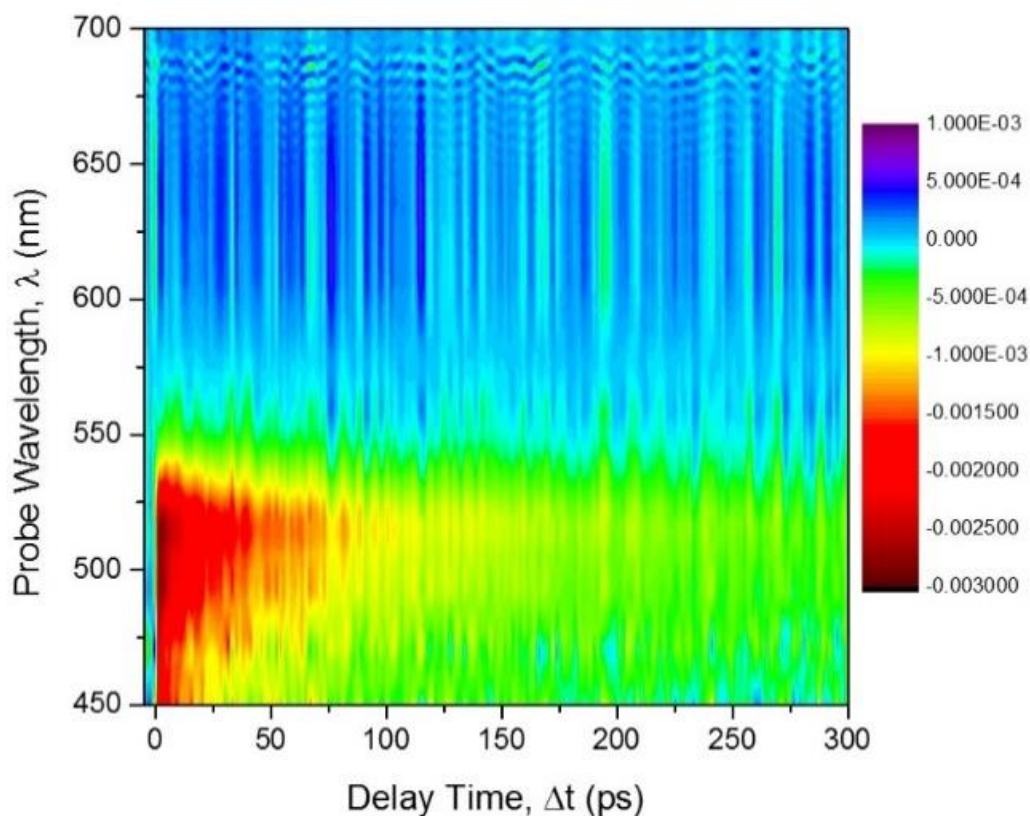


**Figure 6.20.** Contour plot showing the transient absorption spectra of the FeS/TiO<sub>2</sub> nanowire system during Ultrafast Pump/probe spectroscopy. The system is being pumped with 388 nm laser and probed with white light continuum. The change in color corresponds to change in optical density ( $\Delta OD$ ). Courtesy of Dr. Abed Jamhawi.



To quantitatively describe the injection/absorption processes and time-scales, the change in optical density ( $\Delta OD$ ) is analyzed at individual probe wavelengths. Exponential regression extracts the time-scale of the processes. A representative plot is shown in Figure 6.21.

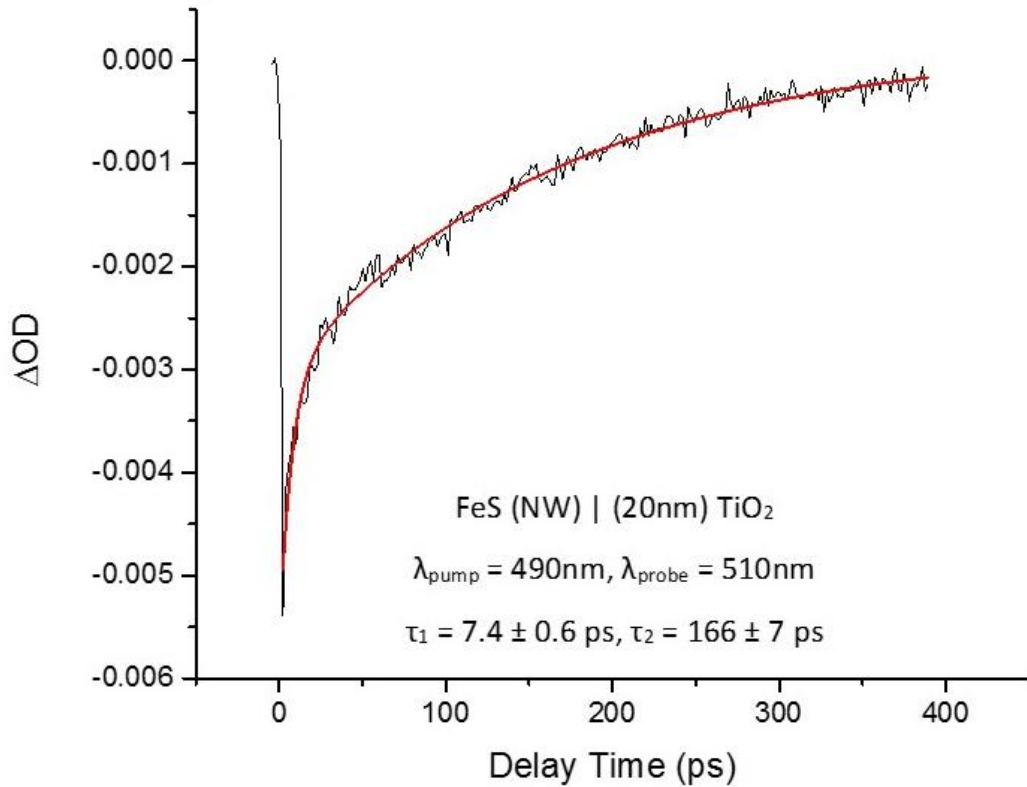


**Figure 6.21.** Plot of  $\Delta OD$  versus delay time at specific pump (490 nm) and probe (510 nm) wavelengths. This data is fit with a double exponential. Courtesy of Dr. Abed Jamhawi.

This plot shows the change in optical density, pumped at 490 nm and probed at 510 nm. A double exponential regression shows a component with a time delay averaging  $\sim 7.5$  ps and a slower component with a time delay  $\sim 166$  ps. The fast component seems to correspond to the successful injection of the electron into the conduction band of the TiO<sub>2</sub>. Since the

experiment was designed with intentional band edge misalignment between the FeS and TiO<sub>2</sub>, this electron must have excited to a state above the conduction band minimum for FeS, then injected into the TiO<sub>2</sub>. The slower component seems to be describing the relaxation of this electron which is excited to the state in the conduction band. Rather than quickly injecting, this “hot” electron relaxes back to the ground state.

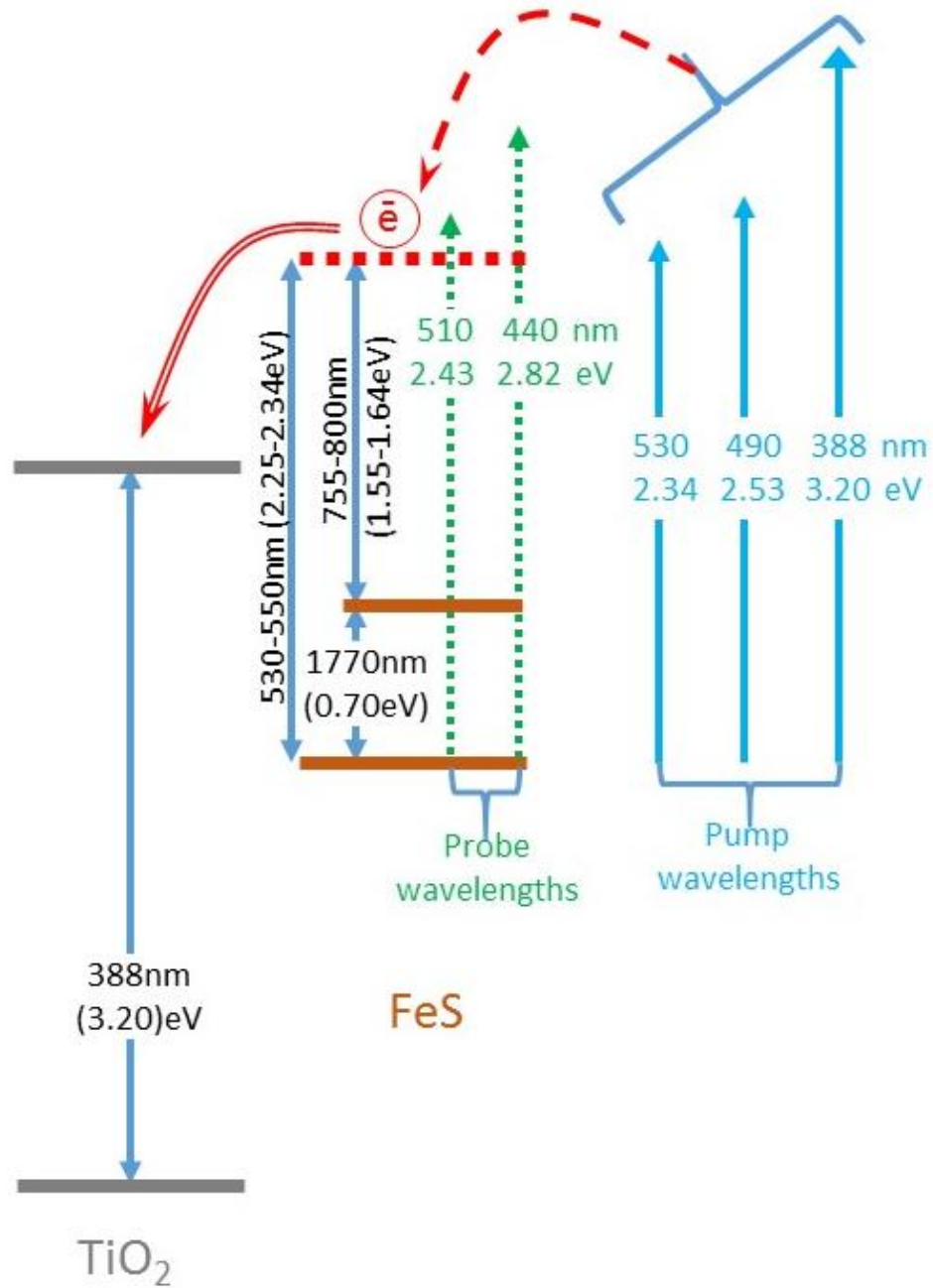


**Figure 6.22.** Schematic display of results of Ultrafast pump probe spectroscopy, showing the possible location of “hot” electron excited state in conduction band. Courtesy of Dr. Abed Jamhawi and Dr. Jinjun Liu.

A summary of these preliminary pump/probe results are schematically in Figure 6.22. Interestingly, the injection/excitation signal is only detected at wavelengths lower than 550 nm, *i.e.* 530, 490, and 388 nm and no signal is detected while pumping with 550, 565, 775 nm. This seems to indicate the location of this “hot” electron state in the conduction band. But these experiments are very preliminary and further experimentation, in both replication of this initial result and analysis of other probe wavelengths to better describe the electronic states.

This experiment successfully demonstrated not only a “hot” electron can excite to a state above the conduction band minimum, also referred to as the lowest unoccupied molecular orbital (LUMO), but that excited electron can be injected into a wide band gap semiconductor. Future work is needed to implement this experimental set up into a functional photoelectrochemical device in order to determine the real effect on photo-efficiency by hot carrier injection.

## CHAPTER VII: SYNTHESIS OF OTHER TRANSITION METAL CHALCOGENIDE NANOWIRES

In order to fully understand the effects of diffusion processes, as well as other important factors in nanoscale phase transformation, a variety of transition metal systems must be investigated, with the metal cations having different self-diffusion rates, different reactant anions, etc. In this section, two phase transformation systems were chosen for experimental study: conversion of SnO<sub>2</sub> nanowires to SnS<sub>x</sub> and conversion of ZnO to ZnS, which is a classic example used in many phase transformation studies in literature involving the Kirkendall Effect. Also, for a stronger conclusion, some observations of other cation and anion systems from literature reports are included in the discussion to provide insight, but could not be performed as a part of this laboratory research, due to materials or time constraint. By observing various materials, with different crystallographic properties, but more importantly with very different cationic diffusion properties, a strong fundamental understanding of phase transformation in nano-scale 1D systems can be achieved.

### 7.1. Conversion of Tin Oxide Nanowires to Tin Sulfide Branched Wires

Tin chalcogenides have been shown to have applications in solar energy and lithium batteries[248-250], but were selected for these experiments primarily due to the large cationic diffusion rates of tin, which will provide insight into nanoscale reaction kinetics and diffusion.

Tin oxide nanowire arrays were synthesized on quartz substrates by reactive vapor transport of tin metal vapor in lean oxygen conditions (5 sccm O<sub>2</sub> with 350 sccm of H<sub>2</sub>). [82, 251-253] These SnO<sub>2</sub> nanowires have diameters ranging from ~200 nm to over 1 μm and very long lengths, on the order of 10's of microns. SEM imaging (Figure 7.1A) shows dense nanowire packing with smooth, faceted surfaces, shown in Figure 7.1B. HRTEM shows a single crystal structure free of defects (Figure 7.1C) and selected area electron diffraction (Figure 7.1D) confirms the tetragonal SnO<sub>2</sub> phase (PDF 00-001-0625).

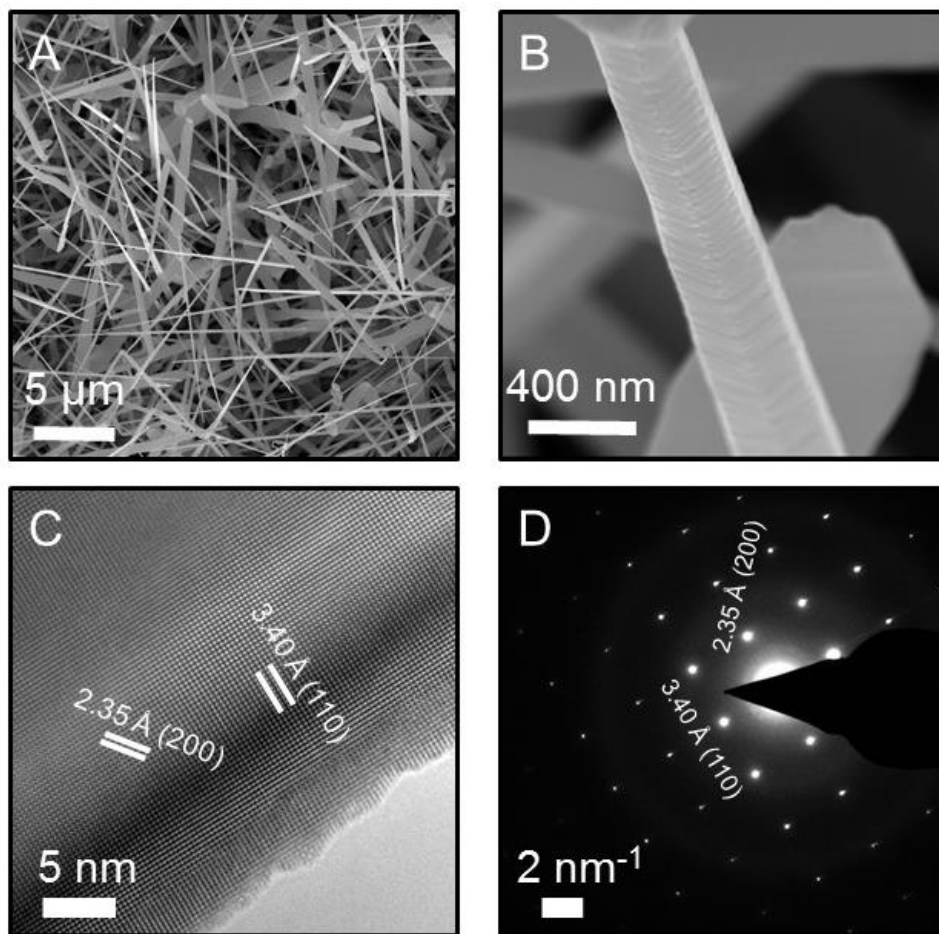


**Figure 7.1.** A) SEM of as grown SnO<sub>2</sub> nanowire array. B) Detail SEM showing the smooth, faceted surface of an individual SnO<sub>2</sub> wire. C) HRTEM and D) SAED of an individual nanowire, showing phase pure, single crystal tetragonal SnO<sub>2</sub>.

The tin oxide nanowires were reacted at 400°C for 1 hour in a 15 Torr 99% H<sub>2</sub>S atmosphere, similar to FeS nanotube synthesis conditions. SEM (Figure 7.2A) shows significant branch formation of tin sulfide, with no apparent deformation of the tin oxide nanowire. TEM (Figure 7.2B) of an individual branched nanowire confirms that single crystal tin sulfide nanowire branches have grown epitaxially from the surface of the tin oxide nanowire. There does not appear to be any oriented growth of the tin sulfide wires, as the nucleation seems random. Most interesting is that there does not seem to be any hollowing or defect formation in the tin oxide nanowire.

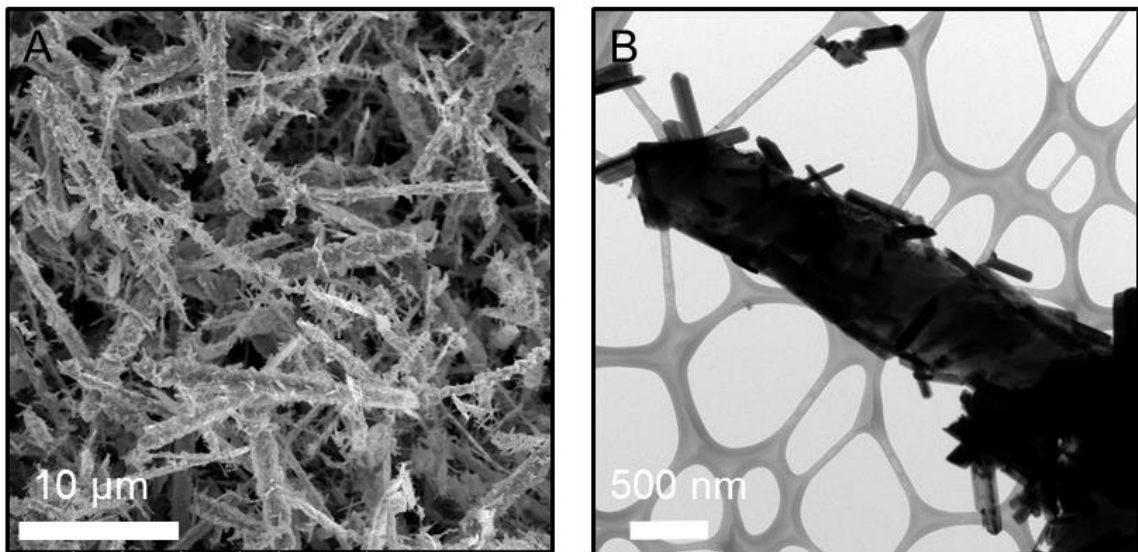


**Figure 7.2.** A) SEM image of branched SnS<sub>x</sub> nanowire array, reacted at 400°C for 1 hour. B) BF-TEM of individual reacted nanowire, showing crystalline sulfide branches growing from the tin oxide nanowire core.

HRTEM (Figure 7.3A) of an individual tin sulfide nanowire branch shows that the nanowires are phase pure and single crystal, with no evidence of oxygen remaining. Analysis of crystal d-spacings (Figure 7.3B), shows that these tin sulfide nanowire branches are single crystal, orthorhombic  $\text{Sn}_2\text{S}_3$  (PDF 01-072-0031).

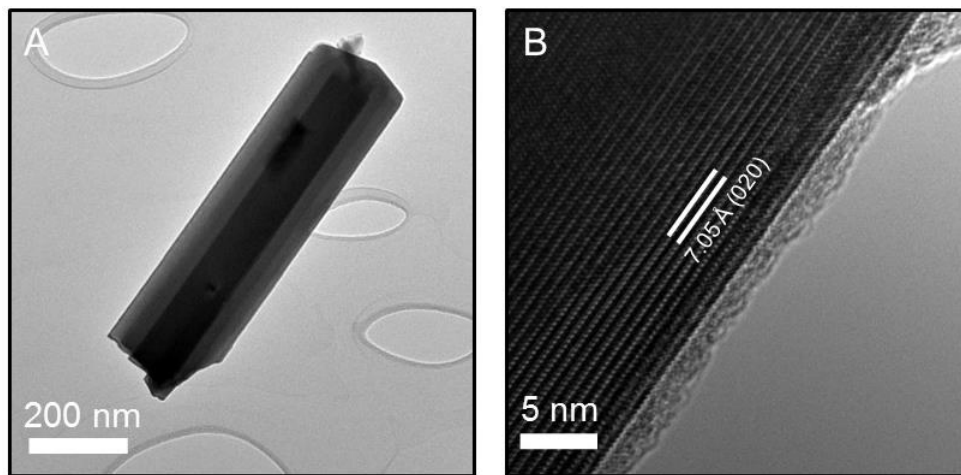


**Figure 7.3.** TEM of a single  $\text{SnS}_x$  nanowire branch. B) HRTEM of the nanowire branch, showing single crystallinity and a dominant d spacing of  $\sim 7.0 \text{ \AA}$ , indicative of orthorhombic  $\text{Sn}_2\text{S}_3$ .

Selected Area Electron Diffraction of multiple tin sulfide nanowires in multiple orientations can be seen in Figure 7.4. There are clear diffraction signals of  $\sim 7.05 \text{ \AA}$ , which is observed in multiple zone axes, and  $\sim 5.50 \text{ \AA}$ , corresponding to (010) and (120) planes for  $\text{Sn}_2\text{S}_3$ , respectively. This suggests that the majority of the nanowire branches, if not all of them, are composed of orthorhombic  $\text{Sn}_2\text{S}_3$ .

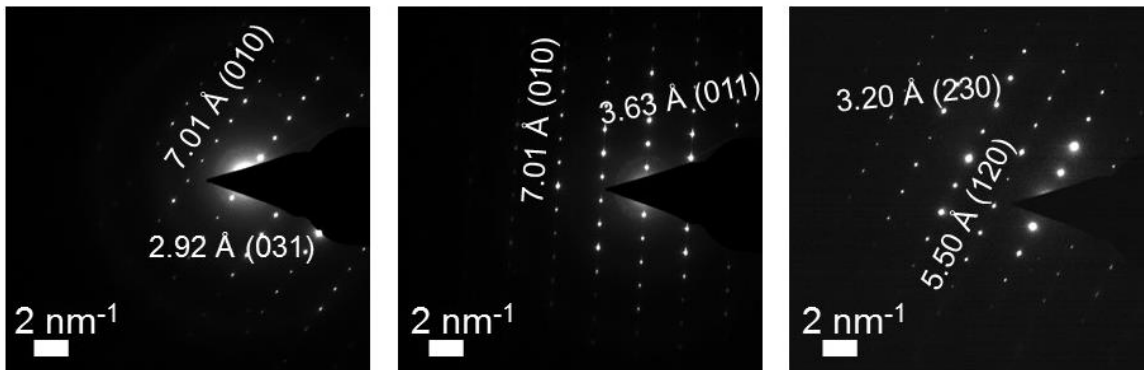


**Figure 7.4.** Selected Area Electron Diffraction (SAED) of multiple tin sulfide nanowire branches in various orientations. This helps to confirm that all of the nanowire branches are single crystal and form the same phase of tin sulfide, orthorhombic  $\text{Sn}_2\text{S}_3$ .

To better understand the growth mechanism of the of  $\text{Sn}_2\text{S}_3/\text{SnO}_2$  nanowires, the reaction with  $\text{H}_2\text{S}$  was performed for only 15 minutes and the resulting nanowires were analyzed. Figure 7.5 shows the BF TEM of the nanowire, with single crystal tin sulfide randomly nucleated on the surface. SAED was taken from multiple sites on the nanowire, focusing on the nanowire core (blue circle), the tin sulfide shell (green circle) and the shell/core interface (red circle).



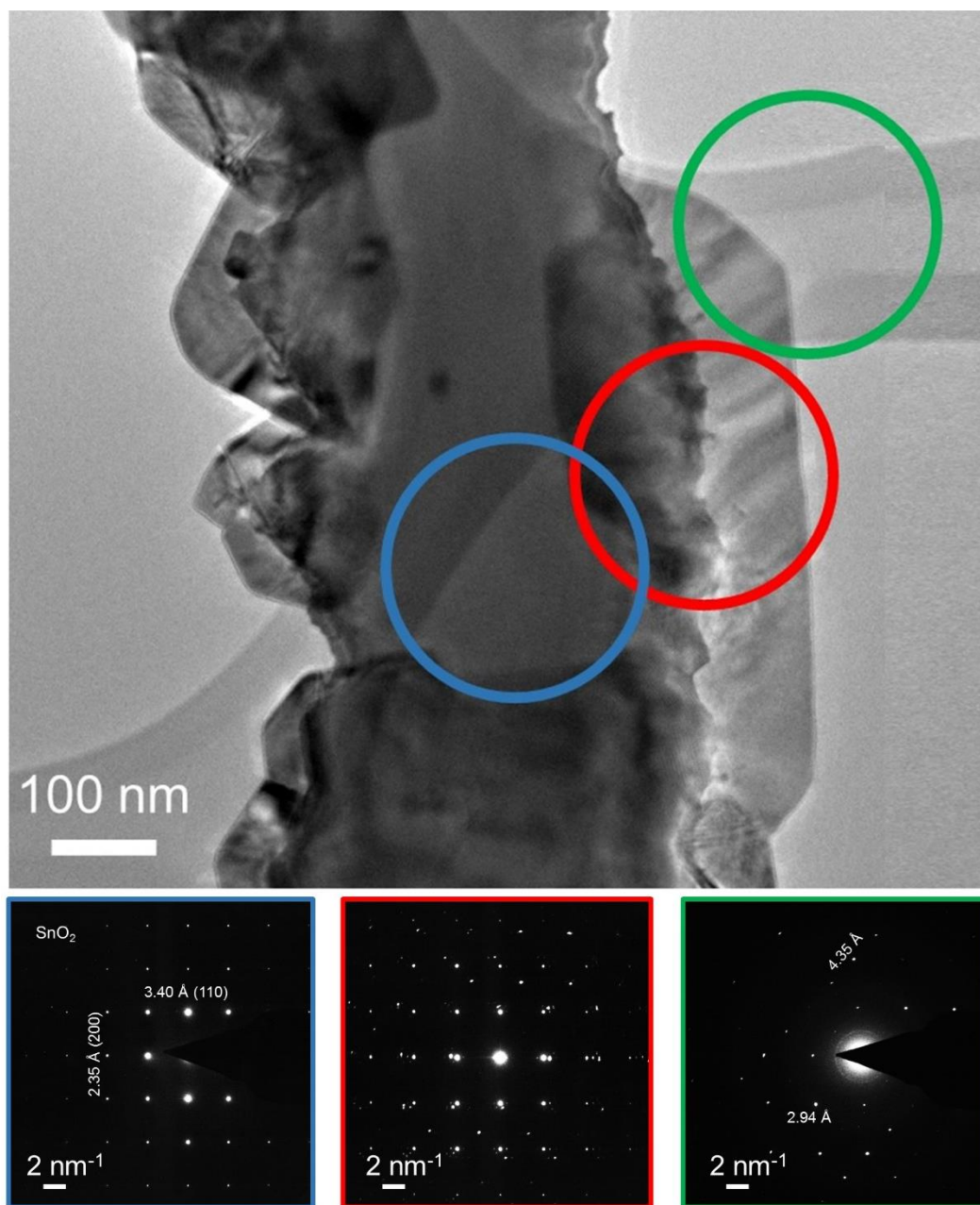


**Figure 7.5.** BF TEM of a single nanowire reacted at 400°C for 15 minutes. Selected Area Electron Diffraction (SAED) focusing on the nanowire core (blue circle), the sulfide shell (green circle) and the tin oxide/tin sulfide interface is shown.

The SnO<sub>2</sub> nanowire core maintains its tetragonal crystal phase, with no signs of vacancy formation, or even reduction of the SnO<sub>2</sub>. The tin sulfide crystal shells are each single crystal, but there seem to be no control of where the nucleation occurs. At the interface, the interesting effect of double diffraction is observed. In double diffraction, the high energy diffracted electron acts as the incident electron beam for the second crystal, forming the doubled pattern. This shows that the tin oxide and tin sulfide are in close crystallographic contact, not merely the physical adsorption of tin sulfide nanoparticles. The measured lattice spacings from the isolated tin sulfide shell show are ~4.35 Å, which could correspond to either the (200) (4.43 Å) or the (210) (4.13 Å) for Sn<sub>2</sub>S<sub>3</sub>, and ~2.94 Å, which could correspond to Sn<sub>2</sub>S<sub>3</sub> (031). It is possible that the tin sulfide is a substoichiometric species, which continues to react with sulfur as the reaction proceeds. As is common in transition metal chalcogenides, the phase diagram for Sn – S is very complicated and there are many possible stoichiometries and crystal structures formed, so a concrete phase identification is difficult.

In attempts to further determine the crystal structure and properties of the tin sulfide phase, multiple spectroscopic analyses were performed. UV Visible absorption was taken for the branched nanowire array and is shown in Figure 7.6A. It shows high overall optical absorption (~7 x 10<sup>4</sup> cm<sup>-2</sup>), with a sharp absorption edge at ~520 nm. Tauc's plot analysis (Figure 7.6B) shows that there is an indirect optical band gap transition of ~ 2.5 eV, which is similar to reported band gaps for SnS<sub>2</sub>.

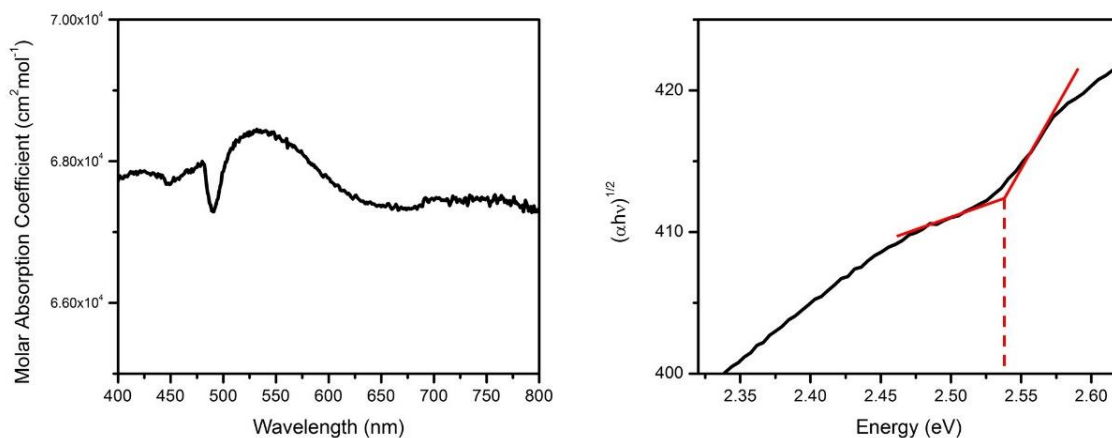


**Figure 7.6.** A) UV Visible absorption spectrum of SnS<sub>x</sub>/SnO<sub>2</sub> nanowire array. B) Tauc's plot analysis showing an indirect optical band gap transition.

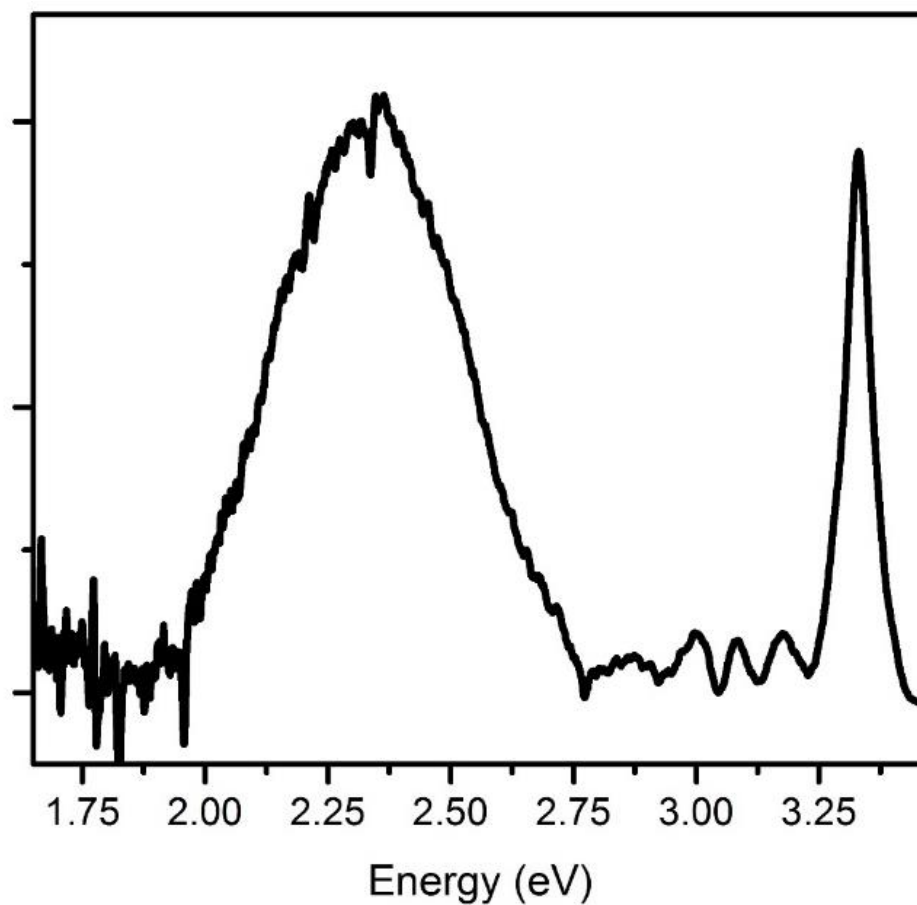


**Figure 7.7.** Cold (125 K) photoluminescence signal for the SnS<sub>x</sub>/SnO<sub>2</sub> branched nanowire array, dispersed on carbon tape. Broad PL peak at ~2.3 eV corresponds to indirect band gap transition of SnS<sub>x</sub> and sharp peak at ~3.3 eV results from the SnO<sub>2</sub> core.

To further characterize the band gap transition, photoluminescence was measured on the array. (Figure 7.7) At room temperatures (298 K), no PL signal was observed. The sample was then transferred to carbon tape and placed in a cooling set up. Liquid Nitrogen (44 K) was pumped into the system until the sample maintained an equilibrium temperature of ~125 K (-145°C). In the visible region, a broad photoluminescence signal is observed at ~2.3 eV, corresponding to an indirect band gap transition similar to that obtained by the Tauc's plot. A sharp PL signal appears at ~3.3 eV, which corresponds to the SnO<sub>2</sub> core.

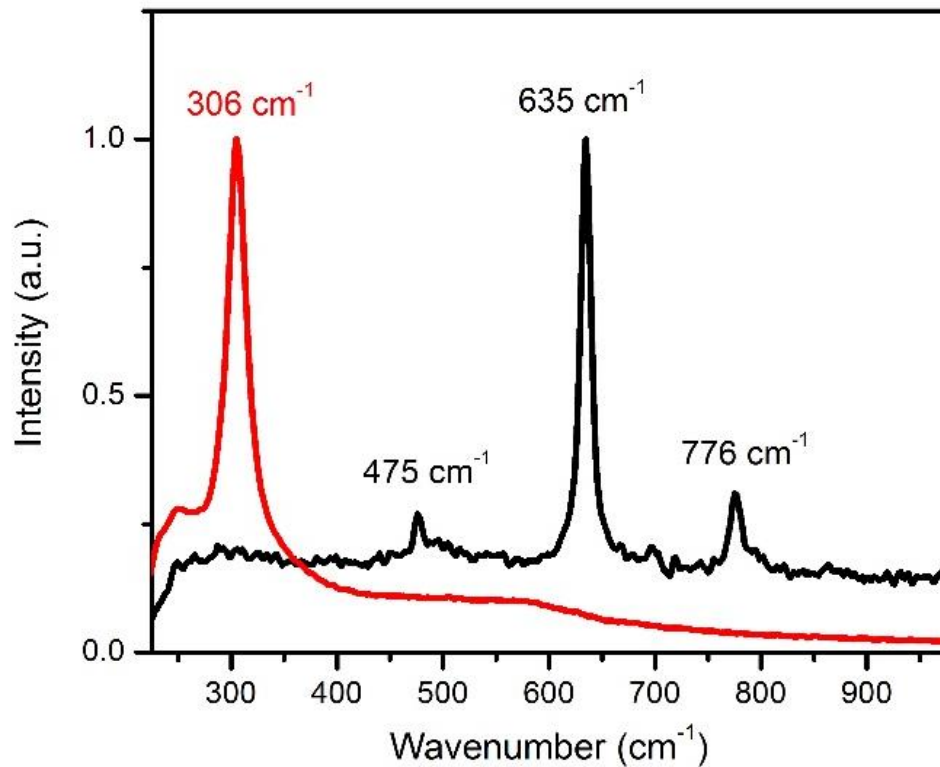


**Figure 7.8.** Raman spectroscopy of the as grown SnO<sub>2</sub> nanowire array (black) on quartz glass. After reaction of SnO<sub>2</sub> with H<sub>2</sub>S at 400°C for 1 hour (red curve), there is no signal from tin oxide.

Raman spectroscopic analysis provides further information on the crystal structure of the branched nanowires, shown in Figure 7.8. The as grown SnO<sub>2</sub> nanowire array shows distinctive Raman shifts at 475, 635, 776 cm<sup>-1</sup>, which corresponds to the E<sub>g</sub>, A<sub>1g</sub>, and B<sub>2g</sub> vibrational modes for octahedral SnO<sub>2</sub>. [254, 255] The relative intensity of the E<sub>g</sub> mode (475 cm<sup>-1</sup>) shows a prevalence of deep oxygen vacancies in the nanowire [256], which is common in many metal oxide nanowires synthesized by CVD. [192] After the reaction to H<sub>2</sub>S at 400°C, there is no longer any trace of the SnO<sub>2</sub> Raman signal, but rather a single, strong Raman shift ~306 cm<sup>-1</sup> is observed, which is consistent with crystalline SnS<sub>2</sub>. [257, 258] Though the band gap information and Raman signal is consistent with SnS<sub>2</sub> formation, the HRTEM and SAED clearly show that this stoichiometric phase is not formed, but suggests that Sn<sub>2</sub>S<sub>3</sub> is formed.

It is interesting that the reaction of SnO<sub>2</sub> with H<sub>2</sub>S does not follow the similar Kirkendall effect driven phase transformation as seen in other metal oxide/H<sub>2</sub>S systems. The question this raises is what is different about the tin cation, compared to those like iron and zinc. While some tin sulfides have a layered structure and this formed nonstoichiometric phase has a large d- spacing of ~7 Å, it does not appear that the diffusion limitations of layered chalcogenides plays a role in this phase transformation, as seen in MoO<sub>3</sub>/MoS<sub>2</sub>. In bulk tin metal, the spontaneous growth of tin “whiskers”, even under ambient conditions, has been observed. This is due to the very high diffusion rates of tin

cations, as well as the dominance of surface diffusion, rather than bulk, in tin systems. The sulfur anion reacts with the tin cations on the nanowire surface, nucleating  $\text{SnS}_x$ , which continue to grow by surface diffusion of the tin cations with the  $\text{SnO}_2$  core acts as a “tin sink”. Since surface diffusion is dominant, rather than bulk diffusion, the Kirkendall Effect does not exist significantly in this case, so there is no noticeable accumulation of vacancies and voids.

## 7.2. Conversion of Zinc Oxide Nanowires to Zinc Sulfide Nanowires

The conversion of ZnO nanowires to hollow ZnS nanotubes has been shown previous and is practically the textbook example of Kirkendall induced hollowing.[101-103] In order to confirm this observation in the  $\text{H}_2\text{S}$  reactor set up used in these phase transformation experiments, ZnO nanowires were reacted at  $300^\circ\text{C}$  in a 15 Torr  $\text{H}_2\text{S}$  atmosphere, very similar conditions to the conversion of  $\text{Fe}_2\text{O}_3$  nanowires to FeS nanotubes. After 1 hour, a polycrystalline ZnS shell is formed on the single crystal ZnO core, shown in Figure 7.9A. There are very clear void accumulation at the sulfide/oxide reaction interface, which is consistent with a Kirkendall Effect induced hollowing. Electron diffraction shows that, while this ZnS shell is not single crystal, the crystals are oriented, which indicates an epitaxial relationship between the ZnO and ZnS.

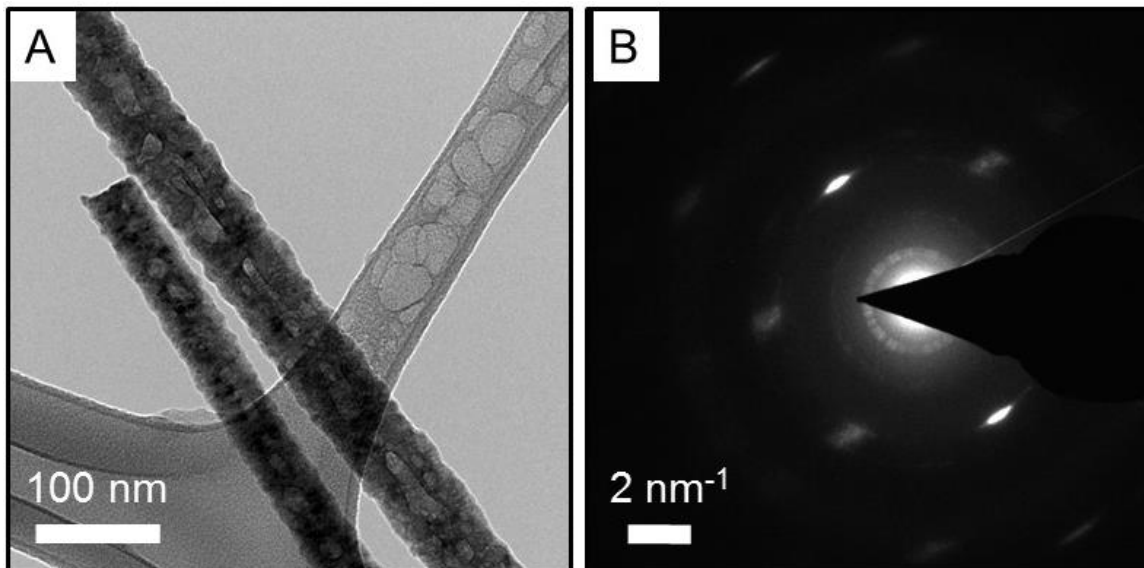


**Figure 7.9.** A) BF TEM of ZnS nanowires with visible voids. B) Electron diffraction showing oriented crystal growth.

This diffraction (Figure 7.9B) suggests that there is an ordering for the formed crystals, showing a 10° to 15° angle between the crystal grains. This indicates some sort of epitaxial relationship between the ZnS shell and the ZnO core. Interestingly, the hollow core formation is not uniform, with random positioning and size of the voids. This may be explained by a weaker epitaxial relationship during the shell formation, than compared to the Fe<sub>2</sub>O<sub>3</sub>/FeS system. This indicated that the epitaxy between the exposed planes of the oxide and the resultant sulfide plays a large role in the resultant nanomorphology, having some impact on the resulting crystallinity of the chalcogenide.

### 7.3. Summary of Phase Transformation in Various Systems

This presented work investigates the effects of phase transformation in sulfur anions with iron, molybdenum, tin, and zinc cations. The first comparison which can be

made is effect of cation diffusion rates on resulting nanomorphologies. Transformation of iron oxide to sulfide and zinc oxide to sulfide both show formation of a hollow nanotube, characteristic of nanoscale Kirkendall Effect resulting from large difference in cationic and anionic diffusion rates. However, the iron sulfide forms a single crystalline shell, with only  $\sim 5^\circ$  between each grain and a clearly defined hollow core. The zinc sulfide conversion shows a larger strain between the crystal grains, with  $10\text{-}15^\circ$  grain boundaries and do not show this uniform core, but random positioned voids with various sizes. Both zinc and iron have high diffusion rates compared to sulfur, so the difference in nanomorphology can be attributed to the epitaxial relationship between the formed sulfide shell and the original oxide core. The exposed edge planes of the  $\text{Fe}_2\text{O}_3$  nanowire have a spacing of  $\sim 2.9\text{\AA}$ , and the FeS grows oriented by the  $\sim 2.5\text{\AA}$  crystal planes. This small lattice mismatch leads to the low angle grain boundaries, but provides strong support for the growing FeS shell during the reaction as the iron oxide core hollows. The zinc sulfide shell is more difficult to characterize, since it is highly polycrystalline with large angle grain boundaries. The weaker epitaxial relationship does not seem to provide enough support for the zinc sulfide shell during formation, compared to the iron sulfide, leading to the variation in void size and position. The epitaxial relationship plays a large role in the resulting nanostructure after phase transformation, especially when the Kirkendall Effect is dominating.

The characteristic hollowing *via* Kirkendall Effect is not observed in the  $\text{MoS}_2$  and  $\text{SnS}_2$  systems. In the case of  $\text{MoO}_3/\text{MoS}_2$  system, the  $\text{MoS}_2$  layered structure strongly inhibits diffusion of both anions into the system, as well as cations out of the system, leading to the core shell structure. The large interlayer spacing,  $\sim 6.2\text{\AA}$ , provides adequate opportunity for the Kirkendall vacancies to be annihilated, rather than agglomerate into



voids. However, in tin oxide to tin sulfide, there is surface nucleation and growth of tin sulfide on the tin oxide nanowire core, which shows no sign of hollowing or decomposition. This phenomenon, it seems, is due to very large diffusion rate of tin cations, coupled with the dominance of surface diffusion, rather than bulk. Even under ambient conditions, tin metal will “grow” 1D whiskers based purely on tin cation diffusion.[252, 259] This strong diffusion rates leads to a domination of surface diffusion, rather than bulk diffusion. This surface diffusion leads to random nucleation of tin sulfide, which then grow into single crystal nanowires, with the tin oxide acting as a tin “sink”. This same random surface nucleation is also seen in sulfurization of tin oxide particles.[260]

These phase transformation experiments with various cations show that nanoscale phase transformation is much more complicated than “larger diffusion leads to vacancy formation.” Moving to a more extreme system, at least in terms of diffusion, lead (Pb) metal cations are very large and, therefore, have very low diffusion rates. Interestingly, oxidation of lead metal particles leads to solid PbO particles, with no hollowing.[71] This is due to the strong preference for oxygen to diffuse in lead and lead oxide crystals[261-263], taking the slow cation diffusion out of the situation. Considering sulfur does not diffuse quickly into most metal oxide systems, the characteristic hollowing to form polycrystalline PbS following sulfurization of Pb particles is observed.[264] This shows that, at least in metal chalcogenide transformations, the particular anion and cation are not significant; so long as the cationic diffusion rates is at least a few orders of magnitude higher than the anionic diffusion in the system, the resulting transformed structure is likely to exhibit hollowing, due to Kirkendall vacancies. Changing the anion to a larger size, and

therefore lower diffusion, such as replacing sulfur with selenium or tellurium, will not significantly impact the hollow structured form. This has been observed in literature reports of formation of copper sulfides, selenides, and tellurides from particles.[59, 61-63] Each of these transformation show a similar hollowing, there does not appear to be any impact based on the anion. The diffusion driving force is not “increased” as originally proposed, just so long as the driving force exists or not. Understanding the synergistic effects of cation diffusion, as well as epitaxial and crystallographic properties of the formed sulfide shell will assist in prediction of the nano-structure of the phase transformed material, but also allow for tailoring of the morphologies.

## CHAPTER VIII: CONCLUSIONS

This dissertation investigates the phase transformation of metal oxide nanowires to chalcogenide, *i.e.* metal sulfide nanostructures. A fundamental understanding of the processes occurring in reactions of metal oxides with reactive gases ( $\text{H}_2\text{S}$ ) allows not only for novel synthesis of semiconductors with nanomorphologies, but also for optimization of nanoscale architecture for desired applications, such as improved photoabsorption and electrocatalysis. Here we report the synthesis and analysis of multiple chalcogenide nanowires formed by phase transformation of metal oxide nanowires:  $\text{MoS}_2$ ,  $\text{FeS}$ ,  $\text{Sn}_2\text{S}_3$ , and  $\text{ZnS}$ . Observation of different cationic diffusion rates leads to different crystallographic structures, forming core-shell structures or hollow nanostructures as a result of the Kirkendall Effect. Of these phase transformed 1D metal chalcogenides, the  $\text{MoS}_2/\text{MoO}_x$  shell/core nanowire architecture were found to have very promising properties for the electrocatalysis of the Hydrogen evolution reaction (HER) in renewable water splitting, so this material system was further analyzed to optimize these catalytic properties by chemical modification. The following is a summary of the observed results, then the conclusions drawn from this work.

As discussed, bulk 2H- $\text{MoS}_2$  can be made more catalytically active by a lithium induced phase transformation to a metastable 1T- $\text{MoS}_2$  crystal. This approach has shown success in formation of 2D sheets, but when applied to the shell/core nanowire system described here, no phase transformation was observed, but the activity still increase due to

an increase in catalytically active sites exposed after disruption of the oriented single crystalline MoS<sub>2</sub> nanowire shell. Another attempt to modify the 2H-MoS<sub>2</sub> nanowire and induce a phase change involved the use of a reducing agent/ chemical electron “dopant”, in this case dilute hydrazine (N<sub>2</sub>H<sub>4</sub>). These chemical treatment also did not induce a phase transformation from 2H to 1T, but did electronically activate the normally chemically inert basal plane of the 2H-MoS<sub>2</sub> nanowire, leading to one of the best reported HER catalytic activity for any MoS<sub>2</sub> architecture to date. Working to understand the phase transformation effects in MoS<sub>2</sub> produced to a strong understanding of the electronic and catalytic properties of the material and helped establish chemically modified MoS<sub>2</sub>/MoO<sub>x</sub> shell/core nanowire arrays as one of the best architectures for electrocatalysis.

In the area of solar energy conversion, pyrite FeS<sub>2</sub> is considered the least expensive and, theoretically, the most efficient solid solar absorber. In attempts to create a high surface area pyrite morphology, Fe<sub>2</sub>O<sub>3</sub> nanowires were reacted with H<sub>2</sub>S at relatively low temperatures (300°C). During these experiments, FeS<sub>2</sub> nanowires were not formed, instead hollow crystalline nanotubes composed of FeS were grown. This hollow morphology is a result of the Kirkendall Effect, caused by the large difference between the diffusion rate of iron cations out of the nanowire compared to the sulfur anionic diffusion rate. This leads to the accumulation of vacancies into voids and the hollow structure. Interestingly, the FeS phase formed by the phase transformation is an understudied symmetric hexagonal structure (NiAs structure) with a theoretical direct band gap transition of ~0.6 eV and experimentally measured as 0.8 – 0.9 eV with high absorption in the solar region. This unique phase has strong potential as a solar absorber and, according to theory, could excite above the band gap leading to a “hot” electron injection and a more efficient

photoelectrochemical energy device. This theoretical “hot” carrier injection has been confirmed by preliminary Ultrafast TAPPS analysis in a  $\text{TiO}_2/\text{FeS}$  system. This is the one of the first reports to investigate the electrochemical properties of this symmetric FeS with NiAs structure and the first report of the nanowire/nanotube morphology. Due to the single crystalline nature of the as grown iron oxide nanowires, this is one of the first reports of Kirkendall Effect induced hollowing in relatively large structures (100 to 300 nm). This is also one of the first practical investigations into hot carrier injection in semiconductors.

To further understand iron oxide to sulfide phase transformation in nanowires,  $\text{SnO}_2$  nanowires and ZnO nanowires were exposed to similar conditions as  $\text{Fe}_2\text{O}_3$ .  $\text{SnO}_2$  nanowires, surprisingly, did not form a hollow core shell structure, but instead nucleated single crystal  $\text{SnS}_x$  nanowire branched growth from the oxide nanowire, with no visible void formation. This tin sulfide formation is dominated by surface diffusion of tin cations, rather than the bulk diffusion seen in the Kirkendall effect. Conversion of ZnO to ZnS, however, shows the Kirkendall induced hollowing during phase transformation. However, these voids were random in position and size, rather than a uniform core observed in the  $\text{Fe}_2\text{O}_3/\text{FeS}$  system. This is due to the strong epitaxial relationship in the iron sulfide system, compared to that zinc sulfide.

The fundamental question raised by these results is what causes some metal oxides to form shell/core structures, hollow structures, or surface nucleation. This, as initially proposed, is not based purely on the metal cation “size” and, therefore its relative diffusion rate. Iron, Molybdenum, and Tin have very similar atomic radii (140 pm, 139 pm and 140.5 pm, respectively), while zinc is significantly smaller at 134 pm. Based purely on a physical diffusion basis, the conversion of these metal oxides should form very similar

structures. This is not the case, experimentally. Other parameters must be taken into account, such as bonding energy of the initial starting metal oxide crystal lattice, the chemical activity of the exposed crystal faces, as well as the chemical structure of the resulting metal sulfide and the epitaxial relationship with the starting oxide, if any exists. In the case of iron oxide to iron sulfide, iron cations diffuse much more quickly to the nanowire surface/reaction interface and sulfur anions, for all practical purposes, does not diffuse into the oxide. The formed sulfide phase, FeS, has a hexagonal crystal structure and has a close epitaxial relationship with the surface exposed iron oxide planes. This facilitates the diffusion of the iron, but also provides stability for the growing iron sulfide shell. In the case of tin oxide to tin sulfide, tin cations diffuse very quickly; the surface diffusion is so favorably that surface “whiskers” will grow on tin metal, due purely to diffusion gradient. During the reaction  $\text{H}_2\text{S}$ , as expected, the sulfur anion does not diffuse into the tin oxide, but surface diffusion of tin cations dominates, rather than bulk diffusion. The sulfur will nucleate tin sulfide on the nanowire surface, then surface diffusion fuels the reaction and crystal growth with tin, having the bulk tin oxide nanowire acting as a tin “sink”. There does not appear to be an epitaxial relationship between the oxide and sulfide, evidenced by the randomness of the sulfide nanowire growth. In the case of  $\text{MoO}_3/\text{MoS}_2$ , there exists the strong diffusion limits for sulfur, but this limitation comes primarily from the  $\text{MoS}_2$  2D layered structure. There is almost no diffusion through the large van der Waals spacing ( $6.2 \text{ \AA}$ ) between the layers, so the sulfur cannot react with the oxide core after the formation of a maximum 8 – 10 nm  $\text{MoS}_2$  layer. Any vacancies, which may have formed during the diffusion will be annihilated in the interlayer spacings, which will negate any agglomeration to form voids or hollowing. The resulting sulfide, in this case, inhibits

the transformation and plays a larger role than the diffusion rate of the transition metal cation. Comparing these results, there are many factors which play a role in nanomorphology formation during phase transformation, which makes absolute statements difficult, but it is this synergy of processes occurring, which allows for these unique structures and unique properties.

The fundamental questions raised at the beginning of this dissertation are first, concerning the feasibility of using post-synthesis gas-solid reaction of metal oxide nanowires to create more complex, chalcogenide nanostructures and understanding the processes which are occurring on the nanoscale, thereby allowing for prediction of the resulting structure based on parameters. Second, after successful creation of these transition metal chalcogenide nanostructures, can these materials be implemented into devices and is any improved activity or efficiency demonstrated. After extensive experimentation and literature review of multiple transition metal chalcogenide systems, the following conclusions and achievements have been reached:

- Gas-solid reactions of metal oxide nanowires with chalcogen rich species ( $\text{H}_2\text{S}$ ) is a promising and efficient method for scalable TMC 1D nanostructure production.
- As a general rule, sulfur and other chalcogen anions have very slow diffusion rates in transition metal oxide systems, usually orders of magnitude lower than the metal cation diffusion rate. This typically leads to an unequal diffusion and accumulation of Kirkendall vacancies, forming hollow structures during phase transformation. However, this model is not simple in predicting formed structure; there are multiple parameters which play a role, such as: crystal structure of the phase transformed chalcogenide, epitaxial relationship with the original oxide nanowire, and surface diffusion properties and activity of the original

oxide surface. These parameters allow for systems with similar cation diffusion rates to form core/shell nanowires, hollow or branched structures.

- The unique properties of phase transformed chalcogenides allowed for the first reported synthesis of FeS with NiAs structure nanowires, a phase of iron sulfide which has been barely investigated. The band structure and electronic properties of this novel material are first described in this work and one of the first investigations, and detection of a “hot” electron excited above the band gap and injected into a wide band gap semiconductor using Ultrafast spectroscopy.
- The phase transformation of MoO<sub>3</sub> nanowires to form MoS<sub>2</sub> lead to an optimized shell/core morphology which provided a conductive, high surface area support for an electrocatalytically active material. Subsequent chemical intercalation and modification have produced one of the best performances to date for any MoS<sub>2</sub> architecture for catalyzing the hydrogen evolution reaction. This chemically modified core/shell nanowire structure has the possibility to be applied to other material systems and provide significant improvements to catalytic applications.

Phase transformation is one of the most efficient way to create chalcogenide materials using metal oxide nanowires and nanoparticles as the starting materials. This post-synthesis processing approach allows for improved scalability and tunability of the electrochemical properties, as well as the morphological aspects. The epitaxial relationship formed in many of the shell/core sulfide/oxide nanostructures allows for improved charge transfer kinetics while maintaining a high active surface area. Exploiting the unique diffusion and crystallographic processes occurring in phase transformation of metal oxide nanowires has already lead to some of the leading catalytic and solar absorbing



architectures and further research will only improve these materials. A firm understanding of how compounds interact on an atomic level in nanomaterials not only has applications in new material synthesis, but has a huge impact in understanding the degradation and transition of nanomaterials in many other applications.

## CHAPTER IX. RECOMMENDATIONS

While this dissertation investigates the diffusion processes and reaction kinetics in phase transformations on the nanoscale by gas-solid reactions, there are many more related areas which can be explored. It has been shown that metal selenides, and even tellurides, have improved catalytic and absorption properties than sulfides, but the synthesis of these compounds is more complex, from a practical point of view. Expanding the investigations to these larger chalcogen anions would be very beneficial from a technological perspective, but would also provide further insight into nanoscale phase transformation. Phase transformation studies do not have to be limited to chalcogenides: understanding how 1D metal oxide nanowires behave in a reducing atmosphere ( $H_2$ ) has not been explored. This will allow for crystalline, metallic nanowires which have many applications. Exploring new material systems, such as perovskites, would be very rewarding and novel if phase transformation can be applied, for example converting lead oxide to lead iodide.

Large scale device fabrication utilizing these phase transformed nanowires would provide a lot of insight into what sorts of morphologies are optimal for various applications. These hollow and branched nanostructures could be ideal for lithium battery electrodes, as well as platforms for other chemical reactions. On this same note, assembling the FeS nanotubes into a functional photoelectrochemical cell would provide very interesting results of how this “hot electron” injection translates to real solar efficiency.

This dissertation has shown that not only are these phase transformed nanostructure beneficial for energy applications, but can be further improved by chemical modification after synthesis. Understanding intercalation processes, as well as chemical dopants, has the potential to open a whole new field in nanoscale research. Too often is the assumption that bulk processes can be easily applied to nano-systems. Chemical reactions and dopants work differently, especially in 1D nanostructures, and the effects of these reactions are different than bulk properties. Understanding not just phase transformation, but chemical modification in nanomaterials will produce some high impact work and real discovery.

## REFERENCES

1. Das, S.K., R. Mallavajula, N. Jayaprakash, and L.A. Archer, *Self-assembled MoS<sub>2</sub>-carbon nanostructures: influence of nanostructuring and carbon on lithium battery performance*. Journal of Materials Chemistry, 2012. **22**(26): p. 12988-12992.
2. Boulineau, A., L. Simonin, J.F. Colin, C. Bourbon, and S. Patoux, *First Evidence of Manganese-Nickel Segregation and Densification upon Cycling in Li-Rich Layered Oxides for Lithium Batteries*. Nano Letters, 2013. **13**(8): p. 3857-3863.
3. Kim, J., D.J. Lee, H.G. Jung, Y.K. Sun, J. Hassoun, et al., *An Advanced Lithium-Sulfur Battery*. Advanced Functional Materials, 2013. **23**(8): p. 1076-1080.
4. Bell, A.T., *The impact of nanoscience on heterogeneous catalysis*. Science, 2003. **299**(5613): p. 1688-1691.
5. Petzold, F.G., J. Jasinski, E.L. Clark, J.H. Kim, J. Absher, et al., *Nickel supported on zinc oxide nanowires as advanced hydrodesulfurization catalysts*. Catalysis Today, 2012. **198**(1): p. 219-227.
6. Chen, M., K.A. Rubin, and R.W. Barton, *COMPOUND MATERIALS FOR REVERSIBLE, PHASE-CHANGE OPTICAL-DATA STORAGE*. Applied Physics Letters, 1986. **49**(9): p. 502-504.
7. Yamada, N., E. Ohno, N. Akahira, K. Nishiuchi, K. Nagata, et al., *HIGH-SPEED OVERWRITABLE PHASE-CHANGE OPTICAL DISK MATERIAL*. Japanese Journal of Applied Physics Part 1-Regular Papers Short Notes & Review Papers, 1987. **26**: p. 61-66.

8. Takayama, T. and H. Takagi, *Phase-change magnetic memory effect in cation-deficient iron sulfide Fe<sub>1-x</sub>S*. Applied Physics Letters, 2006. **88**(1).
9. Yu, B., S.Y. Ju, X.H. Sun, G. Ng, T.D. Nguyen, et al., *Indium selenide nanowire phase-change memory*. Applied Physics Letters, 2007. **91**(13).
10. Jin, B., T. Lim, S. Ju, M.I. Latypov, H.S. Kim, et al., *Ga-doped indium oxide nanowire phase change random access memory cells*. Nanotechnology, 2014. **25**(5).
11. Jin, B., T. Lim, S. Ju, M.I. Latypov, D.H. Pi, et al., *Investigation of thermal resistance and power consumption in Ga-doped indium oxide (In<sub>2</sub>O<sub>3</sub>) nanowire phase change random access memory*. Applied Physics Letters, 2014. **104**(10).
12. IPCC, *Climate Change 2014: Mitigation of climate change. Working Group III contribution to the IPCC Fifth Assessment Report*. 2014: Cambridge, United Kingdom.
13. Joo, S.H., S.J. Choi, I. Oh, J. Kwak, Z. Liu, et al., *Ordered Nanoporous Arrays of Carbon Supporting High Dispersions of Platinum Nanoparticles*. Nature, 2001. **412**(6843): p. 169-172.
14. Si, Y.C. and E.T. Samulski, *Exfoliated Graphene Separated by Platinum Nanoparticles*. Chemistry of Materials, 2008. **20**(21): p. 6792-6797.
15. Sheng, W.C., H.A. Gasteiger, and Y. Shao-Horn, *Hydrogen Oxidation and Evolution Reaction Kinetics on Platinum: Acid vs Alkaline Electrolytes*. Journal of the Electrochemical Society, 2010. **157**(11): p. B1529-B1536.

16. Rostrup-Nielsen, J.R., J. Sehested, and J.K. Norskov, *Hydrogen and Synthesis Gas By Steam and CO<sub>2</sub> Reforming*, in *Advances in Catalysis*, B.C. Gates and H. Knozinger, Editors. 2002. p. 65-139.
17. Cortright, R.D., R.R. Davda, and J.A. Dumesic, *Hydrogen from Catalytic Reforming of Biomass-Derived Hydrocarbons in Liquid Water*. *Nature*, 2002. **418**(6901): p. 964-967.
18. Ashcroft, A.T., A.K. Cheetham, M.L.H. Green, and P.D.F. Vernon, *Partial Oxidation of Methane to Synthesis Gas-Using Carbon-Dioxide*. *Nature*, 1991. **352**(6332): p. 225-226.
19. Rossmeisl, J., A. Logadottir, and J.K. Norskov, *Electrolysis of Water on (Oxidized) Metal Surfaces*. *Chemical Physics*, 2005. **319**(1-3): p. 178-184.
20. Khaselev, O. and J.A. Turner, *A Monolithic Photovoltaic-Photoelectrochemical Device for Hydrogen Production Via Water Splitting*. *Science*, 1998. **280**(5362): p. 425-427.
21. Khan, S.U.M., M. Al-Shahry, and W.B. Ingler, *Efficient Photochemical Water Splitting by a Chemically Modified n-TiO<sub>2</sub>*. *Science*, 2002. **297**(5590): p. 2243-2245.
22. Wolcott, A., W.A. Smith, T.R. Kuykendall, Y.P. Zhao, and J.Z. Zhang, *Photoelectrochemical Water Splitting Using Dense and Aligned TiO<sub>2</sub> Nanorod Arrays*. *Small*, 2009. **5**(1): p. 104-111.
23. Zou, Z.G., J.H. Ye, K. Sayama, and H. Arakawa, *Direct Splitting of Water Under Visible Light Irradiation with an Oxide Semiconductor Photocatalyst*. *Nature*, 2001. **414**(6864): p. 625-627.

24. Joya, K.S., N.K. Subbaiyan, F. D'Souza, and H.J.M. de Groot, *Surface-Immobilized Single-Site Iridium Complexes for Electrocatalytic Water Splitting*. *Angewandte Chemie-International Edition*, 2012. **51**(38): p. 9601-9605.
25. Chhowalla, M., H.S. Shin, G. Eda, L.-J. Li, K.P. Loh, et al., *The Chemistry of Two-Dimensional Layered Transition Metal Dichalcogenide Nanosheets*. *Nature Chemistry*, 2013. **5**(4): p. 263-275.
26. Ho, W.K., J.C. Yu, J. Lin, J.G. Yu, and P.S. Li, *Preparation and Photocatalytic Behavior of MoS<sub>2</sub> and WS<sub>2</sub> Nanocluster Sensitized TiO<sub>2</sub>*. *Langmuir*, 2004. **20**(14): p. 5865-5869.
27. King, L.A., W. Zhao, M. Chhowalla, D.J. Riley, and G. Eda, *Photoelectrochemical Properties of Chemically Exfoliated MoS<sub>2</sub>*. *Journal of Materials Chemistry A*, 2013. **1**(31): p. 8935-8941.
28. Voiry, D., M. Salehi, R. Silva, T. Fujita, M. Chen, et al., *Conducting MoS<sub>2</sub> Nanosheets as Catalysts for Hydrogen Evolution Reaction*. *Nano Letters*, 2013. **13**(12): p. 6222-6227.
29. Voiry, D., H. Yamaguchi, J.W. Li, R. Silva, D.C.B. Alves, et al., *Enhanced Catalytic Activity in Strained Chemically Exfoliated WS<sub>2</sub> Nanosheets for Hydrogen Evolution*. *Nature Materials*, 2013. **12**(9): p. 850-855.
30. Jing, D.W. and L.J. Guo, *WS<sub>2</sub> Sensitized Mesoporous TiO<sub>2</sub> for Efficient Photocatalytic Hydrogen Production from Water Under Visible Light Irradiation*. *Catalysis Communications*, 2007. **8**(5): p. 795-799.
31. Hinnemann, B., P.G. Moses, J. Bonde, K.P. Jorgensen, J.H. Nielsen, et al., *Biornimetic Hydrogen Evolution: MoS<sub>2</sub> Nanoparticles as Catalyst for Hydrogen*

- Evolution*. Journal of the American Chemical Society, 2005. **127**(15): p. 5308-5309.
32. Li, Y., H. Wang, L. Xie, Y. Liang, G. Hong, et al., *MoS<sub>2</sub> Nanoparticles Grown on Graphene: An Advanced Catalyst for the Hydrogen Evolution Reaction*. Journal of the American Chemical Society, 2011. **133**(19): p. 7296-7299.
33. Jaramillo, T.F., K.P. Jorgensen, J. Bonde, J.H. Nielsen, S. Horch, et al., *Identification of Active Edge Sites for Electrochemical H<sub>2</sub> Evolution From MoS<sub>2</sub> Nanocatalysts*. Science, 2007. **317**(5834): p. 100-102.
34. Kibsgaard, J., Z.B. Chen, B.N. Reinecke, and T.F. Jaramillo, *Engineering the Surface Structure of MoS<sub>2</sub> to Preferentially Expose Active Edge Sites for Electrocatalysis*. Nature Materials, 2012. **11**(11): p. 963-969.
35. Kong, D.S., H.T. Wang, J.J. Cha, M. Pasta, K.J. Koski, et al., *Synthesis of MoS<sub>2</sub> and MoSe<sub>2</sub> Films with Vertically Aligned Layers*. Nano Letters, 2013. **13**(3): p. 1341-1347.
36. Wu, Z.Z., B.Z. Fang, Z.P. Wang, C.L. Wang, Z.H. Liu, et al., *MoS<sub>2</sub> Nanosheets: A Designed Structure with High Active Site Density for the Hydrogen Evolution Reaction*. ACS Catalysis, 2013. **3**(9): p. 2101-2107.
37. Wang, H.T., Z.Y. Lu, S.C. Xu, D.S. Kong, J.J. Cha, et al., *Electrochemical Tuning of Vertically Aligned MoS<sub>2</sub> Nanofilms and Its Application in Improving Hydrogen Evolution Reaction*. Proceedings of the National Academy of Sciences of the United States of America, 2013. **110**(49): p. 19701-19706.
38. Lukowski, M.A., A.S. Daniel, F. Meng, A. Forticaux, L.S. Li, et al., *Enhanced Hydrogen Evolution Catalysis from Chemically Exfoliated Metallic MoS<sub>2</sub>*



- Nanosheets*. Journal of the American Chemical Society, 2013. **135**(28): p. 10274-10277.
39. Wang, H.T., Z.Y. Lu, D.S. Kong, J. Sun, T.M. Hymel, et al., *Electrochemical Tuning of MoS<sub>2</sub> Nanoparticles on Three-Dimensional Substrate for Efficient Hydrogen Evolution*. *Acs Nano*, 2014. **8**(5): p. 4940-4947.
40. Tsai, C., F. Abild-Pedersen, and J.K. Norskov, *Tuning the MoS<sub>2</sub> Edge-Site Activity for Hydrogen Evolution via Support Interactions*. *Nano Letters*, 2014. **14**(3): p. 1381-1387.
41. Polking, M.J., H.M. Zheng, R. Ramesh, and A.P. Alivisatos, *Controlled Synthesis and Size-Dependent Polarization Domain Structure of Colloidal Germanium Telluride Nanocrystals*. Journal of the American Chemical Society, 2011. **133**(7): p. 2044-2047.
42. Buck, M.R., I.T. Sines, and R.E. Schaak, *Liquid-Phase Synthesis of Uniform Cube-Shaped GeTe Microcrystals*. *Chemistry of Materials*, 2010. **22**(10): p. 3236-3240.
43. Yu, J.H., J. Joo, H.M. Park, S.I. Baik, Y.W. Kim, et al., *Synthesis of quantum-sized cubic ZnS nanorods by the oriented attachment mechanism*. Journal of the American Chemical Society, 2005. **127**(15): p. 5662-5670.
44. Malakooti, R., L. Cademartiri, Y. Akcakir, S. Petrov, A. Migliori, et al., *Shape-controlled Bi<sub>2</sub>S<sub>3</sub> nanocrystals and their plasma polymerization into flexible film*. *Advanced Materials*, 2006. **18**(16): p. 2189-+.
45. Tang, J. and A.P. Alivisatos, *Crystal splitting in the growth of Bi<sub>2</sub>S<sub>3</sub>*. *Nano Letters*, 2006. **6**(12): p. 2701-2706.

46. Lu, W.G., Y. Ding, Y.X. Chen, Z.L. Wang, and J.Y. Fang, *Bismuth telluride hexagonal nanoplatelets and their two-step epitaxial growth*. Journal of the American Chemical Society, 2005. **127**(28): p. 10112-10116.
47. Son, J.S., M.K. Choi, M.K. Han, K. Park, J.Y. Kim, et al., *n-Type Nanostructured Thermoelectric Materials Prepared from Chemically Synthesized Ultrathin Bi<sub>2</sub>Te<sub>3</sub> Nanoplates*. Nano Letters, 2012. **12**(2): p. 640-647.
48. Sahu, A., L.J. Qi, M.S. Kang, D.N. Deng, and D.J. Norris, *Facile Synthesis of Silver Chalcogenide (Ag<sub>2</sub>E; E = Se, S, Te) Semiconductor Nanocrystals*. Journal of the American Chemical Society, 2011. **133**(17): p. 6509-6512.
49. Chen, L.Q., H.Q. Zhan, X.F. Yang, Z.Y. Sun, J. Zhang, et al., *Composition and size tailored synthesis of iron selenide nanoflakes*. Crystengcomm, 2010. **12**(12): p. 4386-4391.
50. Kim, Y.H., J.H. Lee, D.W. Shin, S.M. Park, J.S. Moon, et al., *Synthesis of shape-controlled beta-In<sub>2</sub>S<sub>3</sub> nanotubes through oriented attachment of nanoparticles*. Chemical Communications, 2010. **46**(13): p. 2292-2294.
51. Choi, J., J. Jin, J. Lee, J.H. Park, H.J. Kim, et al., *Columnar assembly and successive heating of colloidal 2D nanomaterials on graphene as an efficient strategy for new anode materials in lithium ion batteries: the case of In<sub>2</sub>S<sub>3</sub> nanoplates*. Journal of Materials Chemistry, 2012. **22**(22): p. 11107-11112.
52. Franzman, M.A., C.W. Schlenker, M.E. Thompson, and R.L. Brutchey, *Solution-Phase Synthesis of SnSe Nanocrystals for Use in Solar Cells*. Journal of the American Chemical Society, 2010. **132**(12): p. 4060-+.

53. Liu, S., X.Y. Guo, M.R. Li, W.H. Zhang, X.Y. Liu, et al., *Solution-Phase Synthesis and Characterization of Single-Crystalline SnSe Nanowires*. *Angewandte Chemie-International Edition*, 2011. **50**(50): p. 12050-12053.
54. Wu, Y., C. Wadia, W. Ma, B. Sadler, and A.P. Alivisatos, *Synthesis and photovoltaic application of copper(I) sulfide nanocrystals*. *Nano Letters*, 2008. **8**(8): p. 2551-2555.
55. Chikan, V. and D.F. Kelley, *Synthesis of highly luminescent GaSe nanoparticles*. *Nano Letters*, 2002. **2**(2): p. 141-145.
56. Malakooti, R., L. Cademartiri, A. Migliori, and G.A. Ozin, *Ultrathin Sb<sub>2</sub>S<sub>3</sub> nanowires and nanoplatelets*. *Journal of Materials Chemistry*, 2008. **18**(1): p. 66-69.
57. Yin, Y.D., R.M. Rioux, C.K. Erdonmez, S. Hughes, G.A. Somorjai, et al., *Formation of hollow nanocrystals through the nanoscale Kirkendall Effect*. *Science*, 2004. **304**(5671): p. 711-714.
58. Smigelskas, A.D. and E.O. Kirkendall, *Zinc Diffusion in Alpha Brass*. *Trans. AIME*, 1947. **171**(130).
59. Wang, W.S., M. Dahl, and Y.D. Yin, *Hollow Nanocrystals through the Nanoscale Kirkendall Effect*. *Chemistry of Materials*, 2013. **25**(8): p. 1179-1189.
60. Gao, M.R., Y.F. Xu, J. Jiang, and S.H. Yu, *Nanostructured metal chalcogenides: synthesis, modification, and applications in energy conversion and storage devices*. *Chemical Society Reviews*, 2013. **42**(7): p. 2986-3017.

61. Xu, H.L., W.Z. Wang, W. Zhu, and L. Zhou, *Synthesis of octahedral CuS nanocages via a solid-liquid reaction*. *Nanotechnology*, 2006. **17**(15): p. 3649-3654.
62. Li, W.H., R. Zamani, M. Ibanez, D. Cadavid, A. Shavel, et al., *Metal Ions To Control the Morphology of Semiconductor Nanoparticles: Copper Selenide Nanocubes*. *Journal of the American Chemical Society*, 2013. **135**(12): p. 4664-4667.
63. Xiao, G.J., Y. Zeng, Y.Y. Jiang, J.J. Ning, W.T. Zheng, et al., *Controlled Synthesis of Hollow Cu<sub>2-x</sub>Te Nanocrystals Based on the Kirkendall Effect and Their Enhanced CO Gas-Sensing Properties*. *Small*, 2013. **9**(5): p. 793-799.
64. Erlebacher, J. and D. Margetis, *Mechanism of Hollow Nanoparticle Formation Due to Shape Fluctuations*. *Physical Review Letters*, 2014. **112**(15).
65. Jung, N., D.Y. Chung, J. Ryu, S.J. Yoo, and Y.E. Sung, *Pt-based nanoarchitecture and catalyst design for fuel cell applications*. *Nano Today*, 2014. **9**(4): p. 433-456.
66. Wu, W.J. and M.M. Maye, *Void Coalescence in Core/Alloy Nanoparticles with Stainless Interfaces*. *Small*, 2014. **10**(2): p. 271-276.
67. Sarac, M.F., W.C. Wu, and J.B. Tracy, *Control of Branching in Ni<sub>3</sub>Cl-x Nanoparticles and Their Conversion into Ni<sub>12</sub>P<sub>5</sub> Nanoparticles*. *Chemistry of Materials*, 2014. **26**(10): p. 3057-3064.
68. Gusak, A.M. and K.N. Tu, *Interaction between the Kirkendall effect and the inverse Kirkendall effect in nanoscale particles*. *Acta Materialia*, 2009. **57**(11): p. 3367-3373.

69. Nakajima, H. and R. Nakamura, *Diffusion in Intermetallic Compounds and Fabrication of Hollow Nanoparticles through Kirkendall Effect*. Journal of Nano Research, 2009. **7**: p. 1-10.
70. Nakamura, R., J.G. Lee, D. Tokozakura, H. Mori, and H. Nakajima, *Formation of hollow ZnO through low-temperature oxidation of Zn nanoparticles*. Materials Letters, 2007. **61**(4-5): p. 1060-1063.
71. Nakamura, R., D. Tokozakura, H. Nakajima, J.G. Lee, and H. Mori, *Hollow oxide formation by oxidation of Al and Cu nanoparticles*. Journal of Applied Physics, 2007. **101**(7).
72. Lian, J., K. Anggara, M. Lin, and Y.T. Chan, *Formation of Hollow Iron Oxide Tetrapods via a Shape-Preserving Nanoscale Kirkendall Effect*. Small, 2014. **10**(4): p. 667-673.
73. Cabot, A., V.F. Puentes, E. Shevchenko, Y. Yin, L. Balcells, et al., *Vacancy coalescence during oxidation of iron nanoparticles*. Journal of the American Chemical Society, 2007. **129**(34): p. 10358-+.
74. Choi, Y.H., D.H. Kim, H.S. Han, S. Shin, S.H. Hong, et al., *Direct Printing Synthesis of Self-Organized Copper Oxide Hollow Spheres on a Substrate Using Copper(II) Complex Ink: Gas Sensing and Photoelectrochemical Properties*. Langmuir, 2014. **30**(3): p. 700-709.
75. Niu, K.Y., J. Park, H.M. Zheng, and A.P. Aivisatos, *Revealing Bismuth Oxide Hollow Nanoparticle Formation by the Kirkendall Effect*. Nano Letters, 2013. **13**(11): p. 5715-5719.

76. Wang, C.M., A. Genc, H.K. Cheng, L. Pullan, D.R. Baer, et al., *In-Situ TEM visualization of vacancy injection and chemical partition during oxidation of Ni-Cr nanoparticles*. Scientific Reports, 2014. **4**.
77. Wang, C.M., D.R. Baer, L.E. Thomas, J.E. Amonette, J. Antony, et al., *Void formation during early stages of passivation: Initial oxidation of iron nanoparticles at room temperature*. Journal of Applied Physics, 2005. **98**(9).
78. Dhara, S., A. Datta, C.T. Wu, Z.H. Lan, K.H. Chen, et al., *Hexagonal-to-cubic phase transformation in GaN nanowires by Ga<sup>+</sup> implantation*. Applied Physics Letters, 2004. **84**(26): p. 5473-5475.
79. Robinson, R.D., B. Sadtler, D.O. Demchenko, C.K. Erdonmez, L.W. Wang, et al., *Spontaneous superlattice formation in nanorods through partial cation exchange*. Science, 2007. **317**(5836): p. 355-358.
80. Son, D.H., S.M. Hughes, Y.D. Yin, and A.P. Alivisatos, *Cation exchange reactions-in ionic nanocrystals*. Science, 2004. **306**(5698): p. 1009-1012.
81. Schoen, D.T., H.L. Peng, and Y. Cui, *CuInSe<sub>2</sub> Nanowires from Facile Chemical Transformation of In<sub>2</sub>Se<sub>3</sub> and Their Integration in Single-Nanowire Devices*. Acs Nano, 2013. **7**(4): p. 3205-3211.
82. Sunkara, M.K., C. Pendyala, D. Cummins, P. Meduri, J. Jasinski, et al., *Inorganic nanowires: a perspective about their role in energy conversion and storage applications*. Journal of Physics D-Applied Physics, 2011. **44**(17).
83. Lin, Y., T. Xie, B.C. Cheng, B.Y. Geng, and L.D. Zhang, *Ordered nickel oxide nanowire arrays and their optical absorption properties*. Chemical Physics Letters, 2003. **380**(5-6): p. 521-525.

84. Masuda, H. and M. Satoh, *Fabrication of gold nanodot array using anodic porous alumina as an evaporation mask*. Japanese Journal of Applied Physics Part 2-Letters, 1996. **35**(1B): p. L126-L129.
85. Lei, Y., W.K. Chim, J. Weissmuller, G. Wilde, H.P. Sun, et al., *Ordered arrays of highly oriented single-crystal semiconductor nanoparticles on silicon substrates*. Nanotechnology, 2005. **16**(9): p. 1892-1898.
86. Lei, Y. and W.K. Chim, *Highly ordered arrays of metal/semiconductor core-shell nanoparticles with tunable nanostructures and photoluminescence*. Journal of the American Chemical Society, 2005. **127**(5): p. 1487-1492.
87. Ren, Y., W.K. Chim, S.Y. Chiam, J.Q. Huang, C. Pi, et al., *Formation of Nickel Oxide Nanotubes with Uniform Wall Thickness by Low-Temperature Thermal Oxidation Through Understanding the Limiting Effect of Vacancy Diffusion and the Kirkendall Phenomenon*. Advanced Functional Materials, 2010. **20**(19): p. 3336-3342.
88. Chun, S.R., W.A. Sasangka, M.Z. Ng, Q. Liu, A. Du, et al., *Joining Copper Oxide Nanotube Arrays Driven by the Nanoscale Kirkendall Effect*. Small, 2013. **9**(15): p. 2546-2552.
89. El Mel, A.A., M. Buffiere, P.Y. Tessier, S. Konstantinidis, W. Xu, et al., *Highly Ordered Hollow Oxide Nanostructures: The Kirkendall Effect at the Nanoscale*. Small, 2013. **9**(17): p. 2838-2843.
90. Lee, Y.I., N.V. Myung, and Y.H. Choa, *Transformation of metal nanowires into metal nanotubes by a sequential thermal process*. Scripta Materialia, 2013. **68**(7): p. 463-466.

91. Hu, Y.Y., X.T. Huang, K. Wang, J.P. Liu, J. Jiang, et al., *Kirkendall-effect-based growth of dendrite-shaped CuO hollow micro/nanostructures for lithium-ion battery anodes*. Journal of Solid State Chemistry, 2010. **183**(3): p. 662-667.
92. Lv, Y.G., Y. Li, and W.J. Shen, *Synthesis of Co<sub>3</sub>O<sub>4</sub> nanotubes and their catalytic applications in CO oxidation*. Catalysis Communications, 2013. **42**: p. 116-120.
93. Yan, C.L. and D.F. Xue, *Formation of Nb(2)O(5) nanotube Arrays through phase transformation*. Advanced Materials, 2008. **20**(5): p. 1055-+.
94. Yu, Y.H., X. Yin, A. Kvit, and X.D. Wang, *Evolution of Hollow TiO<sub>2</sub> Nanostructures via the Kirkendall Effect Driven by Cation Exchange with Enhanced Photoelectrochemical Performance*. Nano Letters, 2014. **14**(5): p. 2528-2535.
95. Bachmann, J., J. Jing, M. Knez, S. Barth, H. Shen, et al., *Ordered iron oxide nanotube arrays of controlled geometry and tunable magnetism by atomic layer deposition*. Journal of the American Chemical Society, 2007. **129**(31): p. 9554-+.
96. Dang, T.D., A.N. Banerjee, S.W. Joo, and B.K. Min, *Synthesis of Amorphous and Crystalline Hollow Manganese Oxide Nanotubes with Highly Porous Walls Using Carbon Nanotube Templates and Enhanced Catalytic Activity*. Industrial & Engineering Chemistry Research, 2014. **53**(23): p. 9743-9753.
97. Lu, H.B., L. Liao, H. Li, D.F. Wang, Y. Tian, et al., *Hollow MgO nanotube arrays by using ZnO nanorods as templates*. European Journal of Inorganic Chemistry, 2008(17): p. 2727-2732.
98. Li, Q.G. and R.M. Penner, *Photoconductive cadmium sulfide hemicylindrical shell nanowire ensembles*. Nano Letters, 2005. **5**(9): p. 1720-1725.



99. Cao, L.M., X.Y. Zhang, H. Tian, A. Zhang, and W.K. Wang, *Boron nitride nanotube branched nanojunctions*. *Nanotechnology*, 2007. **18**(15).
100. Thangala, J., Z. Chen, A. Chin, C.-Z. Ning, and M.K. Sunkara, *Phase Transformation Studies of Metal Oxide Nanowires*. *Crystal Growth & Design*, 2009. **9**(7): p. 3177-3182.
101. Dloczik, L. and R. Konenkamp, *Nanostructure transfer in semiconductors by ion exchange*. *Nano Letters*, 2003. **3**(5): p. 651-653.
102. Wang, Z., X.F. Qian, Y. Li, J. Yin, and Z.K. Zhu, *Large-scale synthesis of tube-like ZnS and cable-like ZnS-ZnO arrays: Preparation through the sulfuration conversion from ZnO arrays via a simple chemical solution route*. *Journal of Solid State Chemistry*, 2005. **178**(5): p. 1589-1594.
103. Yi, R., G.Z. Qiu, and X.H. Liu, *Rational synthetic strategy: From ZnO nanorods to ZnS nanotubes*. *Journal of Solid State Chemistry*, 2009. **182**(10): p. 2791-2795.
104. Wan, D.Y., Y.T. Wang, Z.P. Zhou, G.Q. Yang, B.Y. Wang, et al., *Fabrication of the ordered FeS<sub>2</sub> (pyrite) nanowire arrays in anodic aluminum oxide*. *Materials Science and Engineering B-Solid State Materials for Advanced Technology*, 2005. **122**(2): p. 156-159.
105. Caban-Acevedo, M., M.S. Faber, Y.Z. Tan, R.J. Hamers, and S. Jin, *Synthesis and Properties of Semiconducting Iron Pyrite (FeS<sub>2</sub>) Nanowires*. *Nano Letters*, 2012. **12**(4): p. 1977-1982.
106. Morrish, R., R. Silverstein, and C.A. Wolden, *Synthesis of Stoichiometric FeS<sub>2</sub> through Plasma-Assisted Sulfurization of Fe<sub>2</sub>O<sub>3</sub> Nanorods*. *Journal of the American Chemical Society*, 2012. **134**(43): p. 17854-17857.

107. Castro Neto, A.H., F. Guinea, N.M.R. Peres, K.S. Novoselov, and A.K. Geim, *The electronic properties of graphene*. Reviews of Modern Physics, 2009. **81**(1): p. 109-162.
108. Novoselov, K.S., A.K. Geim, S.V. Morozov, D. Jiang, Y. Zhang, et al., *Electric field effect in atomically thin carbon films*. Science, 2004. **306**(5696): p. 666-669.
109. Geim, A.K., *Graphene: Status and Prospects*. Science, 2009. **324**(5934): p. 1530-1534.
110. Liu, Z., L. Song, S.Z. Zhao, J.Q. Huang, L.L. Ma, et al., *Direct Growth of Graphene/Hexagonal Boron Nitride Stacked Layers*. Nano Letters, 2011. **11**(5): p. 2032-2037.
111. Ci, L., L. Song, C.H. Jin, D. Jariwala, D.X. Wu, et al., *Atomic layers of hybridized boron nitride and graphene domains*. Nature Materials, 2010. **9**(5): p. 430-435.
112. Kvashnin, A.G., L.A. Chernozatonskii, B.I. Yakobson, and P.B. Sorokin, *Phase Diagram of Quasi-Two-Dimensional Carbon, From Graphene to Diamond*. Nano Letters, 2014. **14**(2): p. 676-681.
113. Yu, W.J., W.M. Lau, S.P. Chan, Z.F. Liu, and Q.Q. Zheng, *Ab initio study of phase transformations in boron nitride*. Physical Review B, 2003. **67**(1).
114. Liu, Q.X., G.W. Yang, and J.X. Zhang, *Phase transition between cubic-BN and hexagonal BN upon pulsed laser induced liquid-solid interfacial reaction*. Chemical Physics Letters, 2003. **373**(1-2): p. 57-61.
115. Hao, S.G., G. Zhou, W.H. Duan, J. Wu, and B.L. Gu, *Transverse pressure induced phase transitions in boron nitride nanotube bundles and the lightest boron nitride crystal*. Journal of the American Chemical Society, 2008. **130**(15): p. 5257-5261.

116. Sachdev, H., R. Haubner, H. Noth, and B. Lux, *Investigation of the cBN/h-BN phase transformation at normal pressure*. *Diamond and Related Materials*, 1997. **6**(2-4): p. 286-292.
117. Eremets, M.I., K. Takemura, H. Yusa, D. Golberg, Y. Bando, et al., *Disordered state in first-order phase transitions: Hexagonal-to-cubic and cubic-to-hexagonal transitions in boron nitride*. *Physical Review B*, 1998. **57**(10): p. 5655-5660.
118. Dang, H.L., Y.D. Liu, W.H. Xue, R.S. Anderson, C.R. Sewell, et al., *Phase transformations of nano-sized cubic boron nitride to white graphene and white graphite*. *Applied Physics Letters*, 2014. **104**(9).
119. Nagao, T., J.T. Sadowski, M. Saito, S. Yaginuma, Y. Fujikawa, et al., *Nanofilm allotrope and phase transformation of ultrathin Bi film on Si(111)-7 x 7*. *Physical Review Letters*, 2004. **93**(10).
120. Kumar, V., A. Sumboja, J.X. Wang, V. Bhavanasi, V.C. Nguyen, et al., *Topotactic Phase Transformation of Hexagonal MoO<sub>3</sub> to Layered MoO<sub>3</sub>-II and Its Two-Dimensional (2D) Nanosheets*. *Chemistry of Materials*, 2014. **26**(19): p. 5533-5539.
121. Tao, X. and Y. Gu, *Crystalline-Crystalline Phase Transformation in Two-Dimensional In<sub>2</sub>Se<sub>3</sub> Thin Layers*. *Nano Letters*, 2013. **13**(8): p. 3501-3505.
122. Wang, F., J.E. Jakes, D.L. Geng, and X.D. Wang, *Spontaneous Phase Transformation and Exfoliation of Rectangular Single-Crystal Zinc Hydroxy Dodecylsulfate Nanomembranes*. *Acs Nano*, 2013. **7**(7): p. 6007-6016.

123. Friedrich, I., V. Weidenhof, W. Njoroge, P. Franz, and M. Wuttig, *Structural transformations of Ge<sub>2</sub>Sb<sub>2</sub>Te<sub>5</sub> films studied by electrical resistance measurements*. Journal of Applied Physics, 2000. **87**(9): p. 4130-4134.
124. Py, M.A. and R.R. Haering, *Structural Destabilization Induced by Lithium Intercalation in MoS<sub>2</sub> and Related-Compounds*. Canadian Journal of Physics, 1983. **61**(1): p. 76-84.
125. Joensen, P., R.F. Frindt, and S.R. Morrison, *Single-Layer MoS<sub>2</sub>*. Materials Research Bulletin, 1986. **21**(4): p. 457-461.
126. Matte, H., A. Gomathi, A.K. Manna, D.J. Late, R. Datta, et al., *MoS<sub>2</sub> and WS<sub>2</sub> Analogues of Graphene*. Angewandte Chemie-International Edition, 2010. **49**(24): p. 4059-4062.
127. Coleman, J.N., M. Lotya, A. O'Neill, S.D. Bergin, P.J. King, et al., *Two-Dimensional Nanosheets Produced by Liquid Exfoliation of Layered Materials*. Science, 2011. **331**(6017): p. 568-571.
128. Joensen, P., E.D. Crozier, N. Alberding, and R.F. Frindt, *A Study of Single-Layer and Restacked MoS<sub>2</sub> by X-Ray-Diffraction and X-Ray Absorption-Spectroscopy*. Journal of Physics C-Solid State Physics, 1987. **20**(26): p. 4043-4053.
129. Mak, K.F., C. Lee, J. Hone, J. Shan, and T.F. Heinz, *Atomically Thin MoS<sub>2</sub>: A New Direct-Gap Semiconductor*. Physical Review Letters, 2010. **105**(13).
130. Frindt, R.F. and A.D. Yoffe, *Physical Properties of Layer Structures: Optical Properties and Photoconductivity of Thin Crystals of Molybdenum Disulphide*. Proceedings of the Royal Society A, 1963. **273**: p. 69-83.

131. Eda, G., H. Yamaguchi, D. Voiry, T. Fujita, M. Chen, et al., *Photoluminescence from Chemically Exfoliated MoS<sub>2</sub>*. Nano Letters, 2011. **11**(12): p. 5111-5116.
132. Tsai, H.L., J. Heising, J.L. Schindler, C.R. Kannewurf, and M.G. Kanatzidis, *Exfoliated-restacked phase of WS<sub>2</sub>*. Chemistry of Materials, 1997. **9**(4): p. 879-&.
133. Coehoorn, R., C. Haas, J. Dijkstra, C.J.F. Flipse, R.A. Degroot, et al., *Electronic-Structure of MoSe<sub>2</sub>, MoS<sub>2</sub>, and WSe<sub>2</sub> .1. Band-Structure Calculations and Photoelectron-Spectroscopy*. Physical Review B, 1987. **35**(12): p. 6195-6202.
134. Wang, H., X.L. Liu, and Z.M. Zhang, *Absorption Coefficients of Crystalline Silicon at Wavelengths from 500 nm to 1000 nm*. International Journal of Thermophysics, 2013. **34**(2): p. 213-225.
135. Donertas, M.E. and M. Gunes, *Light induced degradation of hydrogenated amorphous silicon-germanium alloy (a-SiGe : H) thin films*. Journal of Optoelectronics and Advanced Materials, 2005. **7**(1): p. 503-506.
136. Caballero, R. and C. Guillen, *Cu(In,Ga)Se-2 thin films evaporation for photovoltaic applications*. Boletin De La Sociedad Espanola De Ceramica Y Vidrio, 2004. **43**(2): p. 370-372.
137. Mitchell, K., A.L. Fahrenbruch, and R.H. Bube, *PHOTOVOLTAIC DETERMINATION OF OPTICAL-ABSORPTION COEFFICIENT IN CDTE*. Journal of Applied Physics, 1977. **48**(2): p. 829-830.
138. Leitao, J.P., N.M. Santos, P.A. Fernandes, P.M.P. Salome, A.F. da Cunha, et al., *Study of optical and structural properties of Cu<sub>2</sub>ZnSnS<sub>4</sub> thin films*. Thin Solid Films, 2011. **519**(21): p. 7390-7393.

139. Smestad, G., A. Ennaoui, S. Fiechter, H. Tributsch, W.K. Hofmann, et al., *PHOTOACTIVE THIN-FILM SEMICONDUCTING IRON PYRITE PREPARED BY SULFURIZATION OF IRON-OXIDES*. Solar Energy Materials, 1990. **20**(3): p. 149-165.
140. Consador.F and R.F. Frindt, *CRYSTAL SIZE EFFECTS ON EXCITON ABSORPTION SPECTRUM OF WSe2*. Physical Review B, 1970. **2**(12): p. 4893-&.
141. Klein, A., Y. Tomm, R. Schlaf, C. Pettenkofer, W. Jaegermann, et al., *Photovoltaic properties of WSe2 single-crystals studied by photoelectron spectroscopy*. Solar Energy Materials and Solar Cells, 1998. **51**(2): p. 181-191.
142. Ku, G., M. Zhou, S.L. Song, Q. Huang, J. Hazle, et al., *Copper Sulfide Nanoparticles As a New Class of Photoacoustic Contrast Agent for Deep Tissue Imaging at 1064 nm*. Acs Nano, 2012. **6**(8): p. 7489-7496.
143. Uhuegbu, C., *Solution Growth Technique for Iron Copper Sulphide Ternary Thin Film and Its Optical Characteristics*. American Journal of Scientific and Industrial Research, 2010. **1**(2): p. 392-396.
144. Moreels, I., D. Kruschke, P. Glas, and J.W. Tomm, *The dielectric function of PbS quantum dots in a glass matrix*. Optical Materials Express, 2012. **2**(5): p. 496-500.
145. Merdes, S., R. Mainz, J. Klaer, A. Meeder, H. Rodriguez-Alvarez, et al., *12.6% efficient CdS/Cu(In,Ga)S-2-based solar cell with an open circuit voltage of 879 mV prepared by a rapid thermal process*. Solar Energy Materials and Solar Cells, 2011. **95**(3): p. 864-869.

146. AbuShama, J.A.M., S. Johnston, T. Moriarty, G. Teeter, K. Ramanathan, et al., *Properties of ZnO/CdS/CuInSe<sub>2</sub> solar cells with improved performance*. Progress in Photovoltaics, 2004. **12**(1): p. 39-45.
147. Bernardi, M., M. Palummo, and J.C. Grossman, *Extraordinary Sunlight Absorption and One Nanometer Thick Photovoltaics Using Two-Dimensional Monolayer Materials*. Nano Letters, 2013. **13**(8): p. 3664-3670.
148. Kittel, C., *Introduction to Solid State Physics*. 8 ed. 2004, New York: Wiley.
149. Baikie, T., Y.N. Fang, J.M. Kadro, M. Schreyer, F.X. Wei, et al., *Synthesis and crystal chemistry of the hybrid perovskite (CH<sub>3</sub>NH<sub>3</sub>)PbI<sub>3</sub> for solid-state sensitised solar cell applications*. Journal of Materials Chemistry A, 2013. **1**(18): p. 5628-5641.
150. Im, J.H., C.R. Lee, J.W. Lee, S.W. Park, and N.G. Park, *6.5% efficient perovskite quantum-dot-sensitized solar cell*. Nanoscale, 2011. **3**(10): p. 4088-4093.
151. Sun, S.Y., T. Salim, N. Mathews, M. Duchamp, C. Boothroyd, et al., *The origin of high efficiency in low-temperature solution-processable bilayer organometal halide hybrid solar cells*. Energy & Environmental Science, 2014. **7**(1): p. 399-407.
152. Ito, K. and T. Nakazawa, *ELECTRICAL AND OPTICAL-PROPERTIES OF STANNITE-TYPE QUATERNARY SEMICONDUCTOR THIN-FILMS*. Japanese Journal of Applied Physics Part 1-Regular Papers Short Notes & Review Papers, 1988. **27**(11): p. 2094-2097.
153. Devika, M., N.K. Reddy, K. Ramesh, R. Ganesan, K.R. Gunasekhar, et al., *Thickness effect on the physical properties of evaporated SnS films*. Journal of the Electrochemical Society, 2007. **154**(2): p. H67-H73.

154. Avellaneda, D., G. Delgado, M.T.S. Nair, and P.K. Nair, *Structural and chemical transformations in SnS thin films used in chemically deposited photovoltaic cells*. Thin Solid Films, 2007. **515**(15): p. 5771-5776.
155. Domingo, G., R.S. Itoga, and C.R. Kannewurf, *Fundamental Optical Absorption in SnS<sub>2</sub> and SnSe<sub>2</sub>*. Physical Review, 1966. **143**(2): p. 536-541.
156. Rothwarf, A. and H. Windawi, *THE CONTROLLING INFLUENCE OF THE CU<sub>2</sub>S OPTICAL-ABSORPTION COEFFICIENT ON THE SHORT-CIRCUIT CURRENTS OF CU<sub>2</sub>S-CDS SOLAR-CELLS*. Ieee Transactions on Electron Devices, 1981. **28**(1): p. 64-69.
157. Thanikaikarasan, S., T. Mahalingam, M. Raja, T. Kim, and Y.D. Kim, *Characterization of electroplated FeSe thin films*. Journal of Materials Science-Materials in Electronics, 2009. **20**(8): p. 727-734.
158. Wadia, C., A.P. Alivisatos, and D.M. Kammen, *Materials Availability Expands the Opportunity for Large-Scale Photovoltaics Deployment*. Environmental Science & Technology, 2009. **43**(6): p. 2072-2077.
159. Kubaschewski, O., *Iron - Binary Phase Diagrams*. 1982, New York: Springer-Verlag.
160. Wadia, C., Y. Wu, S. Gul, S.K. Volkman, J. Guo, et al., *Surfactant-Assisted Hydrothermal Synthesis of Single phase Pyrite FeS(2) Nanocrystals*. Chemistry of Materials, 2009. **21**(13): p. 2568-2570.
161. Ennaoui, A., S. Fiechter, C. Pettenkofer, N. Alonso-Vante, K. Buker, et al., *IRON DISULFIDE FOR SOLAR-ENERGY CONVERSION*. Solar Energy Materials and Solar Cells, 1993. **29**(4): p. 289-370.



162. Oertel, J., K. Ellmer, W. Bohne, J. Rohrich, and H. Tributsch, *Growth of n-type polycrystalline pyrite (FeS<sub>2</sub>) films by metalorganic chemical vapour deposition and their electrical characterization*. Journal of Crystal Growth, 1999. **198**: p. 1205-1210.
163. Ennaoui, A., S. Schroetter, S. Fiechter, and H. Tributsch, *INFRARED SPECTROSCOPIC AND X-RAY-DIFFRACTION CHARACTERIZATION OF IRON DISULFIDE THIN-FILMS PREPARED BY METAL ORGANIC-CHEMICAL VAPOR-DEPOSITION*. Journal of Materials Science Letters, 1992. **11**(16): p. 1131-1133.
164. Ennaoui, A., S. Fiechter, H. Tributsch, M. Giersig, R. Vogel, et al., *PHOTOELECTROCHEMICAL ENERGY-CONVERSION OBTAINED WITH ULTRATHIN ORGANO-METALLIC-CHEMICAL-VAPOR-DEPOSITION LAYER OF FES<sub>2</sub> (PYRITE) ON TIO<sub>2</sub>*. Journal of the Electrochemical Society, 1992. **139**(9): p. 2514-2518.
165. Luther, G.W., *PYRITE SYNTHESIS VIA POLYSULFIDE COMPOUNDS*. Geochimica Et Cosmochimica Acta, 1991. **55**(10): p. 2839-2849.
166. Puthussery, J., S. Seefeld, N. Berry, M. Gibbs, and M. Law, *Colloidal Iron Pyrite (FeS<sub>2</sub>) Nanocrystal Inks for Thin-Film Photovoltaics*. Journal of the American Chemical Society, 2011. **133**(4): p. 716-719.
167. Macpherson, H.A. and C.R. Stoldt, *Iron Pyrite Nanocubes: Size and Shape Considerations for Photovoltaic Application*. Acs Nano, 2012. **6**(10): p. 8940-8949.

168. Bi, Y., Y.B. Yuan, C.L. Exstrom, S.A. Darveau, and J.S. Huang, *Air Stable, Photosensitive, Phase Pure Iron Pyrite Nanocrystal Thin Films for Photovoltaic Application*. Nano Letters, 2011. **11**(11): p. 4953-4957.
169. Chianelli, R.R., A.F. Ruppert, S.K. Behal, B.H. Kear, A. Wold, et al., *The Reactivity of MoS<sub>2</sub> Single-Crystal Edge Planes*. Journal of Catalysis, 1985. **92**(1): p. 56-63.
170. Tributsch, H. and J.C. Bennett, *ELECTROCHEMISTRY AND PHOTOCHEMISTRY OF MOS<sub>2</sub> LAYER CRYSTALS .I.* Journal of Electroanalytical Chemistry, 1977. **81**(1): p. 97-111.
171. Anderson, A.B., Z.Y. Alsaigh, and W.K. Hall, *HYDROGEN ON MOS<sub>2</sub> - THEORY OF ITS HETEROLYTIC AND HOMOLYTIC CHEMISORPTION*. Journal of Physical Chemistry, 1988. **92**(3): p. 803-809.
172. Byskov, L.S., M. Bollinger, J.K. Norskov, B.S. Clausen, and H. Topsøe, *Molecular aspects of the H<sub>2</sub> activation on MoS<sub>2</sub> based catalysts the role of dynamic surface arrangements*. Journal of Molecular Catalysis a-Chemical, 2000. **163**(1-2): p. 117-122.
173. Bollinger, M.V., J.V. Lauritsen, K.W. Jacobsen, J.K. Norskov, S. Helveg, et al., *One-Dimensional Metallic Edge States in MoS<sub>2</sub>*. Physical Review Letters, 2001. **87**(19).
174. Hagenbach, G., P. Courty, and B. Delmon, *CATALYTIC ACTIVITY OF COBALT AND MOLYBDENUM SULFIDES IN HYDROGENOLYSIS OF THIOPHENE, HYDROGENATION OF CYCLOHEXENE, AND ISOMERIZATION OF CYCLOHEXANE*. Journal of Catalysis, 1971. **23**(2): p. 295-&.

175. Vrubel, H., D. Merki, and X.L. Hu, *Hydrogen evolution catalyzed by MoS<sub>3</sub> and MoS<sub>2</sub> particles*. Energy & Environmental Science, 2012. **5**(3): p. 6136-6144.
176. Wang, T.Y., L. Liu, Z.W. Zhu, P. Papakonstantinou, J.B. Hu, et al., *Enhanced Electrocatalytic Activity for Hydrogen Evolution Reaction from Self-Assembled Monodispersed Molybdenum Sulfide Nanoparticles on an Au Electrode*. Energy & Environmental Science, 2013. **6**(2): p. 625-633.
177. Peng, Y., H.L. Zhang, S.L. Pan, and H.L. Li, *Magnetic properties and magnetization reversal of alpha-Fe nanowires deposited in alumina film*. Journal of Applied Physics, 2000. **87**(10): p. 7405-7408.
178. Zhang, L.Y., D.S. Xue, X.F. Xu, A.B. Gui, and C.X. Gao, *The fabrication and magnetic properties of nanowire-like iron oxide*. Journal of Physics-Condensed Matter, 2004. **16**(25): p. 4541-4548.
179. Chen, D.L. and L. Gao, *A facile route for high-throughput formation of single-crystal alpha-Fe<sub>2</sub>O<sub>3</sub> nanodisks in aqueous solutions of Tween 80 and triblock copolymer*. Chemical Physics Letters, 2004. **395**(4-6): p. 316-320.
180. Pregelj, M., P. Umek, B. Drolc, B. Jancar, Z. Jaglicic, et al., *Synthesis, structure, and magnetic properties of iron-oxide nanowires*. Journal of Materials Research, 2006. **21**(11): p. 2955-2962.
181. Wang, H.Z., X.T. Zhang, B. Liu, H.L. Zhao, Y.C. Li, et al., *Synthesis and characterization of single crystal alpha-Fe<sub>2</sub>O<sub>3</sub> nanobelts*. Chemistry Letters, 2005. **34**(2): p. 184-185.
182. Woo, K., H.J. Lee, J.P. Ahn, and Y.S. Park, *Sol-gel mediated synthesis of Fe<sub>2</sub>O<sub>3</sub> nanorods*. Advanced Materials, 2003. **15**(20): p. 1761-+.

183. Zhong, L.S., J.S. Hu, H.P. Liang, A.M. Cao, W.G. Song, et al., *Self-assembled 3D flowerlike iron oxide nanostructures and their application in water treatment*. *Advanced Materials*, 2006. **18**(18): p. 2426-+.
184. Fu, Y.Y., R.M. Wang, J. Xu, J. Chen, Y. Yan, et al., *Synthesis of large arrays of aligned alpha-Fe<sub>2</sub>O<sub>3</sub> nanowires*. *Chemical Physics Letters*, 2003. **379**(3-4): p. 373-379.
185. Wang, R.M., Y.F. Chen, Y.Y. Fu, H. Zhang, and C. Kisielowski, *Bicrystalline hematite nanowires*. *Journal of Physical Chemistry B*, 2005. **109**(25): p. 12245-12249.
186. Kim, C.H., H.J. Chun, D.S. Kim, S.Y. Kim, J. Park, et al., *Magnetic anisotropy of vertically aligned alpha-Fe<sub>2</sub>O<sub>3</sub> nanowire array*. *Applied Physics Letters*, 2006. **89**(22).
187. Chueh, Y.L., M.W. Lai, J.Q. Liang, L.J. Chou, and Z.L. Wang, *Systematic study of the growth of aligned arrays of alpha-Fe<sub>2</sub>O<sub>3</sub> and Fe<sub>3</sub>O<sub>4</sub> nanowires by a vapor-solid process*. *Advanced Functional Materials*, 2006. **16**(17): p. 2243-2251.
188. Liu, F., P.J. Cao, H.R. Zhang, J.F. Tian, C.W. Xiao, et al., *Novel nanopyramid arrays of magnetite*. *Advanced Materials*, 2005. **17**(15): p. 1893-+.
189. Cvelbar, U., Z.Q. Chen, M.K. Sunkara, and M. Mozetic, *Spontaneous Growth of Superstructure alpha-Fe<sub>2</sub>O<sub>3</sub> Nanowire and Nanobelt Arrays in Reactive Oxygen Plasma*. *Small*, 2008. **4**(10): p. 1610-1614.
190. Kumar, V., J.H. Kim, C. Pendyala, B. Chernomordik, and M.K. Sunkara, *Gas-Phase, Bulk Production of Metal Oxide Nanowires and Nanoparticles Using a*

- Microwave Plasma Jet Reactor*. Journal of Physical Chemistry C, 2008. **112**(46): p. 17750-17754.
191. Chernomordik, B.D., H.B. Russell, U. Cvelbar, J.B. Jasinski, V. Kumar, et al., *Photoelectrochemical activity of as-grown, alpha-Fe<sub>2</sub>O<sub>3</sub> nanowire array electrodes for water splitting*. Nanotechnology, 2012. **23**(19).
192. Chen, Z.Q., U. Cvelbar, M. Mozetic, J.Q. He, and M.K. Sunkara, *Long-range ordering of oxygen-vacancy planes in alpha-Fe<sub>2</sub>O<sub>3</sub> nanowires and nanobelts*. Chemistry of Materials, 2008. **20**(9): p. 3224-3228.
193. Thurman, R., *Bulk Synthesis of Metal Oxide Nanowires*, in *Chemical Engineering*. 2006, University of Louisville: Louisville. p. 82.
194. Thangala, J., S. Vaddiraju, R. Bogale, R. Thurman, T. Powers, et al., *Large-scale, hot-filament-assisted synthesis of tungsten oxide and related transition metal oxide nanowires*. Small, 2007. **3**(5): p. 890-896.
195. Cummins, D.R., *Synthesis of Molybdenum Oxide Nanowires and Their Facile Conversion to Molybdenum Sulfide*, in *Chemical Engineering*. 2009, University of Louisville: Louisville, KY. p. 51.
196. Chen, Z., D. Cummins, B.N. Reinecke, E. Clark, M.K. Sunkara, et al., *Core-shell MoO<sub>3</sub>-MoS<sub>2</sub> Nanowires for Hydrogen Evolution: A Functional Design for Electrocatalytic Materials*. Nano Letters, 2011. **11**(10): p. 4168-4175.
197. Fleger, S.L., Heckman, J. W., and Klomparens, K.L., *Scanning and Transmission Electron Microscopy: An Introduction*. 1993, New York: Oxford University Press.
198. Fultz, B., Howe, J. M., *Transmission Electron Microscopy and Diffractometry of Materials*. 3rd ed. 2008, New York: Springer-Verlag.

199. Cullity, B.D., and S.R. Stock, *Elements of X-Ray Diffraction*. 3rd ed. 2001, Upper Saddle River, NJ: Prentice Hall.
200. Smith, E., Geoffrey Dent, *Modern Raman Spectroscopy: A Practical Approach*. 2005, New York: John Wiley & Sons.
201. Rutherford, E., *The Scattering of alpha and beta Particles by Matter and Structure of the Atom*. Philosophical Magazine, 1911. **21**(6): p. 669-688.
202. Cummins, D.R., U. Martinez, R. Kappera, D. Voiry, A. Martinez-Garcia, et al., *Mechanistic Origin of High Catalytic Activity in MoS<sub>2</sub> Nanowires Following Chemical Intercalation*. Under Review, 2014.
203. Chen, Z.B., T.F. Jaramillo, T.G. Deutsch, A. Kleiman-Shwarsctein, A.J. Forman, et al., *Accelerating materials development for photoelectrochemical hydrogen production: Standards for methods, definitions, and reporting protocols*. Journal of Materials Research, 2010. **25**(1): p. 3-16.
204. Tan, M.X., P.E. Laibinis, S.T. Nguyen, J.M. Kesselman, C.E. Stanton, et al., *Principles and Applications of Semiconductor Photoelectrochemistry*, in *Progress in Inorganic Chemistry*, K.D. Karlin, Editor. 1994, John Wiley & Sons, Inc.: New York.
205. Walter, M.G., E.L. Warren, J.R. McKone, S.W. Boettcher, Q.X. Mi, et al., *Solar Water Splitting Cells (vol 110, pg 6446, 2010)*. Chemical Reviews, 2011. **111**(9): p. 5815-5815.
206. Chen, Z.B., H.N. Dinh, and E. Miller, *Photoelectrochemical Water Splitting*. Springer Briefs in Energy. 2013, New York: Springer.

207. Pentland, N.B., J. O.; Sheldon, E., *Hydrogen Evolution Reaction on Copper, Gold, Molybdenum, Palladium, Rhodium, and Iron*. Journal of the Electrochemical Society, 1957. **104**(3): p. 182-194.
208. Conway, B.E. and B.V. Tilak, *Interfacial Processes Involving Electrocatalytic Evolution and Oxidation of H<sub>2</sub>, and the Role of Chemisorbed H*. Electrochimica Acta, 2002. **47**(22–23): p. 3571-3594.
209. Daage, M. and R.R. Chianelli, *Structure-Function Relations in Molybdenum Sulfide Catalysts - The Rim-Edge Model*. Journal of Catalysis, 1994. **149**(2): p. 414-427.
210. Hou, Y.D., B.L. Abrams, P.C.K. Vesborg, M.E. Bjorketun, K. Herbst, et al., *Bioinspired molecular co-catalysts bonded to a silicon photocathode for solar hydrogen evolution*. Nature Materials, 2011. **10**(6): p. 434-438.
211. Boettcher, S.W., E.L. Warren, M.C. Putnam, E.A. Santori, D. Turner-Evans, et al., *Photoelectrochemical Hydrogen Evolution Using Si Microwire Arrays*. Journal of the American Chemical Society, 2011. **133**(5): p. 1216-1219.
212. Chen, Z., D. Cummins, B. Reinecke, E. Clark, M. Sunkara, T. Jaramillo, *Core-Shell MoO<sub>3</sub>-MoS<sub>2</sub> Nanowires for Hydrogen Evolution: A Functional Design for Electrocatalytic Materials*. Nano Letters, 2011. **11**(10): p. 4168-4175.
213. Wang, C.H., C.N. Lee, and H.S. Weng, *Effect of acid treatment on the performance of the CuO-MoO<sub>3</sub>/Al<sub>2</sub>O<sub>3</sub> catalyst for the destructive oxidation of (CH<sub>3</sub>)<sub>2</sub>S-2*. Industrial & Engineering Chemistry Research, 1998. **37**(5): p. 1774-1780.

214. Kroger, M., S. Hamwi, J. Meyer, T. Riedl, W. Kowalsky, et al., *P-type doping of organic wide band gap materials by transition metal oxides: A case-study on Molybdenum trioxide*. *Organic Electronics*, 2009. **10**(5): p. 932-938.
215. Rogers, D.B., R.D. Shannon, A.W. Sleight, and J.L. Gillson, *Crystal Chemistry of Metal Dioxides with Rutile-Related Structures*. *Inorganic Chemistry*, 1969. **8**(4): p. 841-849.
216. Eyert, V., R. Horny, K.H. Hock, and S. Horn, *Embedded Peierls instability and the electronic structure of MoO<sub>2</sub>*. *Journal of Physics-Condensed Matter*, 2000. **12**(23): p. 4923-4946.
217. Pourbaix, M., *Atlas of Electrochemical Equilibria in Aqueous Solutions*. 2nd ed. 1974, Houston, TX: NACE International.
218. Ebner, M., F. Marone, M. Stampanoni, and V. Wood, *Visualization and Quantification of Electrochemical and Mechanical Degradation in Li Ion Batteries*. *Science*, 2013. **342**(6159): p. 716-720.
219. Winter, M., G.H. Wrodnigg, J.O. Besenhard, W. Biberacher, and P. Novak, *Dilatometric Investigations of Graphite Electrodes in Nonaqueous Lithium Battery Electrolytes*. *Journal of the Electrochemical Society*, 2000. **147**(7): p. 2427-2431.
220. Li, H., Q. Zhang, C.C.R. Yap, B.K. Tay, T.H.T. Edwin, et al., *From Bulk to Monolayer MoS<sub>2</sub>: Evolution of Raman Scattering*. *Advanced Functional Materials*, 2012. **22**(7): p. 1385-1390.
221. Frey, G.L., R. Tenne, M.J. Matthews, M.S. Dresselhaus, and G. Dresselhaus, *Raman and Resonance Raman Investigation of MoS<sub>2</sub> Nanoparticles*. *Physical Review B*, 1999. **60**(4): p. 2883-2892.



222. Papageorgopoulos, C.A. and W. Jaegermann, *Li Intercalation Across and Along the Van-der-Waals Surfaces of MoS<sub>2</sub>(0001)*. Surface Science, 1995. **338**(1-3): p. 83-93.
223. Stankovich, S., D.A. Dikin, R.D. Piner, K.A. Kohlhaas, A. Kleinhammes, et al., *Synthesis of graphene-based nanosheets via chemical reduction of exfoliated graphite oxide*. Carbon, 2007. **45**(7): p. 1558-1565.
224. Eda, G., G. Fanchini, and M. Chhowalla, *Large-area ultrathin films of reduced graphene oxide as a transparent and flexible electronic material*. Nature Nanotechnology, 2008. **3**(5): p. 270-274.
225. Acrivos, J.V., *On the Intercalation Reaction*, in *Intercalated Layered Materials*, F. Levy, Editor. 1979, D. Reidel Publishing Company: Dordrecht, Holland. p. 33-98.
226. Subba Rao, G.V.S., M.W., *Intercalation in Layered Transition Metal Dichalcogenides*. Intercalated Layered Materials, ed. F. Levy. 1979, Dordrecht, Holland: D. Reidel Publishing Company.
227. Schollhorn, R., E. Sick, and A. Lerf, *REVERSIBLE TOPOTACTIC REDOX REACTIONS OF LAYERED DICHALCOGENIDES*. Materials Research Bulletin, 1975. **10**(10): p. 1005-1012.
228. Kanatzidis, M.G., *Semiconductor physics - Quick-set thin films*. Nature, 2004. **428**(6980): p. 269-+.
229. Hu, B., L.Q. Mai, W. Chen, and F. Yang, *From MoO<sub>3</sub> Nanobelts to MoO<sub>2</sub> Nanorods: Structure Transformation and Electrical Transport*. ACS Nano, 2009. **3**(2): p. 478-482.

230. Desai, P.D., T.K. Chu, H.M. James, and C.Y. Ho, *ELECTRICAL-RESISTIVITY OF SELECTED ELEMENTS*. Journal of Physical and Chemical Reference Data, 1984. **13**(4): p. 1069-1096.
231. Cummins, D.R., Russell, H. B., Jasinski, J. B., Menon, M., and Sunkara, M. K., *Iron Sulfide (FeS) Nanotubes Using Sulfurization of Hematite Nanowires*. Nano Letters, 2013. **13**(6): p. 2423-2430.
232. Wan, D., Y. Wang, B. Wang, C. Ma, H. Sun, et al., *Effects of the crystal structure on electrical and optical properties of pyrite FeS<sub>2</sub> films prepared by thermally sulfurizing iron films*. Journal of Crystal Growth, 2003. **253**(1-4): p. 230-238.
233. Ouertani, B., J. Ouerfelli, M. Saadoun, B. Bessais, H. Ezzaouia, et al., *Characterization of FeS-pyrite thin films synthesized by sulphuration of amorphous iron oxide films pre-deposited by spray pyrolysis*. Materials Characterization, 2005. **54**(4-5): p. 431-437.
234. Lutz, H.D. and P. Willich, *LATTICE VIBRATION-SPECTRA .9. PYRITE STRUCTURE - FIR SPECTRA AND NORMAL COORDINATE ANALYSIS OF MNS<sub>2</sub>, FES<sub>2</sub>, AND NIS<sub>2</sub>*. Zeitschrift Fur Anorganische Und Allgemeine Chemie, 1974. **405**(2): p. 176-182.
235. Blanchard, M., F. Poitrasson, M. Meheut, M. Lazzeri, F. Mauri, et al., *Iron isotope fractionation between pyrite (FeS<sub>2</sub>), hematite (Fe<sub>2</sub>O<sub>3</sub>) and siderite (FeCO<sub>3</sub>): A first-principles density functional theory study*. Geochimica Et Cosmochimica Acta, 2009. **73**(21): p. 6565-6578.

236. Mernagh, T.P. and A.G. Trudu, *A LASER RAMAN MICROPROBE STUDY OF SOME GEOLOGICALLY IMPORTANT SULFIDE MINERALS*. Chemical Geology, 1993. **103**(1-4): p. 113-127.
237. de Faria, D.L., S. Venancio Silva, and M. T. de Oliveira, *Raman Microspectroscopy of Some Iron Oxides and Oxyhydroxides*. Journal of Raman Spectroscopy, 1997. **28**: p. 873-878.
238. Menon, M., *Strain Induced Raman Shift in FeS Crystal*, D.R. Cummins, 2013 - 2014, University of Louisville, **Personal Communication**
239. Vargas, W.E., *Inversion methods from Kiabelka-Munk analysis*. Journal of Optics a-Pure and Applied Optics, 2002. **4**(4): p. 452-456.
240. Sakkopoulos, S., E. Vitoratos, and T. Argyreas, *ENERGY-BAND DIAGRAM FORPYRRHOTITE*. Journal of Physics and Chemistry of Solids, 1984. **45**(8-9): p. 923-928.
241. Perdew, J.P., K. Burke, and M. Ernzerhof, *Generalized gradient approximation made simple*. Physical Review Letters, 1996. **77**(18): p. 3865-3868.
242. Andriotis, A.N., G. Mpourmpakis, S. Lisenkov, R.M. Sheetz, and M. Menon, *U-calculation of the LSDA plus U functional using the hybrid B3LYP and HSE functionals*. Physica Status Solidi B-Basic Solid State Physics, 2013. **250**(2): p. 356-363.
243. Dudarev, S.L., G.A. Botton, S.Y. Savrasov, C.J. Humphreys, and A.P. Sutton, *Electron-energy-loss spectra and the structural stability of nickel oxide: An LSDA+U study*. Physical Review B, 1998. **57**(3): p. 1505-1509.

244. Kresse, G. and D. Joubert, *From ultrasoft pseudopotentials to the projector augmented-wave method*. Physical Review B, 1999. **59**(3): p. 1758-1775.
245. Condit, R.H., R.R. Hobbins, and C.E. Birchenall, *SELF-DIFFUSION OF IRON AND SULFUR IN FERROUS SULFIDE*. Oxidation of Metals, 1974. **8**(6): p. 409-455.
246. Watson, E.B., D.J. Cherniak, and E.A. Frank, *Retention of biosignatures and mass-independent fractionations in pyrite: Self-diffusion of sulfur*. Geochimica Et Cosmochimica Acta, 2009. **73**(16): p. 4792-4802.
247. Danielewski, M., S. Mrowec, and A. Stoklosa, *Sulfidation of Iron at High Temperatures and Diffusion Kinetics in Ferrous Sulfide*. Oxidation of Metals, 1982. **17**(Nos. 1/2): p. 77-97.
248. Reddy, K.T.R., N.K. Reddy, and R.W. Miles, *Photovoltaic properties of SnS based solar cells*. Solar Energy Materials and Solar Cells, 2006. **90**(18-19): p. 3041-3046.
249. Tripathi, A.M. and S. Mitra, *Tin sulfide (SnS) nanorods: structural, optical and lithium storage property study*. Rsc Advances, 2014. **4**(20): p. 10358-10366.
250. Wang, L.Y., L.H. Zhuo, Y.C. Yu, and F.Y. Zhao, *High-rate performance of SnS<sub>2</sub> nanoplates without carbon-coating as anode material for lithium ion batteries*. Electrochimica Acta, 2013. **112**: p. 439-447.
251. Meduri, P., E. Clark, E. Dayalan, G.U. Sumanasekera, and M.K. Sunkara, *Kinetically limited de-lithiation behavior of nanoscale tin-covered tin oxide nanowires*. Energy & Environmental Science, 2011. **4**(5): p. 1695-1699.

252. Nguyen, T.Q., A.K. Thapa, V.K. Vendra, J.B. Jasinski, G.U. Sumanasekera, et al., *High rate capacity retention of binder-free, tin oxide nanowire arrays using thin titania and alumina coatings*. Rsc Advances, 2014. **4**(7): p. 3312-3317.
253. Vendra, V.K., T.Q. Nguyen, T. Druffel, J.B. Jasinski, D.A. Amos, et al., *Nanowire architectures for iodide free dye-sensitized solar cells*. Journal of Materials Chemistry A, 2014. **2**(10): p. 3543-3550.
254. Vijayarangamuthu, K. and S. Rath, *Nanoparticle size, oxidation state, and sensing response of tin oxide nanopowders using Raman spectroscopy*. Journal of Alloys and Compounds, 2014. **610**: p. 706-712.
255. Kaur, M., N.S. Ramgir, U.K. Gautam, S.K. Ganapathi, S. Bhattacharya, et al., *H<sub>2</sub>S sensors based on SnO<sub>2</sub> films: RGTO verses RF sputtering*. Materials Chemistry and Physics, 2014. **147**(3): p. 707-714.
256. Dieguez, A., A. Romano-Rodriguez, A. Vila, and J.R. Morante, *The complete Raman spectrum of nanometric SnO<sub>2</sub> particles*. Journal of Applied Physics, 2001. **90**(3): p. 1550-1557.
257. Chen, D., G.Z. Shen, K.B. Tang, S.J. Lei, H.G. Zheng, et al., *Microwave-assisted polyol synthesis of nanoscale SnS<sub>x</sub>(x=1,2) flakes*. Journal of Crystal Growth, 2004. **260**(3-4): p. 469-474.
258. Gou, X.L., J. Chen, and P.W. Shen, *Synthesis, characterization and application of SnS<sub>x</sub> (x=1, 2) nanoparticles*. Materials Chemistry and Physics, 2005. **93**(2-3): p. 557-566.
259. Woodrow, T.A. and B.P. Works. *Tracer Diffusion in Whisker-Prone Tin Platings*. in *SMTA International Conference*. 2006. Rosemont, IL.

260. Shi, W. and B.A. Lu, *Nanoscale Kirkendall Effect Synthesis of Echinus-like SnO<sub>2</sub>@SnS<sub>2</sub> Nanospheres as High Performance Anode Material for Lithium Ion Batteries*. *Electrochimica Acta*, 2014. **133**: p. 247-253.
261. Thompson, B.A. and R.L. Strong, *Self-Diffusion of Oxygen in Lead Oxide*. *Journal of Physical Chemistry*, 1963. **67**(3): p. 594-597.
262. Pavlov, D., *PROCESSES IN SOLID-STATE AT ANODIC-OXIDATION OF A LEAD ELECTRODE IN H<sub>2</sub>SO<sub>4</sub> SOLUTION AND THEIR DEPENDENCE ON OXIDE STRUCTURE AND PROPERTIES*. *Electrochimica Acta*, 1978. **23**(9): p. 845-854.
263. Laitinen, T. and J.P. Pohl, *THE KINETICS OF OXIDE-GROWTH AND OXYGEN EVOLUTION DURING POTENTIOSTATIC POLARIZATION OF LEAD IN H<sub>2</sub>SO<sub>4</sub> ELECTROLYTES - INVESTIGATIONS ON THE TEMPERATURE-DEPENDENCE*. *Electrochimica Acta*, 1989. **34**(3): p. 377-385.
264. Wang, Y.L., L. Cai, and Y.N. Xia, *Monodisperse spherical colloids of Pb and their use as chemical templates to produce hollow particles*. *Advanced Materials*, 2005. **17**(4): p. 473-+.

## CURRICULUM VITAE

Dustin R. Cummins

### PROFESSIONAL PREPARATION.

**Ph.D. (Dec, 2014)** Chemical Engineering, University of Louisville, Louisville, KY

**M.Eng. (2009)** Chemical Engineering, University of Louisville, Louisville, KY

**B.S. (2008)** Chemical Engineering, University of Louisville, Louisville, KY

Ph.D. Dissertation: “Phase Transformation Studies of Metal Oxide to Dichalcogenides in 1-D structures”

Advisor: M. K. Sunkara

M.Eng. Thesis: “Synthesis of Molybdenum oxide nanowires and their facile conversion to Molybdenum sulfide”

Advisor: M. K. Sunkara

### WORK EXPERIENCE and ACCOMPLISHMENTS

1. Conn Center for Renewable Energy Research, University of Louisville, Louisville, KY  
*Graduate Research Assistant* May 2008 – Jan 2014
  - 4 publications in peer reviewed journals, as well as at least 2 in stages of submission. >150 citations to date.
  - Coordinated collaborations with multiple universities and National Labs: Los Alamos National Lab (Mohite and Gupta), Rutgers University (Chhowalla), Stanford University (Jaramillo), University of Hawaii-Manoa (Galliard), University of Kentucky (Menon).
  - Worked closely with theorists to apply computer modeling and DFT calculations to real world results.
  - Developed strong communication skills, both interpersonal as well as presenting/defending research findings at technical conferences.
  - Participated in PEC Water-Splitting working group for the US Dept. of Energy: networking collaborations and provided research insight
  - Created and optimized synthesis methods for transition metal oxide nanowire arrays and thin films using CVD and plasma applications.
  - Extensive experience in operation, analysis, and instrument maintenance of crystal characterization techniques.
2. Los Alamos National Laboratory, Los Alamos, NM  
*Graduate Student Research Affiliate* July 2013 – March 2014
  - Developed a competency in electrocatalysis and hydrogen production to set-up and operate a water-splitting development and evaluation capabilities, focusing on layered 2D semiconductors and nanowires.

- Investigated crystallographic modifications of MoS<sub>2</sub> nanostructures (e.g. lithium intercalation, electron doping using hydrazine, NH<sub>3</sub>, etc.) and measured the effect on electrocatalysis.
  - Developed synthesis schemes for new nano-morphologies of layered chalcogenide catalysts (MoS<sub>2</sub>, MoSe<sub>2</sub>, WS<sub>2</sub>, WSe<sub>2</sub>).
  - Exposure to graphene synthesis and organic photovoltaics.
3. The Dallas Group of America, Inc., Jeffersonville, IN  
*Engineering Research and Development Co-op* January 2006 - August 2007
- Laboratory Analysis of chemical adsorbents for oils and biodiesel
  - Use and repair of industrial reactors, filtration, and drying equipment and modeling using VBA, specializing in **powder handling and processing**.

## TECHNICAL SKILLS

- Chemical Vapor Deposition and Materials Processing
  - Knowledge of working principles of chemical vapor deposition (**CVD**) and nanowire growth with expertise in designing, building and troubleshooting vacuum reactors and vacuum systems.
  - Experienced with both atmospheric and vacuum plasma systems for materials synthesis.
- Materials Characterization –
  - Expertise in Nanomaterials characterization: Powder X-Ray diffraction (**XRD**), scanning electron microscopy (**SEM**), Energy-Dispersive X-ray (**EDS**), **Raman**, Photoluminescence (**PL**), Optical Absorption Spectroscopy (**UV-Vis**).
  - Limited hands-on experiment, but well versed in transmission electron microscopic (**TEM**) working principles and techniques; experience in analyzing electron diffraction spectra.
  - Very experienced in high-vacuum spectroscopy: X-ray and UV photoelectron spectroscopy (**XPS & UPS**) in both operation and interpretation/deconvolution of the spectra.
  - Working knowledge of optics and focusing/tuning Ultra-Fast femtosecond pulse lasers.
  - Understanding of the working principles of pump-probe spectroscopy, transient absorption, and charge carrier lifetimes.
- Photo-Electrochemistry and Electrocatalysis
  - Experienced in 3 probe measurements of semiconductor performance for water splitting: Hydrogen and Oxygen evolution reaction (**HER and OER**)
  - Analysis of cyclic voltammograms to determine Tafel slope, on-set potentials, solar efficiency, etc.
  - Strong understanding of semiconductor physics, especially **2D Materials** with emphasis in solar energy and water splitting applications.

## AWARDS:

- NASA Kentucky Space Grant Consortium: Graduate Fellowship – 2014
- 2<sup>nd</sup> Place: Best Presentation–Renewable Energy & Energy Efficiency Workshop 2013:Conn Center

## AFFILIATIONS AND ORGANIZATIONS



### Professional:

- Tau Beta Pi: The Engineering Honor Society
- Electrochemical Society
- Material Research Society
- American Institute of Chemical Engineers

### PUBLICATIONS

1. **D.R. Cummins**, R. Kappera, A. Martinez, J. Jasinski, U. Martinez M. Chhowalla, M. K. Sunkara, A. Mohite, and G. Gupta, "Electron Doping of Molybdenum Disulfide Nanowires using Hydrazine", 2014, *In Preparation*.
2. **D. R. Cummins**, U. Martinez, R. Kappera, D. Voiry, A. Martinez, J. Jasinski, D. Kelly, M. Chhowalla, M. K. Sunkara, A. D. Mohite, and G. Gupta, "High Catalytic Activity of Molybdenum Disulfide Nanowires Following Chemical Intercalation", 2014 *Submitted*.
3. **D. R. Cummins**, H. B. Russell, M. Menon, J. Jasinski, And M. K. Sunkara, "Iron Sulfide (FeS) Nanotubes Using Sulfurization of Hematite Nanowires", *Nano Letters*, 13(6), 2013. Citations: **10**
4. B. Pandit, T. Luitel, **D. R. Cummins**, A. K. Thapa, T. Druffel, F. Zamborini, and J. Liu, "Spectroscopic investigation of Photoinduced Charge Transfer Processes in FTO/TiO<sub>2</sub>/N719 Photoanodes with and without Covalent Attachment through Silane-based Linkers", *Journal of Physical Chemistry A*, 117 (50), 2013.
5. Z. Chen, **D. R. Cummins**, E. L. Clark, B. Reinecke, M. K. Sunkara, and T. F. Jaramillo, "Core-shell MoO<sub>3</sub>-MoS<sub>2</sub> Nanowires for Hydrogen Evolution: A Functional Design for Electrocatalytic Materials", *Nano Letters*, 11(10), 2011. Citations: **138**
6. M. K. Sunkara, C. Pendyala, **D. R. Cummins**, P. Meduri, J. Jasinski, V. Kumar, H. B. Russell, E. Clark, and J. H. Kim, "Inorganic nanowires: a perspective about their role in energy conversion and storage applications", *Journal of Physics D-Applied Physics*, 44(17), 2011. Citations: **17**

### CONFERENCE PRESENTATIONS (Speaker\*)

1. **D. Cummins\***, R. Kappera, A. Martinez, J. Jasinski, H. Yamaguchi, M. Chhowalla, M. K. Sunkara, A. Mohite, and G. Gupta, "Enhanced Catalytic Activity in Electron-Doped Molybdenum Disulfide Nanowires for Hydrogen Production", Oral Presentation, 2014 Materials Research Society Spring Meeting, April 21 - 25, 2014, San Francisco, CA.
2. **D. Cummins\***, H. Russell, J. Jasinski, M. Menon, and M. Sunkara, "Iron Sulfide (FeS) Nanotubes using Transformation of Hematite Nanowires to One-Dimensional Pyrite Nanostructures", Poster Presentation, 2013 Materials Research Society Fall Meeting, Dec. 1 - 6, 2013, Boston, MA.

3. **D. Cummins\***, H. Russell, J. Jasinski, M. Sunkara, "Transformation of Hematite Nanowires to One-Dimensional Pyrite Nanostructures", Poster Presentation, 2012 Materials Research Society Fall Meeting, Nov. 25 - 30, 2012, Boston, MA. **(Nominated for Best Poster)**
4. **D. Cummins\***, H. Russell, J. Jasinski, and M. Sunkara, "Synthesis of Phase Pure Pyrite Nanowires/Nanotubes for Solar Energy Applications", Oral Presentation, PRiME 2012, Oct. 7 - 12, 2012, Honolulu, HI.
5. Z. Chen\*, **D. R. Cummins**, B. Reinecke, E. Clark, M. K. Sunkara and T. F. Jaramillo, "MoS<sub>2</sub> Nanostructures As Efficient, Stable, and Earth-Abundant Catalysts for Hydrogen Evolution In Acid", Oct. 17-24, Annual Meeting of American Institute of Chemical Engineers (AIChE), 2011.
6. **D.R. Cummins\***, J.B. Jasinski, and M.K. Sunkara, "Phase transformation of Iron oxide nanowires to Iron sulfide", Oral Presentation, 2010 Fall Annual Meeting of AIChE, Salt Lake City, UT, November 11-17 (2010).
7. M.K. Sunkara\*, C. Pendyala, J.B. Jasinski, J-H. Kim, **D.R. Cummins**, H.B. Russell, "*New materials search using nanowires for solar hydrogen*", Invited Paper, Solar Nanotechnology Symposium, SPIE Photonics West, San Diego, CA, August 3-6, 2010.
8. M.K. Sunkara\*, C. Pendyala, **D. Cummins**, B. Chernomordik, V. Kumar, H. Russell, V. Chakrapani and J. Thangala, "Materials Search for Solar Hydrogen Using Nanowires", Invited Presentation, ECS Spring Meeting, April 25-30, Vancouver, Canada (2010).
9. M.K. Sunkara\*, B. Chernomordik, V. Chakrapani, C. Pendyala, **D. Cummins**, J. Kim, P. Meduri and J. Thangala, "Nitride based materials and nanowire based assemblies for photolysis of water", Gordon Conference on Solar Fuels, February 2-6, 2009, Ventura, CA.
10. M. K. Sunkara\*, C. Pendyala, B. Chernomordik, **D. Cummins**, H. Russell, J. Kim, J. Thangala, "New Materials Search for Solar Fuels using Nanowires, 2010 Electrochemical Society Meeting, Invited Talk